UNIVERSITY OF NOTTINGHAM

DOCTORAL THESIS

Lateral and Vertical Graphene/Hexagonal Boron Nitride Heterostructures Grown by Molecular Beam Epitaxy

---

Author:
James. C. THOMAS

Supervisor:
Prof. Peter. H. BETON

Thesis submitted to the University of Nottingham
for the degree of Doctor of Philosophy

in the

Nottingham Nanoscience
Department of Physics & Astronomy



January 7, 2021

Abstract

Lateral and Vertical Graphene/Hexagonal Boron Nitride Heterostructures Grown by Molecular Beam Epitaxy

by James. C. THOMAS

This thesis discusses the investigation of graphene/ hexagonal Boron Nitride (hBN) heterostructures grown by Sergei V. Novikov and Tin S. Cheng using molecular beam epitaxy (MBE), with a focus on measurements recorded using atomic force microscopy (AFM), in particular conductive AFM (CAFM). MBE is a relatively uncommon deposition technique for graphene growth that offers a route to scaleable high quality material. In this thesis three different carbon sources have been used to grow strained graphene samples at high temperature (up to $\sim$ 1700 °C) on exfoliated hBN flakes. These samples have been subsequently analysed using a range of techniques including AFM, CAFM, lateral force microscopy (LFM), Raman spectroscopy, and angle resolved photoemission spectroscopy (ARPES). A particular focus is placed on the recorded strain of these structures, measured with the aid of the hexagonal graphene/ hBN moiré superlattice pattern formed at the interface of the stacked 2D structure. In order to carry out the CAFM measurements shown, electrical contacting procedures have been developed as part of this work in order to measure electrically isolated graphene/ hBN regions. The most prominent of these methods has been the deposition of a conductive silver nanowire networking layer.

During AFM contact mode scanning the appearance of a graphene/ hBN moiré pattern deformation that follows the tip scan direction was observed and has been investigated. Large differences between trace (forward scan) and retrace (backwards scan) imaging have been seen in the resulting moiré pattern. These differences have been explained by considering the strong tip-surface interaction between the probe and the graphene surface, along with the large locally applied pressure exerted by the tip that increases the graphene/ hBN van der Waals interaction.

Using an electron beam carbon source for MBE graphene growth, a high level of precision has been achieved that has allowed for narrow graphene bands with uniform and tuneable widths below 20 nm to be grown along hBN step edges and around hBN islands. These graphene nanoribbons have formed lateral graphene/ hBN junctions on hBN material produced within the same system using plasma assisted MBE, demonstrating successful sequential growth of these heterostructures. Investigations of these samples are carried out within this thesis, along with a potentially useful hydrogen etching method for hBN that could be used as a lithographic technique in conjunction with these samples.

Acknowledgements

I would like to thank the EPSRC for allowing me to carry out this research and to pursue a PhD degree. A pursuit that has been incredibly enjoyable, due both to the interesting subject matter and fantastic people I have had the pleasure of meeting and working alongside throughout. Undertaking a PhD is no small task, and next to impossible to carry out without collaboration from many helpful and eager colleagues and friends.

First and foremost I would like to thank my PhD supervisor, Peter Beton, for his continued support, ideas, and insight throughout all of the research carried out within this thesis, none of which would be possible without him.

I would also like to thank my secondary supervisor, Sergei Novikov, along with Tin Cheng, whose expertise in MBE growth has been integral in the production of the samples investigated within this thesis, Vladimir Korolkov, who showed me the ropes of AFM scanning that would form the basis of this work, Alex Summerfield whose assistance and knowledge was pivotal in the success of the research carried out here, and Juan Albar who was always keen to lend a helping hand. I would also like to thank all of those who contributed to the growth and investigations of the graphene samples that are discussed, including Jonathan Bradford, Laurence Eaves, Tom Foxon, Tyler James, Andrei Khlobystov, Christopher Mellor, and James Wrigley. I would also like to thank those within the Nottingham nanoscience department who have provided assistance, in particular James Kerfoot, Manal Alkhamisi, Alex Saywell, Philip Moriarty, Alexander Allen, Filipe Junqueira, and Graham Rance. In addition, I would like to thank Neil Wilson and all who helped at the Elletra synchrotron to obtain the ARPES measurements shown within this thesis.

Finally, I would like to thank my close family for their continued patience and unwavering support throughout my PhD and for putting up with my whingeing while writing in the midst of a global pandemic. In particular, both of my parents, Nicola and Andrew Thomas, whose encouragement and support made this mammoth task accomplishable, my sister, Victoria, her husband, Arthur, and their daughter Isabelle.

Contents

Abstract i

Acknowledgements ii

1 Introduction 1
1.1 Thesis Overview . . . 3

2 Theoretical background 5
2.1 Graphene . . . 5
2.1.1 Structural and Electronic Properties . . . 6
2.1.2 Bilayer Graphene . . . 12
2.1.3 Graphene Nanoribbons . . . 14
2.2 Hexagonal Boron Nitride . . . 15
2.2.1 Lattice structure . . . 16
2.2.2 Electrical properties . . . 17
2.3 Graphene/hBN heterostructure . . . 17
2.3.1 Van der Waals interaction . . . 17
2.3.2 The Moiré Pattern . . . 18
Strained Material . . . 20
Superlattice Dirac Points . . . 22
2.4 Atomic Force Microscopy . . . 23
2.4.1 Basic Principles . . . 23
2.4.2 Operational modes . . . 26
Contact mode . . . 26
Conductive mode . . . 28
Non-contact mode . . . 29
2.5 Tip-surface interaction . . . 32
2.5.1 Surface deformation . . . 33

3 Methodology 36
3.1 Optical Microscopy . . . 36
3.2 Scanning Electron Microscopy . . . 37

3.3 Atomic Force Microscopy . . . 39
3.3.1 AFM Calibration . . . 40
Lateral calibration . . . 42
3.4 Angle-Resolved Photoemission Spectroscopy . . . 45
3.5 Raman Spectroscopy . . . 47
3.6 Materials . . . 49
3.6.1 Substrates . . . 49
Silicon Dioxide . . . 49
Sapphire . . . 50
Highly Oriented Pyrolytic Graphite . . . 50
3.6.2 Silver Nanowires . . . 50
3.7 Growth and Deposition . . . 51
3.7.1 Graphene Production . . . 51
3.7.2 MBE Graphene . . . 51
Carbon Filament . . . 54
Elemental Carbon Source . . . 54
E-beam Source . . . 55
3.7.3 Hexagonal Boron Nitride Production . . . 57
MBE hBN . . . 57
3.8 Data Processing . . . 58

4 Processing and Electrical Contact Formation **59**
4.1 Shadow Masking . . . 60
4.2 Epoxy Contacts . . . 60
4.3 Nanowire Deposition . . . 62
4.4 Flake Transfer . . . 66
4.5 Summary . . . 68

5 Strained MBE Grown Graphene **69**
5.1 Introduction . . . 69
5.2 Unstrained Graphene . . . 70
5.3 Strained Graphene . . . 75
5.3.1 Raman Measurements . . . 76
5.3.2 ARPES Measurements . . . 79
5.3.3 Strain Relaxation . . . 82
5.4 Lattice Matched Graphene . . . 86
5.4.1 Lattice Matched Raman Measurements . . . 89
5.4.2 Lattice Matched ARPES Measurements . . . 90
5.4.3 Relaxation of Lattice Matched Material . . . 92

5.5 Lattice Defects . . . 93
5.6 Summary . . . 102

6 Tip-Induced Moiré Deformation **104**
6.1 Introduction . . . 104
6.2 Moiré asymmetries . . . 104
6.3 Force-Distance Curves . . . 105
6.3.1 Force investigations . . . 109
6.4 Heterostructure Stacking Configurations . . . 111
6.5 Strain Maps . . . 113
6.6 Trace-Retrace Differences . . . 116
6.7 Set Point Ramps . . . 120
6.8 Summary . . . 126

7 Step-Flow Growth of Graphene-hBN Lateral Heterostructures **128**
7.1 Introduction . . . 128
7.2 Growth Conditions . . . 129
7.3 Ex Situ Measurements of Nanoribbon Growth . . . 130
7.4 Investigating the Nanoribbon Growth Mechanisms . . . 132
7.4.1 Graphene-only Islands . . . 138
7.5 Raman Measurements of MBE hBN and Graphene Nanoribbons . . . 140
7.6 Conclusions . . . 141

8 Hydrogen Etching of Hexagonal Boron Nitride **143**
8.1 Introduction . . . 143
8.2 Hydrogen Etching . . . 143
8.2.1 The Appearance of hBN Etching . . . 143
8.2.2 Etching of Exfoliated hBN with MBE Graphene Nanoribbons . . . 146
8.2.3 Etching of Exfoliated hBN . . . 149
8.2.4 Etching of MBE Grown hBN . . . 151
8.3 Conclusions . . . 158

9 Conclusions **160**

Bibliography **163**

A Nanowire Manipulation **181**

B FIB Milling **184**

C Spiral Nanoribbon **188**

D hBN Fold Appearance **189**

List of Figures

2.1 Properties of graphene . . . 7
2.2 Graphene Bandstructure . . . 10
2.3 Bilayer Graphene Bandstructure . . . 13
2.4 Graphene Nanoribbons . . . 16
2.5 hBN Bandstructure . . . 18
2.6 The formation of a moiré pattern . . . 19
2.7 Superlattice Dirac Points . . . 21
2.8 AFM basic principles . . . 24
2.9 LFM and CAFM . . . 27
2.10 Amplitude vs Frequency plot . . . 31
2.11 The tip-sample interaction . . . 34

3.1 OM and SEM . . . 38
3.2 Lateral Force Imaging . . . 43
3.3 ARPES . . . 46
3.4 Raman . . . 48
3.5 Mechanical Exfoliation and MBE . . . 52
3.6 Epitaxial Growth . . . 53
3.7 Elemental Carbon Source . . . 55
3.8 E-Beam . . . 56

4.1 Flake attachment and nanowire deposition . . . 61
4.2 NW deposition . . . 62
4.3 NW conductivity tests . . . 64
4.4 AFM of Deposited NWs . . . 65
4.5 Flake transferal . . . 67

5.1 Unstrained Graphene . . . 72
5.2 Comparison with Conductive AFM . . . 73
5.3 Lattice Resolution CAFM . . . 74
5.4 Multiple moiré Wavelengths . . . 76
5.5 Raman for Strained Graphene . . . 77

5.6 ARPES for Strained and Unstrained . . . 81
5.7 ARPES for Multilayer Graphene . . . 82
5.8 Relaxation . . . 83
5.9 Uniaxial Strain . . . 85
5.10 Infinite moiré . . . 86
5.11 F-K Domain Walls . . . 88
5.12 Raman for Lattice Matched Graphene . . . 89
5.13 ARPES for Lattice Matched Graphene . . . 91
5.14 Relaxation of Lattice Matched . . . 93
5.15 F-K Termination Defect Diagram . . . 94
5.16 IV Measurements on Defects . . . 96
5.17 Defects . . . 97
5.18 Termination Defect . . . 98
5.19 Reconstruction . . . 100
5.20 Lattice Matched Defect . . . 101
5.21 Stone-Wales defect . . . 102

6.1 Moiré Asymmetries . . . 106
6.2 Force-Distance Curves . . . 107
6.3 Effect of Force on Moiré Imaging . . . 110
6.4 Effect of Force on Infinite Moiré Imaging . . . 110
6.5 Tip-Induced Theory . . . 111
6.6 Strain Maps . . . 114
6.7 Additional Strain Maps . . . 115
6.8 Trace/Retrace Difference with LFM . . . 117
6.9 Trace/Retrace Images . . . 119
6.10 Varying Force LFM . . . 121
6.11 Set Point Ramp Profiles . . . 124
6.12 Set Point Ramp Profiles Peak Positions . . . 125

7.1 Before and after nanoribbon growth . . . 131
7.2 Nanoribbon growth . . . 132
7.3 Nanoribbon widths . . . 134
7.4 Lattice alignment of hBN and graphene nanoribbons . . . 135
7.5 Nanoribbon Moiré Pattern . . . 136
7.6 Moiré over HOPG . . . 137
7.7 Graphene-only islands . . . 138
7.8 Island Defect Reconstruction . . . 139
7.9 Lateral Heterostructure Raman Spectroscopy . . . 140

8.1 Graphene Nanoribbon growth on Exfoliated hBN 145
8.2 Etching on Exfoliated hBN with Nanoribbon Growth 146
8.3 Additional Etching on Exfoliated hBN with Nanoribbon Growth 148
8.4 Etching of hBN Trenches 149
8.5 Exfoliated hBN Etching 152
8.6 MBE hBN Etching 153
8.7 Etching Orientations 154
8.8 Domain Boundary Etching 156
8.9 Edge Changes at Boundaries 157

A.1 Nanowire manipulation 182
A.2 Nanowire manipulation for devices 183

B.1 FIB milling 185
B.2 FIB milling of hBN flakes 187

C.1 hBN screw dislocation 188

D.1 Appearance of hBN Folds 189

List of Abbreviations

hBN	**h**exagonal **B**oron **N**itride
AFM	**A**tomic **F**orce **M**icroscope/**M**icroscopy
AM-AFM	**A**mplitude **M**odulated **A**tomic **F**orce **M**icroscope/**M**icroscopy
FM-AFM	**F**requency **M**odulated **A**tomic **F**orce **M**icroscope/**M**icroscopy
CAFM	**C**onductive **A**tomic **F**orce **M**icroscopy
NW	**N**ano**W**ire
CVD	**C**hemical **V**apour **D**eposition
STM	**S**canning **T**unneling **M**icroscopy
IPA	**I**so**p**ropyl **A**lcohol
LFM	**L**ateral **F**orce **M**icroscopy
PZT	Lead **Z**irconate **T**itanate
F-K	**F**renkel-**K**ontorova
MBE	**M**olecular **B**eam **E**pitaxy/**E**pitaxial
GNR	**G**raphene **N**ano**r**ibbons
HOPG	**H**ighly **O**riented **P**yrolytic **G**raphite
L-J	**L**ennard-**J**ones
SEM	**S**canning **E**lectron **M**icroscope/**M**icroscopy
ARPES	**A**ngle **R**esolved **P**hoto**e**mission **S**pectroscopy
CCD	**C**harge **C**oupled **D**evice
CNF	**C**arbon **N**ano**f**iber
SEI	**S**econdary **E**lectron **I**maging
FAD	**F**ree **A**ir **D**eflection
InvOLS	**Inv**erse **O**ptical **L**ever **S**ensitivity
LHS	**L**eft-**H**and **S**ide
RHS	**R**ight-**H**and **S**ide
XPS	**X**-ray **P**hotoelectron **S**pectroscopy
UV	**U**ltra**v**iolet
RF	**R**adio **F**requency
CNT	**C**arbon **N**ano**t**ubes
RHEED	**R**eflection **H**igh-**E**nergy **E**lectron **D**iffraction
UHV	**U**ltra-**H**igh **V**acuum
SPM	**S**canning **P**robe **M**icroscopy

FIB	**F**ocussed **I**on **B**eam
PPC	**P**oly**p**ropylene **C**arbonate
PDMS	**P**oly**dim**ethyl**s**iloxane
FFT	**F**ast **F**ourier **T**ransform
FWHM	**F**ull **W**idth at **H**alf **M**aximum
SPEM	**S**canning **P**hoto**e**mission **S**pectroscopy
DFT	**D**ensity **F**unctional **T**heory
ZZ	**Z**ig**z**ag

Chapter 1

Introduction

Since its first successful isolation in 2004 [1] graphene has led a tidal wave of related research and prompted the discovery of numerous other interesting two-dimensional materials, and subsequent heterostructures [2]. Research surrounding two dimensional materials continues to increase in recent years owed, in large part, to the increased interest in van der Waals heterostructures. These planar structures offer a wide range of interesting and novel device possibilities, with an almost limitless number of material combinations. One of the most widely reported of these heterostructures, both experimentally and theoretically, is that of the graphene-hexagonal boron nitride interface. This arrangement combines the most highly studied 2D material, graphene, with that of a wide-gap semiconductor. The properties of graphene are widely reported and have been extensively investigated using a variety of techniques including optical spectroscopy [3, 4], electrical measurements [5], as well as a range of scanning probe microscopy methods [6–9]. The most promising properties being its Dirac-like electronic transport, and stability under ambient conditions, give rise to an increased interest into its use in electronic devices. Boron nitride is also a relatively well reported material [10, 11]. In its hexagonal form (hBN) boron nitride acts as a semiconductor with a large band gap between 5.0-6.0 eV [11], that can, for many purposes, be treated as an insulator or tunnel barrier. Furthermore, the atomic structure of hBN is isostructural with graphene, with the exception that B and N atoms make up the two sub-lattices and that it exhibits a near matching lattice constant ~ 1.8 % larger than that of graphene, resulting in hBN often being referred to as white graphite.

Most commonly these heterostructures have been created using mechanical exfoliation or chemical vapour deposition (CVD). In this thesis the graphene investigated has been grown using the far less widely explored method of molecular beam epitaxy (MBE) at high temperatures (~ 1700 °C). The result is a highly strained graphene layer with a lattice constant which extends up to that of hBN, currently unreported elsewhere experimentally. The prospect of lattice matched graphene/hBN heterostructures is of importance as it is widely anticipated among theoreticians [12–15] that this commensurate form will lead to the appearance of a bandgap in graphene of $\sim 2k_BT$

(where k_B is the Boltzmann constant and T is the temperature), a requirement for its use as the operational material in transistor devices.

Atomic force microscopy (AFM) is one of the most widely used surface imaging techniques in nanoscience, and yet the crystal deformation induced by the probe tip on the surface of two-dimensional materials remains relatively unexplored despite commonly being used to image such materials. While the investigation of this deformation contained within this thesis is concentrated on the graphene-hBN heterostructure, the results can be extended and should be considered for all two-dimensional heterostructure AFM imaging, particularly during contact mode scanning.

Within this thesis the use of conductive atomic force microscopy (CAFM) as a method of probing the electrical characteristics of highly strained graphene grown by MBE on mechanically exfoliated hBN has been explored extensively. Conductive AFM, is a technique that is similar to scanning tunnelling microscopy (STM). In CAFM the tip is moved across the target surface operating under contact mode AFM using a measure of the tip-sample force as feedback, allowing for separate conductive and topography measurements to be recorded simultaneously, an advantage over STM. Furthermore, CAFM gives an increased insight into the tip-sample interaction that STM cannot provide alone, with force curves and current measurements operating in tandem. Other additional AFM scanning techniques also complement CAFM by providing readily available alternatives. These include a variety of ambient condition AFM scanning approaches including AC mode imaging using an amplitude modulated signal, and contact mode imaging with simultaneous conductive channel and lateral force measurements. A combination of these techniques have been used to explore the observed effects of applying large amounts of force to the graphene/hBN heterostructure by an AFM tip. These include significant changes to the local strain and the large scale hexagonal superlattice pattern (known as the moiré pattern).

In order to apply a sample bias to the heterostructure surface for CAFM of MBE graphene samples grown on exfoliated hBN, connections to individual flakes are required in many cases. A variety of approaches that each try to avoid damaging the fragile graphene material (notably circumventing lithographic techniques involving surface contaminating polymeric photoresists) have been developed as part of this thesis. These consist of direct flake connection using thin gold wire (15 μm diameter) with conductive epoxy resin, flake transfer using a stamping technique, and, most extensively, silver nanowire (NW) conductive networks formed by drop deposition of NWs suspended in an isopropyl alcohol (IPA) solvent solution (including combinations of these techniques).

The MBE graphene samples shown within this thesis have been grown by Sergei V. Novikov and Tin S. Cheng. This growth has included three different sources; carbon filament, tantalum encased carbon powder filament (for an atomic carbon source),

and electron beam evaporation of carbon. The latter has facilitated precise step-flow growth of thin graphene bands with a tuneable and uniform width down to less than 20 nm. Investigations into the growth mechanisms and structure of these samples are presented within this work using a variety of AFM approaches. In addition, a potentially useful fabrication technique of hBN hydrogen etching has been explored that may be used to create novel device structures.

1.1 Thesis Overview

In chapter 2 the theoretical principles that form the basis of the investigations within this thesis are discussed. These include the introduction of the structural and electronic properties of graphene and hBN, and the formation of the superlattice moiré pattern present at heterostructures between the two materials. Following this discussion, the basic physical principles of the main technique used within this thesis, atomic force microscopy, is discussed at length. The practices involved with the use of this technique, along with the many other experimental methods employed, including scanning electron microscopy, angle-resolved photoemission spectroscopy, and Raman spectroscopy are all outlined in chapter 3 alongside the sample preparation and growth procedures that were used by Sergei V. Novikov and Tin S. Cheng for the production of the MBE graphene samples that are investigated.

In the following chapter, chapter 4, the various approaches that were trialed and developed as part of this work in order to prepare electrically isolated MBE graphene regions for CAFM are considered. These processing methods include the use of conductive epoxy contact formation, transferal of individual exfoliated flakes, and the deposition of silver nanowires to form a conductive networking layer.

The various AFM and processing procedures discussed in the earlier sections are then used in chapter 5 to investigate the properties of graphene grown at high temperatures using the three different MBE sources. The different growth conditions have resulted in regions of graphene that can be unstrained, strained, and lattice matched relative to the underlying hBN, determined using a range of methods including analysis of the moiré pattern present on the heterostructure. A large section of analysis was carried out using CAFM. During this form of imaging, using contact mode AFM as the feedback mechanism, changes in the graphene-hBN moiré pattern were observed to occur, including both pattern distortion and movement of the moiré superlattice. This behaviour, due to the locally applied pressure of the AFM tip, is investigated in detail in chapter 6. In this chapter the different moiré deformations that were observed are explored using force-distance measurements, creating strain maps from high resolution CAFM images, and using lateral force microscopy to carry out repeated single line scans while increasing the applied normal force.

The third carbon MBE source used to grow graphene by Sergei V. Novikov and Tin S. Cheng, using electron beam evaporation of carbon, has allowed for more precise graphene growth. In chapter 7 this growth has been used to produce narrow strips of graphene at step edges on MBE grown hBN. In this chapter the conditions used to facilitate nanoribbon growth of graphene are described, before investigation of the growth mechanisms involved through the use of AFM and CAFM investigations of the grown material. In the subsequent chapter, chapter 8, the hydrogen etching of hBN has been investigated on these graphene nanoribbon/MBE hBN samples, along with exfoliated hBN and other MBE hBN material, as a potentially useful lithographic processing technique.

Finally, in chapter 9, the main conclusions from the various investigations discussed in this thesis are summarised.

Chapter 2

Theoretical background

In order to investigate two dimensional materials it is important not only to understand their crystal lattices, including their structural, electronic, and mechanical properties, but it is also crucial to grasp the physical principles governing the various techniques that are utilised to gather information about the samples that have been studied.

The following sections focus on elucidating the important properties of the two primary materials involved in this study, graphene and hexagonal boron nitride. The physical and electronic structure of both materials are discussed and approached from a tight binding perspective, including variations of bilayer graphene and graphene nanoribbons.

After discussing the individual materials, the physics following the formation of the graphene/hBN heterostructure is examined theoretically, in particular the formation of the hexagonal moiré pattern prevalent in many of the recorded images seen in later chapters. The relevant electronic implications of the heterostructure superlattice are explained, along with discussion of strain on constituent layers of these heterostructures.

In order to image the resulting structures a range of techniques have been used. This chapter concludes with an explanation of the underlying physical concepts of the primary imaging technique that forms the centre of the investigations within this thesis, atomic force microscopy and the varieties thereof. These include lateral force imaging (LFM) and conductive AFM (CAFM). It is important to understand the operations of this imaging method from a theoretical perspective in order to explain the results shown in later chapters recorded for the graphene and hBN surfaces that have been investigated.

2.1 Graphene

Graphene was the first ever successfully isolated two-dimensional material, discovered by *Novoselov et al* [1] in 2004 by mechanical exfoliation. Since its discovery it has

been the subject of countless scientific articles due to its unique properties that will be outlined below.

2.1.1 Structural and Electronic Properties

Graphene is a two dimensional crystalline allotrope of carbon that takes the shape of a honeycomb-structured atomic lattice. This atomic network is often described as a hexagonal lattice with a two atom basis, known as the A and B hexagonal sublattices as shown in figure 2.1a, with a thickness of a single atom. Each layer of graphene is held together by strong in-plane σ, as well as weaker out-of-plane π, covalent bonds between neigbouring carbon atoms in opposite sublattices. The σ bonds arise from the $2s$, $2p_x$, and $2p_y$ carbon orbitals which hybridise into an sp^2 configuration resulting in the 120° bond angles that make up the hexagonal lattice structure, whereas the $2p_z$ orbital perpendicular to the lattice plane is responsible for the π bonding [16]. These layers are in turn stacked to form the bulk material graphite, with interlayer, out-of-plane, and relatively weak, van der Waals bonding. The inter-layer spacing of graphene is approximately 3.35 Å. The real space lattice vectors, $\mathbf{a_G^1}$ and $\mathbf{a_G^2}$, are shown in figure 2.1a, and are given by

$$\mathbf{a_G^1} = a_G(\frac{\sqrt{3}}{2}, \frac{1}{2}), \mathbf{a_G^2} = a_G(\frac{\sqrt{3}}{2}, -\frac{1}{2}), \tag{2.1}$$

where a_G is the graphene lattice constant of 2.46 Å [17]. The three nearest neighbouring atoms on the graphene lattice are positioned at the points given by the vectors

$$\boldsymbol{\delta_G^1} = a_G(\frac{\sqrt{3}}{3}, 0), \boldsymbol{\delta_G^2} = a_G(\frac{-\sqrt{3}}{6}, \frac{1}{2}), \boldsymbol{\delta_G^3} = a_G(\frac{-\sqrt{3}}{6}, -\frac{1}{2}), \tag{2.2}$$

for the A sublattice (indicated on figure 2.1a), with those for the B sublattice being -$\boldsymbol{\delta_G^1}$, -$\boldsymbol{\delta_G^2}$, and -$\boldsymbol{\delta_G^3}$ [16]. The reciprocal lattice vectors, $\mathbf{b_G^1}$ and $\mathbf{b_G^2}$, have a similar hexagonal form given by

$$\mathbf{b_G^1} = \frac{2\pi}{a_G}(\frac{\sqrt{3}}{3}, 1), \mathbf{b_G^2} = \frac{2\pi}{a_G}(\frac{\sqrt{3}}{3}, -1). \tag{2.3}$$

Several important high symmetry locations exist within the reciprocal lattice, labelled on figure 2.2a. The centre of the 1^{st} Brillouin zone, the Γ point lies at the origin, and is surrounded by the six M points, and three pairs of K and K' points with coordinates given by,

$$\Gamma = (0, 0), M = \frac{2\pi}{a_G}(\frac{\sqrt{3}}{3}, 0), \tag{2.4}$$

$$K = \frac{2\pi}{a_G}(\frac{\sqrt{3}}{3}, \frac{1}{3}), K' = \frac{2\pi}{a_G}(\frac{\sqrt{3}}{3}, -\frac{1}{3}), \tag{2.5}$$

for the points highlighted in figure 2.2a, with the additional points easily derived from this figure using symmetry.

Many of the electronic properties of graphene can be understood by only considering the out-of-plane $2p_z$ orbitals as the $2s$, $2p_x$,and $2p_y$ orbitals are even under reflection in the graphene plane [16]. By following the tight-binding model framework first used by *Wallace et al* [18, 19] the energy dispersion/band structure of graphene can be determined. The tight-binding model is a theoretical technique that superposes the wavefunctions for each atom within a repeated (e.g. crystal) structure, by considering the atom itself and the influence of the potential due to the nearest neighbour atoms. Figure 2.1b represents this diagrammatically. This assumption of only using the nearest neighbours is reasonable due to the exponential decay of atomic wave functions.

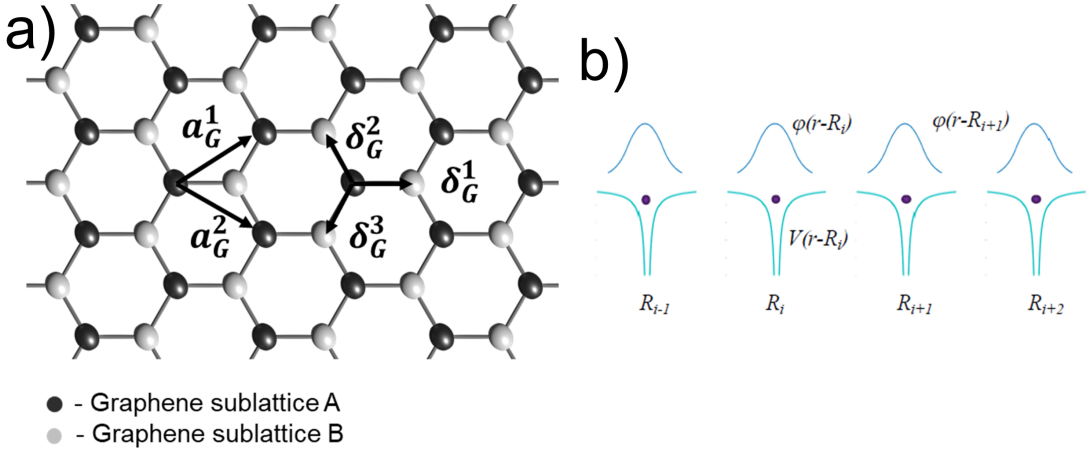


FIGURE 2.1: a) Shows the hexagonal crystal lattice of graphene. Both shades represent the position of carbon atoms, one for each sublattice. b) The tight binding model approach. The purple dots represent atomic species which can be represented by the wavefunction, ψ, indicated by the blue curves, sitting in a periodic potential, V, indicated by the turquoise curves.

For a single atom basis the wavefunction, $\Psi_k(r)$, can be written in a form that satisfies Bloch's theorem. That is to say that all solutions for $\Psi_k(r)$ for a periodic potential $V(r)$ can be expressed as a function that possesses the same periodicity as the potential, allowing for the consideration of only electrons from the unit cell. This is written as a weighted sum of atomic wavefunctions $\psi(r-R_i)$ centred on each lattice point R_i as,

$$\Psi_k(r) = \frac{1}{\sqrt{N}} \sum_{i=1}^{N} e^{i\mathbf{k}\cdot\mathbf{R_i}} \psi(\mathbf{r} - \mathbf{R_i}), \tag{2.6}$$

where N is the number of atoms summed over. From this, the energy of an electron within the crystal can be found using,

$$E(k) = \int \Psi_k^* H \Psi_k dr, \tag{2.7}$$

where the Hamiltonian is a combination of the atomic potential and the surrounding potential due to the neighbouring lattice,

$$H = H_{atom} + \Delta V(r). \tag{2.8}$$

Which for a summation across the lattice gives,

$$E(k) = \frac{1}{N} \sum_i \sum_j e^{i\mathbf{k}\cdot(\mathbf{R_i}-\mathbf{R_j})} \int \psi^*(r - R_j) H \psi(r - R_i) d\mathbf{r}, \tag{2.9}$$

that can be reduced to,

$$E(k) = E_{atom} + \alpha + \sum e^{-i\mathbf{k}\cdot\mathbf{R_j}} \int \psi^*(r - R_j) \Delta V(r) \psi(r) d\mathbf{r}, \tag{2.10}$$

when considering only the nearest neighbour atoms in the lattice of the single basis. Equation 2.10 comprises of three terms; the energy component due to the atom where the electron originates, E_{atom}, the α term due to the change in the on-site energy, which is given by,

$$\alpha = \int \psi_A^*(r) \Delta V(r) \psi_A(r) d\mathbf{r}, \tag{2.11}$$

and the overlap integral (the final term in equation 2.10) due to coupling of electrons on different sites. As stated above, equation 2.6 gives the wavefunction for a single atom basis. However, the graphene lattice consists of both A and B sublattices, and can be generalised in the form,

$$\Psi_k(r) = A(k) u_A(k, r) + B(k) u_B(k, r), \tag{2.12}$$

which is simply the linear combination of the wavefunctions for sublattice A and B. Where the electron wavefunction for sublattice A, $u_A(k, r)$, is given by the following expression in terms of momentum, k, and position, r, taken from equation 2.6,

$$u_A(k, r) = \frac{1}{\sqrt{N}} \sum_{i=1}^{N} e^{i\mathbf{k}\cdot\mathbf{R_i}} \psi_A(\mathbf{r} - \mathbf{R_i}), \tag{2.13}$$

and the electron wavefunction for sublattice B, $u_B(k, r)$, is given by the similar expression,

$$u_B(k, r) = \frac{1}{\sqrt{N}} \sum_{i=1}^{N} e^{i\mathbf{k}\cdot(\mathbf{R_i}+\boldsymbol{\delta})} \psi_B(\mathbf{r} - \mathbf{R_i} - \boldsymbol{\delta}), \tag{2.14}$$

where the lattice point location, $\mathbf{R_i}$, is shifted by the vector $\boldsymbol{\delta}$ corresponding to the displacement between the two sublattices given by equation 2.2. By using the expression for energy in equation 2.7 the energy can be described as,

$$E(k) = \frac{1}{N}\sum_i \sum_j e^{i\mathbf{k}\cdot(\mathbf{R_i}-\mathbf{R_j})} \int (A^*(k)\psi^*_{Aj} + B^* e^{-i\mathbf{k}\cdot\boldsymbol{\delta}}(k)\psi^*_{Bj}) H (A(k)\psi_{Ai} + B(k)e^{i\mathbf{k}\cdot\boldsymbol{\delta}}\psi_{Bi}) d\mathbf{r}. \tag{2.15}$$

This expression can be written in the simpler form,

$$E(k) = \sum_j e^{-i\mathbf{k}\cdot\boldsymbol{\rho_j}} H_j, \tag{2.16}$$

where $\boldsymbol{\rho_j}$ is the separation between lattice points $\mathbf{R_j} - \mathbf{R_i}$, and H_j is given by the following expression,

$$H_j = \int (A^*(k)\psi^*_A(r-\rho_j) + B^*(k)e^{-i\mathbf{k}\cdot\boldsymbol{\delta}}\psi^*_B(r-\rho_j-\delta)) H (A(k)\psi_A(r) + B(k)e^{i\mathbf{k}\cdot\boldsymbol{\delta}}\psi_B(r-\delta)) d\mathbf{r}. \tag{2.17}$$

Equation 2.17 is an expression of the sum of terms in $A(k)^*A(k), B^*(k)A(k)$, etc. and as such can be written in the form of a matrix expression given by,

$$E = (A^*(k), B^*(k)) \begin{pmatrix} H_{AA} & H_{AB} \\ H_{BA} & H_{BB} \end{pmatrix} \begin{pmatrix} A(k) \\ B(k) \end{pmatrix}, \tag{2.18}$$

where the diagonal terms are given by,

$$H_{AA} = \int \psi^*_A(r) H \psi_A(r) d\mathbf{r} = \int \psi^*_A(r) H_{atom} \psi_A(r) d\mathbf{r} + \int \psi^*_A(r) \Delta V(r) \psi_A(r) d\mathbf{r} = E_{p_z} + \alpha, \tag{2.19}$$

where equation 2.8 has been used to substitute for H, and the definition given for the on-site energy change, α, in equation 2.11 has also been used. Here E_{p_z} is the energy term due to the out-of-plane p_z atomic orbital energy levels. A similar expression to that shown in equation 2.19 can be found for the H_{BB} diagonal term. Since it is only necessary to consider the very nearest neighbours due to the exponential decay contribution to the wavefunction, only single atoms on the first sublattice are considered here (the nearest neighbours all lie on the second sublattice), with the inter-sublattice contributions contained in the off-diagonal terms. For the off-diagonal H_{AB} term of equation 2.18,

$$H_{AB} = \sum_{n.n.} e^{-i\mathbf{k}\cdot(\boldsymbol{\rho_j}-\boldsymbol{\delta})} \int \psi^*_A(r-\rho_j) H \psi_B(\mathbf{r}-\boldsymbol{\delta}) d\mathbf{r} = f(k) \int \psi^*_A(r) H \psi_B(r-\delta) d\mathbf{r} = -f(k)t, \tag{2.20}$$

In this expression the $n.n.$ notation indicates summation over the nearest neighbours, i.e. the three nearest atomic positions on the B sublattice given by the displacement

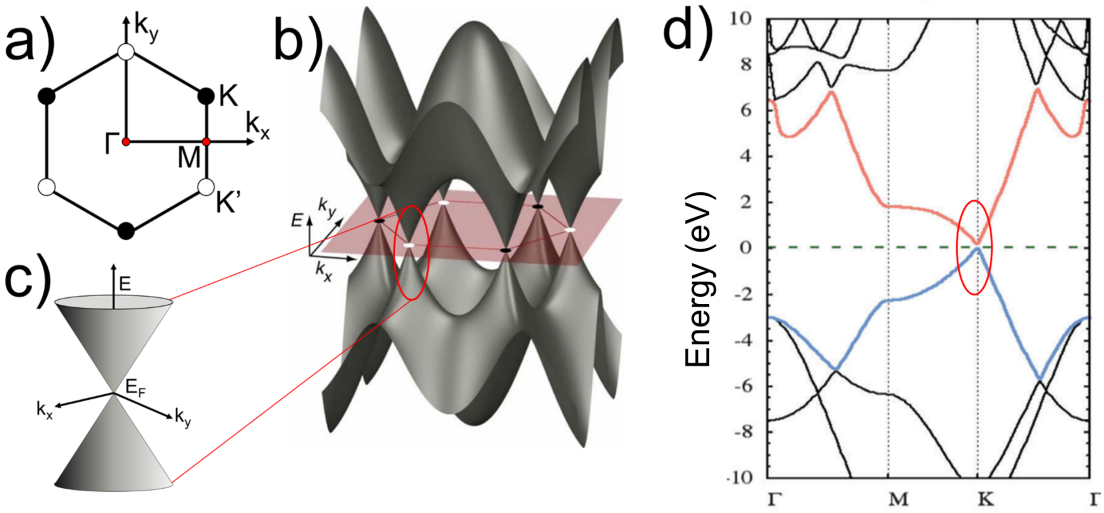


FIGURE 2.2: a) The brillouin zone of graphene, with the points of high symmetry labelled, and the wave vector directions indicated. b) The energy dispersion/band structure of graphene according to equation 2.25 in three dimensions. The Brillouin zone boundary can be seen as a red line, with the Dirac points, K and K', highlighted. The Fermi energy is indicated by the red shaded plane. Image modified from Beenakker et al [20]. c) Zoom in of the energy bands near to the Dirac point, i.e. the Dirac cone. d) A band diagram for graphene along the Γ, M, K, Γ path. Here the Fermi level is indicated by the green dashed lines, and the conduction and valence bands are highlighted by red and blue colouring respectively. The location of the Dirac cone is highlighted. Band diagram adapted from [21].

vectors in equation 2.2 as $\boldsymbol{\delta}_{\mathbf{G}}^{\mathbf{1}}$, $\boldsymbol{\delta}_{\mathbf{G}}^{\mathbf{2}}$, and $\boldsymbol{\delta}_{\mathbf{G}}^{\mathbf{3}}$. Substituting in for these displacement vectors yields the sum of phase factors given by $f(k)$ in equation 2.20, where,

$$f(k) = \left(exp\left(\frac{ik_x a_G\sqrt{3}}{3}\right) + exp\left(\frac{-ik_x a_G\sqrt{3}}{6} + \frac{k_y a_G}{2}\right) + exp\left(\frac{-ik_x a_G\sqrt{3}}{6} - \frac{k_y a_G}{2}\right)\right). \tag{2.21}$$

The final term in equation 2.20 is the overlap integral t, given by,

$$-t = \int \psi_A^*(r)\Delta V(r)\psi_B(r-\delta)d\mathbf{r}, \tag{2.22}$$

which, due to symmetry, remains the same for all three nearest neighbour atoms.

The second off-diagonal term in equation 2.18, H_{BA}, is simply the complex conjugate of H_{AB},

$$H_{BA} = H_{AB}^* = -f^*(k)t, \tag{2.23}$$

as it represents the inverse situation of the first sublattice interacting with the second, and the two sublattices are chemically identical. Returning to the matrix equation 2.18

and using the values for the derived matrix elements, with the $E_{p_z} + \alpha$ term labelled as E_0, the eigenvalue equation is obtained.

$$\begin{pmatrix} E_0 & -tf(k) \\ -tf^*(k) & E_0 \end{pmatrix} \begin{pmatrix} A(k) \\ B(k) \end{pmatrix} = E \begin{pmatrix} A(k) \\ B(k) \end{pmatrix}. \tag{2.24}$$

By setting E_0 to be the reference energy, $E_0 = 0$, the Hermitian Hamiltonian matrix becomes a hollow matrix (diagonal terms are zero). The energy eigenvalues of this equation are then given by,

$$E = E_0 \pm |f(k)| \longrightarrow E = \pm t\sqrt{1 + 4cos^2\frac{k_y a_G}{2} + 4cos\frac{\sqrt{3}k_x a_G}{2}cos\frac{k_y a_G}{2}}. \tag{2.25}$$

Hence, for the Γ point where k_x and k_y are equal to zero, see equation 2.4, $f(k)$ becomes $\pm 3t$. Here the positive value indicates the bonding orbital, with the negative representing the anti-bonding orbital, resulting in a band gap at the Γ point of $6t$. For the K and K' points given by equation 2.5, substituting into equation 2.25 for the x and y wavevector components results in an energy eigenvalue, for both positions, of zero. This leads to the zero band gap/semi-metallic nature of graphene.

In order to investigate this behaviour further, the regions close to the K and K' points can be considered by writing $\mathbf{k} = \mathbf{k_K} + \mathbf{q}$, where $\mathbf{k_K}$ is the position at the K and K' points (using K and K' positions of $(0, \pm 4\pi/3a_G)$ for simplicity), and $\mathbf{q} = (q_x, q_y)$ represents a small perturbation around the K points. After substituting these adjusted wavevectors into equation 2.21 using Euler's relationship between complex exponentials and trigonometric functions, and ignoring second order terms or higher of q values (due to the definition of q being small), $f(k)$ can be written as,

$$f(k) = \frac{i\sqrt{3}a_G}{2}(q_x \pm iq_y), \tag{2.26}$$

resulting in an energy dependence on q of,

$$E = \pm\frac{\sqrt{3}ta_G}{2}|q| = \pm\hbar v_F|q|. \tag{2.27}$$

Where v_F is the Fermi velocity. Equation 2.27 states a linear dependence between the energy and momentum near to the K and K' points in graphene. This leads to an energy dispersion with a linear band structure at each of the K and K' points at the corners of the Brillouin zone resulting in a conical shape, the Dirac cone (illustrated in figure 2.2b-d), where the conduction and valence band meet at the Fermi energy positions known as the Dirac points. At this position there is a density of states of zero. This zero band gap nature is not unique to graphene, other three-dimensional

materials such as HgTe and α-Sn (grey tin) are also gapless semiconductors, however, the high degree of electron-hole symmetry, linear dispersion around the Dirac point, two-dimensional structure, and chiral nature of the electron states gives graphene its exceptional electronic properties [5, 7, 19, 22].

The linear energy dispersion around the Dirac points in graphene given by equation 2.27 demonstrates an energy-momentum relationship that is linear, i.e. $E \propto k$, in contrast to the $E \propto k^2$ relationship seen in conventional semiconductors. This results in a carrier Fermi velocity that is independent of an energy or momentum dependence for graphene given by $v_F = \sqrt{3}ta_G/2\hbar$, which numerically is approximately 10^6 ms^{-1}. In conventional semiconductors electrons and holes obey the Schrödinger equation, whereas the charge carriers in graphene are described by the relativistic Dirac equation. The electrons and holes in graphene are analogue to relativistic particles with a rest mass of zero and an effective speed of light of $c \approx 10^6$ ms^{-1}, 300 times smaller than that of light but displaying many of the properties of quantum electrodynamics for massless fermions [17, 23, 24].

The density of states of graphene near to the Dirac point, $n_s(E)$, is given by the equation,

$$n_s(E) = g_s \times g_v \times (\frac{1}{2\pi})^2 \times 2\pi q \times \frac{dq}{dE} = \frac{2}{\pi(\hbar v_F)^2}|E|, \tag{2.28}$$

where g_s is the spin degeneracy of 2, and g_v is the valley (or pseudospin) degeneracy of 2 arising from the K and K' point symmetry. The density of states for low energies near to the Dirac point is linearly dependent on the energy, with a zero value at the Dirac point where $E = E_F$.

2.1.2 Bilayer Graphene

Bilayer graphene consists of two individual layers stacked on top of one another. The second layer is most commonly displaced from the first with half of the atoms in the upper layer situated directly over the centre of a hexagon in the lower layer, with the other half located directly above an atom in the lower layer. This type of stacking is known as Bernal stacking, seen in figure 2.3a and b), and is more common than AA stacked bilayer graphene where both layers are exactly aligned. Bilayer (and few layer) graphene is classified as a pseudo-2D sp^2 hybridized carbon structure. The extra degree of freedom in bilayer graphene allows for rotational misalignment of the two graphene layers, referred to as twisted bilayer graphene, that can be finely tuned (with sub-degree accuracy) resulting in structures displaying interesting properties including the recent observation of superconductivity in twisted bilayer graphene with an angle of 1.1°, known as the "magic angle" [25].

For the rotationally aligned Bernal stacked structure, the interlayer hopping between the two A sublattices is significant, whereas the hopping between the two B sublattices is comparatively negligible. The sublattice A hopping parameter, $t_\perp$, can be taken as 0.4 eV [19], and is an order of magnitude smaller than the nearest neighbour in plane hopping parameter. Nevertheless, by including this interlayer hopping the energy eigenvalues can be found to be [19],

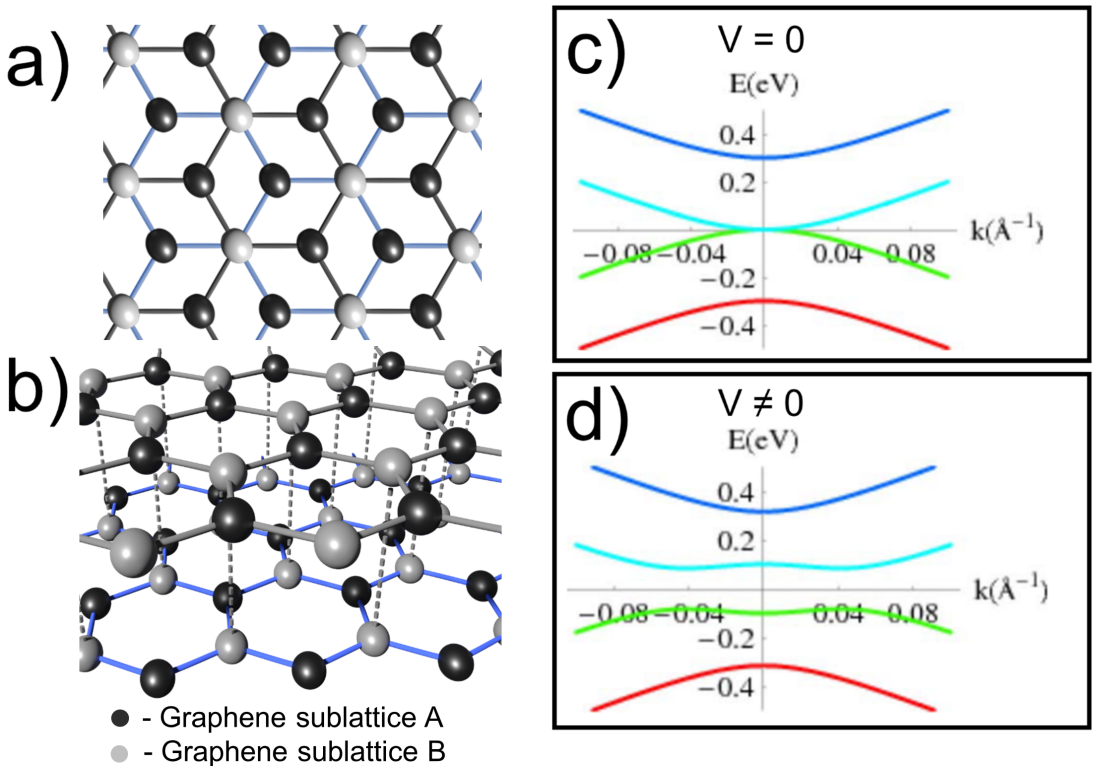


FIGURE 2.3: a) and b) show top-down and side views respectively of the Bernal stacked bilayer graphene arrangement. The graphene A and B sublattices are indicated, with the upper layer B sublattice atoms situated directly above B sublattice atoms in the lower layer, and upper A sublattice atoms situated above lower layer hexagon centres. The van der Waals interaction is indicated by the dotted lines, with lateral in-plane bonding highlighted as grey and blue in the upper and lower layers respectively for clarity. c) and d) show the band structure near to the K and K' locations for bilayer graphene without a perpendicular electric field, c), and with an applied electrical field, d), modified from [17].

$$E(k) = \pm\frac{1}{2}t_\perp \pm \sqrt{\frac{t_\perp^2}{4} + \frac{3}{4}t^2 a_G^2 |q|^2}, \tag{2.29}$$

where t, a_G, and q are as defined in section 2.1.1. The two separate $\pm$ signs indicate the four individual eigenvalues. This band structure results in the conduction and valence bands touching at the K and K' points. However, by investigating the behaviour near

to these points, as carried out for the monolayer graphene at the Dirac points, the energy dependence can be given as

$$E(k) \approx \pm\frac{3t^2a_G^2|q|^2}{4t_\perp} \approx \pm\frac{\hbar^2q^2}{2m^*}, \tag{2.30}$$

where the effective electron mass, m^*, is given by $|t_\perp|/(2v^2) \approx 0.054m_e$, where v is the electron velocity, and m_e is the mass of a free electron [19].

The result of equation 2.30 shows bilayer graphene displays the behaviour of a gapless semiconductor with a parabolic band dispersion in the low energy limit near to the Dirac point, strongly contrasting with the linear energy dispersion of single layer graphene [5]. This band structure is shown in figure 2.3c.

The situation becomes even more intriguing when applying a voltage, V, between the graphene layers perpendicular to their planes. In this case the energy eigenvalues are given by

$$E^2(k) = \frac{3t^2a_G^2|q|^2}{4} + \frac{t_\perp^2}{2} + \frac{V^2}{4} \pm \sqrt{\frac{t_\perp^2}{4} + (t_\perp^2 + V^2)\frac{3}{4}t^2a_G^2|q|^2}, \tag{2.31}$$

which, similarly to equation 2.29 can be considered near to the K and K' points to give a dispersion near to the Fermi energy of

$$E \approx \pm\Big(\frac{V}{2} - \frac{V\hbar^2v^2}{t_\perp^2}k^2 + \frac{\hbar^4v^4}{t_\perp^2 V}k^4\Big), \tag{2.32}$$

where the assumption that $\hbar vk \ll V \ll |t_\perp|$ is made for simplicity. This behaviour takes the form of a "Mexican hat" shape near the Fermi energy shown in figure 2.3d. Importantly, equation 2.32 shows that a band gap is present at the K and K' points where k = 0, where a gap, equal to V, is present. The conduction band minima are situated at $k = \pm V/(\sqrt{2}\hbar v)$ corresponding to a minimum band gap of $V(1 - \frac{V^2}{2t_\perp^2})$. This behaviour of an easily tunable band gap in bilayer graphene was experimentally confirmed by *Castro et al.*[26] and *Oostinga et al.*[27], and can reach up to approximately 250 meV [28, 29]. This tunability of the band gap makes bilayer graphene a very promising material for digital electronics applications [7].

2.1.3 Graphene Nanoribbons

Graphene nanoribbons (GNRs) are monolayer graphene strips with well defined widths, typically below approximately 50 nm, and lengths that far exceed this value. The electronic properties of GNRs depend heavily on the termination nature of their edges, which may be either zigzag or armchair [30]. Zigzag and armchair edge terminations are shown schematically in figure 2.4a. These edges are distinguished from the lattice

orientation of the edge parallel to the infinite GNR direction. Tight binding calculations used to model these materials [17, 19] predict that the bandstructure of zigzag terminated GNRs with a finite width has energy states that display metallic behaviour, as shown by the flat band in the zigzag GNR bandstructure in figures 2.4b iii) and iv) [19].

In the case of perfect zigzag GNRs the missing carbon atoms at the ribbon edge all originate from one of the graphene sublattices, either sublattice A or sublattice B. As a result, the corresponding wave function components relating to the K and K' valleys vanishes at the boundaries, leading to the metallic behaviour described above. However, for armchair terminated GNRs the number of atoms missing from the A and B sublattices is equal, which leads to behaviour that can be either metallic or semiconducting, depending on the width, L, of the GNR. The bandstructure of a relatively wide armchair terminated GNR is shown in figures 2.4b i) and ii). For armchair GNRs with a small width, a band gap is expected. This energy gap is approximately given by [19],

$$\Delta \approx \frac{\hbar v}{L}, \tag{2.33}$$

with values up to 200 meV confirmed experimentally for ribbons with widths below 15 nm [31]. For widths above this value the bandgap becomes far too small for current electronic applications. For practical application of graphene as a replacement to Si in transistor technology a required on/off ratio in excess of 10^6 is required, whereas only 10^3 is achievable with a bandgap of $\sim$ 360 meV [32].

2.2 Hexagonal Boron Nitride

Boron nitride can come in many different forms including amorphous, cubic, and wurtzite [11]. However, the most stable form is hexagonal boron nitride. Hexagonal boron nitride is a van der Waals material similar to graphene and can be mechanically exfoliated to form atomically flat surfaces. The structure of hBN, described below, makes the material a near ideal substrate for graphene and graphene growth. Historically silicon dioxide (SiO_2) has been used as a substrate for graphene investigation, however SiO_2 is comparatively far rougher, with a root mean square roughness of $\sim$ 0.2 nm, than achievable with hBN, with near atomically flat terraces with a roughness of $\sim$ 0.03 nm, comparable to the near perfect situation of layers in HOPG [6, 9, 11, 14, 33–35]. This provides a great advantage over SiO_2, allowing for investigation of more pristine graphene uninhibited by surface roughness.

In addition, studies have shown that SiO_2 as a substrate for graphene causes significant charge inhomogeneity in the graphene, whereas using hBN as a substrate results

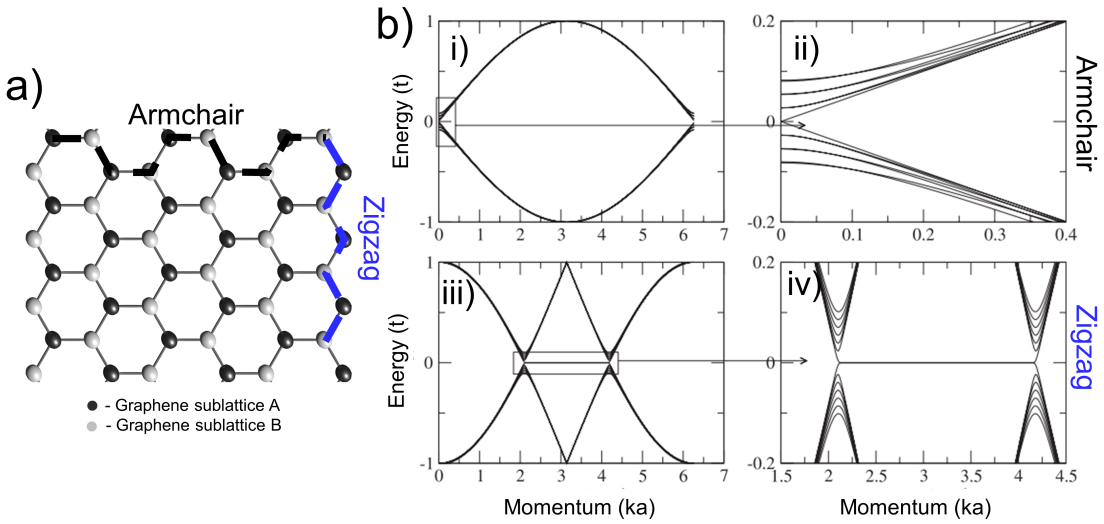


FIGURE 2.4: a) The graphene lattice structure, with A and B sublattices coloured separately, and the armchair edge and sublattice A terminated zigzag edges highlighted. The edge parallel to the infinite GNR dimension defines the categorisation of the nanoribbon. b) The electronic band structure of armchair, top row (i) and ii)), and zigzag, bottom row (iii) and iv) edged nanoribbons, modified from [17]. Panels ii) and iv) show zooms near to the zero energy of panels i) and iii). For the case of zigzag GNRs, an energy state existing at zero energy, seen in iv), results in metallic behaviour. For armchair GNRs a band gap is expected at the Dirac point for small widths. The energy is measured in units of the hopping parameter, t (∼3 eV).

in a much greater charge carrier mobility measured in devices, with mobilities between 3-10 times larger than SiO_2 and comparable to suspended graphene [9, 35–37], indicative of lower inhomogeneity of charge distribution in the graphene.

These combined properties couple to make hBN a near optimal substrate for both studying graphene experimentally, and for potential electrical application [11].

2.2.1 Lattice structure

The lattice structure of hBN is very similar to graphene, so much so that the primitive lattice vectors, reciprocal lattice vectors, and nearest neighbour vectors are identical to those given in equations 2.1, 2.3, and 2.2 respectively. However, for hBN the lattice constant, a_{BN}, is slightly ($\sim 1.8\%$) larger, with $a_{BN} = 2.50$ Å [11]. hBN is formed from two different atomic species. In graphene the A and B sites are both filled by carbon atoms, whereas in hBN one sublattice consists solely of boron atoms, while the other contains only nitrogen atoms, see figure 2.1a for the lattice structure of hBN. Bulk hBN consists of several layered stacks, with each layer situated directly above the next, alternating to have N atoms positioned directly above B atoms, as shown schematically in figure 2.5a.

2.2.2 Electrical properties

The electronic properties of hBN can be formulated in a similar way to those of graphene, with the most notable difference being the inequivalence of the two constituent atoms. Using a similar approach to that used in the previous section for graphene, i.e. using the tight binding model, the dispersion relation is given by [16]

$$E = \pm\sqrt{v_{BN}^2 k^2 + (\Delta_{BN}/2)^2}, \tag{2.34}$$

where Δ_{BN} is the difference between the on-site energies E_N and E_B for the $2p_z$ orbitals of nitrogen and boron respectively ($\approx$ 4.6 eV), and v_{BN} is the Dirac velocity for hBN. From equation 2.34 the hBN bandgap is expected to equal approximately Δ_{BN}, indicating that it is a wide bandgap semiconductor. Experimentally this bandgap has been found to be slightly larger than predicted, with a value of $\sim$ 5.97 eV [11, 38], and as such can be treated as an insulator for most purposes and is often used as a tunneling barrier in certain device structures [39–42]. The band structure for hBN is shown in figure 2.5c.

2.3 Graphene/hBN heterostructure

Graphene/hBN heterostructures can be formed either by mechanical stamping of exfoliated flakes, or through the growth of one material on the surface of another [2]. The heterostructures investigated within this thesis consist of a variety of different samples. These include graphene grown directly by MBE onto mechanically exfoliated hBN on a sapphire substrate, and hBN grown by MBE on a highly oriented pyrolytic graphite (HOPG) substrate. In addition, some of the MBE hBN samples have included further growth of graphene by MBE. The layers that make up these heterostructures are held together by van der Waals interactions between the constituent layers.

2.3.1 Van der Waals interaction

The van der Waals interaction is generally an attractive force, far weaker than both ionic or covalent attraction, between two atoms that originates due to fluctuations in the electron orbitals of an atom. These fluctuations result in a momentarily polarized atom that, in turn, stimulates induced and opposite dipoles in nearby atoms. These dipole-dipole interactions cause attraction between the two atoms. This form of the interaction is known as the London dispersion force. Similarly, the van der Waals interaction can also be induced by permanent dipoles in atoms (Keesom interaction), or a combination of the two (Debye interaction). In all forms the van der Waals potential scales with distance, r, as $V \propto \frac{1}{r^6}$.

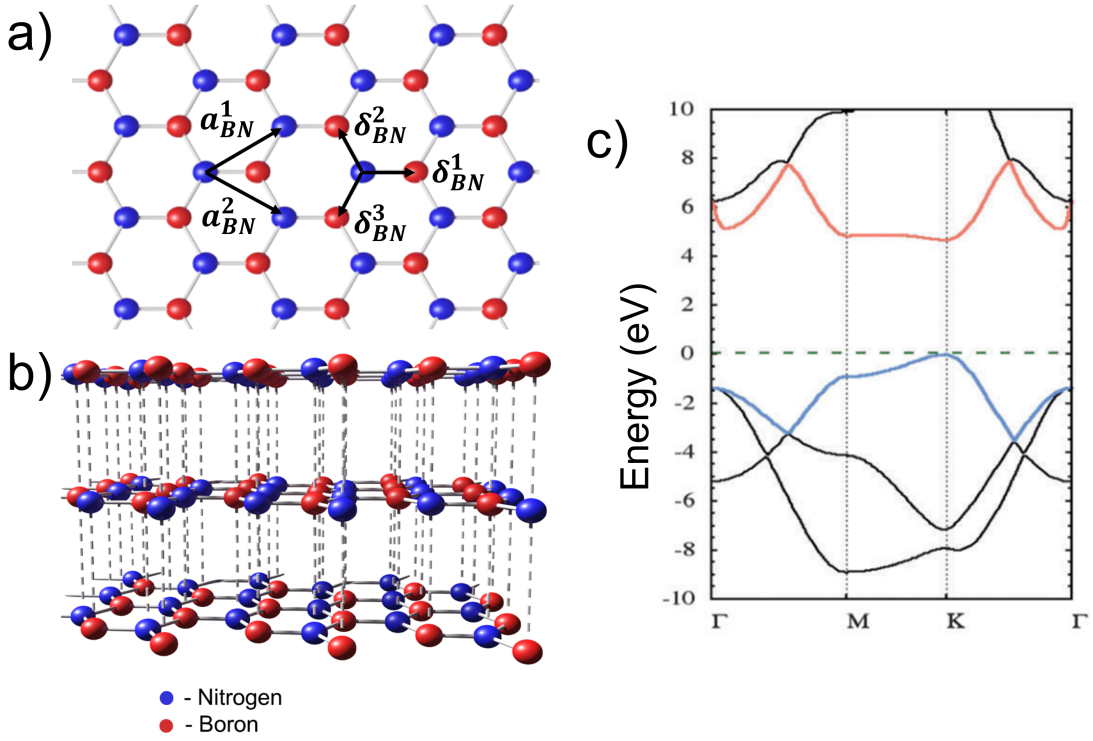


FIGURE 2.5: a) A top down view, and b) a side view, of the hBN structure, with boron and nitrogen atoms coloured as indicated. Each hBN layer sits directly on top of another, alternating between N and B atoms. c) The electronic bandstructure of hBN, modified from [21]. The large band gap between the valence band (blue) and conduction band (red) of ∼5 eV can be seen, with the Fermi energy indicated by the green dotted line.

2.3.2 The Moiré Pattern

A moiré pattern is any pattern produced by the beating of two separate periodic patterns that are overlaid to form a long range pattern with its own periodicity. They may appear for a variety of different shapes and sizes, but in the graphene/hBN heterostructure there is an overlay of two separate hexagonal lattices with different, but similar, sizes resulting in a larger hexagonal superlattice. The moiré superlattice for uniform graphene, where the lattice constant remains the same, and different to the underlying hBN, can be easily visualised by considering two overlaid hexagonal patterns of different sizes. This is the case for a perfect moiré pattern, illustrated in figure 2.6a-c, where the moiré superlattice vector length is given by [9, 12, 43]

$$\lambda_S = \frac{(1+\delta_a)a_G}{\sqrt{2(1+\delta_a)(1-cos\phi)+\delta_a^2}}, \tag{2.35}$$

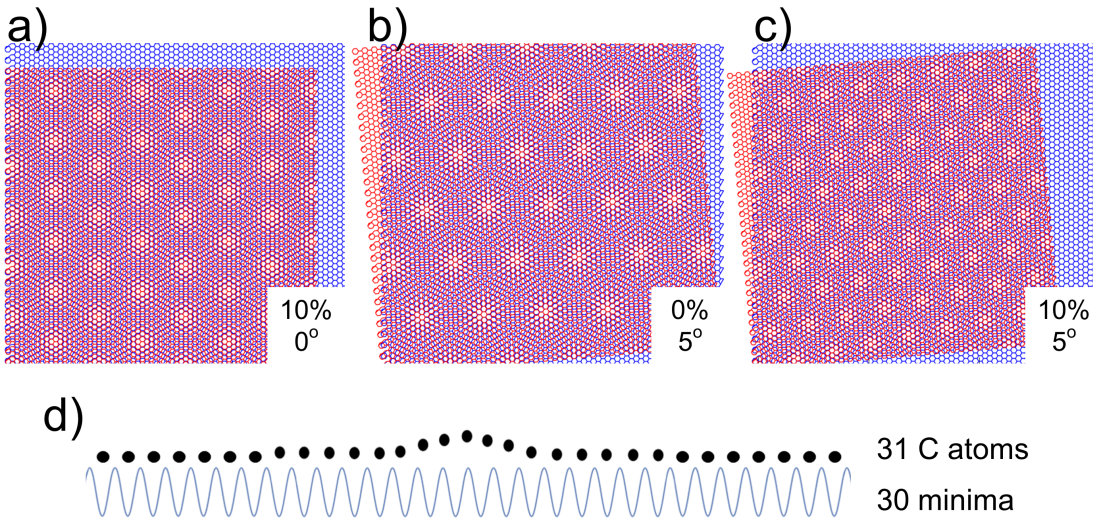


FIGURE 2.6: a), b), and c) overlaid hexagonal patterns with indicated lattice mismatches and angles of rotation. The underlayer with an unchanging size, and the overlayer hexagonal patterns are shown in blue and red respectively (analogous to the hBN and graphene lattices, with exaggerated differences). The moiré patterns can clearly be seen to decrease in wavelength as either the mismatch or angle is increased. d) Schematic demonstrating the Frenkel-Kontorova model of highly strained graphene on hBN. The black spots indicate carbon atoms in graphene as a cross sectional slice of the surface. The blue line indicates the Pierls van der Waals potential of the underlying hBN. Near to the F-K defect line the graphene is incommensurate, an extra row of carbon atoms causes a periodicity in the graphene lattice constant resulting in a buckling at the F-K defect line.

where δ_a is the fractional lattice mismatch, $\delta_a = \frac{a_{BN}-a_G}{a_G}$, and ϕ is the angle between the graphene and the hBN lattices. The relationship shown here between ϕ and λ_S, and between δ_a and λ_S is shown graphically in figure 2.7a. For rotationally aligned graphene on hBN, i.e. where $\phi = 0$, the moiré superlattice is in line with the graphene lattice directions. However, for misorientation angles, $\phi \neq 0$, the moiré pattern exists at an angle, θ, to the graphene lattice given by,

$$tan\theta = \frac{sin\phi}{(1+\delta_a) - cos\phi}. \tag{2.36}$$

For the above equations it can be seen that the moiré pattern increases in size as either the lattice mismatch increases, or the relative lattice rotation approaches zero. For small angles and small lattice mismatch, θ and $\delta_a \ll 1$, both valid assumptions for the MBE grown heterostructures explored in this thesis, equation 2.35 is reduced to [16, 44],

$$\lambda_S \approx \frac{a_G}{\sqrt{\delta_a^2 + \phi^2}}. \tag{2.37}$$

For rotationally aligned samples, like the ones grown here, the angle of rotation, ϕ, is zero which, as stated above, leads to a θ value of zero from equation 2.36, and further reduces equation 2.37 to

$$\lambda_S \approx \frac{a_G}{\delta_a}. \tag{2.38}$$

Using the lattice mismatch between graphene and hBN of 1.8% the maximum moiré pattern that can be observed for the graphene/hBN heterostructure is $\sim$ 13.7 nm. However, far larger moiré patterns have been observed in this work and reported elsewhere [44, 45].

Strained Material

Larger moiré patterns in excess of the expected maximum have been observed for graphene/hBN heterostructures and can be explained by strain (tensile or compressive) in either of the constituent materials. This strain can be expressed as a small change in the graphene constant, $a_G \rightarrow a_G + \Delta a_G$, which, by using the definition of δ_a with this new value of a_G, results in equation 2.38 becoming

$$\lambda_S \approx \frac{a_G^2}{a_{BN} - a_G - \Delta a_G}. \tag{2.39}$$

Equation 2.39 can hence be used to accurately determine the amount of strain present in a graphene layer by simply measuring the superlattice wavelength, λ_S. In addition, the uniformity of the superlattice can also be used to judge the directionality of the strain, if the moiré pattern wavelength is not equal in all directions.

In the case of graphene on hBN, the attraction between the two materials can be modeled using a simple Frenkel-Kontorova (F-K) model (shown in figure 2.6d) of a one-dimensional chain of elastically linked atoms, placed within a background potential formed due to the van der Waals attraction of the hBN, known as the Peierls potential [46, 47]. In this model the hBN is assumed to undergo no structural changes (with the reverse true for hBN grown on HOPG). This is a valid assumption for the samples where the hBN is in bulk form, although large changes in its structure are expected during the graphene growth due to thermal expansion/contraction as large substrate temperatures in excess of 1700°C are used. The samples have been investigated at room temperature, after the sample has relaxed, so that these changes can be neglected in this modeling.

When the atoms in the chain fall into the Peierls potential minima the two lattices are locally commensurate, see the regions on either side of the diagram in figure 2.6d, occurring for high levels of strain. However, between these regions the F-K model allows for strain relief in the form of an incommensurate transition to a region where the

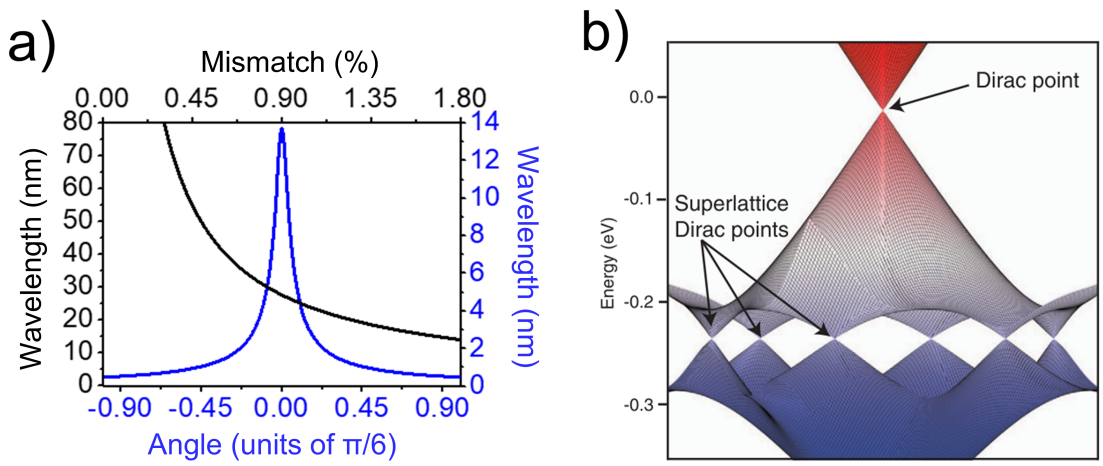


FIGURE 2.7: a) The relationship between lattice mismatch and superlattice wavelength (black line and labels), and lattice misorientation angle and superlattice wavelength (blue line and labels) for the hBN/graphene moiré pattern. For the lattice mismatch, a misorientation angle of zero is used, and for the misorientation angle a graphene/hBN mismatch of 1.8% is used. b) A diagram showing the superlattice Dirac points, situated around the primary Dirac point, in the valence band. A similar structure is seen in the conduction band, above the Fermi energy. Panel replicated from [9]

top layer buckles as shown in the centre of panel d) in figure 2.6, due to the elasticity of the chain, and the difference in lattice constants between the two materials[46, 48, 49]. This formation results in a graphene lattice constant that varies across the surface, with a periodicity matching that of the moiré pattern, and a moiré cell that is more strained in the centre, tending towards a lattice matching commensurate state, with strain relief at the moiré cell boundaries in the form of F-K defects. Each commensurate phase region is separated by solitons, with widths given by

$$\lambda_{FK} \propto \sqrt{\frac{Y}{\gamma_{PP}}}, \tag{2.40}$$

where Y is the materials Young's modulus, and γ_{PP} is the Peierls potential depth. The transition between a commensurate phase and an incommensurate phase occurs when the soliton magnitude becomes similar to the size of the commensurate region [46].

Moiré patterns can be used to interpret important properties about the graphene lattice. This can be through the use of equations 2.35 to 2.39 to determine possible lattice mismatch and orientational properties, as well as to identify defects, uniaxial or asymmetric strain, and step edges [50]. This can be particularly useful as the moiré pattern acts akin to a magnifying glass on the lattice, allowing for these properties to be distinguished without the need for ultrahigh resolution lattice imaging [16, 51].

Importantly, for graphene on hBN where there is no lattice mismatch, i.e. the graphene is highly strained to match the hBN lattice constant, the moiré pattern tends towards an infinite size, and the symmetry between the A and B graphene sublattices is broken [52, 53]. This is because in this configuration one sublattice sits above the boron atoms in the underlying hBN, while the other is situated directly above the nitrogen atoms. This breaking of sublattice symmetry has been theoretically predicted to open up a band gap in the graphene electronic structure of up to ∼50 meV for lattice matched material [9, 13, 15, 53], a trait that would be particularly useful for graphene device construction, with a smaller gap expected for lower strain.

However, for the situation where the lattice mismatch is non-zero, there will be a periodic sublattice configuration. For example, the A sublattice may be situated above a boron atom in one position, while elsewhere within the moiré unit cell it resides above a nitrogen atom. Using the periodicity of the moiré pattern, when moving a distance λ_S away from one of these locations the position will return to its original configuration. This results in a return to a sublattice symmetry when averaged over the superlattice wavelength, where no sizeable band gap is expected to open [9].

By considering the F-K model described earlier there may be a variation in the commensurability phase of the graphene to the hBN whereby different regions of the moiré pattern result in different heterostructure configuration, with a strain variation across the surface [49, 54–58]. This may lead to an energy gap forming at the Dirac point for the commensurate state where the sublattice symmetry is locally broken [59], although, as in the case discussed above, this energy gap varies across the superlattice wavelength, returning a sublattice symmetry and resulting in a non-sizable global band gap [46].

Superlattice Dirac Points

One interesting result of the additional periodicity introduced by the superlattice is that of the superlattice Dirac points [12]. These features, displayed in figure 2.7b , originate from the consideration of the electronic effect that the hBN substrate has on the local density of states of the graphene lattice, modelled by considering the interlayer hopping between the two constituent layers [9, 60]. Second order perturbation theory estimates the potential strength induced by the hBN to be 0.06 eV [61]. The reciprocal lattice vectors for the superlattice can be determined from equations 2.35 and 2.36 to be

$$\mathbf{G_S} = \frac{4\pi}{\sqrt{3}\lambda_S}(cos\theta, sin\theta), \tag{2.41}$$

with θ, the angle between the graphene lattice and the moiré pattern, increased by 60° and 120° for the additional superlattice wavevectors.

In suspended graphene $\mathbf{k} \rightarrow -\mathbf{k}$ backscattering processes along the reciprocal lattice vectors, given by $\mathbf{b_G}$ in equation 2.3, are forbidden due to the electron chirality, the potential imposed by the hBN lattice permits this backscattering to occur. As long as the symmetry between the two graphene sublattices remains then the Dirac fermion chirality prevents the opening of an energy band gap at the Dirac point. Instead, a new set of six Dirac points appear both in the valence band and the conduction band. The energies where these new Dirac points open are located where the periodic hBN potential connects the $\mathbf{k}$ and $-\mathbf{k}$ bands. This occurs when $2\mathbf{k} = \mathbf{b_G}$, and can be found to be

$$E = \frac{\hbar v_F |\mathbf{G}|}{2} = \frac{2\pi\hbar v_F}{\sqrt{3}\lambda_S}, \tag{2.42}$$

when considering the linearity of the graphene band structure near to the primary Dirac points [9]. As a result of equation 2.42 the superlattice Dirac points move to a higher energy for smaller moiré patterns. Experimentally, these secondary Dirac points have been observed as dips in scanning tunneling spectroscopy measurements recorded either side of the primary Dirac point in several papers [43, 60, 62, 63], with the energy dependence on moiré wavelength stated by equation 2.42 also confirmed.

2.4 Atomic Force Microscopy

The majority of the imaging techniques used throughout this investigation can be given the collective name of atomic force microscopy, despite a range of subdivisions of techniques being used. These include AC, or tapping mode, in both frequency and phase modulated operation, and contact mode including lateral force microscopy (LFM), force spectroscopy, and conductive AFM (CAFM). Details about the AFM systems used, calibration methodology, and data processing can be found in chapter 3.

2.4.1 Basic Principles

In traditional AFM a sharp tip positioned on the end of a narrow cantilever is used to probe the surface of a material. A schematic of one of the tips used in this project can be seen in figure 2.8a. The successful operation of AFM relies on a combination of different technologies. Firstly, the movement of the tip relative to the sample surface needs to have a sub-nanometer accuracy. This is achieved using piezoelectric transducers. Piezoelectric materials, quartz and lead zirconate titanate (PZT) being two of the most common, are materials whose crystal structure is modified by an applied electric potential that acts to change the density across the entire substance. Hence, by adjusting the geometry of a mass of piezoelectric crystals that are usually positioned

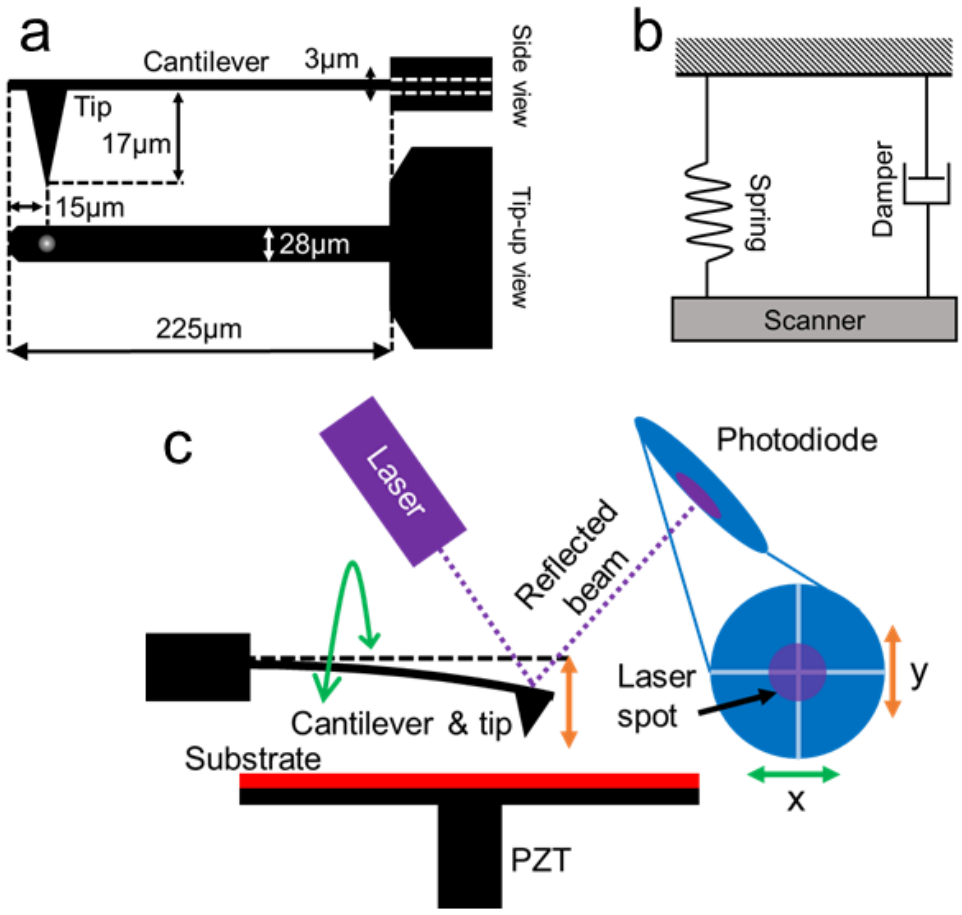


FIGURE 2.8: a) The dimensions of the AFM tips that were used (BudgetSensors ElectriMulti75-G). These tips have an initial tip radius <25 nm, a resonant frequency ~75 kHz, a force constant, k, of ~3 N/m, and a Cr/Pt conductive coating. b) A diagram showing the damping mechanism used to eliminate situational vibrations for one dimension. The scanner is held by a spring that absorbs the vibrations, these oscillations are then eliminated by a damper. c) An illustration of the cantilever and beam setup. A laser is reflected off of the reverse side of the cantilever and towards a photodiode separated into quadrants. The electronic output of the individual quadrants can be monitored with the signal magnitude dependent on the position of the laser spot. If the cantilever is deflected up/down then the laser spot moves in the y-direction (orange arrows), alternatively if the tip is twisted laterally (as in LFM) the laser spot moves in the x-direction (green arrows).

between two metal plates, the application of a voltage can be used to position an AFM tip above a sample surface with a precision of around 0.01 nm that is determined by the noise level in the applied electronic signal. In most AFM setups the finer x-, y-, and z-directional movements are generally applied by moving the sample relative to the tip using piezoelectric transducers, as shown by the PZT column in figure 2.8c.

The next problem faced by AFM operation is isolation from environmental vibrations. These vibrations can be larger than a few micrometers, and are often caused by the movement of people within a building, as well as many other factors including nearby vehicles and building work. These noise contributions are accentuated by placing the AFM at higher levels in a building, while operating at, or below, ground floor can help to minimise these effects. These vibrations can also be can be lessened simply by using a damping setup as illustrated in figure 2.8b. Here the scanner is placed on a series of springs and dampers that, in combination with the use of anti-vibration tables and suitable system enclosures, act to suppress the environmental vibrational noise to levels well below the nanometer scale. The systems used in this thesis were confirmed to have noise levels below 30 pm in the height channel. In addition, to limit background electronic interference, and to protect the highly sensitive internal circuitry of the AFM system, metallic plating or meshes can be used as a Faraday shield to block external electromagnetic radiation.

In order to reduce surface, and tip, contamination primarily due to hydrocarbons and water vapour when imaging under ambient conditions scanning can be carried out within an enclosed, high vacuum environment. Furthermore, to reduce noise due to thermal influences such as drift brought on by expansion/contraction of the surface, and Brownian motion in the sample, AFM may also be carried out at low temperature (liquid nitrogen cooled to 77 K for example).

The movement of the cantilever tip as it interacts with the surface is often measured using an optical lever, i.e. by monitoring the deflection of a laser beam that is reflected off the reverse side of the cantilever as shown in figure 2.8c. The laser is focused onto the reflective surface above the position of the tip apex and near the end of the cantilever for increased sensitivity. The reflected beam then reaches a photodiode that is split into four separate quadrants, illustrated in figure 2.8c. Each of the four quadrants that make up the photodiode produce an individual electronic signal with a magnitude that depends on the intensity of incident laser light on that segment. Before the tip is moved towards the sample surface the laser spot is positioned in the centre of the photodiode so that each of the four quadrants give identical readings. When the cantilever is then deflected by interacting with the surface, the laser spot moves in the y-direction of the photodiode (orange arrows in figure 2.8c), changing the signal contribution of each of the four quadrants, thus allowing a deflection that is proportional to the force acting on the tip to be measured. Alternatively, if the end of the cantilever is twisted around its own axis by lateral forces the laser spot moves in the x-direction of the photodiode (green arrows in figure 2.8c). This is the signal that is measured in lateral force microscopy.

Alternatively, the qPlus sensor measures the behaviour of the cantilever without the use of an optical lever. The qPlus sensor consists of a quartz crystal tuning fork

on which the probe tip (usually an etched wire) is attached to one of the forks tines. This tine is oscillated using a driving force applied to the gold electrodes situated along the length of the piezoelectric tuning fork, while the second is held stationary. The bending and oscillation of the fork can then be determined by monitoring the piezoelectric voltage induced in the sensors electrodes [64].

2.4.2 Operational modes

The following sections describe the different atomic force microscopy operational modes that have been utilised in this project, all of which use the principles outlined above, beginning with the simplest case of contact mode imaging, a technique that forms the basis of conductive mode AFM, and ending with the most commonly used tapping mode imaging technique.

Contact mode

The deflection of the cantilever from its horizontal position is directly proportional to the force applied on the tip (as stated above), this simple relationship is analagous to Hooke's law where the restoring force, F, is given by,

$$F = -k\delta z, \tag{2.43}$$

where δz is the deflection of the cantilever, and k is the cantilever spring constant that depends on the geometry and material properties according to

$$k = \frac{Ewt^3}{4L^3}, \tag{2.44}$$

where E is the Young's modulus, w, t, and L are the cantilever width, thickness, and length respectively (28 μm, 3 μm, and 225 μm in figure 2.8a). In practice the deflection is measured in volts according to the photodiode response. However, by calibrating the cantilever through analysing force-distance curves and carrying out a thermal tune it is possible to determine the correct scaling factors to convert the measured deflection into a force measurement, usually of the order nN. Hence, by moving the tip towards the surface of a material using PZT transducers while simultaneously measuring the deflection, it is possible to carry out force-distance curves that provide information on the tip-surface interaction.

The deflection of the cantilever can be used as a feedback input to control the height of the tip. In contact mode imaging the deflection is used as the set point of the system, i.e. the deflection, and consequently the tip-sample force, is held constant as the tip is raster scanned across the sample surface in the x- and y- directions by

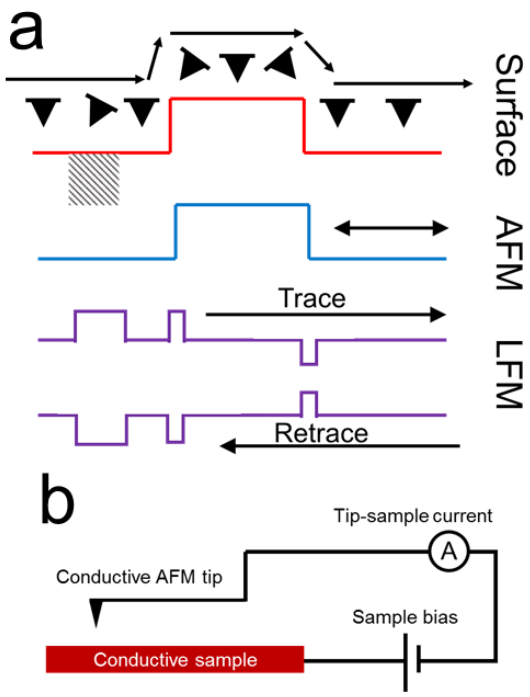


FIGURE 2.9: a) Shows a tip being moved across a sample surface. The shaded region represents an area with different frictional properties. The blue and purple lines indicate the output signal by AFM (both trace and retrace are identical) and LFM trace and retrace. Both modes show a different picture of the surface, with LFM providing additional frictional information. b) The basic circuit used in CAFM. A voltage bias is held between a conducting tip and sample, while the current flowing between the two is measured.

adjusting the z-direction piezoelectric transducer accordingly. This means that if the deflection voltage is increased from the set point (cantilever deflected upwards), then the tip is retracted until the set point is reached, with the reverse true for an increase in deflection voltage. The corresponding z-piezo voltage signal can be converted into a sample height value and displayed as a topographical image of the surface, following calibration of the piezoelectric transducers.

In lateral force microscopy the cantilever is scanned at an angle of 90°. This means that the cantilever is positioned perpendicularly to the fast scan direction. This acts to maximise the twisting of the cantilever, since in this orientation the frictional/lateral force on the tip opposes the fast scan direction. A standard contact mode scan is carried out as detailed above using the cantiler deflection as the feedback signal, with the additional monitoring of the lateral cantilever twisting, indicated by the green arrows in figure 2.8c, by recording the optical lever laser spot movement on the photodiode in the x-direction. The resultant image shows a very different picture to standard AFM

imaging, as displayed in figure 2.9a. Here the forward scan path (trace) and backwards scan path (retrace) show significant differences due to the lateral force opposing scan direction, with topographical changes appearing as peaks and troughs in the signal. In addition, areas with different frictional/adhesional forces acting on the tip also cause lateral displacement, providing additional information about the surface that is not available through standard AFM imaging.

Contact mode AFM can provide very useful feedback about the tip-sample interaction through the use of force-distance curves and deflection monitoring and also has a distinct speed advantage over tapping mode AFM as it is not limited by a settling time, leading to very high achievable scan speeds. However, rough surfaces can cause both tip and surface damage, and contact mode AFM can generally only be carried out in the repulsive regime due to unstable attractive forces, that can be relatively strong near to the sample, causing sudden snap-to-surface of the tip which is discussed in more detail in section 2.5 [65].

Conductive mode

Conductive atomic force microscopy is a subset of contact mode imaging that can be carried out simultaneously with contact scanning, allowing for an easy comparison of topographic and conductive features, contrary to scanning tunneling microscopy where no such distinctions can be made. In CAFM an electrical potential difference is applied between a conductive AFM tip, and a conductive sample. The tip itself is usually a standard AFM tip that has been coated with a thin metallic layer. The current flowing through the tip is then measured using an electric current amplifier, see figure 2.9b for an illustration of the CAFM circuit. This current can be on the scale of picoamperes, and is proportional to the conductance of the sample, as well as the contact radius of the conductive tip [23, 66]. For a metallic point contact model for an AFM tip with a typical radius of 20-50 nm, and a room temperature electron mean free path of $\sim$ 10-50 nm [66] a suitably small contact resistance ($\sim$ 1-100Ω) is estimated.

As a result of scanning under ambient conditions, the presence of contaminants on both the CAFM tip and the target sample are likely to create a thin insulating boundary for normal forces that have not resulted in contaminant layer penetration. This insulating layer may facilitate a tunneling current, similar to the main functional principle of STM [67], a result of quantum mechanical electron tunneling, resulting in a measured current that decreases exponentially as the insulating tunnel barrier (corresponding to the contaminant layer thickness or tip height) is increased.

Conductive AFM images consist of a current value measured at each pixel of a contact mode AFM scan, with a deflection value used as the set point, while the sample is

held at a constant voltage relative to the tip. Alternatively, the tip can be held at a particular position, with a constant deflection, while the sample bias voltage is ramped allowing for current-voltage (current spectroscopy) measurements to be recorded. The current channel can also remain open while carrying out force-distance curves to obtain information about the current dependence on the applied tip-sample force. As it is essential that CAFM is carried out in contact mode of operation, the conductively coated tip is often prone to changes where the tip coating is worn away. These can cause significant and sudden changes in the amount of current measured. CAFM has been used in a variety of ways to categorise different materials, with a strong representation for graphene characterisation [41, 42, 68–76]

Non-contact mode

In non-contact mode AFM a set of piezoelectric transducers, positioned at the cantilever holder, are used to oscillate the cantilever at a particular frequency. The driving signal of this oscillation is provided by an applied alternating current to the transducers that gives non-contact mode its alternative name of AC mode imaging. The oscillation of the tip is then changed by the tip-surface interaction which can in turn be converted into a measurement of the force gradient, $\frac{dF}{dz}$, of the interaction using cantilever physics. The system is modeled as a damped harmonic oscillator where the external force on the system is given by

$$F_{ext} = F(z) + F_0 \cos \omega t = m\frac{d^2z}{dt^2} + c\frac{dz}{dt} + k(z-d), \tag{2.45}$$

where $F(z)$ is the tip-sample interaction force, $F_0 \cos \omega t$ is the driving force of the cantilever oscillation with an amplitude of F_0, and an angular frequency of ω. On the right hand side of the equation m is the mass of the cantilever, z is the displacement of the tip from its equilibrium position (with no external forces), d is the undeflected height of the cantilever from the sample surface, k is the cantilever spring constant, and c is the viscous damping coefficient, given by $c = m\omega_0/Q$. Here ω_0 is the cantilever resonant frequency, and Q is the quality factor. Using equation 2.43 the equilibrium of the stationary cantilever, z_0 is found when $F(z_0) = k(z_0 - d)$. By considering small perturbations on this position of $z \rightarrow z_0 + z_1(t)$, and approximating the tip-sample force as

$$F(z) \approx F(z_0) + z_1(t)\frac{dF}{dz} + \ldots, \tag{2.46}$$

equation 2.45 can be rearranged after substituting in to give

$$F_0 \cos \omega t = m\frac{d^2z_1}{dt^2} + c\frac{dz_1}{dt} + (k - \frac{dF}{dz})z_1(t), \tag{2.47}$$

which is simply the equation for a driven oscillating cantilever, similar to equation 2.45 without the tip-sample force term, but with a modified, force dependent spring constant of

$$k_{new} = k - \frac{dF}{dz}, \tag{2.48}$$

which, using the resonant frequency equation of $\omega_0 = (\frac{k}{m})^{\frac{1}{2}}$, and carrying out a binomial series expansion neglecting higher order terms and assuming $\frac{1}{k}\frac{dF}{dz} \ll 1$, gives a new resonant frequency that is dependent on the force gradient of

$$\omega_{0new} = \omega_0 - \frac{\omega_0}{2k}\frac{dF}{dz}. \tag{2.49}$$

There is a shift in resonant frequency, $\Delta\omega_0$, equal to the second term in equation 2.49. This is the main principle used in both amplitude modulated AFM (AM-AFM) and frequency modulated AFM (FM-AFM). In AM-AFM the cantilever tip is oscillated at a drive frequency that is held constant, and is usually chosen to be close to the resonant frequency of the cantilever away from the surface, where $F(z) = 0$, to maximise the recorded signal. As the tip approaches the surface the force gradient experienced by the tip leads to a change in the effective resonant frequency given by equation 2.49. This results in a change to the oscillation amplitude. AM-AFM uses a set value for this amplitude. This is monitored, in the case of an optical lever operated system, using the measured photodiode voltage difference between the upper and lower quadrants (figure 2.8). If the recorded amplitude changes then the system reacts to either further engage, or retract, the tip in order to compensate for this change, ensuring that the amplitude remains constant. As demonstrated by the above equations, a constant amplitude implies a constant resonant frequency difference, which in turn implies that $\frac{dF}{dz}$ remains unchanged during operation and so the tip follows a path of constant force gradient across the sample.

Alternatively, in FM-AFM the phase difference between the oscillating system and its driving frequency is monitored experimentally using a lock-in amplifier [65]. Mathematically this phase difference can be found by first considering the solution to the above equation for a driven harmonic oscillator (equation 2.47) of the form [77]

$$z_1 = A\cos(\omega t - \phi), \tag{2.50}$$

where ϕ is the phase difference between the cantilever oscillation and the driving frequency. A can be found to be,

$$A = \frac{F_0}{c\omega\sin\phi + (k_{new} - \omega^2 m)\cos\phi}, \tag{2.51}$$

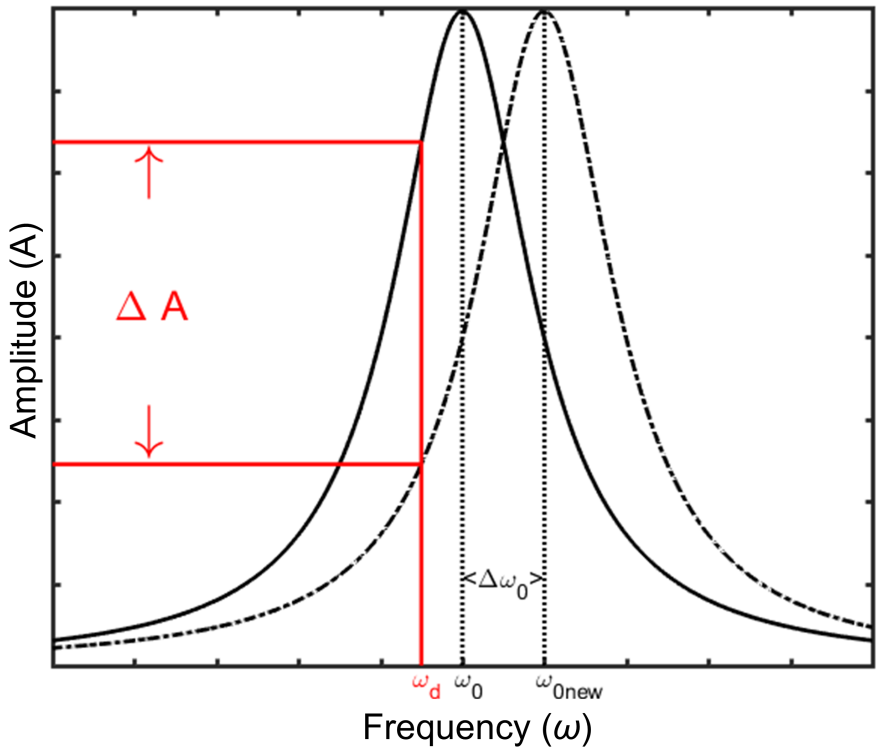


FIGURE 2.10: This figure shows the amplitude vs frequency of a driven cantilever. The solid line shows an ideal Lorentzian for a cantilever with a zero tip-sample force, the oscillation resonates at ω_0. The dotted line demonstrates a shift of this amplitude curve along the frequency axis by a distance $\Delta\omega_0$ due to the presence of a force gradient. In AM-AFM the drive frequency, ω_d, remains constant, resulting in an amplitude difference, ΔA, shown in red, when the tip is lowered. The tip height is then adjusted to keep this value constant, and hence $\Delta\omega_0$ and the force gradient remain the same. In FM-AFM the driving frequency is adjusted to match the resonant frequency, ω_{0new}, and then maintained with a constant frequency shift, $\Delta\omega_0$.

and by considering the derivative of equation 2.47 we arrive at the following equation for the phase difference,

$$\phi = \arctan\left(\frac{\omega c}{m(\omega_{0new}^2 - \omega^2)}\right). \tag{2.52}$$

Equation 2.52 demonstrates the relationship between the tip oscillation frequency and the phase difference. As the tip approaches a surface the resultant force gradient leads to a shift in the resonant frequency, $\Delta\omega_0$, as described earlier. In the case of FM-AFM the driving frequency of the system can be adjusted to ensure that the cantilever is continually oscillated at its effective resonant frequency ω_{0new}. This is achieved by monitoring the recorded phase difference using the lock-in amplifier in a technique known as frequency locking.

In FM-AFM as the tip is laterally scanned across a surface the height is adjusted

to maintain a constant oscillation frequency set point so that, as previously with AM-AFM, the frequency shift, $\Delta\omega_0$, remains constant, and the tip follows a contour with an unchanging force gradient.

In this thesis it is the first approach, of monitoring the oscillation amplitude using an optical lever, that has been used for all ambient non-contact AFM measurements.

Non-contact mode AFM is generally less damaging than contact mode imaging to both the tip and surface as lower forces can be applied to achieve an image, but can also be far slower than contact mode imaging, particularly while imaging away from the small amplitude limit (as used within this thesis). Larger forces can also be realised in non-contact mode AFM by using an increased amplitude, resulting in a larger cantilever restoring force that can be used to overcome attractive tip-sample forces and eliminating snap-to-surface which allows for imaging in the attractive regime, a trait that is not shared with contact mode AFM.

2.5 Tip-surface interaction

During scanning of the surface using AFM there are a range of forces acting between the surface and the tip, collectively known as the tip-surface interaction. One of these has already been described above in the form of the van der Waals force, with the other main force considered here being that of Pauli exclusion. The strongly repulsive Pauli exclusion force is known as an exchange force and arises due to the quantum mechanical Pauli exclusion principle which states that two indistinguishable fermions may not occupy the same quantum state simultaneously. This occurs when the tip comes into contact with the target material and the corresponding electron orbitals overlap. A simple, and reasonably accurate, picture of the tip sample system can be achieved in the form of an empirical potential combining a short-range repulsive term primarily due to Pauli exclusion, and a long-range attractive term arising from the van der Waals interaction among other forces. Both the Morse potential (discussed in more detail in section 6.4 of chapter 6) and the Lennard-Jones potential (L-J potential) are suitable for modelling the tip-surface interaction. The L-J potential, shown in figure 2.11a is a fitted potential that weighs up the attractive and repulsive forces by considering their relative strength-distance behavior, and is given by

$$V(r) = E_0[(\frac{r_0}{r})^{12} - 2(\frac{r_0}{r})^6], \tag{2.53}$$

where E_0 is the depth of the potential well, and r_0 is the separation, r, at the potential minimum. The first term in the square brackets is a fitted term for the repulsive interaction, with the second arising from the attractive interactions. Since the force is simply the negative differential of this potential, it is clear that the overall magnitude

is attractive (repulsive) on the right (left) hand side of the minimum, as illustrated by the red line in figure 2.11b.

In contact mode AFM the scanning usually takes place in the repulsive regime where the deflection of the tip is positive and the cantilever is deflected away from the sample. The restoring force experienced by the cantilever follows equation 2.43, and is plotted in figure 2.11b alongside the force due to the L-J potential. In this representation each of the dashed lines labelled 1 to 4 illustrates the cantilever restoring force with an unchanging spring constant for several positions. Each of the positions is defined by a cantilever surface separation of d_n, where n is the position number. When these lines intersect the interaction force line (red) there is an equilibrium position. The measured deflection of the cantilever is given by the difference between the separation at this intersection and the value of cantilever separation d. As the value of d is reduced, i.e. the probe approaches the surface, the cantilever line moves in the direction of 1 to 4 and multiple equilibrium positions appear. In the case of line 2 (green) there are 3 such positions. As the tip is approached, the position with the largest separation value is the true value, whereas in withdrawal (moving from line 4 to 1), the lower equilibrium position is the true value thus resulting in an asymmetry in the force felt during approach or withdrawal in this regime (the middle position is unstable).

For line 3 (blue) there is a position where the gradient is equal to that of the interaction force (red) resulting in an unstable position. At this point the probe undergoes a jump to contact into the blue equilibrium position at a lower separation. At lower values of r, e.g. line 4 (pink), there is only a single stable equilibrium point that continues as the attractive tip-sample force reduces, and becomes repulsive. This is where contact mode AFM usually takes place, as the instabilities at separation values above, and near to, the minimum position, r_0, can cause sudden deflection changes. However, the region of the force curve that can be probed can be reduced by increasing the spring constant of the cantilever, but this increases the significance of thermal fluctuations in the cantilever deflection resulting in a loss of sensitivity in the measurements. The instabilities described above are avoided in AC mode by oscillating the cantilever and recording the force gradient by observing changes in the corresponding resonant frequency.

2.5.1 Surface deformation

In the case of graphene on hBN the forces between the tip and the graphene surface can be large enough to induce local changes in the lattice constant that are observable both directly and through utilizing the moiré pattern formation. In their 2016 article *Yankowitz et al* [78] observed pressure induced modification of exfoliated graphene

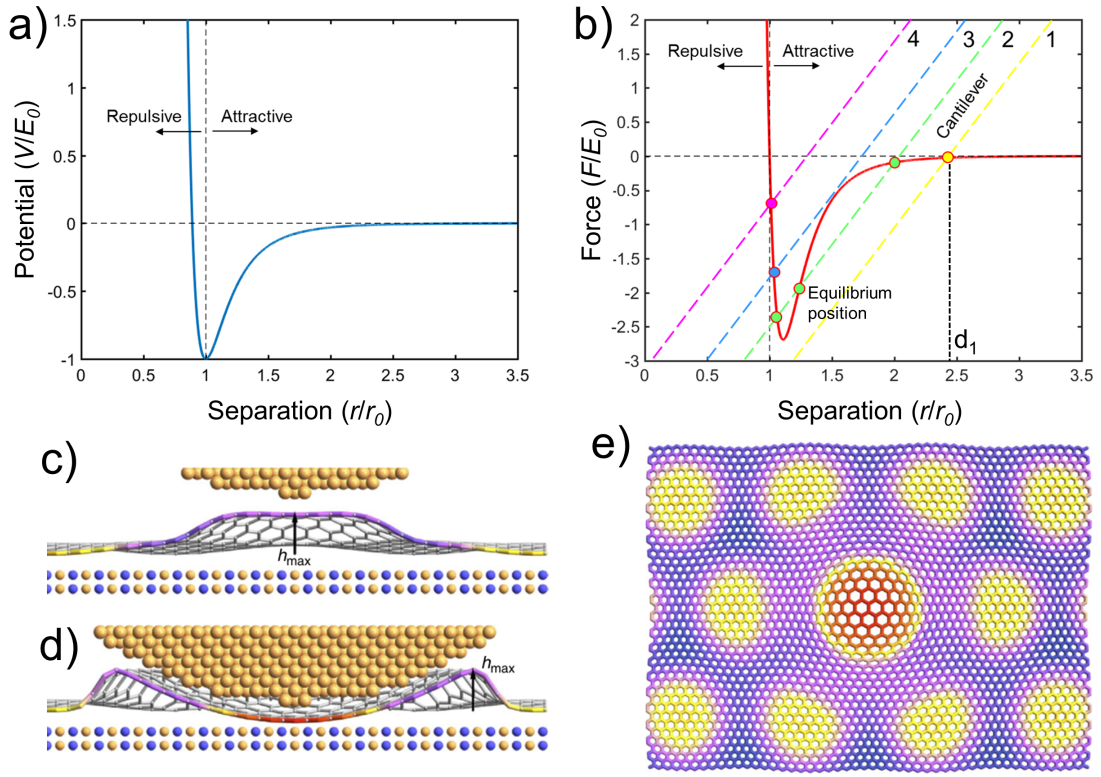


FIGURE 2.11: a) The Lennard-Jones potential. b) The negative of the derivative of the L-J potential (L-J force) is shown in red. The black dashed lines are in the same position in a) and b) at $F = 0$ and $r = r_0$. The coloured dashed lines labelled 1-4 indicate the cantilever restoring force, with the L-J force intersects showing the graphical solutions of equilibrium positions. The point at which these lines intersect $F = 0$ is the cantilever sample separation, d. c), d) Representation of an STM tip approaching a graphene hBN heterostructure. c) The tip sample attraction lifts the graphene above the surface. d) The tip exerts a pressure on the graphene, pushing it closer to the hBN and altering the lattice constant locally as shown in e). The red region shows the highly strained, commensurate graphene, with the yellow and blue indicating progressively less strain. Images c), d), and e) modified from *Yankowitz et al* [78].

on hBN to become locally commensurate by reducing the interlayer separation of the heterostructure. They propose that there is a modulation in the adhesion potential that matches the moiré pattern, due to carbon-boron and carbon-nitrogen stacking configurations, that results in an expanded lattice near to the stronger, and energetically favourable, carbon-boron stacked regions. As a probe (STM tip in the case of *Yankowitz et al*, although the same principles will be true for an AFM tip) approaches the graphene surface the van der Waals attraction between the two acts to lift the graphene away from the surface, modifying the strain and, as a result, the lattice constant. A depiction of this can be seen in fig 2.11c. As the tip is then pressed against the surface as it approaches, the pressure exhibited causes the graphene underneath the tip to move closer to the hBN lattice, where the resultant increased adhesion causes

the graphene lattice constant to match the hBN, becoming commensurate (see figure 2.11d and e)). A consequence of this effect manifests itself in the imaging of the moiré pattern. In this case, as the tip is scanned across the surface with a high tip pressure the stacking boundaries that make up the moiré pattern are pushed until the in plane elasticity of the lattice overcomes the strain, and the graphene snaps back to its original position. This causes the moiré pattern to lose its symmetry, and leads to different patterns depending on scan direction.

Chapter 3

Methodology

In the following section the fundamental physics that underpins the mechanisms that have been used throughout this thesis are briefly described, before specifying further details of the methods used to achieve results through these means. The most prolific imaging technique of optical microscopy is first discussed, followed by scanning electron microscopy (SEM) and the scanning probe imaging approaches of atomic force microscopy. For AFM the theoretical principles outlined in the previous chapter are elaborated upon, with a greater focus on how they were used to produce data, and the operation of the systems that were used. In addition, the techniques of angle resolved photoemission spectroscopy (ARPES) and Raman spectroscopy are also described.

Following this, the materials that have been used in this study, including silver nanowires and carbon nanotubes, along with the substrates; silicon dioxide, highly oriented pyrolytic graphite, and sapphire; are described in terms of physical properties.

3.1 Optical Microscopy

The optical microscope uses visible light, i.e. electromagnetic radiation with wavelengths within the 380-740 nm range, to image materials. A sample is illuminated using a white light source, in this thesis the sample was lit by a top down halogen lamp light source. Since a halogen lamp is an incandescent light bulb, the spectrum of light produced is continuous. This light interacts with the sample that is under investigation, and is either absorbed, reflected, or transmitted by the material. The reflected light passes through a series of lenses and is used to create an enlarged virtual image of the sample that can be focused onto an eyepiece or camera/charge coupled device (CCD) in order to record images digitally.

The lens arrangement consists of an objective lens and an eyepiece that act together to produce the magnified image, see the diagram in figure 3.1a with the magnification dependent on the chosen objective lens.

When optically imaging hBN flakes on a SiO_2/Si or sapphire substrate flakes of varying thicknesses can be easily identified by their colour and contrast [79]. Thinner flakes usually exhibit a colour towards the shorter end of the visible spectrum, with thicker flakes appearing to have a more reddish colour due to the increased likelihood of transmission for longer wavelength light, figure 3.1b shows an example of this, where a raised orange/red region is clearly visible.

The maximum theoretical performance of an optical microscope is limited by diffraction. The Abbe diffraction limit for a microscope gives a minimum resolvable separation of two features as,

$$d = \frac{\lambda}{2nsin\theta} = \frac{\lambda}{2NA}, \tag{3.1}$$

where λ is the wavelength of light, n is the refractive index of the medium, θ is the half-angle spot size of the focused light, and NA is the numerical aperture equal to $nsin\theta$. For a high quality optical system a numerical aperture of $\sim$ 1.5 can be achieved. This gives a theoretical resolution limit for visible light with a small wavelength (e.g. blue light with λ = 400 nm) of 133 nm. This value is far larger than the structures that are to be studied in this thesis; such as the atomic lattice, surface features and moire patterns.

However, it is important to note that this is the theoretical minimum resolvable distance, and that smaller objects that reflect or emit light will still be visible as they will still interact with light. For example, for the nanowire studies in this thesis with dimensions of $\sim$ 60 nm x 10 μm (diameter x length) the diameter lies far below the resolution limit, but individual nanowires are still clearly visible optically, as seen in figure 3.1c.

In order to resolve features below the Abbe diffraction limit alternative techniques must be employed.

3.2 Scanning Electron Microscopy

In scanning electron microscopy the Abbe diffraction limit (equation 3.1) is significantly reduced to achieve possible resolution of less than 1 nm by substituting photon illumination, with a relatively large wavelength of $\sim$ 500 nm, for electron illumination, with a far smaller de Broglie wavelength ($\sim$ 10 pm for an energy of 10 kV) given by

$$\lambda = \frac{h}{mv}, \tag{3.2}$$

where h is the Planck constant, m is the mass of the particle moving at a velocity, v. The electrons are generated by an electron gun in a collimated beam, typically with energies between 2-20 kV. This beam is then passed through a series of electromagnetic lenses to focus it onto a point on the sample surface, where it is raster scanned using

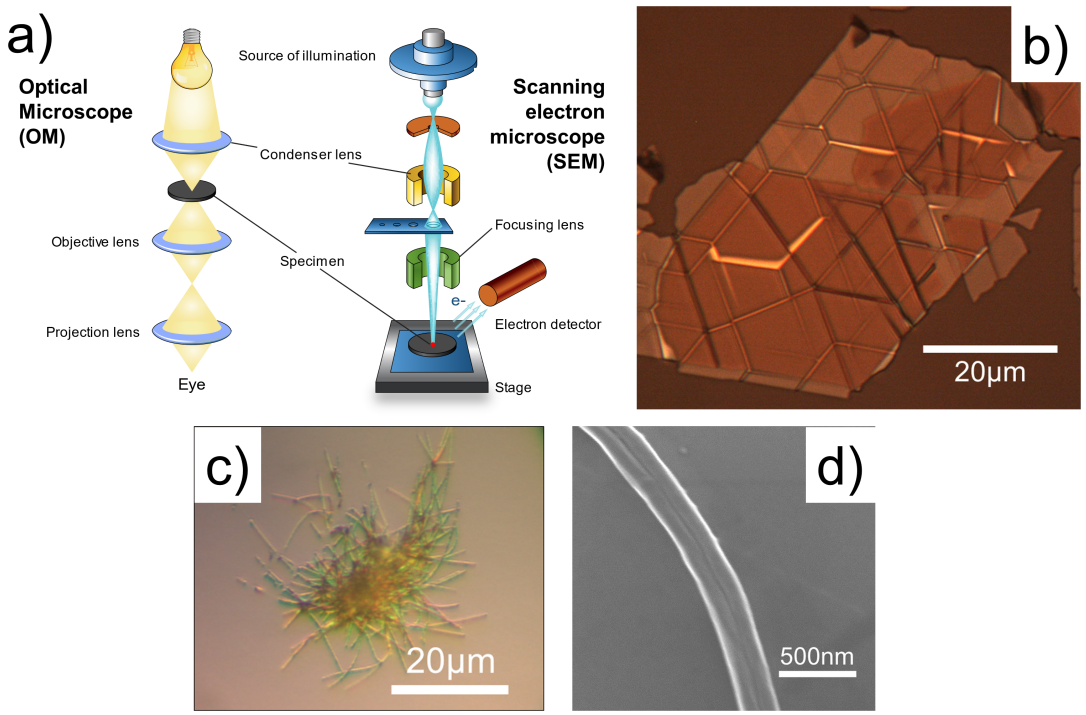


FIGURE 3.1: a) The optical microscope and SEM lens setup. b), c) OM images recorded with a 100X magnification objective of a hBN flake on a sapphire substrate, and a bundle of Ag nanowires on a SiO_2/Si substrate. The raised regions in b) (confirmed with AFM) appear redder optically. In c) the individual Ag nanowires can be distinguished despite having a diameter of 60 nm, below the Abbe diffraction limit. d) An SEM image recorded in SEI mode with an e-beam operated with 15 kV of two carbon nanofibers (CNFs) pushed together on a SiO_2/Si substrate. The curved edges of the CNFs with a large angle of incidence to the beam show up as brighter due to increased secondary electron emission. Figure a) modified from [80]

deflection coils to manipulate the beam direction. The electrons that collide with the sample undergo two main mechanisms. The first involves the backscattering of incident electrons. Primary electrons from the electron beam are directed away from the sample due to the high electromagnetic fields close to the atomic nuclei. This redirection of the primary electron path leads to a loss in the kinetic energy of the incident electron in the form of Bremstrahlung (braking) radiation.

The high energy backscattered electrons from this mechanism can be used for SEM imaging. These emitted electrons can originate from deep within the sample. Elements with large atomic numbers backscatter more electrons due to the stronger electromagnetic fields associated with the nuclei of heavier elements. This results in a technique which can be used to produce an image showing contrast between regions with different chemical composition.

The second mechanism involves the emission of secondary electrons; the primary

electron from the e-beam transfers its own energy to that of an electron close to the surface, ejecting the surface/secondary electron. This usually occurs for outer shell electrons, with the secondary electrons here known as Auger electrons. Alternatively, for ejection originating from the inner shells, an electron within the material may fall into the energy state that the ejected electron occupied, resulting in the emission of a characteristic x-ray of the material with an energy corresponding to the difference in energy between the respective states, with the primary electron filling the higher energy state.

The emission of secondary electrons is the most commonly used detection source for imaging, where the intensity of secondary electrons is recorded for each position during the raster scan to build a picture of the surface. Secondary electrons are emitted primarily from near the surface of a sample ($\sim$ 15 nm depth) due to the low energy of the emitted electrons, as a result this leads to a greater amount of emitted electrons from regions where the angle of incidence is greater, i.e. the electron escape distance is lower, resulting in steeper contoured regions showing up with a greater intensity than flat regions that are perpendicular to the e-beam. This is demonstrated by the secondary electron imaging (SEI) image shown in figure 3.1d of a pair of carbon nanofibers pushed close together. For the SEM imaging carried out for this thesis, secondary emission imaging has been used.

3.3 Atomic Force Microscopy

The two ambient AFM systems that were used for measurements were an Asylum Research Cypher-S, and an Asylum Research MFP3D, with most results recorded on the former. In both cases the same tips were used. These consist of the BudgetSensors Multi75Al-G and NuNano Scout 70 cantilevers for AC only imaging, and the BudgetSensors ElectriMulti75-G and NuNano Spark 70 Pt when conductive measurements were required. The dimensions of the BudgetSensors tips can be seen in figure 2.8a and both have a length, width, and thickness of 225 μm, 28 μm, and 3 μm. The tip has a height of 17 μm and is set back 15 μm from the cantilever end. All cantilevers have resonant frequencies of $\sim$ 70-75 kHz, spring constants of $\sim$3 N/m, and are made primarily of silicon. The Multi75Al-G tips have a 30 nm aluminium coating and a tip radius of below 10 nm, whereas the ElectriMulti75-Gs have a larger tip radius of < 25 nm with a conductive Cr/Pt coating. Similarly the Scout 70 probes have a thin aluminium coating on the back side, and a tip radius below 10 nm, whereas the Spark 70 probes have a 5 nm Ti/40 nm Pt coating on both sides with a tip radius < 30 nm. The NuNano probe dimensions consist of a length, width, and thickness of 225 μm, 30 μm, and 2.5 μm. The tips have a height of 6 μm and are set back 7.5 μm from the cantilever end.

When conductive AFM measurements were carried out the setup shown in figure 2.9b was usually achieved by placing a counter electrode in contact with the sample, which was in turn connected and controlled by the AFM system using the Asylum Instruments software. Using a digital hand-held multimeter prior to conductive measurements the sample voltage was zeroed before zeroing the current measurement. In addition, a 10 MΩ resistor was also used to run a voltage sweep to ensure systems were running correctly before recording. For the MFP3D AFM system a single gain tip holder was used with a sensitivity of ±2 nA which required a resistor to be placed in series for accurate measurements. The Cypher AFM system used a dual gain tip holder that records current over two channels simultaneously with sensitivities of ±10 nA and ±10 μA.

Contact mode imaging, including CAFM, was only carried out after a series of AC mode scans to ensure that the area of interest was reasonably flat (features below $\sim$ 10 nm). This was to limit pieces of debris or large objects causing wear on the AFM tip which in turn leads to significant changes in the conductivity measurements that are recorded.

Other changes in the tip-sample current measurements were due to surface debris or molecules becoming adsorbed to the tip, a process that is encouraged by the applied potential on the tip. This could often be overcome by carrying out many fast scans of an area at different scan angles and direction to clean the tip (and surface). In addition, anodic oxidation can also cause a problem by inducing oxidation in either the surface or the tip during CAFM that acts to suppress the amount of current that can flow. This effect was minimised by always scanning with a negative sample bias reducing the effect of anodic oxidation on the tip, but created issues where voltage sweeps for IV curves were required. A further technique that was used when the current measured by the tip underwent a sudden drop was to briefly increase the sample bias magnitude to between 0.5 and 5 V. While this approach may seem drastic due to the large amount of current passing through the tip, no changes to the graphene sample were seen as a result of the voltage burst. This large current essentially re-welds the tip apex with the conductive coating, allowing for current to flow again. It can also melt the conductive coating completely off of the tip, and has only been used as a last resort.

3.3.1 AFM Calibration

Prior to the recording of any AFM measurements the tips were automatically tuned to find their resonant frequency using the system software. This was carried out by oscillating the tip through a range of different frequencies and monitoring the amplitude. The magnitude of the oscillation was then normalised to be 1 V before approach. The driving frequency is chosen to be -5% from the resonant frequency. This is so that the

oscillation is at the steepest part of the response curve (figure 2.10) where the system is at its most sensitive.

The above non-contact mode tuning for AC imaging using the ambient AFM systems was carried out regardless of the following imaging type (AC or contact/conductive AFM). This was to ensure that a soft surface approach can be realised, in which the sample is approached slowly using tapping mode, before a subsequent approach in contact mode, reducing the risk of the tip crashing and causing damage to either itself or the sample.

In addition, or alternatively if the cantilever tuning procedure above gives an unsatisfactory result, thermal tuning of the tip can be used to determine the resonant frequency of the tip. During thermal tuning the cantilever is held at room temperature, and the deflection of the laser spot is monitored. The thermal Brownian motion of the atoms in the cantilever acts as a flat white-noise driving force (i.e. no preference in driving frequency). As the Brownian motion with frequencies close to the resonant value are weighted higher, the resultant amplitude-frequency response of the system mirrors that of figure 2.10, where the resonant frequency can be readily extracted [81].

In the case of contact mode imaging, or force-distance curves, where a quantitative force experienced by the AFM tip is required, two key values are needed to provide an accurate result, in addition to the measured deflection (this is the recorded deflection minus the free air deflection (FAD) prior to approach). These key values are the inverse optical lever sensitivity (InvOLS) and the spring constant of the cantilever. The InvOLS value corresponds to the amount of bend the cantilever experiences per unit volt of change in deflection (units of nm/V), and can be determined using a force-distance curve carried out on a clean, solid surface (i.e. modeling both tip and surface as undeformable). In practice a Si/SiO_2 sample has been used. After recording a curve of force versus tip height the approximately linear repulsive region, where the tip is in contact and hence all z-piezo movement corresponds to tip bending, can be modeled as a straight line and the InvOLS value extracted.

Using the InvOLS value it is now possible to determine the spring constant, k, of the cantilever using the thermal tuning method outlined above. Following a thermal tune, the region around the resonant frequency can be modeled using a Lorentzian, ignoring additional fundamental modes and noise. The equipartition theorem relating the systems temperature to its average particle energies applied to the cantilever is given by [81],

$$\frac{1}{2}k_BT = \frac{1}{2}k\langle z^2\rangle, \tag{3.3}$$

so that,

$$k = \frac{k_BT}{\langle z^2\rangle}, \tag{3.4}$$

where k_B is the Boltzmann constant, T is the temperature, and $\langle z^2 \rangle$ is the mean square cantilever displacement that can be determined from an integral of the modeled Lorentzian, leading to a quantitative value for the spring constant, k. With these two values the force experienced by the cantilever can be calculated using,

$$F = k \times InvOLS \times (Deflection - FAD). \tag{3.5}$$

In practice this force value can vary due to drift in the FAD during an extended series of scans (in which case an average of the FAD before and after the scanning has been used), along with any changes in the position of the laser spot on the reverse of the cantilever affecting the InvOLS value. The main shift occurring during the switching between the calibration SiO_2 sample and the heterostructure of interest.

Lateral calibration

The procedure for calibrating the lateral forces in LFM must be carried out following the determination of the normal InvOLS and spring constant values, as these are required for calcultaion. The method used in this thesis follows that proposed by *D. F. Ogletree et al* [82], also known as the wedge method, and requires a sloped calibration sample [83, 84].

First, we consider the forces acting on a cantilever as it passes over a surface with a known slope of angle θ. A diagram of this situation can be seen in figure 3.2a and b, where the forces applied to the surface, the load, L, and the tractive force, T, as well as the reactive forces, the normal component perpendicular to the surface, N, and the frictional forces opposing motion, f, are all labelled in the case of both uphill (+) and downhill (−) scanning. From this consideration it is clear that,

$$N_{\pm} = L\cos\theta \pm T_{\pm}\sin\theta, \tag{3.6}$$

$$f(N_{\pm}) = T_{\pm}\cos\theta \mp L\sin\theta, \tag{3.7}$$

are true. During measurements the voltage from the lateral signal, V_T, is recorded where $\alpha V_T = T$, and α is the calibration value that needs to be determined.

In order to progress further a functional form of the frictional force, f, is required. Experimentally, and making use of Johnson-Kendall-Roberts (JKR) theory [82], this can be shown to be a linear function with a significant force offset due to tip-surface adhesion, A, represented by $f(N_{\pm}) = \mu(N_{\pm} + A)$. Using this along with equation 3.7, and combining with equation 3.6 to eliminate $T_{\pm}$ we arrive at,

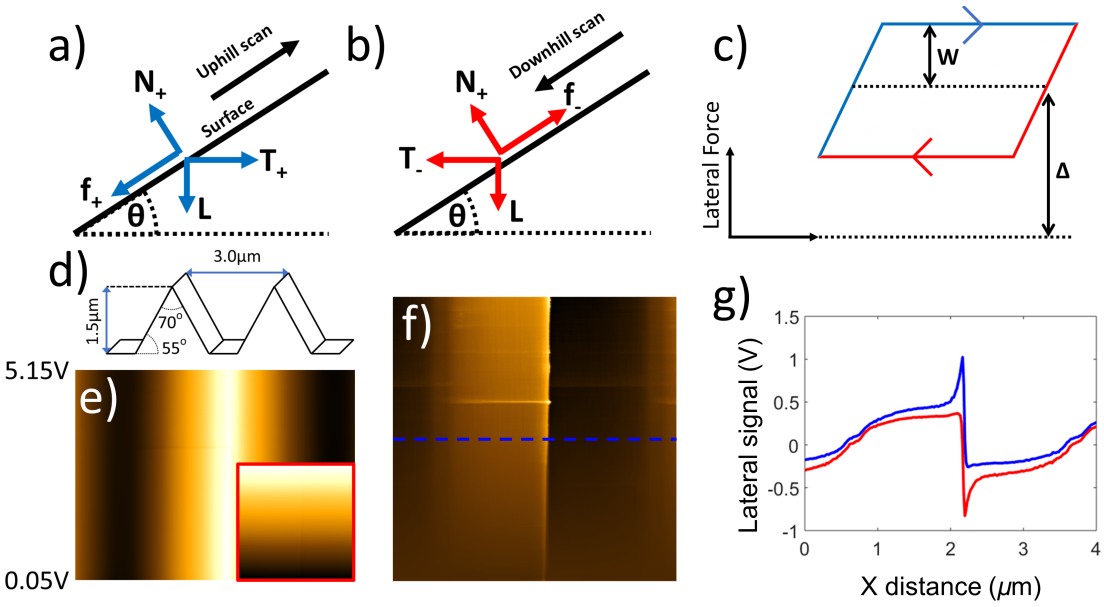


FIGURE 3.2: a) and b) show a diagrammatic representation of the forces involved when scanning an AFM tip across a surface with a slope of θ for uphill and downhill scan directions respectively. The cantilever load (L), surface normal force (N), tractive force (T), and frictional force (f) are indicated for uphill (+) and downhill (-) scan directions. c) shows a friction loop for a surface, where the trace and retrace profiles are connected at the turn around point of the tips. The friction loop width (W) and offset (Δ) used in calculations are indicated. d) shows a diagram of the sloped silicon calibration sample used to calibrate the tips. e) is a topography image of a set point ramp taken across one of the peaks in d). The spatial x-direction is 4 μm, with a black to white scale of 0 to 1.8 μm, whereas the y-direction shows applied normal force. The inset shows the corresponding deflection channel image with a deflection value (black to white) matching that of the y axis in e) of 0.05 to 5.15 V. f) shows the lateral trace image of the same set point ramp with an identical y scale of 0.05 to 5.15 V seen in e). The black to white colour scale in f) represents a lateral signal of -0.529 to 2.760 V. g) shows the trace and retrace single line profiles taken along the line shown in f).

$$N_{\pm} = \frac{L \pm \mu A \sin\theta}{\cos\theta \mp \mu \sin\theta}, \tag{3.8}$$

and hence (from equation 3.6),

$$T_{\pm} = \frac{\mu A + L(\mu \cos\theta \pm \sin\theta)}{\cos\theta \mp \mu \sin\theta}. \tag{3.9}$$

Now, since the lateral deflection of the cantilever depends on the tip movement direction, the trace and retrace signals form a friction loop, as demonstrated in figure 3.2c. The model friction loop in figure 3.2c shows how the lateral force measured by the tip reacts to a surface. The blue portion demonstrates the tip moving uphill, from left to right as indicated by the arrow, with the red portion showing the downhill right to left movement. For a flat surface the offset of the friction loop, Δ, should be zero,

providing there is no free air deflection offset. However, Δ becomes positive for a positive gradient, and negative for a negative gradient. Experimentally the friction loop offset is the average lateral force, given by $\Delta = \frac{1}{2}(T_+ + T_-)$. Another important property of the friction loop is the half-width, W, that is half the difference between the trace and retrace lateral signals. For a flat surface it is this value that is converted using the calibration value, α, into the lateral force. The friction loop half-width is given by $W = \frac{1}{2}(T_+ - T_-)$.

In practice the friction loop half-width and offset, which, as demonstrated by equation 3.9, are both functions of load, can be recorded as such using a wedge calibration sample. In this method a cantilever tip is scanned in contact mode across a tilted sample to produce an image. As the tip is scanned, the normal load on the tip is progressively increased. Figure 3.2e shows a topography image taken with slow scan disabled (i.e. a single scan line is scanned repeatedly) in order to circumnavigate any spatial differences on the surface. Following each scan line the deflection set point is incremented so that the y-axis of the images shown in figure 3.2e and f) represents the normal applied force. Figure 3.2e shows a topography image of the wedge sample, passing over a single peak, parallel to the slope, as shown in the diagram in d) for the wedge sample that was used. The normal set point was increased from 0.05 V, to 5.15 V, as labelled, with the inset of e) showing the corresponding deflection channel image for clarity. The lateral force channel is shown in f), with a profile given in g).

By averaging the lateral signals on the topographically sloped sections of the trace and retrace profiles for each scan line, i.e. the regions either side of the central peak/trough in the lateral trace/retrace profiles shown in figure 3.2g, we have a value for V_T at each load, and for both scan directions and slopes. These values can then be used to calculate, and plot, V_Δ and V_W, the voltage signals relating to Δ and W where $\alpha V_\Delta = \Delta$ and $\alpha V_W = W$ (where α is the same lateral force calibration factor mentioned earlier), as functions of load.

From the above equations Δ and W can be expressed as,

$$\Delta = \frac{\mu L + \mu A \cos\theta}{\cos^2\theta - \mu^2 \sin^2\theta} \tag{3.10}$$

and

$$W = \frac{L \sin\theta \cos\theta (1 + \mu^2) + \mu^2 A \sin\theta}{\cos^2\theta - \mu^2 \sin^2\theta} \tag{3.11}$$

By looking instead at the gradients of these values, $\Delta' = d\Delta/dL$ and $W' = dW/dL$, we can eliminate the adhesion force A offset, as well as any offset in the lateral signal that may be present, giving

$$\Delta' = \frac{\mu}{\cos^2\theta - \mu^2 \sin^2\theta} \tag{3.12}$$

and

$$W' = \frac{(1+\mu^2)\cos\theta\sin\theta}{\cos^2\theta - \mu^2\sin^2\theta}. \tag{3.13}$$

Taking the ratio of these two equations gives an expression for μ,

$$\mu + \frac{1}{\mu} = \frac{2W'}{\Delta'\sin 2\theta} = \frac{2V'_W}{V'_\Delta \sin 2\theta} \tag{3.14}$$

that is simply a quadratic equation that can be solved to find two different values for the friction coefficient μ. With a value of μ the lateral calibration value, α, can easily be found using either equation 3.12 or 3.13, given that $\alpha V'_\Delta = \Delta'$ and $\alpha V'_W = W'$. Experimentally the plots of V_Δ and V_W against load mentioned earlier can be used in order to find the calibration value.

In practice these calculations have been carried out using user defined panels sourced from the Asylum instruments forum. Each lateral ramp image results in four possible calibration values, one pair for the left-hand side (LHS) slope and one for the right-hand side (RHS) slope. Each side has two mathematical solutions due to the possible values of μ found by solving equation 3.14. As such one solution from each pair can be rejected, as it does not physically make sense (e.g when $\mu > 1$, or if the solution is imaginary). This results in a single solution for the LHS slope and a single solution for the RHS slope, which can be averaged for a greater degree of accuracy.

3.4 Angle-Resolved Photoemission Spectroscopy

Angle-resolved photoemission spectroscopy, ARPES, is a photoelectron spectroscopy technique, often referred to as angle-resolved ultra-violet photoemission spectroscopy, ARUPS. It is a method that allows for observation of the electronic structure in crystallographic materials.

Electromagnetic radiation within the ultra-violet (UV) spectrum (i.e. with wavelengths between 10 to 400 nm) is used to probe the valence electrons of a material [85, 86]. In order to probe the core-level electrons in a surface, higher energy (lower wavelength) X-rays are required, in a technique known as X-ray photoelectron spectroscopy (XPS) [87]. For ARPES experiments the UV radiation must be well calibrated with a narrow linewidth. Suitable sources include lasers (energies of 7 or 11 eV), a plasma helium discharge ($\sim$ 20 eV), or synchrotron radiation as used in the ARPES measurements recorded in this thesis ($\sim$20-200 eV).

ARPES provides a technique to measure the energy and momentum of photoemitted electrons from the material under investigation. This allows for the determination of the electron wavevector following photon initiated ejection, which can be used to

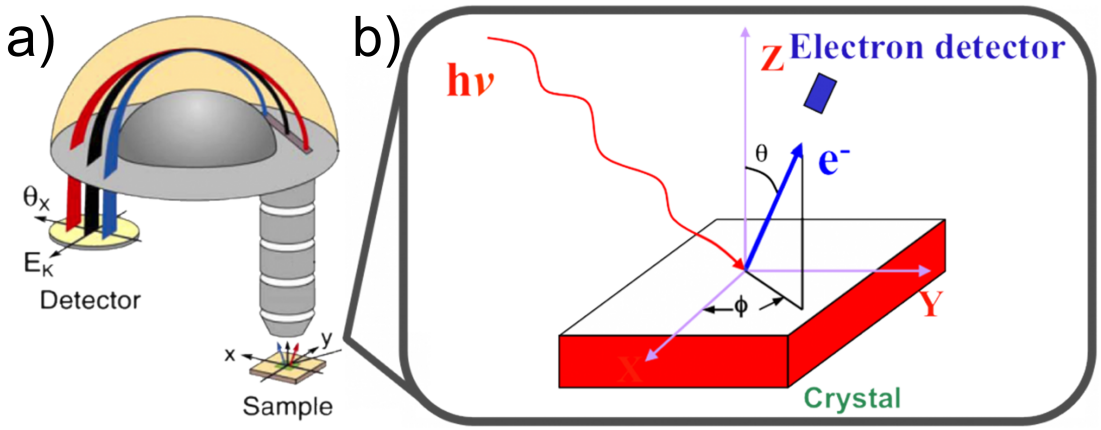


FIGURE 3.3: a) A schematic of an electron detector used in ARPES. The electrons are directed onto a 2D multi-channel plate to record the energy and momentum of the ejected electrons. b) A diagram of the UV radiation incident on the sample surface. The incident UV light has an energy $h\nu$. The resultant photoemitted electron is ejected at an angle defined by θ and ϕ, with both the angle and energy subsequently measured by the electron detector. Figure adapted from [88]

draw conclusions about the initial wavevector of the electron within the material, revealing information about the electron band structure. In order to accomplish this a hemispherical electron detector similar to the one illustrated in figure 3.3a is used. The ejected electrons are directed onto a two-dimensional multi-channel detector plate that records the electron ejection angle, θ (indicated in figure 3.3b), and the electron energy.

The electron ejection and detection is described by a three step model as follows: i) UV radiation incident on the samples, shown in figure 3.3b with an energy of $h\nu$, is transferred to an electron within the valence band of the crystal. This electron is excited from its initial state to a final state within the material. ii) The electron moves through the material to reach the surface. iii) The electron crosses through the surface and exits the material into the vacuum state, with its own kinetic energy at an angle, θ, as shown in figure 3.3b [88–90]. The momentum attributed to the incoming UV photon is considered negligible, and so according to conservation of momentum the final momentum of the photoemitted electron is equal to that of the initial electron momentum within the solid. The periodic surface of the crystal structure acts as a 2D scattering potential on the photoemitted electron. As a result of the interaction between the electron with this potential, the scattered electron wavevector parallel to the crystal surface outside the sample is equal to the electron wavevector within the material plus a reciprocal lattice vector of the surface, $\mathbf{G}$, resulting in

$$\mathbf{k}_{\parallel}^{\mathbf{outside}} = \mathbf{k}_{\parallel}^{\mathbf{inside}} + \mathbf{G}, \tag{3.15}$$

where $\mathbf{k}_{\parallel}^{\mathbf{outside}}$ is the electron wavevector following ejection and parallel to the surface, and $\mathbf{k}_{\parallel}^{\mathbf{inside}}$ is the wavevector within the material that is parallel to the surface. However, due to the the Bloch wave theorem for periodic lattices the addition of the reciprocal lattice vector causes no change in the wavevector, leading to an equivalence between $\mathbf{k}_{\parallel}^{\mathbf{outside}}$ and $\mathbf{k}_{\parallel}^{\mathbf{inside}}$.

The wavevector of the electron perpendicular to the surface, $\mathbf{k}_{\perp}$, is not conserved during ejection of the electron, however, this is not important in the case of 2D materials where the interest lies only in surface states [88–90].

3.5 Raman Spectroscopy

Raman spectroscopy is a technique that is commonly used throughout material science and chemistry to identify the chemical and molecular structure of materials. First reported by *C. Raman* in 1953 [91] this phenomenon involves the probing of vibrational modes within a target material using highly monochromatic light. In practice, incident, single-wavelength light, most often from a laser source, is passed through a beam splitter and microscope objective lens and focused onto a sample surface (as shown in figure 3.4a). The incident photon, with an associated energy of $h\nu$, then interacts with the surface in a number of possible ways before being collimated by a pin hole/slit and entering the spectrometer, as shown in figure 3.4. The various possible interactions are indicated in the Jablonski diagram in figure 3.4b. In this figure four possible radiative electron transmissions are highlighted. The first, indicated in green, is elastic Rayleigh scattering. In this form of scattering the incoming photon is absorbed by an electron in a lower energy state, that is raised to a higher virtual state, located between the initial state and a higher electron energy state with a difference equal to that of the original photon energy. This energy is then re-radiated as the electron falls back to the lower energy state, emitting a photon with the same wavelength as that of the incident light. In Raman scattering several additional energy states above the ground state are involved, these arise due to the vibrational motion of the chemical bonds within the target material, and can be due to linear, rotational, or torsional movements of the material structure. In Stokes Raman scattering, indicated in red in figure 3.4b the incident photon is absorbed by an electron in the ground state to a virtual state below the next energy level, which then falls back into a vibrational state, emitting a photon with an energy matching the difference between the excited virtual state and the new vibrational mode. The scattered photons energy is red-shifted from that of the incident photon by an energy corresponding to that of the vibrational. In contrast, anti-Stokes Raman scattering involves the absorption of the incoming photon by an electron initially within one of the vibrational states to a higher energy virtual state, before the re-radiation of a scattered photon with a higher, blue-shifted energy

compared to the incident light, as the excited electron relaxes back to the ground state. Since the possible vibrational states for a given material are the same for the Stokes and anti-Stokes mechanisms, the absolute shift in energy for both Raman scattering cases are approximately equal for each of the vibrational modes.

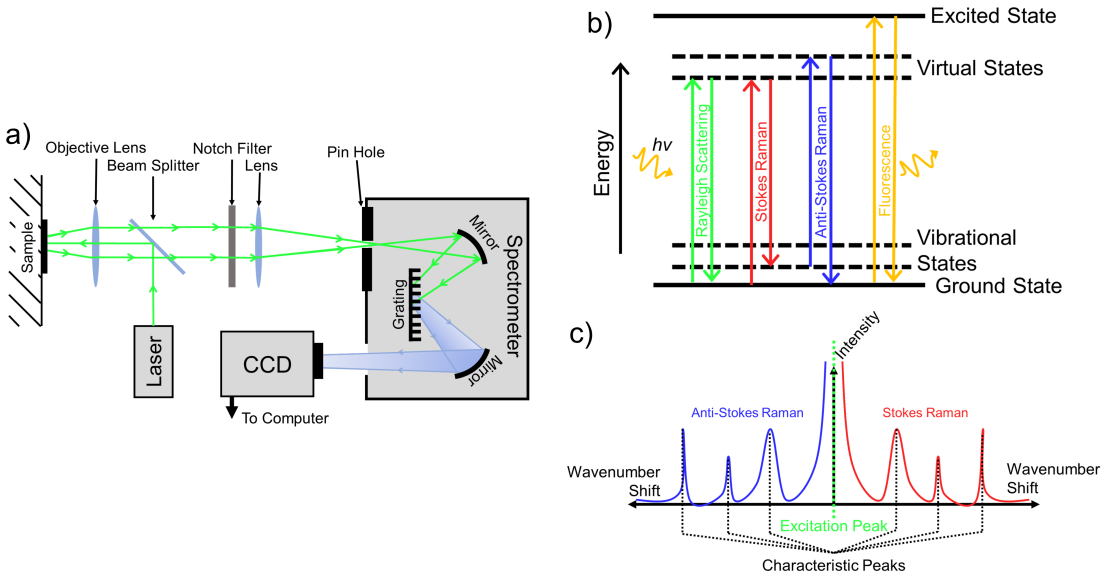


FIGURE 3.4: a) A typical Raman configuration. The direction of the ray path in this diagram is indicated by the arrows, with the constituent pieces labelled. b) An example Jablonski diagram showing the four main radiative electron transmissions, Rayleigh scattering (green), Stokes (red) and anti-Stokes (blue) Raman scattering, and fluorescence (yellow). c) An example Raman spectrum of intensity against wavenumber shift relative to the central excitation peak from the incident probing light, including Stokes (indicated in red) and anti-Stokes (indicated in blue) characteristic Raman peaks.

Figure 3.4c shows a model Raman spectrum. In this spectrum the y-axis corresponds to the measured intensity of the signal incident on the CCD of the setup in a), with the x-axis showing the shift in the wavenumber (or frequency) of the recorded photons relative to the high intensity central excitation peak, that exists due to Rayleigh scattering, at a frequency matching that of the original monochromatic light. The wavenumber shift, $\Delta\nu$, can be calculated using,

$$\Delta\nu = \frac{1}{\lambda_{excite}} - \frac{1}{\lambda_{Raman}}, \tag{3.16}$$

where λ_{excite} is the wavelength of the probing excitation light, and λ_{Raman} is the wavelength of the measured Raman scattered light. The wavenumber shift is usually measured in inverse centimetres (cm^{-1}) and can be calculated by multiplying the value of $\Delta\nu$ by 10^7 if the units used for λ_{excite} and λ_{Raman} are in nanometres. As shown by the example spectrum shown in figure 3.4c the data recorded due to the red-shifted

Stokes Raman scattering process has a positive wavenumber shift, whereas the blue-shifted anti-Stokes Raman scattering process results in a negative wavenumber shift. In practice the high intensity excitation peak seen in figure 3.4c is usually eliminated using either a band pass or notch filter placed within the beam path, as shown in a).

The characteristic Raman peaks seen on either side of the spectrum shown in figure 3.4c each correspond to a different vibrational mode of the electron that was probed, and as such are dependent on the molecular and structural properties of the target under investigation. The positions and relative intensities of these peaks allow for the identification of the material by comparison with expected peak locations, and can also reveal information about the structure including the amount of strain present, a technique that is very useful when investigating 2D materials such as graphene and hBN [45, 92, 93]. The characteristic peaks of the Stokes and anti-Stokes spectra portions both arise from the same vibrational modes and as a result they are positionally symmetrical about the excitation peak, however the Raman peak intensities between the Stokes and anti-Stokes peaks can vary depending on the initial population distribution of the ground state and vibrational states.

3.6 Materials

In the following sections the various materials that have been used or investigated in this thesis are described. These include the substrates; silicon dioxide, sapphire, and HOPG. These are followed by discussion of the silver nanowires (NWs) used for deposition and manipulation.

3.6.1 Substrates

A range of substrates were used throughout this work depending on the required criteria. For example, for MBE growth, where substrate temperatures in excess of 1500°C are required, a suitable substrate that remains intact, and ideally with a low thermal expansion, is essential.

Silicon Dioxide

Silicon dioxide, SiO_2, is a very widely used substrate in material science due to its chemical and physical properties. SiO_2 can be routinely grown through thermal oxidation of silicon wafers (Si/SiO_2). Chemically it is very stable, relatively inert, and resistant to many etchants that can be used to remove additional materials during device constructions. It has a high dielectric strength of 10^7 Vcm^{-1}, and a large energy bandgap of 8.9 eV, leading to its use as an insulator and as a gate dielectric in transistor

devices. SiO_2 is also relatively thermally stable, with a high temperature stability of up to 1600°C.

In addition, the dielectric properties of the oxide layer allow for identification of thin flakes of exfoliated crystals, down to bilayer and monolayer distinction for graphene and hBN using optical microscopy [94–96]. This makes Si/SiO_2 an ideal substrate for fast and convenient selection of thin van der Waals crystal flakes for transfer or device fabrication.

Sapphire

Similar to silicon dioxide, sapphire is a very chemically stable and inert material. Sapphire, Al_2O_3, is an insulating substrate which has a hexagonal structure with a lattice constant of 4.77 Å. Importantly for high temperature MBE growth, sapphire can remain stable at up to 2050 °C and has a high thermal conductivity of 42 W/(mK). These properties make sapphire a good substrate for the high temperature MBE growth of graphene on exfoliated hBN, with the hBN exfoliated directly onto the sapphire surface.

Highly Oriented Pyrolytic Graphite

Highly oriented pyrolytic graphite, HOPG, is the bulk form of graphene, consisting of many individual graphene layers held together by interlayer van der Waals forces. These layers can be exfoliated to reveal a clean surface with very large atomically flat terraces. Additionally, the exfoliation of this material can be used to isolate individual graphene layers, as carried out by *Geim et al.* in their seminal paper [1]. The stacking configuration of HOPG is generally in the Bernal stacking form, as demonstrated for bilayer graphene in figure 2.3a and b) in section 2.1.2. HOPG is highly conducting and thermally stable for temperatures up to 2000 °C. The similarities of its lattice structure, identical to that of graphene described in section 2.1.1, with hexagonal boron nitride make it a near ideal substrate for growing hBN by MBE, with high temperatures achievable due to the thermal properties outlined above.

3.6.2 Silver Nanowires

In order to carry out electrical measurements of material grown on the insulating sapphire substrate, or exfoliated/transferred material on SiO_2, electrical contacts were formed through deposition of silver, Ag, nanowires, to form a conducting network as will be discussed later in chapter 4[97–101]. The nanowire solution that was used consisted of silver nanowires held in a liquid suspension of isopropyl alcohol with

a concentration of 0.5 % (obtained through Sigma-Aldrich). The nanowires themselves have average expected dimensions of 10 μm in length and 60 nm in diameter, although these values were observed to vary significantly with NWs in excess of 28 μm recorded.

3.7 Growth and Deposition

3.7.1 Graphene Production

Typically, graphene is produced through one of two methods. These most common methods are mechanical exfoliation and chemical vapour deposition. Mechanical exfoliation, also known as the 'scotch tape' method, is a technique in which adhesive tape is used to repeatedly sever the weak interlayer bonding of a stacked, layered material, such as HOPG, until very thin flakes down to a single atomic layer are achieved and placed onto a chosen substrate material, as shown in the diagram in figure 3.5. It was this method that was first used to successfully isolate graphene material [1]. Through mechanical exfoliation flakes with dimensions up to 100 μm and varying thicknesses can be produced.

Chemical vapour deposition is a particularly useful graphene growth technique due to its scalability, high achievable quality, and ability to directly grow 2D vertical heterostructures [102–107]. In CVD a heated substrate is placed within a chamber, in the presence of flowing gases. These gases react with the heated surface, where the target material is formed. For CVD growth of graphene, hydrocarbon gases, such as methane, are used as the source of carbon, reacting with a, typically copper, catalytic substrate.

In this thesis the far less widely used method of molecular beam epitaxy has been implemented by Sergei V. Novikov and Tin S. Cheng for graphene production. MBE graphene production is considerably more costly than growth by CVD due to the conditions required, with extremely high temperature (in excess of 1600 °C) needed to promote graphene growth, and to allow for significant carbon re-evaporation rates to produce large carbon aggregate free regions.

3.7.2 MBE Graphene

In the molecular beam epitaxy process the deposited species is evaporated, or sublimated, from a source, with the resultant beam directed at a heated target substrate. MBE growth is a widely used technique in semiconductor fabrication and allows for slow, precise layered growth that can include sample doping. Figure 3.5b shows an example diagram of a deposition chamber similar to the one used for graphene growth. In this diagram the material source is presented as a carbon filament effusion cell, with

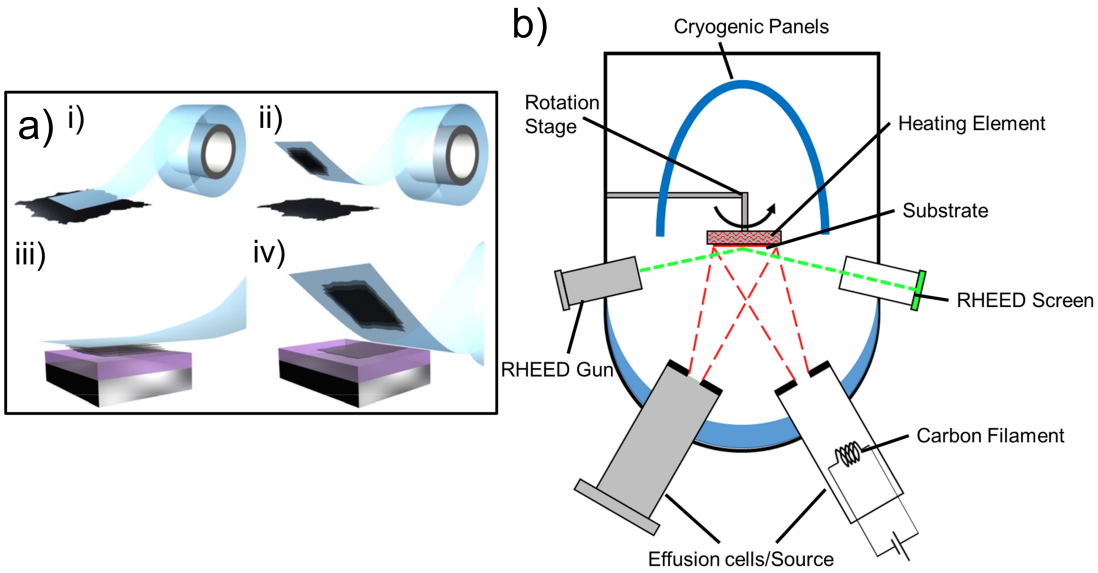


FIGURE 3.5: a) A diagram demonstrating the mechanical exfoliation, or micromechanical cleaving, technique. i) Adhesive tape is applied to the bulk material. ii) as the tape is removed the upper layers of the material remains attached. iii) After repeated exfoliation to achieve thin flakes, the layers are placed in contact with a substrate. iv) Removing the tape leaves freshly cleaved layers on the substrate surface (held in place by van der Waals forces), while the upper most layers remain on the tape. Diagram from [108]. b) Labelled diagram of a MBE deposition chamber.

only one source required for the single species material. The particle beam is directed at a heated substrate stage. This substrate stage is rotated during growth to allow for an even surface coverage. Cryogenic panels within the growth chamber help to maintain an ultra-high vacuum environment by providing a surface for adsorption. A reflection high-energy electron diffraction (RHEED) instrument, consisting of an electron gun and screen, is used to monitor the crystal growth in situ.

As the beam from the carbon source reaches the substrate, the material is adsorbed onto the surface, where the high temperature facilitates the processes seen in figure 3.6 (from reference [109]), and allows for the formation of highly ordered lattice material. At location (a) in figure 3.6 deposited atoms approach the surface. At (b), after reaching the surface, the adatoms diffuse across it. These adatoms may meet to form dimers (c), or attach to existing islands (d). Once attached to an island the atom may detach and move away from the island (e), or diffuse along its edge (f). Deposition may also occur on top of islands (g) and (h), where similar processes can occur. At high substrate temperatures adatoms may re-evaporate, leaving the surface (i).

In this work, three individual carbon sources have been used to grow graphene. These are each outlined below, and include the use of a carbon filament, a separate tantalum encased carbon filament, and an electron beam (e-beam) source. In most cases

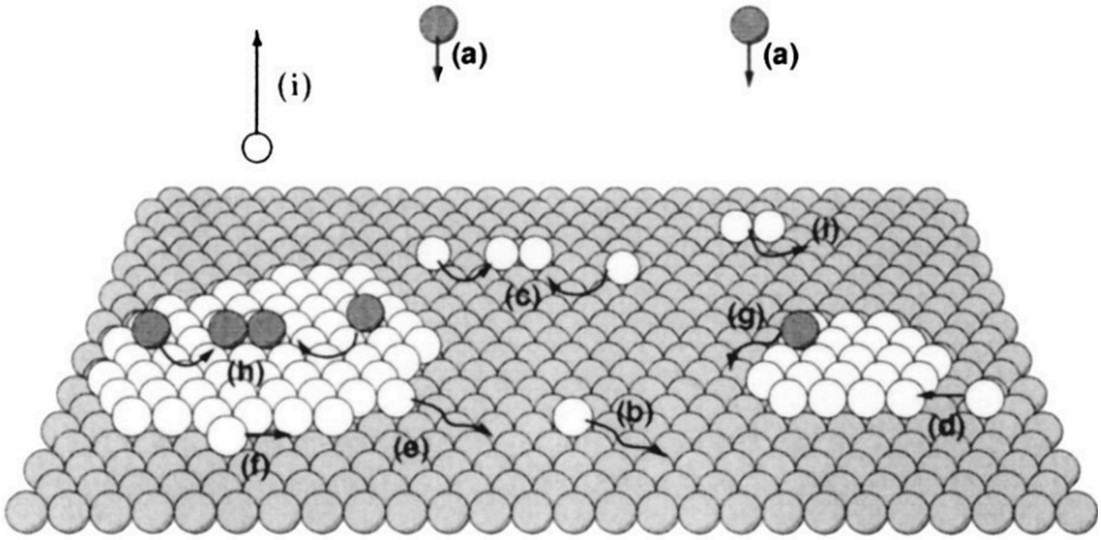


FIGURE 3.6: A diagram showing the typical processes involved during MBE growth described in the text. Diagram from [109].

the MBE graphene investigated within this thesis was grown on hBN flakes positioned on a sapphire substrate, with exceptions shown in chapters 7 and 8 where graphene was grown on MBE hBN on a HOPG substrate. In the prior case, hexagonal boron nitride flakes around 10-100 nm thick with lateral dimensions of 20-100 μm were mechanically exfoliated using the method shown in figure 3.5a before being placed onto 1 x 1 mm^2 polished sapphire (0001) substrates. These substrates were cleaned in toluene overnight and subsequently placed in an Ar/H_2 (95:5) atmosphere at 400°C for eight hours. Following this, the samples were placed within a custom built GENxplor MBE system from Veeco at a base pressure of $\sim 10^{10}$ Torr, and annealed at 400 °C for 30 minutes [44].

While growing at the high substrate temperatures in excess of 1600 °C used within this thesis it is important to consider the expansion and contraction of the two constituent materials - graphene and hBN - that each possess different thermal coefficients of expansion, $\propto_g$ and $\propto_{BN}$ [44]. The coefficient for bulk hBN is -3 x 10^{-6}/K at 300 K, remaining negative, but with a reduced magnitude, up to 800 K [110]. For graphene there is disagreement in the literature, with some arguing that $\propto_g$ is negative at 300 K becoming positive at values above 350 K [111], while others argue the value remains negative up to 400 K [112]. The highest temperature where data is available suggests, alternatively, that $\propto_g$ remains positive, in agreement with theory [113]. In both cases, for graphene and hBN, the growth temperatures exceed the values where the thermal coefficients have been measured in the literature, however the difference between $\propto_g$ and $\propto_{BN}$ is likely to be a cause of strain formation and variation across the MBE

grown graphene during post-growth cooling, with strain maintained by nucleation sites acting to pin the material in position [44].

Carbon Filament

The primary method of carbon deposition that was used involved sublimating a high purity pyrolytic graphite filament using a large current utilizing the Joule heating process, while simultaneously heating the substrate to high temperatures. These carbon filaments had a typical filament shape, and were positioned within a Knudsen effusion cell. Using this type of carbon source the flux could be controlled by adjusting the amount of current passing through the high purity filament, however there can be inconsistencies between different filaments, and at different stages of a filaments use as the carbon source is depleted and the respective conductance is changed as a result. In addition, these filaments may fail due to the extreme conditions, with blown filaments preceding the AFM observation of significant carbon aggregate coverage.

The growth times and temperatures for the samples produced in this way were approximately 1600°C, measured using a thermocouple situated on the substrate heater, for 5 hours, with values for individual samples shown provided in table 5.1 in chapter 5. The sample stage rotation speed was kept at 10 revolutions per minute throughout all growths, and a current flowing through the carbon filament was held between 103 and 114 A.

While using a carbon filament source, the flux produced by the sublimated carbon contains a mixture of carbon clusters [114, 115]. These clusters are predominantly monatomic carbon, C_1, or clusters consisting of 2 or 3 carbon atoms, C_2, and C_3, with larger clusters, C_n, less likely. The high presence of these clusters means that for graphene to be successfully produced they must first be dissociated by the high substrate temperature, or incorporated within the graphene structure. However, these incoming carbon clusters will also lead to the formation of carbon aggregate deposits on the surface that, while having the potential to initiate graphene growth [44], will produce lower quality graphene and limit the size of clean, pristine regions.

Elemental Carbon Source

The second carbon deposition source that was implemented by Sergei V. Novikov and Tin S. Cheng to produce some of the samples that have been included within this thesis was designed to limit the amount of larger carbon clusters, while raising the proportion of solitary carbon atoms, C_1. This was achieved by replacing the carbon filament with a separate Joule-heated element that consisted of high purity carbon powder encased within a tantalum shell with a thickness of approximately 0.05 mm [116]. Figure 3.7a shows a schematic of the carbon source that was used, with panel

b) showing a cross-sectional slice of the schematic in a). When the filament is heated to approximately 2000 °C the sublimated C from the encapsulated powder reacts with the tantalum tube to form tantalum carbide [117, 118]. Carbon atoms then diffuse through the tantalum carbide towards the cylinders outer wall, where the atomic carbon is evaporated and directed towards the substrate. The resultant carbon flux is consisted mainly of atomic carbon species, confirmed using mass analysis [118], with fewer aggregates present in graphene grown using this source [116].

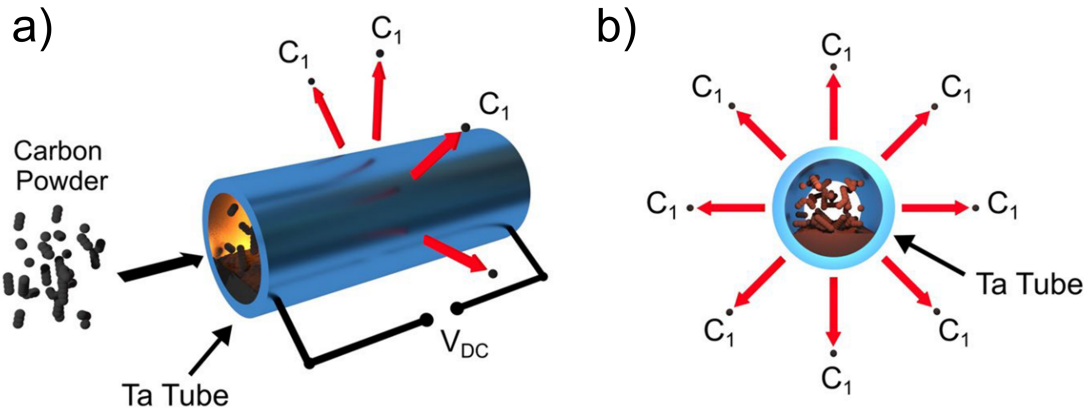


FIGURE 3.7: Schematic of the carbon filament source used for elemental carbon deposition. a) Carbon powder is placed within a tantalum tube that acts as the heating element/filament. b) Cross-sectional diagram of a). The sublimated carbon reacts with the tantalum cylinder. Solvated carbon atoms then diffuse through the tantalum carbide and evaporate at the surface with a predominantly atomic carbon composition. Figures from [116].

The sample stage rotation that was used during growth was 10 revolutions per minute, with a current for the atomic carbon source of 110 - 115 A. The substrate growth temperatures and times for these growths are provided in the relevant sections of the text, including in table 5.1 in chapter 5, and were approximately 1700 °C and 3 hours.

E-beam Source

The method by which the electron-beam source produces a carbon flux in order to grow graphene by MBE is drastically different from the two Joule-heated sources discussed in the previous sections. Figure 3.8 shows a schematic of a typical electron beam source. In e-beam deposition a heated cathode filament, typically tungsten (shown in orange in figure 3.8), is used as an electron source. Electrons ejected from this filament are accelerated by a high voltage applied between the filament and a metal plate with a hole to collimate the electrons into a beam. This electron beam is then focussed onto the target material, situated within a crucible holder, by a strong

magnetic field. An additional, varying, lower strength magnetic field is used to scan the electron beam across the target to provide an even surface spread of the arriving beam. The incoming electron beam heats the target material surface, evaporating it to produce a flux that can be used in MBE. The electron beam evaporator source that was

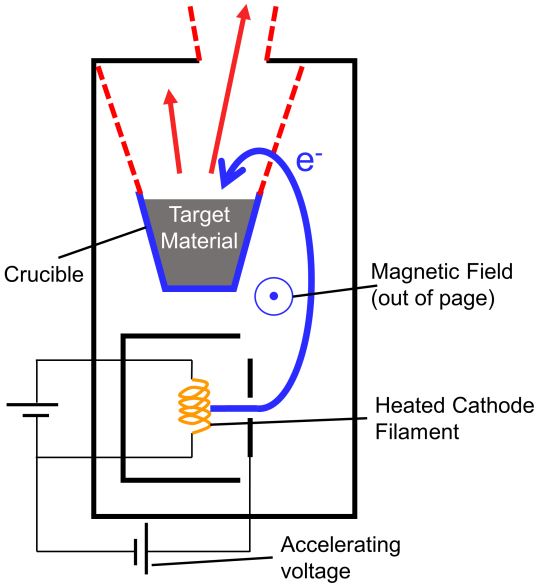


FIGURE 3.8: Labelled diagram showing the operation of the e-beam carbon source. A heated cathode filament is used as the electron beam source, and is accelerated using a high voltage. This beam is directed towards the surface of the target material, situated within a cooled crucible, by a magnetic field.

used was produced by Dr. Eberl MBE-Komponenten GmbH (model EBVV 63-T4) and fitted with a high purity carbon anode target. For all samples an e-beam accelerating voltage of 5 kV and a substrate rotation of 10 revolutions per minute were used, along with a 200 - 400 mA e-beam current and a growth time of 2 hours at 1675 °C for the MBE graphene on hBN seen in chapter 5, and table 5.1.

The e-beam carbon source has allowed for more precise graphene growth with an increased stability and tunability of the carbon flux produced, over that of the carbon filament method of growth, that has allowed for thin strips of graphene to be produced along surface step edges. For this graphene nanoribbon growth, explored in chapter 7, the same e-beam source was used under different conditions. For these growths a lower temperature to those used in previous depositions was implemented of 1390 °C, along with a far shorter growth time. The growth included a ramp up of the e-beam current to 300 mA (using a ramp rate of 10 mA/min), before being held at this current for a growth time of between zero and several minutes, then a ramp down at a rate of 100 mA/min. Specific details for individual samples can be found within the text at the relevant sections in chapter 7.

3.7.3 Hexagonal Boron Nitride Production

The growth of a wide proportion of the MBE graphene samples that have been investigated within this thesis have taken place on top of hexagonal boron nitride flakes, with hBN chosen due to the appealing properties of the material described in section 2.2. These flakes have been produced through mechanical exfoliation, as shown in figure 3.5a, onto a sapphire substrate. The bulk hBN powder used during exfoliation was obtained from Kenji Watanabe and Takashi Taniguchi, and was grown using high temperature and pressure [8].

For the samples shown in chapters 7 and 8 the hexagonal boron nitride material was grown using MBE.

MBE hBN

For the MBE hBN material grown within this thesis, a separate growth chamber to that which was used to grow graphene was employed. This second chamber, similar to the schematic in figure 3.6, was part of the same MBE ultra-high vacuum (UHV) system as that used for the MBE graphene deposition. In order to grow hBN by MBE multiple sources are required, with additional parameters, such as flux ratio, to those used for graphene growth. The boron source used by Sergei V. Novikov and Tin S. Cheng for hBN grown directly on bulk HOPG substrates was a high-temperature Veeco effusion cell, consisting of a radiatively heated B filled crucible. For the nitrogen source a high efficiency, conventional Veeco radio-frequency (RF) nitrogen plasma source was used to provide a beam with high active nitrogen fluxes.

For these growths, shown in chapters 7 and 8, freshly cleaved HOPG substrates (1 x 1 cm^2) were cleaned by using a thermal cycle to 400 °C for approximately 8 hours in an Ar/H2 (95:5) atmosphere before being transferred into the custom-designed high-temperature dual chamber GENxplor MBE system. Ultra-high vacuum conditions with a base pressure of $\sim 10^{-10}$ mbar was used during growth. The hBN layers were then grown using plasma-assisted MBE with a substrate temperature of 1390 °C, using the beam sources described above. Boron sublimation was carried out at a temperature of $\sim$ 1875 °C. The nitrogen source was operated with a N_2 flow of 2 sccm and an RF power of 550 W. The same substrate rotation speed of 10 revolutions per minute was used with a growth time of 3 hours for all of the MBE hBN samples investigated.

The lateral heterostructure samples shown in chapter 7 consist of combined MBE hBN and MBE graphene growth. While grown within the same UHV system, in most accounts the HOPG substrate that was used was removed from the system following MBE hBN growth. This was to allow for ex-situ AFM measurements prior to re-introduction to the system that was followed by MBE graphene growth within a second MBE chamber. However, samples have been grown, and are shown in chapter

7, where the HOPG substrate is not removed from UHV following hBN growth, and is moved directly into the graphene growth chamber for subsequent growth.

3.8 Data Processing

Most of the scans taken using AFM, CAFM and LFM have been processed using the Gwyddion software package [119]. The images have undergone several standard imaging techniques. Where appropriate the images have been analysed by first leveling the data by mean plane subtraction. This involves fitting a plane across the image, usually due to a surface offset relative to the scanner, which is then subtracted across all of the data. Secondly the images rows are aligned. This is computed automatically by the Gwyddion software and consists of shifting each line so that the median of differences between vertical neighbour pixels becomes zero. Other methods that have also been used include profile extraction, distance measurements, scale/colour adjustments, analysis of statistical quantities, and more.

Matlab software [120] has also been used to produce select CAFM images, in particular in the cases where many individual scans have been imaged while a variable is changed between each frame. Matlab has also been used to produce force-distance curves, and strain maps.

Chapter 4

Processing and Electrical Contact Formation

Many of the samples investigated throughout this thesis have conductive substrates, such as those grown on HOPG, or the low temperature growth on hBN flakes similar to those shown in figure 3.1b in chapter 3, with a typical lateral dimension of up to $\sim$ 50 μm. The MBE grown graphene samples that have been produced using a substrate temperature on the lower end of the growth range result in a visible carbon aggregate coverage over the entirety of the insulating sapphire substrate, with the exception of the corners where the sample clip holders block the carbon to leave uncoated sapphire regions. These carbon layers have a thickness that depends strongly on the MBE growth parameters, measured by scraping a trench into the carbon with plastic tweezers followed by recording AFM topography profiles. Typically the carbon aggregate depth on the sapphire is around 80 nm. For these samples electrical contact can be made simply by placing a wire directly onto the carbon, achieved, for example, by using a metal clip. For these samples electrical contact processing is unnecessary. However, for samples grown at higher temperatures, with a substrate in excess of $\sim$1500 $^{\circ}$C, measured using a thermocouple situated on the substrate heater itself, the carbon is re-evaporated. This results in a carbon free sapphire substrate surface, with electrically isolated graphene on hBN flakes. In this case an electrical connection needs to be made in order to apply a bias to the surface/tip before the graphene surface can be investigated electronically using scanning probe microscopy (SPM).

Conventionally electrical contacts are made using industry standard lithography techniques. These methods involve the deposition and subsequent removal of photoresists which are often polymeric. They allow for highly precise and defined contacts to be made. However, these processes, while suitable for bulk semiconductor application, can severely impact the graphene, or other 2D material, by introducing contamination that cannot be easily removed through cleaning processes, and negatively impacts the investigation of the single layer material using scanning probes. Furthermore, lithographically created contacts are expensive and have a low yield

since only one or two flakes at a time may be contacted.

In this study, these methods are avoided, opting for a variety of more novel approaches to conserve sample cleanliness. Attempts at several different techniques were pursued. Shadow masking, construction of conductive epoxy contacts, and focussed ion beam (FIB) milling were all trialled with varying degrees of success, before arriving at the deposition of silver nanowires with a tuned coverage to provide a conducting network across samples. Once deposited these nanowires form a mesh that connects isolated regions, while still allowing for investigation of the graphene surface using SPM techniques due to the relatively low nanowire concentration. Furthermore, an SPM tip can be used to precisely manipulate the position of these nanowires, and slice them if necessary.

4.1 Shadow Masking

Shadow masking is a conceptually simple technique. It involves using a shadow mask, in this case an arrangement of glass plates were used, held near to the sample to block the incoming deposition. The presence of the mask leaves a clean substrate beneath in the desired pattern. To create electrical contacts on a sample with a large flake concentration a 10 nm/100 nm titanium/gold layer was deposited using metal evaporation. The boundary where the shadow mask was placed had a significant chance of randomly intersecting a flake, providing electrical contact to the surface. However, in practice the boundary between the Au contact and the substrate was not sharp enough for reliable electrical measurements due to diffusion of Au underneath the mask. As a method for direct electrical contacting, shadow masking was quickly abandoned, however, it was used for testing and in combination with other methods discussed below.

4.2 Epoxy Contacts

This technique involves manually connecting thin Au wire to individual flakes, with typical lateral dimensions of up to 50 μm, using conductive epoxy resin. The epoxy used was Polytec EC101 silver conductive epoxy. The painting of the epoxy was carried out underneath an optical microscope with a long working distance using insulin needles to deposit the resin, as illustrated in figure 4.1a. A further set of needles was then used to position small pieces of thin (50 μm and 15 μm diameters) gold wires on the surface. This was successfully trialled across SiO_2 and sapphire substrates where epoxy contacts with dimensions as low as 100 μm, with connected Au wire, were achieved. The contacts were then cured using a hot plate at a temperature of

100°C for 1 hour. This technique was extended to exfoliated hBN flakes on a sapphire substrate where connections were successfully made to individual flakes as shown in figure 4.1b. The hBN flake in this example has dimensions of around 30 μm by 35 μm. Despite the surprising accuracy with which these contacts can be made using careful handling, there are a number of limitations. The wire placement has a tendency to move sporadically with a slight nudge which may damage large areas of the surface as it is dragged across, the epoxy can cover large sections of the material with target flakes being at great risk, and the height of the epoxy contacts is very large, limiting the AFM direction of approach. This method was not used on graphene samples due to these limitations, and because of the greater success rate of nanowire deposition. However, the process of using conductive epoxy contacts combined with Au wire was used in some samples for contacts to the substrate.

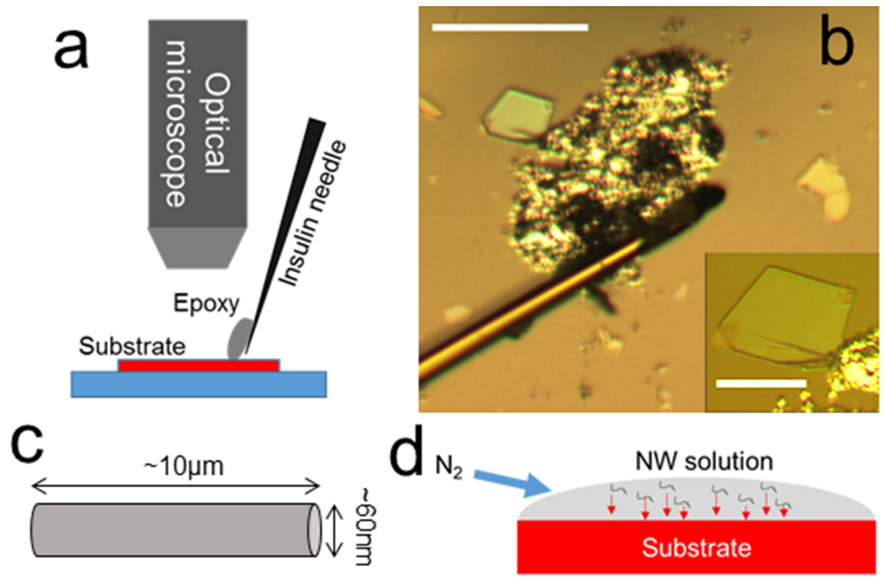


FIGURE 4.1: a) The setup used to create conductive epoxy contacts, an example of which is shown in b). b) Optical micrograph of a contact made using epoxy to connect a 15 μm diameter Au wire to a hBN flake exfoliated on a polished sapphire (0001) substrate. Inset shows the flake with an increased magnification. Scalebars are 100 μm and 30 μm for the main image and the inset respectively. c) A schematic showing the mean expected dimensions of the Ag nanowires with a length of 10 μm and a diameter of 60 nm. d) The nanowire deposition technique. The nanowire solution is drop deposited onto the surface before being dried using a N_2 stream.

4.3 Nanowire Deposition

The nanowire solution that was used consisted of silver nanowires held in a liquid suspension of isopropyl alcohol with a concentration of 0.5% (obtained through Sigma-Aldrich). The nanowires themselves have average expected dimensions of 10 μm in length and 60 nm in diameter, see figure 4.1c, although these values were observed to vary significantly, with nanowire lengths in excess of 28 μm observed. The nanowire solution was further diluted using IPA (with an IPA to NW solution ratio of 10:1) before drop depositing onto a substrate as shown in the diagram in figure 4.1d. The nanowires then adhere to the surface where attractive van der Waals forces hold them in place. After a short period of time of 5 seconds the substrate was dried using a stream of inert N_2 gas to remove any excess solution and prevent drying stains forming on the surface.

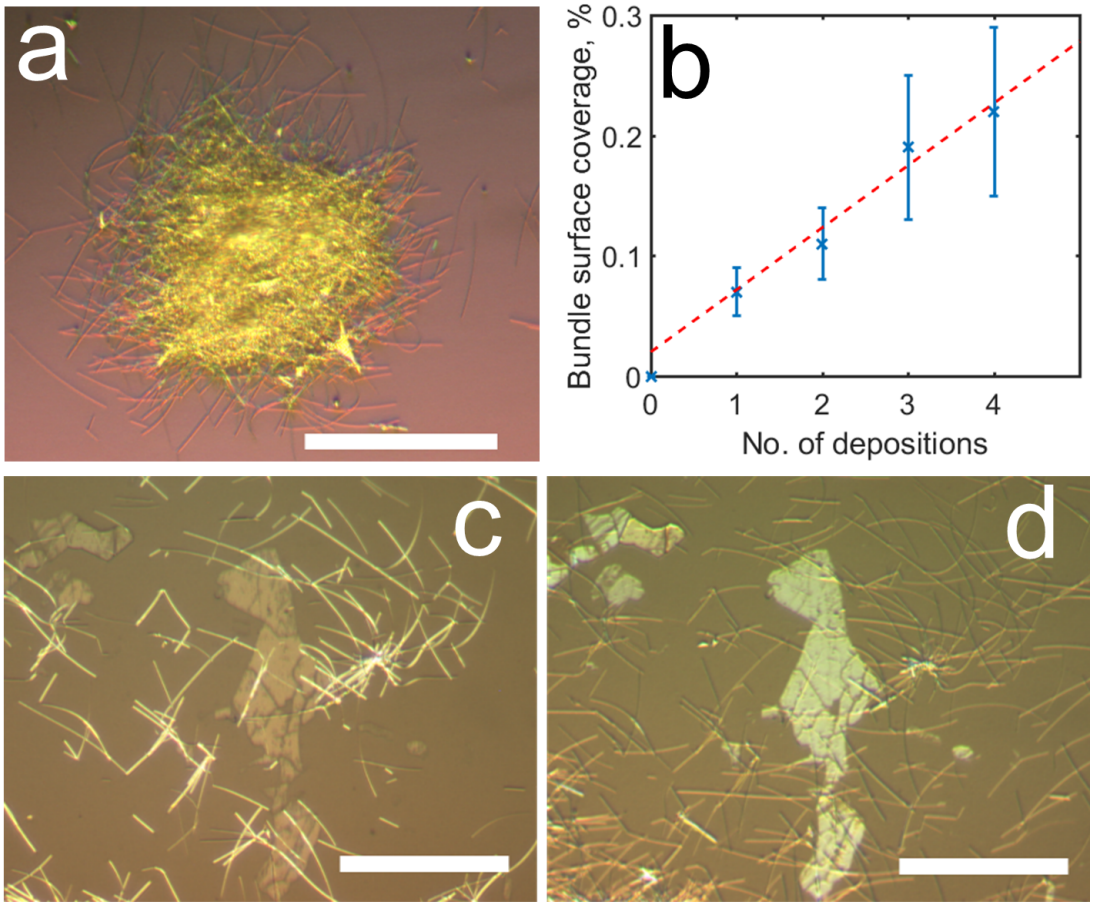


FIGURE 4.2: a) An optical micrograph of a nanowire bundle on SiO_2. b) Percentage coverage of a SiO_2 suface after periodic depositions of a 200:1 (IPA : nanowire solution) mixture. c), d) Optical microscope images of the same region after 1, and after 2 depositions of a 10:1 (IPA: nanowire solution) mixture. Scalebars all measure 50 μm.

The primary aim of the nanowire deposition was to form a conducting mesh-like networking layer across the entire substrate that would allow for macroscopic conduction across the substrate surface and onto the graphene layer on top of the hBN flake, while simultaneously maintaining a low enough coverage to be able to image the graphene between the networking layer. Several preparatory experiments were carried out in order to achieve this. Depositions were made across SiO_2, sapphire, and graphite substrates to ensure that the adhesion between the nanowires and the surface was enough for successful deposition to be carried out efficiently. Cleanliness tests were also made to confirm that the method does not contaminate the graphene surface, with areas on hBN flakes recorded using AFM before and after a nanowire deposition showing that the process of deposition does not lead to any noticeable debris appearing on the surface. Furthermore, scans were recorded showing the presence of clean graphene/hBN moiré patterns (described in section 2.3.2 of chapter 2) following deposition, demonstrating that the technique has a sufficient cleanliness for graphene imaging.

As the contents of the nanowires in suspension are under constant thermal motion bundles of nanowires form that can be visible to the naked eye. These bundles are deposited along with the rest of the nanowires in suspension, an example can be seen in fig 4.2a. In this image the individual nanowires that make up the bundle can also be seen. The average surface area covered by one of these bundles has been calculated to take up an area of $3.3 \pm 0.9\text{x}10^{-9}$ m^2 based on a sample size of 5 such bundles. After each of 4 separate depositions of a low nanowire concentration with a ratio of 200:1 of IPA to nanowire solution the number of these bundles was counted across a 6 x 6 mm SiO_2 substrate. Figure 4.2b shows the surface area of the substrate that was covered by the nanowire bundles as a function of subsequent depositions. This relationship is linear, and importantly it demonstrates that the bundle surface coverage is sufficiently small enough to not pose an issue of covering areas, or flakes, of interest. This information allows for sequential depositions that can be used to gradually build up a desired concentration. The ratio of IPA to nanowire suspension mixture that has been used for creating conductive networks was 10:1. This concentration was found to provide a reasonable coverage, while leaving enough space between nanowires to prevent problems while imaging underlying materials using AFM. Figure 4.2c and d) show the same hBN flake after 1 and 2 nanowire depositions respectively using this ratio. Usually three to four depositions of this concentration are required to provide a conducting network across the entire substrate, with periodic depositing allowing for the coverage to be monitored and ceased when a sufficient layer is achieved.

The nanowire networks that have been formed through deposition conduct with a low resistance. This has been measured by depositing a high concentration of nanowires

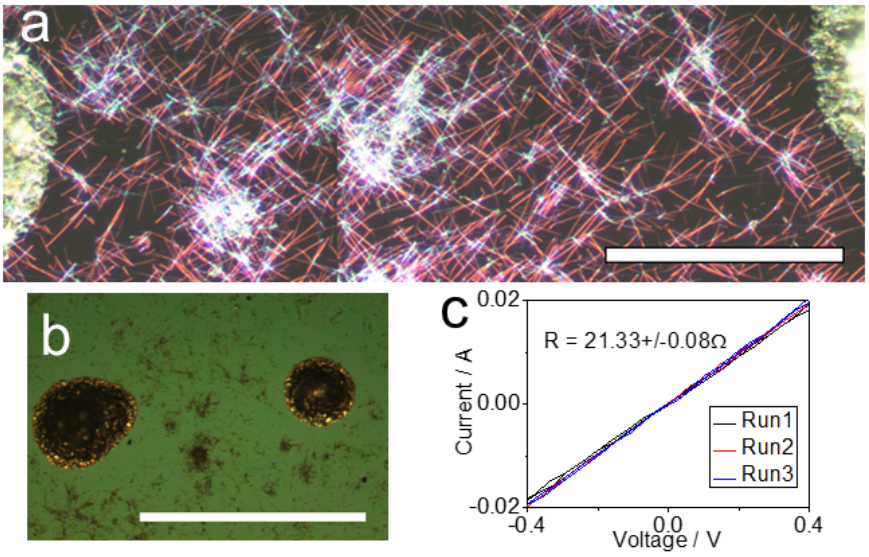


FIGURE 4.3: a) A mosaic of three separate optical microscope images with an increased magnification of the region between the two epoxy contacts on SiO_2 shown in b). The individual nanowires can clearly be seen in a), with the nanowire bundles observable in both a) and b). Scalebars for a) and b) are 100 μm and 500 μm respectively. c) The current voltage characteristics measured between the two contacts in b) through the network shown in a).

onto two epoxy contacts, created as described earlier, on SiO_2 and using a probe station to record the current voltage characteristics between the two contacts. Figure 4.3a shows an optical micrograph of the nanowire network between the two conductive epoxy contacts, shown in figure 4.3b with a lower magnification. The corresponding IV characteristics for three consecutive voltage sweeps can be seen in figure 4.3c and follows Ohmic behaviour with a resistance of $\sim$20 Ω.

By using nanowire deposition it is hence possible to create a conductive network across a substrate surface to a flake. However, this process has been shown to pose a low risk of covering areas in nanowire bundles, as well as the nanowires themselves, that can obscure some measurements, for example in X-ray diffraction. Furthermore, this method has been found to only be reversible through the use of ultrasonics which would cause extensive damage to the flakes under investigation.

A diagram showing an example of how this technique was successfully implemented in conjunction with a shadow mask deposited Au/Ti contact and conductive epoxy contacting is shown in figure 4.4a. In this labelled diagram a Au wire has been attached with conductive epoxy to a Au/Ti contact that has been patterned using shadow masking with metal evaporation. A drop deposited Ag nanowire network bridges the electrical gap from the gold contact, across the insulating substrate surface, onto the graphene/hBN heterostructure on top of the previously isolated flake.

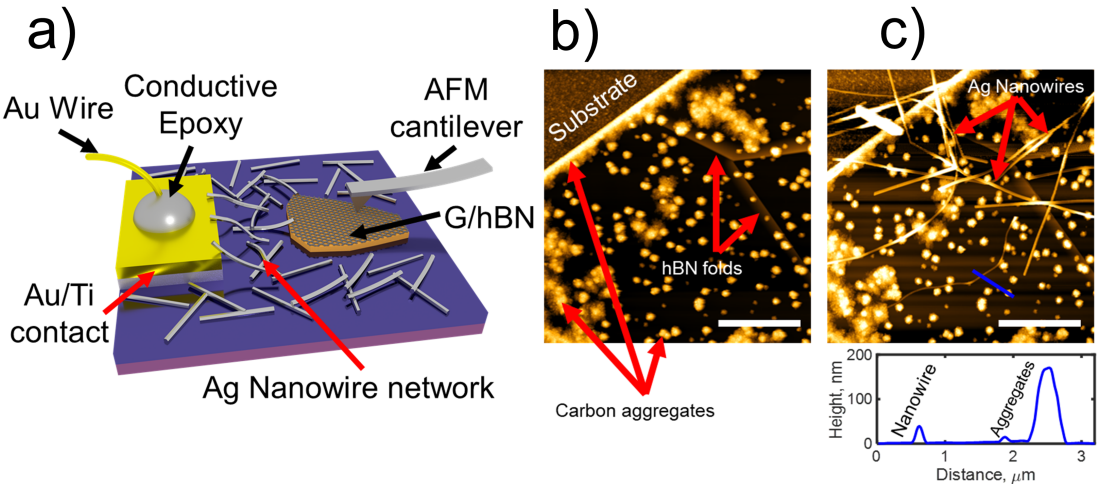


FIGURE 4.4: a) A schematic of the intended system. Graphene on an hBN flake is connected to a Au contact through a Ag nanowire networking pathway. A conductive AFM tip, and a Au wire, connected using conductive epoxy, complete the circuit through the AFM system. b) and c) show AC topographic AFM images measured before and after a nanowire deposition respectively. In this test sample the substrate is covered in carbon, and so appears raised compared to the flake. Some of the sample features are labeled. The bright spots are carbon aggregates positioned on the flake surface, and can be much larger than the nanowire diameter, as demonstrated by the profile recorded through the blue line in c). Scalebars are 5 μm.

When imaging this graphene surface using conductive AFM a voltage is applied between the Au wire and the AFM cantilever tip included in the diagram in figure 4.4a allowing the current flowing through the CAFM tip to be recorded.

Panels b) and c) of figure 4.4 show topographic AFM images recorded on a hBN/graphene heterostructure before and after a deposition of Ag NW's. The key features of this surface are labelled, with the numerous high contrast areas indicating carbon aggregate clusters on the hBN flake surface, along with folds in the hBN layers seen in both images. The upper left-hand side of these images show the edge of the flake and the substrate below. Following deposition in panel c) the network of nanowires is shown to cover the flake, with the nanowire diameter measured to be 40 ± 5 nm compared to an aggregate size in excess of 160 nm in the profile provided, recorded along the blue line in c). The size and concentration of the nanowires provides very little disruption when imaging the underlying material between the conducting network.

Additional investigation involving the manipulation of deposited and transferred nanowires to form novel structures has also been carried out and is included in appendix A.

4.4 Flake Transfer

Flake transfer has been used as a technique to preserve samples consisting of a large number of flakes by moving particular flakes of interest between substrates prior to further processing. In some cases this is an important step used to allow for processing for electrical measurements while preventing sample-wide techniques, such as NW deposition, that have the potential to introduce contamination across the entire sample that may negatively influence other techniques, and allows for the majority of the sample to be preserved for later study. Flake transfer has predominantly been used in this work for samples of high importance displaying uncommon features, such as the highly strained, lattice matched graphene described in section 5.4 of chapter 5. Furthermore, transfer to an Si/SiO_2 substrate has the additional advantage that a gate voltage can be applied.

Flake transfer also allows for accurate placement to within close proximity of pre-formed electrical contacts, reducing the required nanowire network density. The basic principle of this stamping procedure involves lifting an entire flake off of the sapphire growth substrate by melting polypropylene carbonate (PPC) around the flake and then allowing it to cool before lift off. The flake, and PPC, can then be placed onto a second substrate and acetone used to remove the PPC. In order to do this, stamps fashioned after those used by Kim et al [121] were made. A schematic of these stamps can be seen in figure 4.5a. A 0.5 mm^2 square section of PDMS (polydimethylsiloxane) polymer sheet is placed on a glass slide. On top of this sheet a PDMS droplet (elastomer mixed with a curing agent) is deposited, and subsequently baked at 110°C for 15 minutes to harden. A thin PPC layer is then spin coated over the structure, ensuring the PDMS dot has been covered, before a 5 minute bake on a hot plate at 80°C.

Once made, this stamp can be accurately positioned using a set of micrometers and an optical microscope located directly above the slide, so that the PDMS dot is above a chosen sample flake. The stamp is then carefully lowered into contact with the substrate mounted on a heating element at 40°C, at which point the PPC becomes softer. This is then left to harden and cooled to ∼30°C before lifting the stamp, and with it, the chosen flake. To deposit the flake onto a new substrate the flake is brought into contact and the substrate temperature is raised to above 80°C at which point the PPC separates from the stamp along with the flake, as displayed in figure 4.5c. After immersion overnight in acetone at room temperature followed by toluene immersion the PPC appears entirely removed from the substrate, see figure 4.5d. As mentioned above, this method has been used to successfully transfer flakes of interest, for example those shown in figure 4.5b-e (the sample shown in panels c-e is the sample referred to as sample C in table 5.1 and elsewhere in chapter 5). The sample shown in b) shows several flakes, with the target flake shown in the inset image, that were transferred

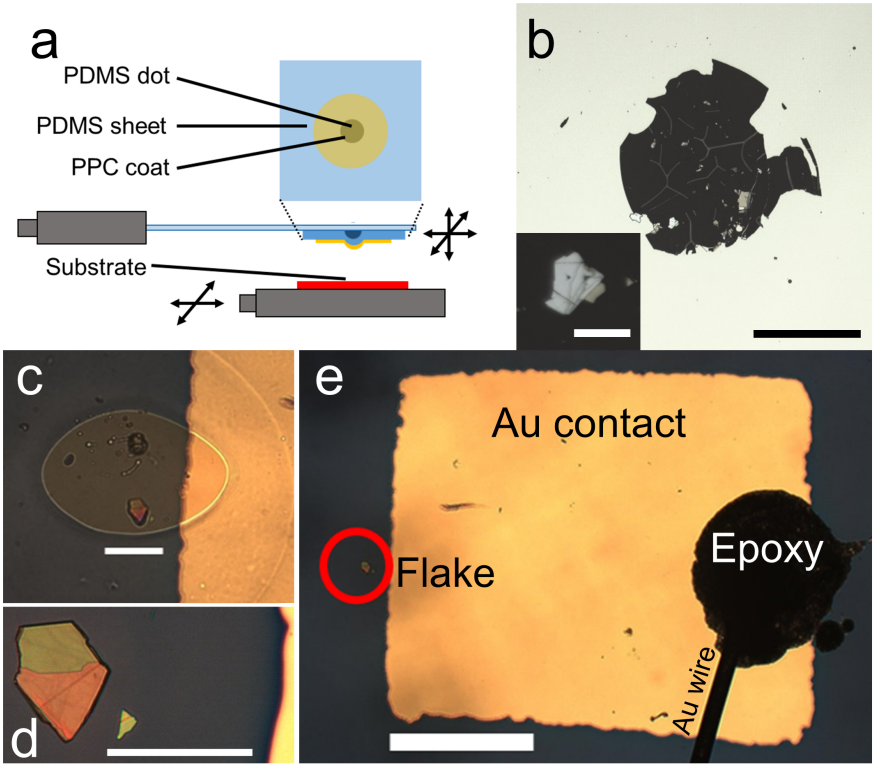


FIGURE 4.5: a) A schematic representation of the transfer stamp and apparatus. The stamp consists of a PDMS dot covered in a PDMS sheet, that is in turn spin coated with PPC. The substrate and stamp can both be accurately positioned using a set of micrometers. b) An optical micrograph showing a stamped region placed directly onto a Au contact. The black areas show the carbon aggregates that covered the growth substrate and have also been transferred. The inset shows one of the flakes in this region with an increased magnification. c), d), e) Optical microscope images of a flake with lattice matched graphene-hBN regions. c) The flake within the vicinity of the Au contact after stamping, and before solvent cleaning. The surrounding PPC covers the local area. d) Shows the flake with an increased magnification, the change in colour represents a change in flake thickness. e) The prepared sample before nanowire deposition. The flake shown in d) is circled. An epoxy connection has been made to the Au contact far from the flake to provide an electrical connection. The sample shown in panels c-e) is referred to as sample C in chapter 5. Scalebars are 250 μm, 25 μm, 100 μm, 50 μm, and 500 μm in b), b) inset, c), d), and e) respectively.

directly onto a Au contact. In this case the initial sample substrate had a carbon aggregate layer following growth that has been carried over with the transferred flake. The transferred flake shown in panels c-e) was placed near to a pre-formed Au contact. Subsequent processing included contacting using a Au wire and conductive epoxy, as seen in panel e) of figure 4.5, that was followed by Ag nanowire deposition. The schematic shown in figure 4.4a shows a diagrammatic representation of this setup.

Using conductive AFM, the graphene on the hBN flakes surfaces has appeared

to be undamaged by the transfer process. This has also been the case for the lattice matched and highly strained graphene where no observed relaxation has occurred, and moiré patterns along with atomic resolution have been imaged following transfer. However, often in these cases the moiré patterns are no longer easily measurable using AC mode imaging, and can only be observed using contact mode or CAFM. This is due to a thin layer of residual PPC on the surface that can be almost entirely removed during solvent cleaning, comparable to material left behind following conventional lithographic techniques (not investigated in this work), that is swept aside while using contact mode AFM imaging, as has been used for the bulk of the measurements seen within this thesis, but may inhibit AC mode imaging.

4.5 Summary

For the graphene samples investigated in this thesis that have been grown at high temperature on hBN flakes with an insulating sapphire substrate it is important to create electrical contacts to the surface of the flakes. In this section, this has been attempted using a variety of different techniques. Epoxy contacts were formed, creating connections to individual flakes, however this method has a high risk of damaging the chosen flake. Shadow masking was seen to be ineffective as a way of contacting flakes due to diffusion of Au beneath the shadow mask. However, both of these techniques have been successfully used in conjunction with the more successful method of nanowire deposition. The drop deposition of Ag nanowires suspended in solvent has proven to be a useful procedure, creating a conductive network across the entire sample in a clean way. The nature of the nanowires has allowed for contact to be made to the surface of graphene covered hBN flakes and to isolated regions on these flakes (for example on areas where there are many graphene cracks). The small diameter of these nanowires provides a conducting network that permits SPM scanning between its large gaps. Furthermore, flake transfer has been used to help preserve samples preventing nanowire deposition from being required to cover entire areas of interest, and also allows for the creation of devices on different substrates, such as SiO_2 that allows for the application of a gate voltage. A final processing technique of focused ion beam milling was also investigated as a method for scribing patterns into hBN flakes and aggregate layers and is provided in appendix B.

The graphene samples grown by MBE on hBN flakes with a sapphire substrate grown at high temperature, with no carbon aggregate layer requiring the additional processing developed in this chapter, are those that display the greatest amount of strain. In the following chapters many of these samples are investigated using conductive AFM where the methods shown here, in particular nanowire deposition, are employed to provide an electrical connection to the graphene regions.

Chapter 5

Strained MBE Grown Graphene

5.1 Introduction

The graphene samples that have been grown throughout this work have been investigated using a wide range of methods. This chapter focuses on the characterisation of the graphene samples grown on hBN mechanically exfoliated onto a sapphire substrate using molecular beam epitaxy by Sergei V. Novikov and Tin S. Cheng, and provides an introduction as to how the techniques involved have been used to extract information about the samples in the following chapters. The graphene grown here has been shown previously to cover the entire hBN flake surface [44], forming continuous domains with dimensions in excess of 20 μm. All of the data shown within this chapter has been recorded as part of this thesis unless otherwise stated.

AFM has played a key role and has been used in both tapping and contact mode to observe surface features. These include the surface cleanliness, frequency and size of carbon deposits and graphene domains, cracks in strained material, and presence of bilayer islands. In addition AFM imaging facilitates the estimates of growth rates across multiple samples including observations of growth direction and of areas, such as aggregates, that act to initiate growth. AFM can also be used to determine the thickness of the carbon aggregate layer on the sapphire substrate by scratching this layer before imaging. The less widely used technique of conductive AFM has been used as an extension, with procedures for measuring these samples developed as part of this work to include investigation of electrical properties of the samples such as the conductivity variation across the surface, current-voltage (IV) relationships, changes in the density of states, frequency of defects, and graphene quality. These methods allow for the observation of the hBN/graphene moiré pattern to confirm the presence of graphene and reveal information about the surface such as the strain present, irregular/uniaxial strain and lattice matching, and the presence of defects in the lattice, as well as lattice resolution images to provide further information such as lattice alignment and uniformity of heterojunctions.

Raman spectroscopy has been used to further characterise graphene, and to provide information such as the quality of graphene, amount of aggregates present, and to confirm graphene strain. Angle resolved photoemission spectroscopy has also been used on select samples, and allows for further electronic properties to be revealed including the band structure close to the Dirac point.

The following sections in this chapter will present data recorded for unstrained graphene for these MBE grown graphene samples, highlighting interesting features, followed by graphene samples with high strain, displaying moiré patterns in excess of the predicted maximum of 14 nm [60]. Next, data recorded from samples showing extreme strain where the graphene has become lattice matched with underlying hBN, a feature that has been unreported by any other research group, is presented and discussed. The results shown demonstrate the usefulness of the techniques involved, with a focus on CAFM, and how these methods have been used to determine important sample features, providing essential feedback in developing the novel MBE grown graphene samples discussed in this thesis.

5.2 Unstrained Graphene

Figure 5.1a shows a large scale topographic image recorded using AC mode AFM of an archetypal MBE graphene on hBN sample. The sample shown in this figure, referred to as sample A in table 5.1 showing details of all of the samples shown in this chapter, was grown at a substrate temperature of 1520 °C and a growth time of 5 hours with a carbon filament source achieving monolayer coverage. Typically, for the MBE graphene grown on exfoliated hBN at temperatures below ∼1500 °C, the deposited carbon forms an aggregate layer covering the insulating sapphire substrate in an approximately 80 nm thick layer (depending on growth conditions) that provides an electrical connection to the graphene on hBN flakes. For these samples the processes described in section 4 are unnecessary for conductive AFM imaging. Since the sample shown in figure 5.1 was grown at a temperature above 1500 °C there was a relatively low aggregate coverage. To ensure a good electrical connection to facilitate CAFM, the sample underwent Ag nanowire deposition before conductive measurements took place.

In figure 5.1a the regions with lowest contrast correspond to monolayer graphene on hBN terraces with sizes typically of tens of microns. Scattered across these regions, with average separations of around 1 μm are large high contrast spots. These spots are carbon aggregate clusters residing on the hBN surface. During growth these clusters have formed, and initiate the growth of the surrounding graphene domains [44].

Folds, or wrinkles, in the layered material are common on exfoliated hBN flakes. These folds appear with a smooth gradient, and in general have not been observed to

TABLE 5.1: Details of the graphene samples shown within this chapter.

Sample	Carbon Source	Growth Temp (°C)	Growth Time (Hrs)	CAFM Processing
A	C-filament	1520	5	Ag nanowires & epoxy contacts
B	C-filament	1520	5	N/A
C	C-filament	1675	5	Au contact deposition, Ag nanowires, flake transfer
D	E-beam (5kV)	1675	2	N/A
E	E-beam (5kV)	1675	2	N/A
F	E-beam (5kV)	1675	2	N/A
G	Atomic Carbon Source	1680	3	N/A
H	Atomic Carbon Source	1710	3	Ag nanowires

act as preferential nucleation sites. This may be due to the observation that the positions of these folds are not permanent at higher temperatures, and have been seen to rearrange following heating to temperatures in excess of ∼1000°C (discussed further in chapter 8 and shown in appendix D). In contrast, the step edges in the hBN often act as nucleation sites for carbon aggregates. The result of this can be seen towards the lower portion and right-hand-side of figure 5.1a, where lines of carbon aggregate clusters are located along hBN step edges.

Figure 5.1b and c) show AFM images of one of the flat regions of graphene on hBN, indicated in a) by the red circle. The topographic image, recorded using AC mode AFM, shows the uniformity of the area. A hexagonal pattern can be seen both in the topographic image, and in the phase image shown in c). This hexagonal pattern is a superlattice moiré pattern, formed by the interface of the graphene/hBN heterostructure. This moiré pattern has a height variation of $\sim 70 \pm 30$ pm, as demonstrated by the profile inset in figure 5.1b. The clear visibility of the moiré pattern also demonstrates the cleanliness of the sample, following nanowire deposition.

The wavelength of the superlattice has been measured using two-dimensional fast Fourier transform (2DFFT) analysis to be 14.1 ± 0.3 nm in these images. The six resonance points in the reciprocal domain, forming corners of a hexagon in reciprocal-space, correspond to the moiré wavelengths along the six directions of the hexagonal pattern. The six distances recorded were then averaged to reach the value of 14.1 ± 0.3 nm. This value of 14.1 ± 0.3 nm is in agreement with the expected theoretical maximum of ∼14 nm [60] for rotationally aligned and unstrained graphene. The graphene grown in this investigation has previously been shown to be orientationally aligned

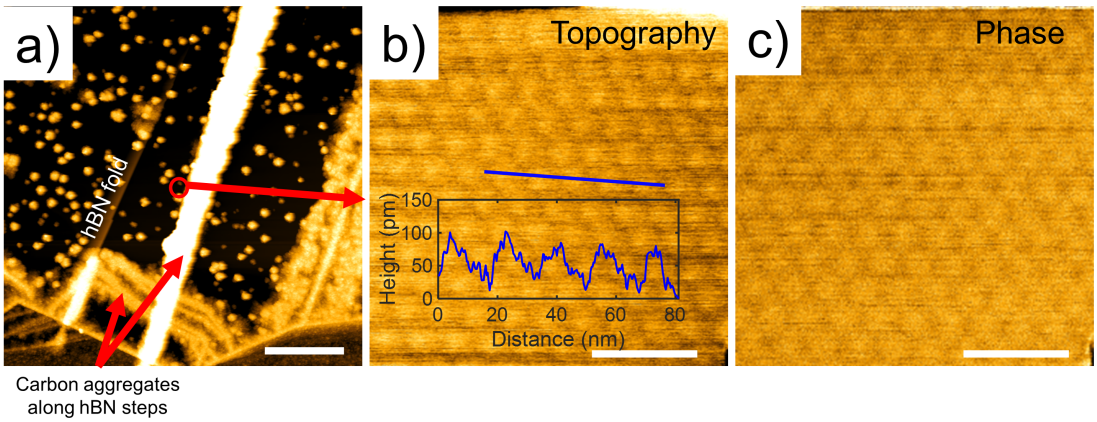


FIGURE 5.1: a) AC mode AFM topographic image showing a large region of the graphene/hexagonal boron nitride surface of sample A. The bright spots indicate carbon aggregates. b) and c) AC mode topographic image and phase image respectively measured within the red circle indicated in a). Visible in both b) and c), the hexagonal moiré pattern formed at the heterostructure has a wavelength of 14.1 $\pm$ 0.3 nm (determined from 2DFFT), and a height of approximately 70 $\pm$ 30 pm, as shown by the profile measured along the blue line in b). The scalebar in a) measures 5 μm, and the scalebars in b) and c) measure 50 nm. The profile has an averaged width of 10 pixels.

with the underlying hBN [44], with further evidence of this given later in chapter 7.

These results show that this region of graphene is unstrained and uniform. The phase image shown in figure 5.1c shows the same moiré pattern as seen in the corresponding topographic image. The change in phase caused by the target surface while imaging may occur due to variations in a number of different surface properties. These include the composition of the sample, tip-surface adhesion and frictional forces, and viscoelasticity of the material. In many cases the moiré pattern appears clearer in the phase image than the topographic image. This can be an indication of the condition of the tip, with sharper tips providing more precision in topographic imaging, and blunter tips leading to greater frictional and adhesion properties due to an enlarged apex, resulting in a greater contrast in the phase image. It can also be dependent on the composition of the tip, and is affected by changes in the tip, or changes in the material adhered to the tip.

Figure 5.2 shows a similar moiré pattern that also indicates unstrained graphene material. The sample, referred to as sample B in table 5.1, was grown with a substrate temperature of 1520°C and a growth time of 5 hours using the carbon filament source. In this case there was a significant aggregate layer present on the insulating sapphire surface, negating the requirement of Ag nanowire deposition. Figure 5.2a and d) both show the same region on this sample, with panel a) showing the topographic channel recorded in AC mode AFM, while d) shows the current channel of a CAFM image

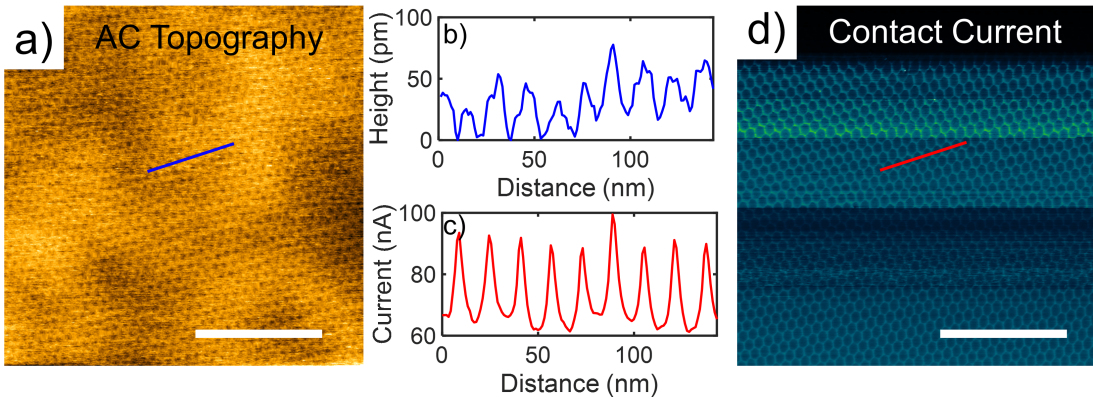


FIGURE 5.2: a) An AC mode topographic height image of sample B showing the same region as the current channel conductive AFM image in d). The height profile in b) and the current profile in c) are measured along the respective lines in a) and d). The moiré wavelength measures 14.4 $\pm$ 1.2 nm (extracted using a 2DFFT). The profiles are measured along the same positions, and have an averaged width of 4 pixels. The scalebars in a) and d) measure 200 nm.

recorded using contact mode AFM. In both a) and d) the moiré pattern is clearly visible, and has a wavelength measuring 14.4 $\pm$ 1.2 nm. The current channel image was recorded by applying a bias of -0.5 V to the sample, and recording the current passing through the conductive tip during a standard contact mode AFM scan and thus, to first order, the tip-sample separation is constant along the trajectory of the tip. The colourbar and profile both show absolute current. The horizontal lines in this image, where strong changes in current appear, are due to small changes in the tip while scanning, such as picking up/dropping off material. This is a common side effect of scanning under ambient conditions, due to the large amount of surface contaminants.

The profiles that are shown in figure 5.2b and c) are measured along identical trajectories in figures a) and d). While the moiré pattern seen in a) is very clear, the pattern shown in the current image is far sharper, with peaks and troughs that are much more well defined, as can be seen in the accompanying profiles. The increase in the image sharpness/clarity for the current CAFM images can allow for high resolution imaging of these surfaces under ambient conditions. This is far more difficult to achieve using AC mode imaging, or contact mode topography imaging, making CAFM a very useful technique for imaging these samples. Figure 5.3 shows an example of the achievable resolution for CAFM imaging of graphene on hBN under ambient conditions.

The sample shown in figure 5.3a and b) is sample C in table 5.1, and was grown with a substrate temperature of 1675°C for 5 hours using a carbon filament source. The graphene was grown on exfoliated hBN flakes on a sapphire substrate. Following

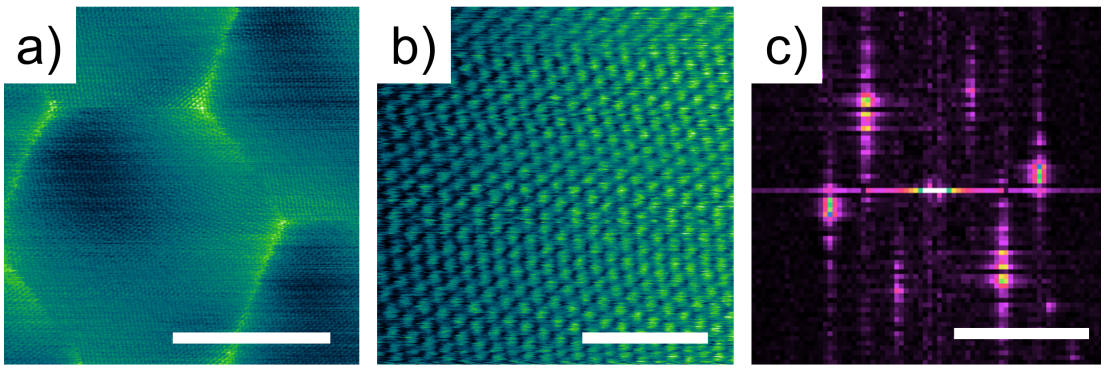


FIGURE 5.3: CAFM current images of sample C where the graphene lattice is visible, displaying the high resolution easily achievable under ambient conditions. a) Image showing a moiré unit cell for graphene on hBN with high resolution. b) CAFM image showing the graphene lattice at the centre of the moiré cell shown in a). The scalebars measure 10 nm in a), and 2 nm in b). The colourbars have minima of 3.58 μA and 3.65 μA, and maximums of 3.86 μA and 3.8 μA in a) and b) respectively. The lattice constant for b) was determined to be 0.249 $\pm$ 0.007 nm using the 2DFFT shown in c), where the scalebar measures 5 nm^{-1}.

growth the flakes were transferred to a SiO_2 sample next to a pre-patterned Au electrical contact, and Ag nanowires were drop deposited to provide a contact electrode.

Figure 5.3a shows a 17 $\pm$ 1 nm moiré pattern with lattice resolution, with a smaller image of the centre of a moiré cell shown in b). The sample was held at -0.1 V while imaging. The moiré pattern differs in its detail to the more rounded moiré pattern seen earlier in figure 5.1b and c), and exhibits far sharper moiré cell boundaries. These differences are due to the tip-surface interaction and are investigated in detail in chapter 6.

In panel b) of figure 5.3 the lattice directions can be seen to have an associated wavyness to them, a result of drift from expansion/contraction of the surface while imaging. To minimise this effect the high scan rates permitted by contact mode imaging were implemented. In panel c) the central region of a 2DFFT of the image in panel b) can be seen. The hexagonally ordered bright spots surrounding the central spot indicate the first order peaks that correspond to the lattice periodicity and were used to extract the lattice constant values. The lattice constant extracted for the graphene image shown in b) is 0.249 $\pm$ 0.007 nm. This value is in agreement with the expected graphene/graphite lattice constant of 0.246 nm [17]. The moiré wavelength of the sample shown in figure 5.3a of 17 $\pm$ 1 nm is larger than the expected maximum value of $\sim$14 nm [60] for rotationally aligned graphene. This enlargement implies strain in the graphene of 0.38 $\pm$ 0.09 % using equation 2.39 from section 2.3.2, and assuming no structural changes in the bulk hBN. Far larger moiré patterns have been observed, and are shown in the following sections.

5.3 Strained Graphene

The samples that are shown in this section exhibit moiré patterns greater than the expected maximum value of ∼14 nm [60]. These samples have been grown at higher substrate temperatures than those that exhibit superlattice wavelengths close to, or below, 14 nm. As a result of this high temperature growth the insulating sapphire substrate is not coated with carbon, due to a suppression of nucleation, and as such require nanowire depositions, or other processing, to allow for conductive measurements to take place.

Varying degrees of strain have been observed across these samples, indicated by the sizes of their respective moiré pattern wavelengths, with larger wavelengths indicating increased strain. Figure 5.4 shows a hBN flake with MBE graphene grown using the carbon e-beam source, a growth time of 2 hours, and a substrate temperature of approximately 1650°C (sample D in table 5.1). On the same flake several regions within close proximity to each other are shown to exhibit different amounts of strain.

Figure 5.4a) shows the flake as a whole with an optical micrograph image. AC mode topographic images are shown in the remaining figures, all recorded within the red box in a). Of the locations that were investigated on this flake the region shown in c) displayed the highest amount of strain. This can be seen by the two inset figures in c)i) and c)ii) showing equally sized areas. These two regions are situated only 500 nm apart, yet the moiré pattern differs from 33 $\pm$ 2 nm, indicating a graphene strain of 1.08 $\pm$ 0.05 % (as determined from equation 2.39), to a wavelength of 55.7 $\pm$ 4 nm, indicating a strain of 1.39 $\pm$ 0.03 %. However, on the lower plateau of the large region shown in figure 5.4b the graphene appears relaxed. This can be seen in the graphene/hBN moiré pattern shown in figure 5.4d and e). Here the moiré wavelength, λ_S, is determined to be 13.79 $\pm$ 0.09 nm, indicating unstrained graphene.

From these images it can be seen that the region that is unstrained consists of a much larger and clearer section, with far fewer carbon deposits/aggregate clusters than the area where a high strain was recorded. The high strain region consists of a comparatively small area, with a width of 2 μm, surrounded by carbon aggregate lines (collected along hBN step edges or cracks, similar to those highlighted in figure 5.1a). This detail is one which has often been observed in samples with high strain, and suggests correlation between graphene strain and aggregate cluster presence. During growth the aggregates have acted as pinning sites to hold the as-grown graphene in place at the high substrate temperatures that have been used, preventing the release of strain when the sample has been returned to room temperature following the growth process.

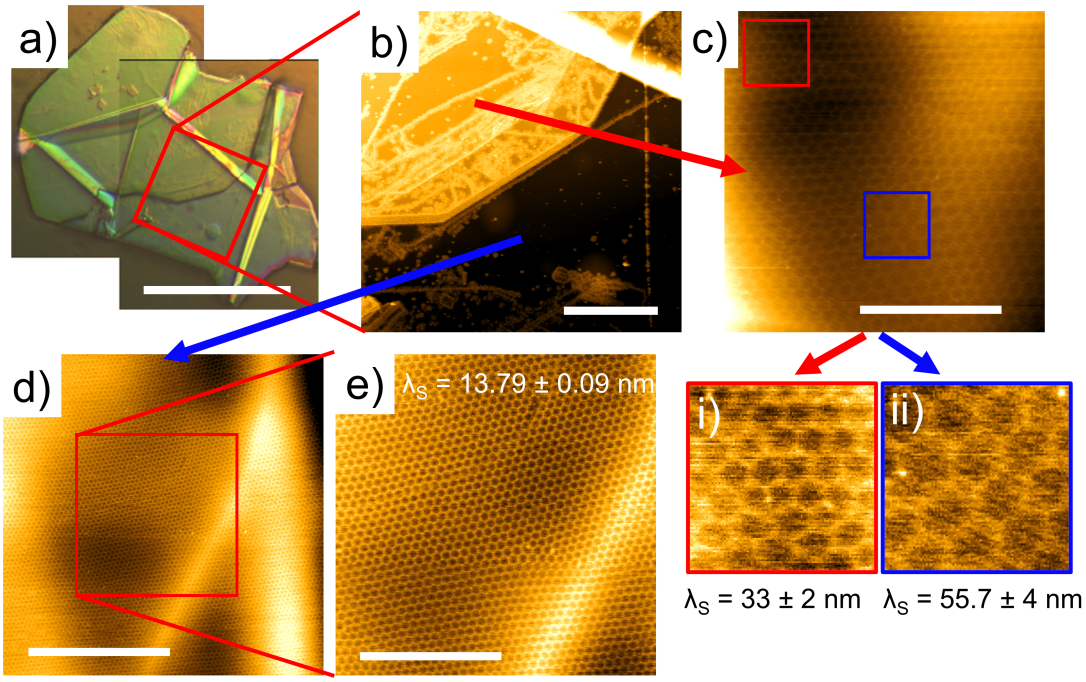


FIGURE 5.4: All AFM images in this figure have been recorded on the graphene grown on a hBN flake shown in the optical micrograph in a) (sample D in table 5.1), and are all AC mode topographic images. b) displays the region bounded by the red box in a). c) shows a strained region, indicated on b) by the red arrow. The graphene/hBN moiré pattern can be seen, with the two areas indicated by the red and blue boxes given in figures i) and ii), with each displaying a different size moiré pattern as indicated. d) shows the region indicated by the blue arrow in b). Here the observed moiré pattern is 13.79 $\pm$ 0.09 nm, as shown in e), an image showing the region bounded by the red box in d). The scalebars measure 50 μm in a), 10 μm in b), 500 nm in c) and d), and 250 nm in e). The moiré wavelengths have been determined using 2DFFTs of the images.

5.3.1 Raman Measurements

Raman results recorded at the regions displaying varying graphene strain on sample D were recorded. Figure 5.5 shows two Raman spectra recorded on the regions shown in figure 5.4d for unstrained graphene with a 13.79 $\pm$ 0.09 nm wavelength moiré pattern (shown in blue), and the region shown in figure 5.4c for strained graphene with a moiré wavelength that varies around ~30-50 nm corresponding to a graphene strain of 1.0-1.3 % (shown in red). These Stokes Raman spectra were measured using a Horiba-Jobin-Yvon LabRAM Raman microscope, with a probing laser wavelength of 532 nm operating at >4 mW with a 600 lines/mm grating and a Synapse CCD detector that was calibrated using a Si(100) sample for reference.

In figure 5.5a the Raman peaks have been labelled. In panels b) and c) the two indicated regions of the Raman spectra for strained graphene shown in a) are expanded.

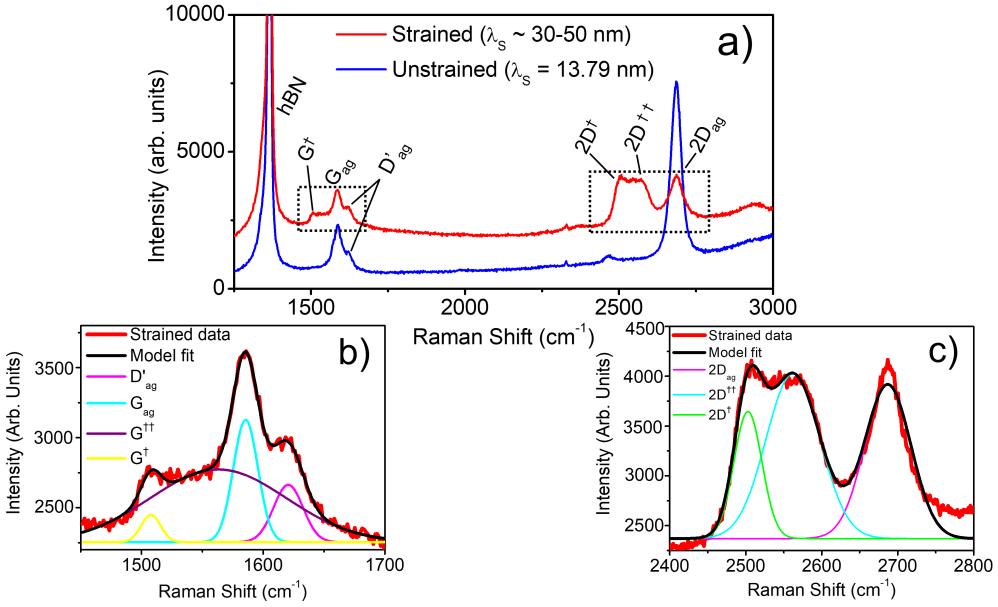


FIGURE 5.5: a) Raman spectra for unstrained MBE graphene on hBN (blue data), measured at the region shown in figure 5.4d of sample D with a 13.79 $\pm$ 0.09 nm moiré wavelength, and strained MBE graphene on hBN (red data), measured at the region shown in figure 5.4c with a $\sim$ 30-50 nm moiré wavelength. The two data sets have been offset in the y-direction for clarity. Panels b) and c) show zoomed sections of the indicated regions in panel a), along with peak fitted multi Lorentzian curves, and the combined result of these curves (in black). In b) the fitted Lorentzians correspond to the D'$_{ag}$, G_{ag}, G††, and G† Raman peaks, whereas in c) the Lorentzians correspond to the $2D_{ag}$, 2D††, and 2D† Raman peaks.

These two regions have been fitted to a summation of Lorentzian curves (shown by the black line), using the OriginPro software package with the individual peak fits plotted. The values of the positions and respective full width at half maximum (FWHM) for these fits are provided in table 5.2. In these Raman spectra the hBN peak, due to the E2g phonon mode [122], is recorded with a location at 1365 cm^{-1} and 1366 cm^{-1} for the unstrained and strained measurements respectively, matching within the $\pm$ 4 cm^{-1} error bounds (calculated using the standard deviation, $\sigma = \frac{FWHM}{2\sqrt{2\ln 2}}$).

The spectra seen in figure 5.5a show some significant differences. For the unstrained graphene there is a single 2D peak at 2685 cm^{-1}. However, for the strained region this has split into three separate peaks, labelled 2D† (2503 cm^{-1}), 2D†† (2562 cm^{-1}), and $2D_{ag}$ (2687 cm^{-1}). Shifts in the 2D band in the graphene Raman signature are indicative of strain, with the amount of red-shifting being directly proportional to the mechanical strain [45, 123]. Figure 5.5 demonstrates this red-shifting for both the 2D† and 2D†† peaks relative to the single 2D peak for unstrained graphene, with shifts of 182 $\pm$ 22 cm^{-1} and 123 $\pm$ 34 cm^{-1}. The peak labelled $2D_{ag}$ remains unshifted

TABLE 5.2: The positions and full width half maximum (FWHM) values of the peak fitted Lorentzians for the data shown in figures 5.5 (for sample D) and 5.12 (for sample F)

Peak	**(cm^{-1})**	**Unstrained**	**Strained**	**Lattice matched**
$\mathbf{D}_{ag}$	Position	-	-	1355
	FWHM	-	-	37
hBN	Position	1365	1366	1366
	FWHM	9	10	8
$\mathbf{G}^{\dagger}$	Position	-	1508	1491
	FWHM	-	16	16
$\mathbf{G}^{\dagger\dagger}$	Position	-	1563	1547
	FWHM	-	111	113
$\mathbf{G}_{ag}$	Position	1585	1586	1582
	FWHM	33	20	25
$\mathbf{D'}_{ag}$	Position	1625	1621	1620
	FWHM	21	24	23
$\mathbf{2D}^{\dagger}$	Position	-	2503	2468
	FWHM	-	37	31
$\mathbf{2D}^{\dagger\dagger}$	Position	-	2562	2527
	FWHM	-	71	101
$\mathbf{2D}_{ag}$	Position	2685	2687	2685
	FWHM	36	61	52

from the unstrained 2D peak, and is attributed to carbon aggregate presence. Similar results for a wider range of strained material can be seen in reference [45] where the relationship between the red-shift and strain is investigated.

The graphene G peak (located at 1585 cm^{-1}), present in all sp^2 carbon materials and labelled as G_{ag}, and its shouldering D'_{ag} peak (at 1625 cm^{-1}), a result of double resonance of the D peak (drowned out by the hBN) that itself is due to non-sp^2 binding of carbon - and as a result is attributed to the presence of defects, are both present and unshifted in the strained and unstrained graphene Raman spectra. However, there is an additional splitting and red-shifting of the G peak observed in the strained material into the $G^{\dagger}$ peak (at 1508 cm^{-1}) and broader $G^{\dagger\dagger}$ peak (at 1563 cm^{-1}). The very broad $G^{\dagger\dagger}$ peak in figure 5.5b is likely a result of Lorentzian fitting where some contribution from the hBN peak's tail off has occurred, however a relatively broad peak is expected (see S.I of reference [45]).

The relative intensity of the 2D and G Raman peaks is often used to gauge the graphene quality, with the 2D peak being approximately 4 times the intensity of the G peak in exfoliated graphene [92, 124]. In these spectra the ratio for the unstrained region measures ~ 4.2 indicating high quality graphene, whereas the ratio of the $2D^{\dagger}$ and $G^{\dagger}$ peaks in the strained region is ~ 2.6, indicating, in general, a lower quality. This change can be explained by the comparative locations on the sample surface where the Raman measurements took place, and a relatively large laser spot size of approximately 1 μm^2 that will overlap with areas of aggregated carbon. The strained region can be seen in figure 5.4b (indicated by the red arrow) to be a smaller region enclosed by carbon aggregates, compared to the larger, and visibly clearer, area where the unstrained measurements took place (indicated by the blue arrow in figure 5.4b).

These Raman results indicate the high quality of the MBE graphene that has been grown, and confirm the high strain levels that are present in the graphene lattice.

5.3.2 ARPES Measurements

Micro angle resolved photoemission spectroscopy (μ-ARPES) measurements were recorded for these graphene-hBN heterostructure samples by Dr Neil R Wilson (University of Warwick) at the Elettra Sincrotrone in Trieste. A synchrotron light source was required for these μ-ARPES measurements in order to provide high enough spatial resolution (spot size of approximately 1 μm in diameter) for these samples, with graphene regions on the order of a few microns in size. Results were measured following a thermal anneal at 400 °C for a total of 2 hours in ultrahigh vacuum before measurement to remove adsorbates that accumulated during exposure to the atmosphere. Figure 5.6a shows the same flake that was shown in the optical and AFM images from figure 5.4 (sample D), with Raman measurements of the same regions shown in figure 5.5.

Panel b) of figure 5.6 shows a scanning photoemission microscopy (SPEM) image of the flake. In this mode of imaging each pixel represents an integration of an ARPES energy-momentum spectrum recorded at this position. The spectra was chosen to be recorded around the graphene K point so that a high value on this map indicates the presence of graphene. Clear similarities between the regions of graphene seen by the SPEM image and the optical image, with areas matching locations of carbon aggregates in the AFM image in figure 5.4b, allow for previously identified regions to be measured using μ-ARPES.

The results of these measurements can be seen in figure 5.6c and d) for the region previously identified as strained by AFM and Raman spectroscopy (with $\lambda_S \sim$ 30-50 nm), and panels f) and g) for the unstrained region (where λ_S was measured to be 13.79 $\pm$ 0.09 nm). Panels c) and f) show constant energy slices through the Dirac cone approximately $\sim$ 2 eV below the Fermi energy. In these figures the central spot corresponds to the top of the hBN band seen in the energy-momentum spectra shown in panels d) and g), measured along the red dashed lines in c) and f). The energy band spectra shown in panels d) and g) appear identical, and show the expected graphene Dirac cone for the heterostructure valence band. Furthermore the hBN is shown to be aligned by the position of the hBN band peak, with an energy difference from the Dirac point to the first hBN band measured to be 2.5 $\pm$ 0.2 eV in d), and 2.4 $\pm$ 0.2 eV in g), close to agreement with the expected value estimated using density functional theory (DFT) to be $\sim$ 2.95 eV [15]. Panel e) in figure 5.6 shows an extended region of the band structure measured for the strained graphene-hBN heterostructure, displaying the expected valence band structure [15]. These μ-ARPES measurements show that no resolvable changes to the heterostructure band structure can be seen between the strained and unstrained regions on this sample.

Figure 5.7a shows an amplitude channel image (recorded in AC mode) of a graphene-hBN heterostructure sample, referred to as sample E in table 5.1, where large regions of bilayer and multilayer graphene have been recorded. A large hBN blister in the lower left-hand side of the image dominates topography channel images (not shown), which were used to determine the graphene layer heights that have been indicated in panel a), showing large regions (in the order of μm in diameter) of bilayer and trilayer graphene on bulk hBN.

Using μ-ARPES, measurements were recorded around this location, and can be seen in panels b-d) of figure 5.7. In the first energy-momentum spectra of the graphene K point, in panel b), the hBN band that was seen in figure 5.6d and g) can also be seen. Here it is measured to be positioned at 2.8 $\pm$ 0.2 eV from the Fermi energy (in agreement with the predicted value of $\sim$ 2.95 eV [15]). In all three of the panels from b-d) of figure 5.7 there are multiple energy bands present (albeit only faintly visible in c)). In b) the energy difference between the Dirac point and the next band is measured

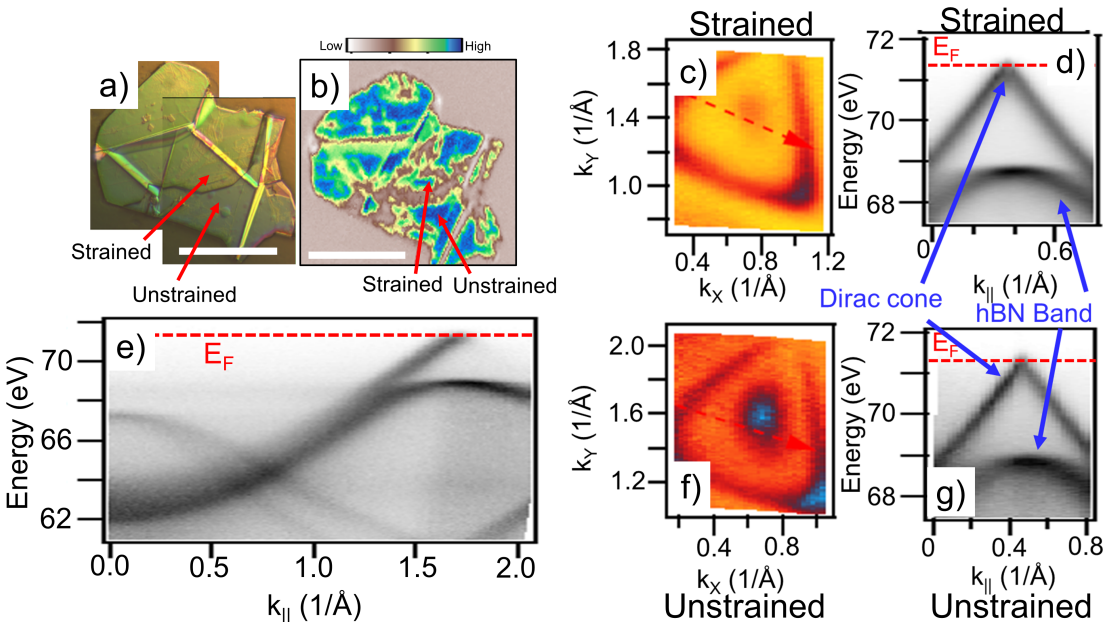


FIGURE 5.6: Panel a) shows the same optical microscopy image of sample D, as seen in figure 5.4a, where regions of high and low strain were determined through AFM imaging. Panel b) shows the same heterostructure region as a) as a photoemission image recorded using ARPES. Each pixel level corresponds to the integration of an ARPES E-k spectrum measured at this position, with higher values indicating regions of aligned graphene. Panels c) (strained region) and f) (unstrained region) show constant energy slices through the Dirac cone and around the graphene K point, measured below the Fermi energy. Spectra showing the heterostructure band structure recorded through the K point, along the dashed red lines in c) and f), are provided in panels d) and g), with an expanded region recorded in e).

to be 0.34 ± 0.11 eV at the K point, similarly in panel c) a difference of 0.34 ± 0.08 eV was measured. In panel d) the energy difference measured at the K point has a slightly larger value of 0.39 ± 0.10 eV.

Panels e) and f) of figure 5.7 (taken from [17]) show DFT predictions for the graphene bandstructure close to the K point for bilayer and trilayer Bernal stacked Graphene. In these predictions the energy from the Dirac point to the lower valence energy band is measured to be ~ 0.30 eV for bilayer graphene, and ~ 0.42 eV for trilayer graphene. The values measured in panels b) (0.34 ± 0.11 eV) and c) (0.34 ± 0.08 eV) are both in agreement with the expected structure of bilayer graphene (seen in e)), with bands that match the expected diagram. The value recorded for panel d) (0.39 ± 0.10 eV) is closer to the value expected for trilayer graphene, with a structure that closely resembles that of the valence bands shown in the diagram in f), with the additional, less linear bands around the Dirac point present. These additional bands are also present, although far more faintly, in panels b) and c) suggesting, in agreement with the AFM

image in a), that the region under the beam spot (with a 1 μm diameter) is a mixture of monolayer, bilayer, and trilayer graphene.

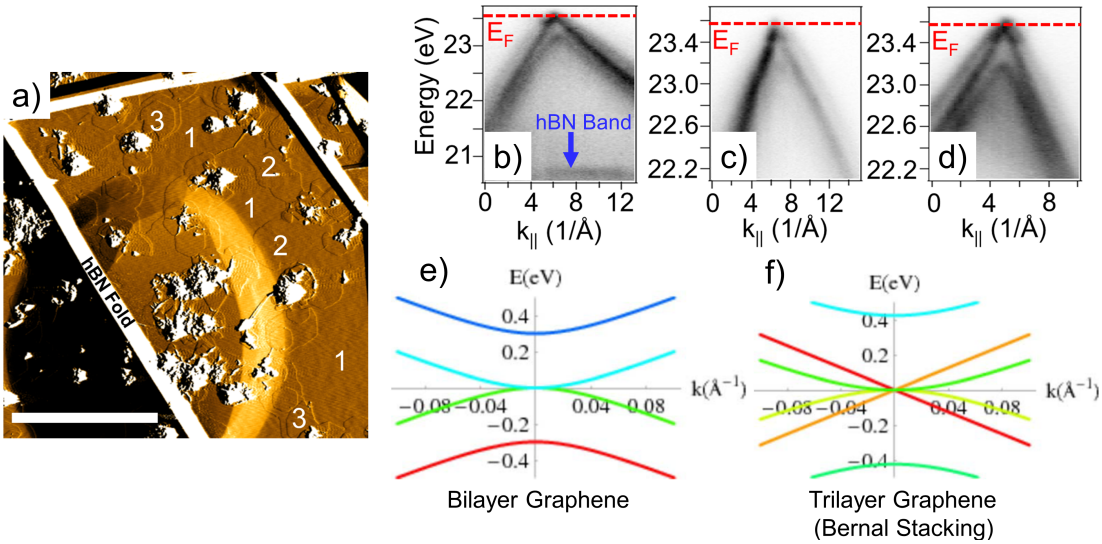


FIGURE 5.7: Panel a) shows the amplitude channel for an AC mode AFM image of sample E displaying multilayer graphene growth. There is a large hBN blister covering the a large portion of this image, as well as hBN folds (indicated). Some of the graphene layers have been indicated showing large regions of bilayer and trilayer graphene. The scalebar measures 2 μm. Panels b-d) show ARPES spectra passing across the graphene K point recorded at different positions around the area shown in a). In these spectra multiple bands are seen. Panels e) and f) show the expected band structure around the K point for bilayer and trilayer graphene with Bernal stacking (taken from [17])

5.3.3 Strain Relaxation

In many cases for the sample grown at high temperature cracks in the graphene have appeared, resulting in relaxation of the graphene lattice. Figure 5.8a shows a sample (sample G in table 5.1) where very highly strained material was observed elsewhere (up to lattice matched with a value of 1.8% strain). This sample was grown at a substrate temperature of 1680°C for 3 hours using the atomic carbon source filament. The area shown in figure 5.8a is covered in graphene cracks. This is made clearer in the magnified images shown in a)i) and a)ii). The cracking across the surface is a result of the highly strained material that has been grown, relieving its strain as the sample is cooled to room temperature.

Figure 5.8b shows an image recorded on the sample shown in figure 5.4 (sample D), but on a separate hBN flake. In this topographic AC mode image the graphene crack can be seen as a black horizontal depression in the surface. This depression is shown to have sharp edges, with a depth of 370 $\pm$ 80 pm, close to the expected

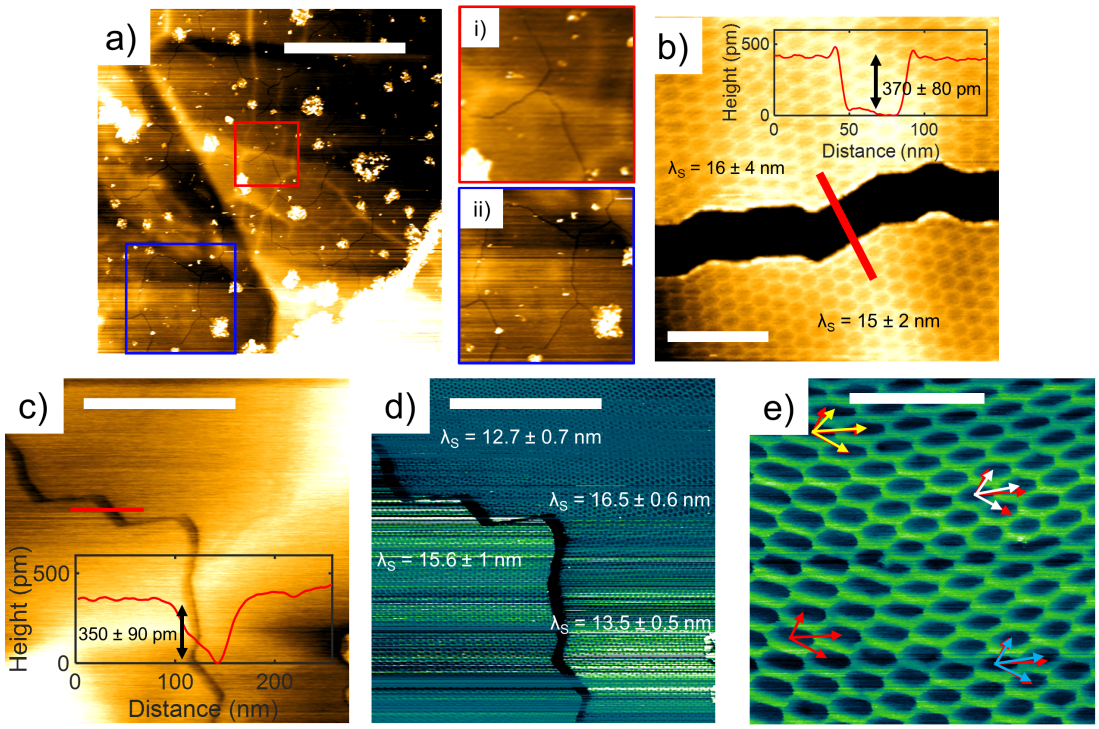


FIGURE 5.8: a) AC topography AFM image showing an extreme case of cracking/strain relaxation of graphene grown at high temperature on hBN (sample G in table 5.1). i) and ii) show the regions in a) bounded by the red and blue boxes respectively, with increased magnification. b) AC topography AFM image showing a closer look at a crack in the graphene on sample D. The inset profile is measured along the red line. The hBN moiré pattern can be seen on both sides of the crack. c) contact mode topographic, and d) CAFM current images showing the same cracked region on sample C. The wavelength of the moiré pattern seen across various regions of the graphene has been determined using 2DFFT , and is indicated on the figure in d). The inset profile shown in c) was measured along the red line in c). e) shows a region near to a crack on sample C, where the moiré pattern is very irregular. The sets of arrows indicate the three moiré directions at that location, with the red arrows from the lower left position repeated to highlight the changes in moiré directions. The scalebars measure 2 μm in a), 100 nm in b), 500 nm in c) and d), and 100 nm in e). The current scales in d) and e) have maximums of 5.8 μA and 9.1 μA and minimums of 1.4 μA and 5.3 μA.

graphene thickness of 335 pm [125]. Furthermore, the mirrored facets of both edges of the crack confirms the identification of the observed feature as a graphene crack. The edges of the crack also appear as highly faceted, with directions that are all at angles of 30° to connected edges. This suggests that the edges of the crack are a combination of zig-zag and armchair edges. The width of the gap is measured to be 42 $\pm$ 5 nm in b). The moiré patterns on either side have been determined to measure 16 $\pm$ 4 nm above the crack, and 15 $\pm$ 2 nm below the crack. These values suggest low strain remains in the graphene, with a different amount present on either side. Both values are very

close to the expected maximum value of 14 nm.

Figures 5.8c, d) and e) have all been measured on sample C, grown at a substrate temperature of 1675°C for 5 hours with a carbon filament source. This was the same sample as shown in figure 5.3. Figure 5.8c and d) show the contact mode topographic and CAFM current channel (recorded with a sample bias of -1 V) images respectively of the same location. The width of the crack in these figures has a maximum value of 58 ± 7 nm, and a depth of 350 ± 90 pm. In the CAFM image, figure 5.8d, the recorded current drops to zero as the AFM tip is positioned over the exposed hBN within the trench formed by the crack. Confirming that the graphene has monolayer thickness and the exposed region is hBN.

The moiré patterns observed in various regions of figure 5.8d have been indicated on the figure, and have wavelengths ranging from 12.7 ± 0.7 nm to 16.5 ± 0.6 nm. In addition, this superlattice wavelength varies over short distances on either side of the crack, further revealing different levels of strain across the region. In all cases the levels of strain are very low, and the sample is generally relaxed. The observation of moiré wavelengths below 14 nm here suggests a misalignment of the graphene and hBN due to the relaxation following the graphene tearing.

The pattern towards the top of the image in d) appears highly non-uniform. A higher magnification image of a region further above this, where this non-uniform pattern can be seen more clearly, is shown by a CAFM current image in figure 5.8e (recorded with a sample bias of -0.5 V). In this image the moiré pattern can be seen to be highly non-uniform. Three red arrows indicating the superlattice directions in the lower left of the image have been overlaid across the figure to highlight the changes in the moiré pattern. At each of these locations the local moiré directions have also been shown, with a different colour for each position. The cause of this non-uniformity across the moiré pattern is due to the directionality of the strain release imposed by the cracks. The cracks have allowed the graphene to relax in some directions, but graphene pinning aggregates have prevented relaxation along other directions. Furthermore, the relaxation in some directions and not others can allow for small rotations of the graphene lattice relative to the hBN, which, as shown by figure 2.6 in section 2.3.2, can lead to a decrease in the moiré pattern wavelength.

Figure 5.9 shows an extreme case of non uniform strain observed in MBE graphene/hBN heterostructures. These images were recorded on sample C, the same as shown in figure 5.3, and figure 5.8c-e. Figure 5.9a and b) show a region of this sample with highly non-uniform strain. The same moiré pattern can be seen in both the topographic channel, a), and the current channel, b) (recorded with a surface voltage of -0.5 V). The moiré superlattice in the lower portion of these images becomes highly anisotropic, whereas towards the top of the image the pattern returns to a hexagonal structure. This suggests that the amount of strain along the y-direction is higher in the lower

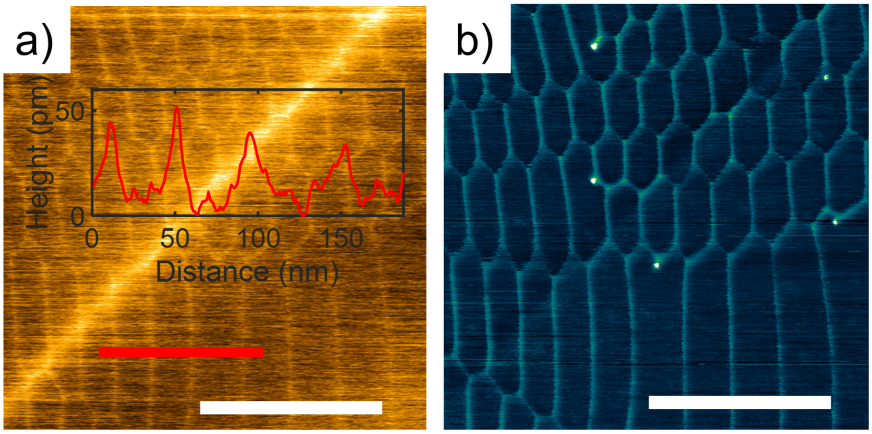


FIGURE 5.9: a) shows a contact mode height image, while b) shows the corresponding CAFM current images. In a) the featured moiré pattern can be seen to elongate towards a uniaxial pattern towards the lower portion of the image. The corresponding CAFM image in b) shows the same pattern, with large current spikes at the termination of moiré lines (discussed in section 5.5). The inset profile in a) is measured along the red line in the main figure. The scalebars measure 200 nm in both images. The maximum and minimum currents displayed in b) are 1.4 μA to 2.8 μA. All images recorded on sample C in table 5.1.

portion of the image.

The topographic diagonal crease seen in figure 5.9a is aproximately 150 $\pm$ 30 pm in height. This is likely a feature below the upper layers, possibly a fold in an underlying hBN flake on which the main flake has been exfoliated. The height profile seen as an inset in figure 5.9a, measured along the red line in the main image, shows a moiré pattern with a topographic range of 48 $\pm$ 5 pm. Visible in figure 5.9b are sharp, localised peaks in the measured current channel. These appear as bright spots in the current image. Their locations can be seen to exist at positions where the moiré lines terminate, and indicate the presence of lattice defects. These defects are investigated in more detail in section 5.5.

The large scale of the superlattice in the images shown in figure 5.9, particularly along the stretched direction (close to a y-axis alignment in these examples), of several hundred nanometres implies that the strain observed is near lattice matched with hBN along that direction, with an estimated wavelength of between 160 to 200 nm, indicating strain of around 1.68 to 1.71%. The wavelength along the shorter direction (close to the x-axis) ranges between 35 to 50 nm in d), indicating a contrasting strain of 1.13 to 1.34 %. A graphene strain of 1.80% from its relaxed form indicates a graphene that is lattice matched with the underlying hBN.

5.4 Lattice Matched Graphene

As described previously (in section 2.3.2), an increase in the superlattice period of the graphene/hexagonal boron nitride moiré pattern indicates that the difference between the two corresponding atomic lattices is reduced. As this difference approaches zero, the moiré pattern wavelength diverges towards infinity, provided the two materials are orientationally aligned. This divergence towards an infinite moiré pattern has been observed for some samples grown with a high substrate temperature, close to 1680°C.

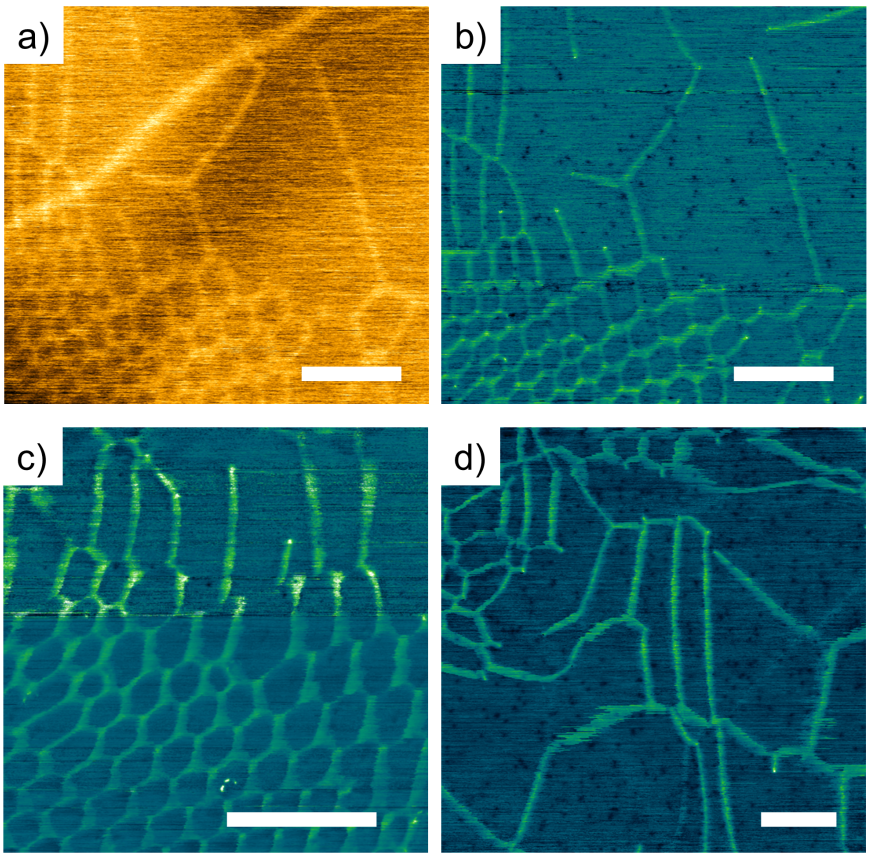


FIGURE 5.10: a) and b) show the same lattice matched graphene area grown at high temperature on hBN region recorded with contact mode AFM and CAFM respectively. c) and d) show CAFM images of two additional regions, with c) measured at a different area on the same flake as a) and b), and d) shows a region on the same sample, but a different flake to the other images. The scalebars measure 200 nm in all images. The current colourbars scale from 1.9 to 3.5μA in b), 1.2 to 2.3 μA in c), and 5.4 to 8.1 μA in d). All images in this figure were recorded on sample C.

Figure 5.10 shows three example locations where lattice matched regions have been seen. All images in this figure were measured on the same sample, referred to as sample C in table 5.1, with flakes transferred to a SiO_2 substrate near to a pre-patterned

Au contact after growth, followed by Ag nanowire deposition, as outlined in section 4. Figure 5.10a and b) show the same location for the contact mode AFM topographic channel, a), and the CAFM mode current channel, b) (measured with a surface voltage of -0.5 V). The moiré pattern can be seen in both images, with an additional diagonal crease similar to figure 5.9c seen in the topographic channel. Figure 5.10c and d) show two other CAFM current images showing locations where the graphene strain is close to lattice matched with the hBN (both c) and d) were recorded with a surface voltage of -0.5 V). Individual regions free of moiré lines in these images are on the scale of hundreds of nm, with areas in excess of 0.1 μm^2 seen in figure 5.10d.

The regions of graphene where lattice matched material has been located are typically in areas surrounded by graphene pinning carbon aggregates, similar to the area indicated by the red arrow in figure 5.4b. The bright moiré lines in these images correspond to Frenkel-Kontorova (F-K) domain walls where the mismatch strain is localised [46]. Many of these F-K lines terminate as the moiré pattern diverges towards infinity in these figures, as seen in figure 5.9 for the samples with high uniaxial strain. These termination points, observed to have a high conductivity by the current spikes in these figures, are characterised by lattice defect locations, as discussed in section 5.5.

Figure 5.11a shows a contact mode topographic image of a lattice matched region. This sample was grown at approximately 1700°C for 3 hours using the atomic carbon source, sample H in table 5.1, with silver nanowires deposited after growth to allow for conductive measurements to be taken. Images of the current variation for this area of highly strained graphene are shown in figure 5.11b (recorded simultaneously with figure 5.11a using a sample bias of -50 mV) and demonstrate that the current flow is significantly greater when the probe is above the F-K domain walls as compared with the neighbouring lattice-matched regions, and even higher where the walls terminate (the bright point-like features in figure 5.11b).

A current profile extracted from this region shows an increase in current by a factor $\sim$3 above a domain wall (shown in the current profile in figure 5.11d). A topographic height profile extracted from the contact mode image (provided in figure 5.11c) shows that the cantilever probe is withdrawn by 47$\pm$4 pm as it passes over the domain wall; this is close to the effective height determined in figure 5.9c and provides strong evidence that the probe-sample separation is constant during the electrical measurements. The increase in current must therefore be due to a variation in the intrinsic electronic properties of graphene in the nanoscale regions close to the domain walls.

A higher current flow from the AFM probe to the surface when it is positioned above a F-K domain wall is indicative of a higher density of states in these regions. The value of the energy gap which is formed in lattice-matched graphene/hBN has been predicted to be $\sim$50 meV [126], close to $2k_BT$ at room temperature. The lower currents

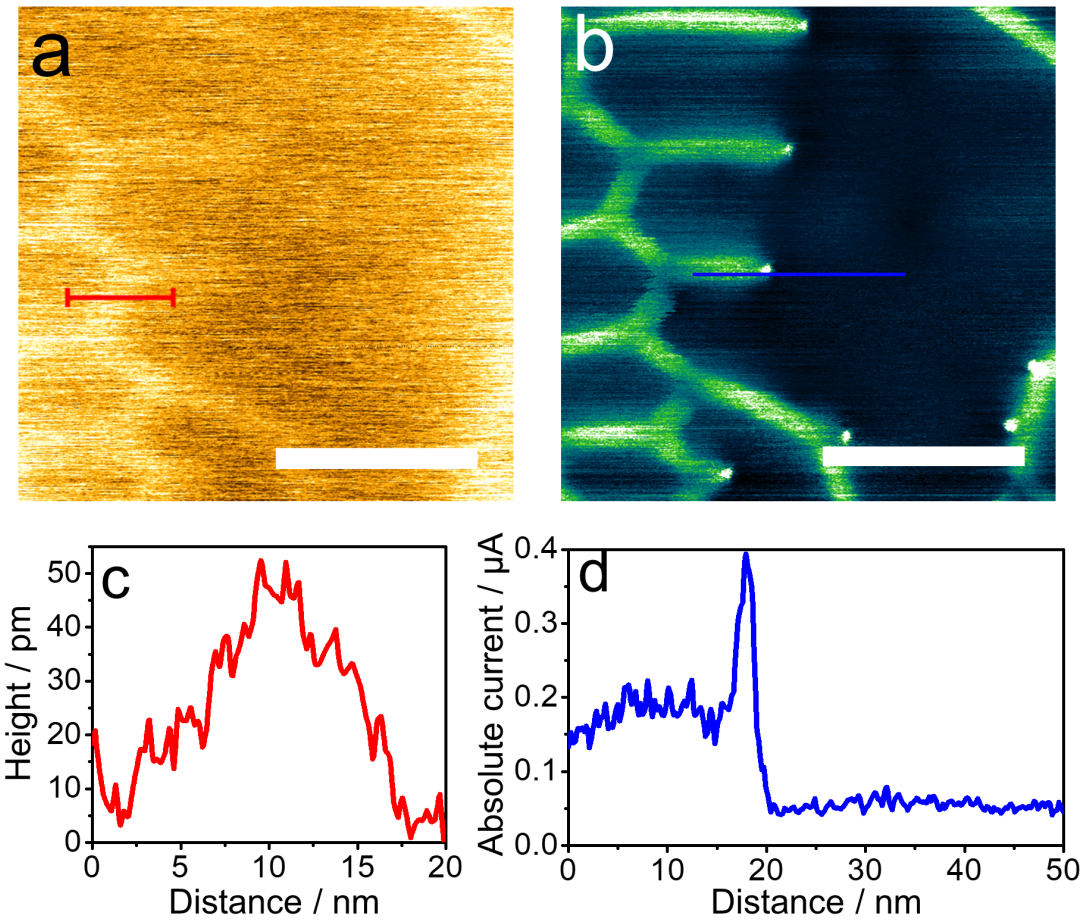


FIGURE 5.11: a) Contact mode AFM height trace image recorded simultaneously with b) on sample H. b) CAFM image recorded with a sample bias of -50 mV showing high current flow above F-K domain walls and very high current at bright pointlike features due to defects in the graphene lattice. The scale bar is 50 nm in a) and b). The colormap contrast ranges from -0.03 to -0.41 μA in b) and spans a range of 280 pm in a). c) Height profile averaged along the line with a width of 20 pixels indicated in a). d) A current profile measured along the line shown in b). The current measured at the termination points is $\sim$2.5 times the value recorded at the F-K lines, when measured relative to the current within the intermediate regions.

measured above the lattice-matched regions are consistent with a lower density of states which might be expected in the presence of a band gap which is of order a few times k_BT. Interestingly, the lattice-matching is absent in the graphene folds which form the F-K domain walls and the band gap in these regions would be expected to be smaller or completely absent. While there has been no detailed study of the quantum properties of F-K domain walls embedded in lattice-matched graphene, the one-dimensional symmetry is likely to promote analogies with conduction in carbon nanotubes.

5.4.1 Lattice Matched Raman Measurements

Figure 5.12a shows the amplitude channel of an AFM image recorded using AC mode of a lattice matched region of MBE graphene grown on an exfoliated hBN flake on sample F. In this instance the amplitude channel appeared to show the moiré pattern with a higher contrast level than the other channels. The F-K defect lines seen in figure 5.12a can be seen to diverge towards infinity within the large $\sim$4 μm^2 area within this image. The inset of figure 5.12a shows a second amplitude channel AFM image of the area shown in the main panel, with an extended region on display.

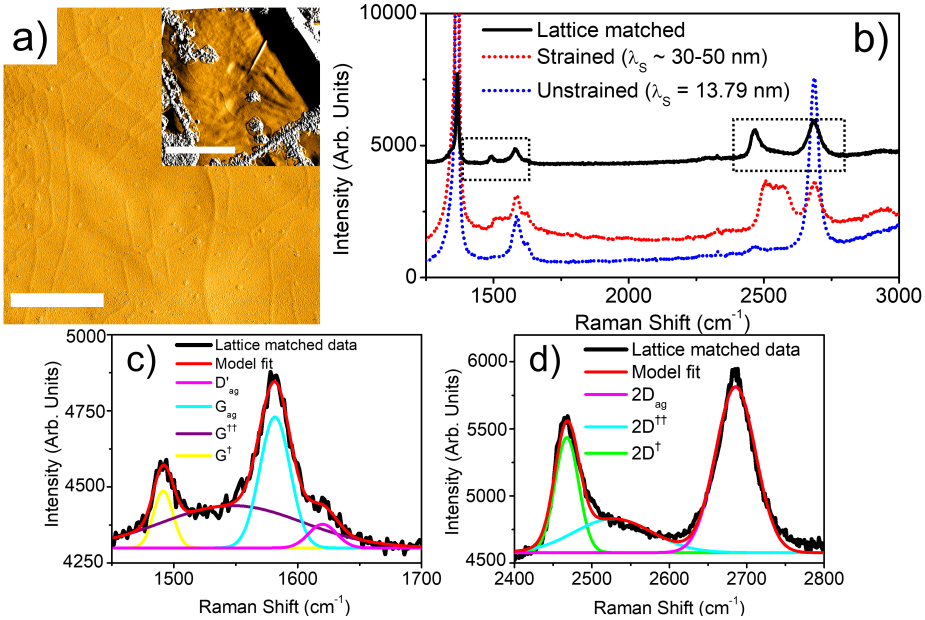


FIGURE 5.12: a) An AFM amplitude channel image recorded in AC mode of a lattice matched MBE graphene on hBN region (sample F), where the moiré pattern diverges towards infinity. The inset shows a zoomed out amplitude channel image of the same region. The scalebars measure 500 nm in the main image, and 2.5 μm in the inset. b) Raman spectroscopy results measured on the lattice matched region shown in a) are shown by the black data. The blue and red dotted lines show the data plotted in figure 5.5 for unstrained and strained graphene respectively on sample D, with offsets in the y-axis applied for clarity. Panels c) and d) show zoomed regions of the lattice matched data in b) at the indicated locations. Included in these figures are peak fitted Lorentzian curves corresponding to the D'$_{ag}$, G$_{ag}$, G††, and G† Raman peaks in c), and the 2D$_{ag}$, 2D††, and 2D† Raman peaks in d). Also shown in panels c) and d), in red, is the sum of the fitted Lorentzians.

Raman spectra measurements were recorded within the region shown in figure 5.12a using the same methodology described previously, with the resultant data plotted in panel b) in black alongside data shown earlier in figure 5.5 for the strained (shown in red) and unstrained (shown in blue) locations on sample D seen in figure 5.4. In figure 5.12b the spectra have been offset along the y-direction for visual clarity.

Panels c) and d) of figure 5.12 show the lattice matched Raman data within the regions indicated in panel b), with peak fitted Lorentzians for the expected Raman peaks (fitted using OriginPro software package) shown alongside their combined summation plotted in red. The measured locations of these peaks and their respective FWHMs are provided in table 5.2. The Raman peaks that were observed to remain unshifted previously for the strained graphene displaying a moire periodicity of $\sim$ 30-50 nm, are again seen here to remain unchanged by the additional strain, with the hBN, G_{ag}, D'_{ag}, $2D_{ag}$ peaks located at 1366 cm^{-1}, 1582 cm^{-1}, 1620 cm^{-1}, and 2685 cm^{-1} respectively (with corresponding FWHMs shown in table 5.2).

The same peaks seen in the strained graphene spectra arising from the splitting of the 2D and G signature Raman peaks are visible in the lattice matched spectra with further red-shifting of the $2D^{\dagger}$, $2D^{\dagger\dagger}$, $G^{\dagger}$, and $G^{\dagger\dagger}$ peaks of 217 cm^{-1}, 59 cm^{-1}, 94 cm^{-1}, and 38 cm^{-1} with respect to the 2D and G peaks in the unstrained material (compared to 182 cm^{-1}, 123 cm^{-1}, 77 cm^{-1}, and 22 cm^{-1} for the strained measurements). This increase in red-shift is consistent with the results shown in reference [45] and further displays the relationship between Raman peak shift and graphene strain.

The ratio of the $2D^{\dagger}$ and $G^{\dagger}$ peaks in the lattice matched region is $\sim$4.8 which is significantly larger than the 2.6 value seen for the strained region, and suggests a high graphene quality similar to that of exfoliated graphene (where an approximate value of 4 is expected) [92, 124].

5.4.2 Lattice Matched ARPES Measurements

Micro angle resolved photoemission spectroscopy measurements were measured by Dr Neil R Wilson at the Elettra Sincrotrone in Trieste for the lattice matched graphene-hBN heterostructure shown in figure 5.12, in the same way as was carried out for the strained material shown earlier in figure 5.6. Figure 5.13a shows an energy-momentum spectrum for the valence bands of the lattice matched graphene region shown in figure 5.12 on sample F measured over the graphene K point, displaying the expected Dirac cone structure. As described earlier in section 5.4 there is a predicted energy gap for lattice matched graphene on hBN heterostructures of $\sim$ 50 meV [126]. In order to view this proposed energy gap in the sample under investigation using μ-ARPES the Fermi energy must be raised into the conduction band through electron doping to allow for spectroscopy measurements to take place either side of the Dirac point. In order to achieve this an estimated $\sim$ 0.4 nm monolayer of Li atoms was deposited (via metal evaporation) across the sample surface. Figure 5.13b shows the corresponding μ-ARPES energy-momentum spectrum for the same lattice matched region on sample F as a) recorded following electron doping. In this figure the Fermi energy can be seen to have been raised by 0.26 $\pm$ 0.08 eV, with the tip of the conduction band portion of

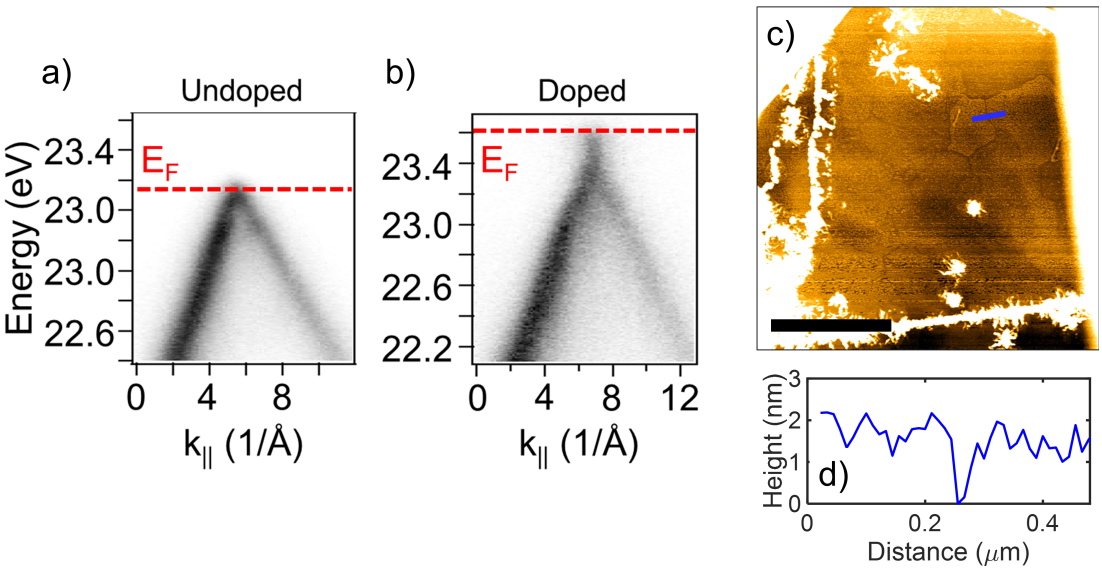


FIGURE 5.13: Panels a) and b) show ARPES spectra measured through the graphene K point, showing the energy bands of the Dirac cone recorded on the lattice matched region of sample F identified in figure 5.12. Panel a) shows data recorded before alkali doping of the sample, with b) showing measurements recorded post-doping. In b) the Fermi level is raised to be within the conduction band of the graphene, with these bands positioned above the Dirac point visible in b). Panel c) shows the same region on sample F as seen in the inset of figure5.12a, recorded using AC mode AFM, with the topographic channel displayed, and taken following doped ARPES measurements after an estimated 0.4 nm thickness Li deposition. Cracks have appeared across the surface, with a profile, measured along the blue line in c), shown in d) to indicate a depth of $\sim$ 1.5 nm. The scalebar in panel c) measures 2 μm.

the Dirac cone visible above the Dirac point. However, the predicted energy gap of 50 meV is beyond the energy resolution that has been achieved in this spectrum. The key factor contributing to the sharpness of these energy bands is the uniformity of the graphene surface. The region, shown in the AFM image seen in figure 5.12, displays a moiré pattern wavelength that tends towards the infinite, with some smaller uniformly lattice matched areas. The presence of the Frenkel-Kontorova defect lines along with the local presence of carbon aggregates seen in the inset of figure 5.12a, and smaller wavelength moiré pattern seen towards the edges of panel a) are contributing factors to the lack of spectral resolution in figure 5.13b.

Following μ-ARPES measurements of the electron doped sample the region was re-imaged using AFM. Figure 5.13c shows the topographic channel of an AC mode AFM scan of the same region seen in the AFM images in figure 5.12. In this image the surface can be seen to have been coated in material, from the Li metal deposition, with no clean areas of graphene present and a high surface roughness with variations of $\sim$ 0.5 nm seen in the profile in panel d) measured along the blue line in c). Also visible

in this image are cracks with a depth of $\sim$ 1.4 nm, as shown by the profile in d). This cracked surface, and significant crack depth, suggests that the amount of deposited Li may have been higher than expected, and that the underlying graphene had relaxed during, or after, the deposition. The visibility of these cracks suggest that they have appeared during or after the Li deposition, and not before as they have not been filled in by the metal evaporation. It is most likely that the Li deposition was the cause of the graphene relaxation, possibly a result of intercalation of Li atoms underneath the graphene layer [127], which suggests that the measurements shown in panel b) recorded after doping are not for lattice matched/strained material as intended.

5.4.3 Relaxation of Lattice Matched Material

Figure 5.14 shows a set of AC mode AFM phase images of sample G, grown at a substrate temperature of 1680°C for 3 hours using the atomic carbon source. On this sample very large areas, in excess of 5 x 5 μm, of a moiré pattern exhibiting behaviour diverging towards an infinite wavelength were observed. Figure 5.14a shows one of these large regions. This figure is a mosaic image made up of 16 smaller AC mode AFM phase images. Graphene regions displaying a diverging superlattice wavelength can be seen across the entire area, with one example shown in figure 5.14c. This figure shows the region indicated in a), with the moiré pattern indicating near lattice matching, resembling those shown in figure 5.10, clearly visible. The large number of carbon aggregate clusters scattered across the surface may be a large contributing factor to the extended, continuous lattice matched domains.

The large amount of strain displayed by the graphene samples that leads to lattice matching causes the material to become comparatively more fragile than unstrained graphene samples. While imaging in contact mode on the sample that has been shown in figure 5.10 the sample cracked, resulting in the relaxation of the previously strained graphene material, and a disappearance of the highly strained graphene/hBN moiré. In the case of the sample shown in figure 5.14, the same region was scanned before and after a two month period of being stored under ambient conditions. Following this period, the region that had previously been confirmed to be lattice matched was observed to have become covered in graphene cracks. Figure 5.14b and d), show AC mode AFM phase images of similar locations to those shown in a) and c) following this two month period. The dotted red circles encompass carbon aggregate clusters on the surface that have been used as a guide for the eye in order to locate the same regions before and after the two month period, with matching aggregates circled in a) and b), and c) and d). Spanning the entire surface in figure 5.14b are a network of strain relieving graphene cracks. These can be seen more clearly in figure 5.14d. Also faintly visible in d) is a moiré pattern with a superlattice wavelength of approximately 16 nm

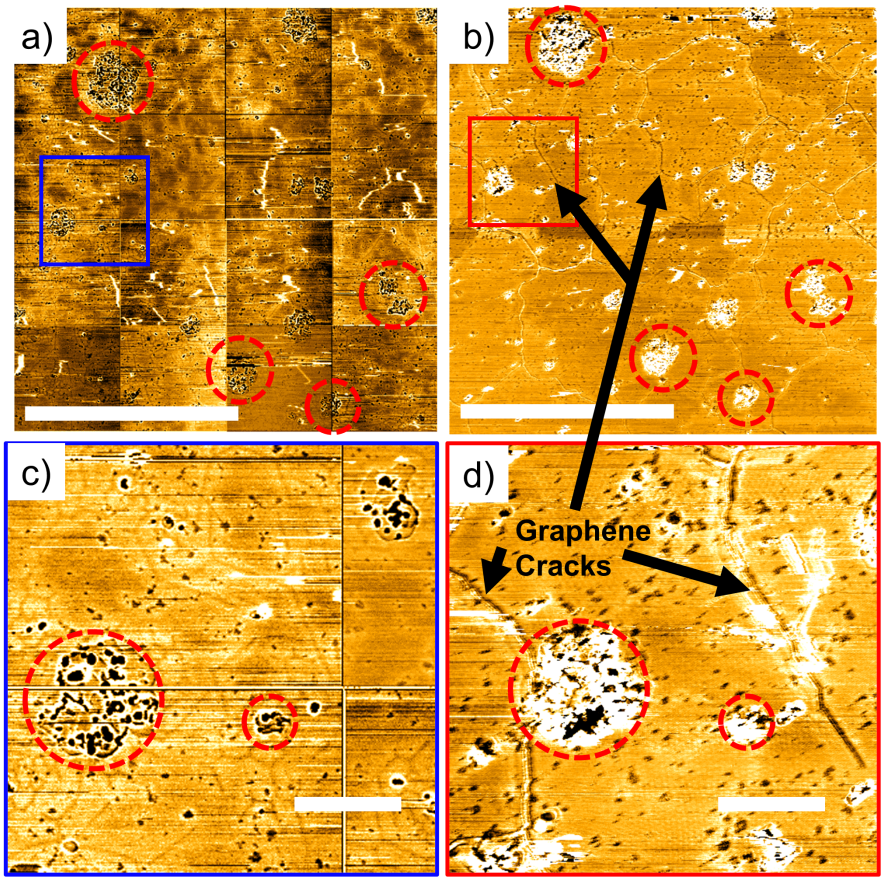


FIGURE 5.14: a) and c) before relaxation, and b) and d) after relaxation AC mode phase images of a lattice matched graphene sample (referred to as sample G in table 5.1). The red dotted circles highlight recognisable features used to locate the same location. A lattice matched moiré pattern spans the entire surface of image a), shown with an increased magnification in c) for clarity. Image a) consists of a mosaic of several individual images, recorded by Juan D. Albar. Image b) is covered in cracks across the surface. These can also be seen in d), where a moiré pattern of approximately 16 nm was recorded. The areas shown in c) and d) are indicated in a) and b) by the blue and red boxes respectively. The scalebars measure 2 μm in a) and b), and 250 nm in c) and d).

across the graphene surface, confirming that the graphene has relaxed. In other lower strained samples, with moiré wavelengths near to 14 nm, no spontaneous relaxation has been observed over time periods spanning several years.

5.5 Lattice Defects

As explained in section 2.3.2, the regions where the moiré pattern wavelength diverges signify areas where the graphene has become lattice matched to the underlying hBN.

This further suggests that these cell boundaries/moiré lines correspond to the Frenkel-Kontorova domain walls, with a level of strain that varies across the moiré cells with strain relief at the F-K lines as described by *Woods et al.* [46], and outlined in section 2.3.2 and the accompanying figure 2.6a and b). For the samples displaying lattice matched properties, on the areas away from the moiré lines the carbon atoms that make up the graphene lattice match the lattice constant of the hBN, with the strain relief located at the F-K line.

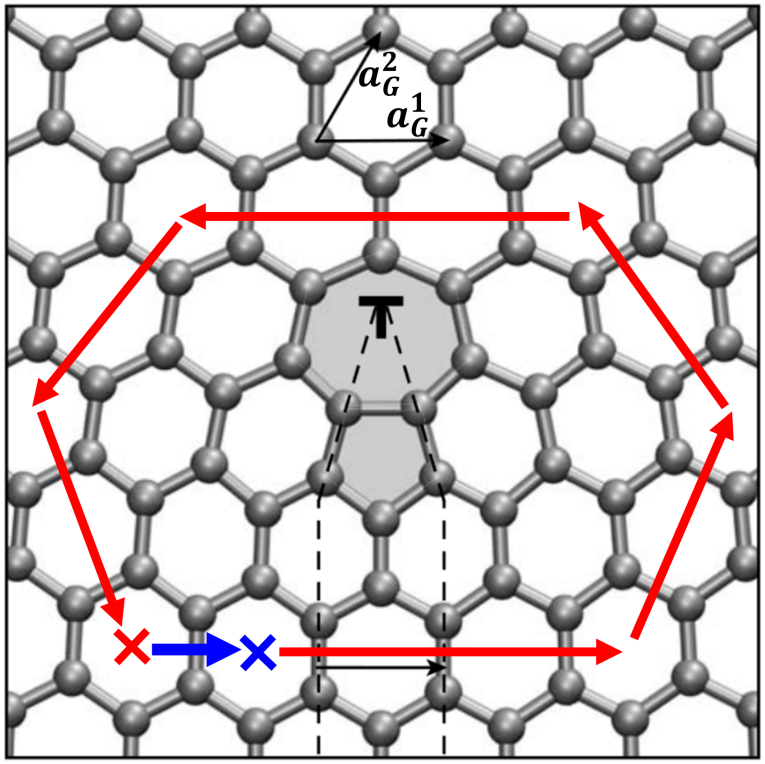


FIGURE 5.15: A diagram, taken from [128] that shows a potential graphene lattice configuration at F-K line termination defect sites. The lattice vectors $\mathbf{a}_\mathbf{G}^\mathbf{1}$ and $\mathbf{a}_\mathbf{G}^\mathbf{2}$ are indicated. The shaded regions highlight cells that are not cornered by six carbon atoms, and the dotted lines indicate the location of the additional row of carbon atoms originating at the dislocation core. The red arrows follow a Burgers path around the defect, starting at the blue cross and ending at the red cross. The resulting Burgers vector is shown in blue, and is perpendicular to the additional carbon atom row.

The origin of these F-K lines, as seen in figure 5.11, appear to exist at highly conducting locations. If the assignment to F-K domain walls is correct then the moiré lines must terminate at the origin of an edge dislocation in the graphene lattice [45, 46]. The diagram shown in figure 5.15displays a potential graphene lattice configuration for these locations. At the defect, located at the centre of figure 5.15, there are two lattice

cells that are not cornered by six carbon atoms that have been shaded. This results in an extra row of carbon atoms, indicated by the region between the dotted lines. A path following an equal number of steps along opposing lattice directions, known as a Burger path, is shown by the red arrows, starting at the blue cross and ending at the red cross. The resultant Burgers vector between the start and end positions (indicated by the blue arrow) is perpendicular to this additional row, and indicates that a defect is enclosed within the path.

These defects, referred to here as F-K termination points, have been seen through the observation of enhanced current flow over these regions, seen as an accompanying bright spot in the lattice matched CAFM images. The corresponding increase in conductance is far greater than that seen over the strain relieving F-K lines, with a value measured that is six times larger than over the lattice-matched regions in figure 5.11d. From a chemical perspective, the large amount of varying strain at these locations is likely to cause imperfect sp^2 hybridisation, with the possibility of broken unsatisfied carbon bonds, leading to a higher local density of states.

Figure 5.16 shows a variety of current vs. voltage characteristics recorded using conductive AFM measurements, along with current CAFM images, all recorded on sample C. In many cases reliable IV results were difficult to obtain using CAFM due to a variety of combining factors including tip changes due to wear, debris adsorption to the tip, thermal drift, and anodic oxidation (described in section 3.3). Figure 5.16a shows a graphene on hBN region with high uniaxial strain leading to the three parallel F-K defect lines seen in the image. The various spots on the image show the locations where IV measurements were recorded on the surface. These IV measurements were recorded with the same conductive tip as the image, by moving the tip into contact mode at the highlighted locations and varying the tip-sample bias. These measurements are shown in figure 5.16b. Each measurement represents an average of 10 voltage sweeps between $\pm$1.5 V. The measurements show non-Ohmic behaviour, with a steeper curve seen on top of the F-K defect lines. The non-Ohmic behaviour is most likely due to quantum mechanical tunneling occurring between the tip and the sample. The resistances that have been extracted by modeling the behaviour near to zero as Ohmic are found to be $4.2\pm0.1 \times 10^{8}\Omega$ and $1.37\pm0.02 \times 10^{10}\Omega$. The lower of the two resistances is recorded over the F-K defect line, as would be expected from the current CAFM image in figure 5.16a. Figure 5.16c shows a current profile measured across the red line shown in a) where a -0.5 V bias was applied to the sample.

Figure 5.16d shows a CAFM image of an an F-K termination defect and a lattice matched region, with corresponding IV measurements recorded over the indicated locations shown in panel e). Similarly to figure 5.16b each measurement corresponds to the average of 10 IV sweeps. The data shown for the measurements recorded

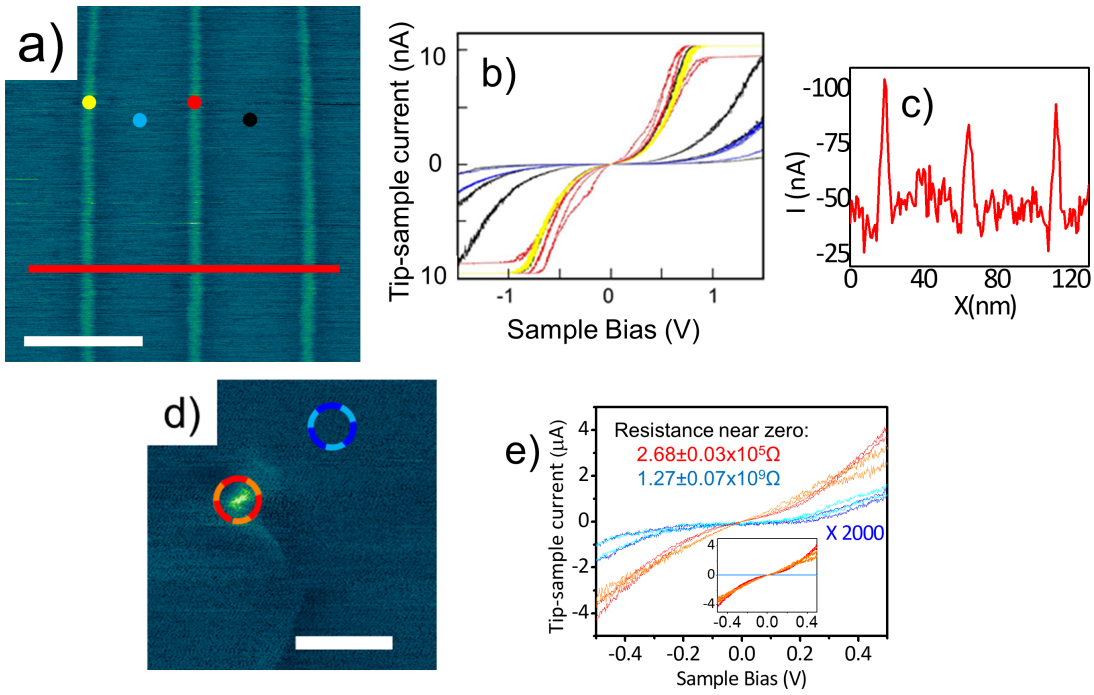


FIGURE 5.16: a) a CAFM current image showing a uniaxially strained region of graphene on hBN. Panel b) shows current-voltage measurements recorded at the corresponding coloured spots in a). Those measured on the F-K lines (red and yellow) display a much larger current. c) a current profile measured along the red line in a) (the current values are negative due to a -0.5 V bias used). Panel d) shows a defect located at the end of a F-K line (seen faintly in the lower portion of the image). IV measurements recorded on the defect, within the red/orange circle, and off the defect, within the blue circle, are shown in e). For the main figure in e) the off-defect measurements are shown at 2000 times their actual value, with the true value shown in the inset figure. Scalebars measure 150 nm in a) and 20 nm in d). Absolute current ranges are 60 to 244 nA in a), and 5 to 10 μA in d). All images were recorded on sample C.

away from the defect are multiplied by a factor of 2x10^3, since they were considerably smaller, as would be expected from previous CAFM images of F-K termination defects. The corresponding resistances calculated near zero are 2.68$\pm$0.03x$10^5\Omega$ and 1.27$\pm$0.07x$10^9\Omega$ on and off the defect respectively. This indicates a resistance value that is $\sim$4700 times lower on the defect.

As seen earlier in figures 5.9, 5.10, and 5.11, defects characterised by high local current have been observed at each of the origin points of F-K lines on near lattice matched moiré patterns. However, these points are also present on less strained graphene-hBN moiré patterns as shown in figures 5.17a and b). In this case the F-K termination defect still acts in the same way, as a source of a moiré line, which distorts

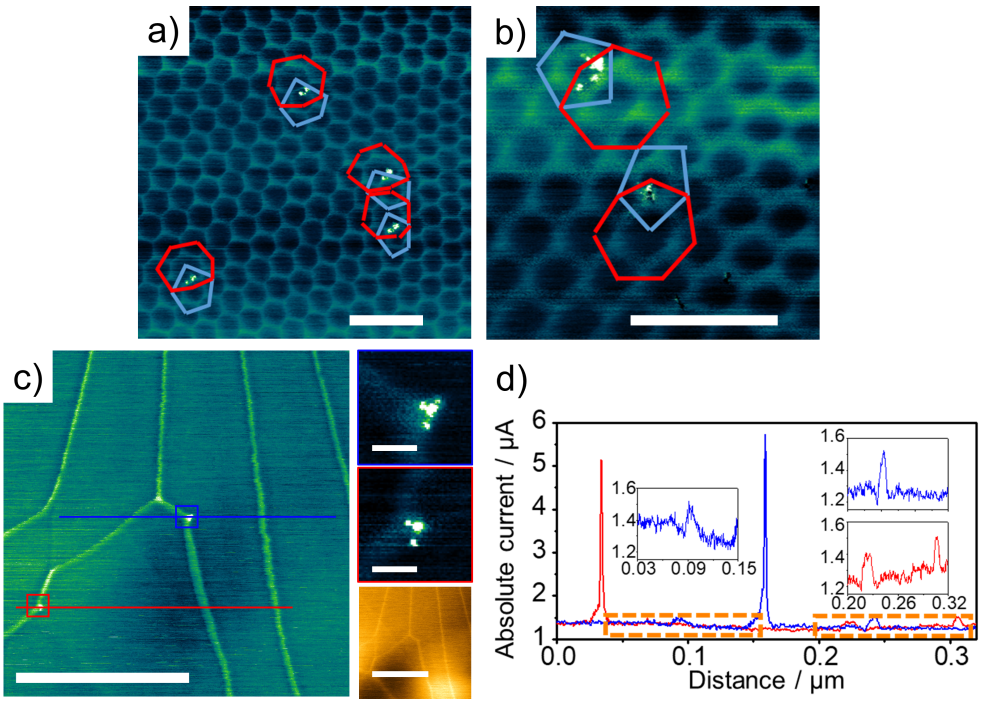


FIGURE 5.17: a) and b) CAFM current images showing lattice defects. The red and blue rings are centred on moiré cells that are surrounded by 7 and 5 cells respectively. The moiré pattern in both images is measured to be 13 nm. c) a lattice matched moiré region with two F-K termination defects. These defects are shown with a different current scale in the blue and red bordered insets, corresponding to the blue and red squares in the main figure. The bottom inset figure shows a contact height image of the same region as c). The profiles shown in d) are measured along the blue and red lines in c). The inset graphs show expanded sections of the profiles, indicated by the orange dotted boxes, where the profile passes over the F-K lines. The scalebars are both 50 nm in a) and b), 200 nm in c) and topographic inset in c), and 10 nm in the current insets in c). The current ranges are 190 to 370 nA in a), 100 to 290 nA in b), 1.00 to 1.75 μA in c), and 1.2 to 2.5 μA in both insets in c). All images recorded on sample C.

the moiré pattern in such a way as to create a moiré cell bounded by seven cells, adjacent to one bounded by five moiré cells, as opposed to the usual six of the hexagonal lattice. This phenomena is highlighted in figure 5.17a and b) by the red heptagons and blue pentagons, and can be seen at each of the observed defects. The extent of the increase of the measured conductivity at these termination points is difficult to measure due to their small size and the comparatively large size of the AFM tip. Figure 5.17d shows a pair of current profiles measured across the termination points shown in c) along the corresponding lines, and passing through the defects that have been enlarged in the insets. In this case, the current values measured at the termination defects are around 20 times that recorded at the F-K lines (shown in the insets of d)), when measured with respect to the current seen on the lattice away from the F-K lines.

However, due to the sharpness of these peaks and aliasing of the signal it is likely that the increase in current may be greater still.

The current recorded directly above these defect points is consistently far greater than that measured elsewhere. As discussed above, the diagram in figure 5.15 shows a possible lattice configuration for these defects, where the non-uniform structure and strain distribution leads to an enhanced conductivity at the defect location. The F-K termination points that have been examined more closely have appeared to have two or three highly conductive sections to them, as seen in figure 5.17. However, this is most likely due to the shape of the tip apex, since in figures where several defects are imaged each defect appears identical to each other, see figure 5.17a and the insets of c).

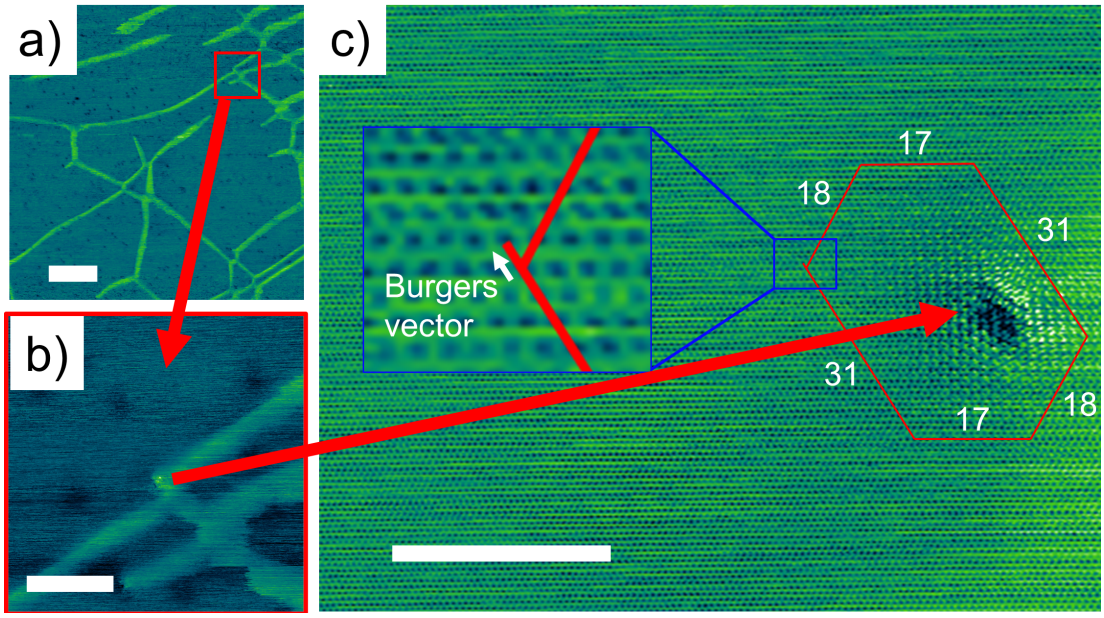


FIGURE 5.18: a) CAFM current image of a lattice matched region of graphene on hBN. b) a CAFM current image of the region bounded by the red square in a). The defect at the centre of the image is shown in c) with lattice resolution. The red lines in c) follow an equal number of steps, indicated by the numbers, along the graphene lattice in opposite direction, encompasing the defect within - known as a Burgers circuit. The inset shows a zoomed image of the start and end points, with the difference indicated by the Burgers vector. The scalebars measure 200 nm in a), 50 nm in b), and 10 nm in c). The colourbar measures 1.18 to 1.64 μA in a), 1.8 to 2.5 μA in b), and 0.7 to 2.5 μA in c). Images recorded on sample C.

In figure 5.18 an F-K termination point within an extended moiré pattern has been imaged with high resolution. Figure 5.18 shows three CAFM images of the graphene surface recorded on sample C. Image c) shows the area around the defect highlighted by b) with lattice resolution, and b), in turn, shows the area marked by the red square

in a). The inset in c) shows a zoom in on the start and end points of the Burgers circuit that was carried out around the termination point, with the Burgers vector indicated. This has been achieved by counting the same amount of lattice points in the positive and negative directions of each crystallographic direction in a path that encircles the defect. The number of steps taken along each of the crystallographic directions are indicated on the image in figure 5.18c. The resulting Burgers vector indicates that there is a source of an additional row within the loop, i.e. a defect is present and enclosed within the path as expected for the configuration shown in figure 5.15. This observation provides direct confirmation that the sources of network lines correspond to the introduction of an additional row of carbon atoms, further suggesting the F-K defect line structure. In addition, the lattice orientation with respect to the Burgers vector matches that of the diagram in figure 5.15.

As previously mentioned, in the discussion of the conductive AFM results shown in figure 5.18c the atomic scale defect has a large influence on the local current. In addition to this, in the images of defects with an enhanced magnification in figure 5.19 a secondary hexagonal pattern can be observed to be superimposed onto that of the graphene lattice. This can be faintly observed in the images shown in figure 5.19b and e), whereas the corresponding topographical channel images, or lateral force images, of these regions do not exhibit this behaviour.

The defects shown in figure 5.19 are those shown in figure 5.18 for lattice matched material, in panels a-c) of figure 5.19, and the lower defect in figure 5.17b for unstrained material (in d-f)). Figures 5.19 c) and f) show the reciprocal-space 2DFFT maps of the images given by a) and d) respectively. These figures help to distinguish the different hexagonal patterns buried in the CAFM images, with bright spots indicating the reciprocal lattice points of both structures. From these the reciprocal lattice vectors can be determined, and are indicated on figures c) and f) by the red and white arrows, corresponding to the lattice and secondary patterns respectively. The directions of these patterns have been converted into real-space and are indicated in figures a) and d) for the lattice directions, and b) and e) for the secondary patterns.

The secondary hexagonal pattern has been identified as the result of quasiparticle scattering of the graphene charge carriers, similar to those seen by *Rutter et. al.*on epitaxial graphene grown on silicon carbide (0001) [129]. These interference patterns occur in electronic imaging due to quasiparticle scattering resulting from the symmetry of the graphene Bloch states. As described by *Rutter et. al.*[129], the scattering pattern seen in the reciprocal-space images corresponds to a pattern that is expected to be $1/\sqrt{3}$ times that of the lattice in reciprocal-space, and rotated by 30°. This means that the real space pattern is $\sqrt{3}$ times larger than the graphene lattice, while also at a 30° rotation (i.e. $(\sqrt{3}\text{x}\sqrt{3})\text{R}30°$).

From the measurements shown in figure 5.19c the ratio of reciprocal lattice length

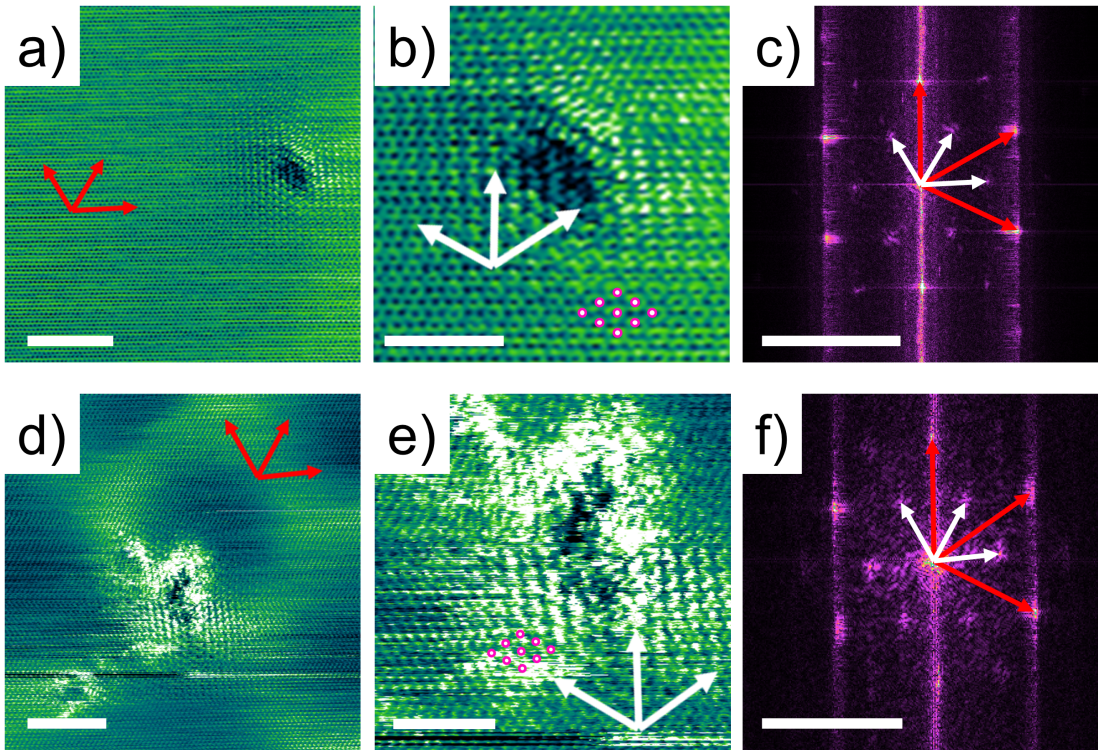


FIGURE 5.19: a) and b) show CAFM images of the same defect as imaged in figure 5.18 for lattice matched material with two different magnifications. Image c) shows the reciprocal-space map of a 2DFFT of a). The red arrows in this figure represent the reciprocal lattice vectors, with the white arrows representing the reciprocal lattice vectors of the $(\sqrt{3}x\sqrt{3})R30°$ scattering pattern. The directions of these arrows have been transformed into real-space directions, and are shown in panels a) and b) indicating the lattice and scattering pattern directions on these figures respectively. The pink dots in b) and e) highlight the scattering pattern in real-space. Figures d), e), and f) show analogous images for a separate defect on unstrained material, shown in a larger scale image in figure 5.17b (the lower of the two defects in this image) where a moiré pattern of 13 nm has been measured. The scalebars measure 5 nm in a) and d), 2.5 nm in b) and e), and 5 nm^{-1} in c) and f). The colourbars range from 0.7 to 2.5 μA in a) and b), and 135 to 250 nA in d) and e). All images recorded on sample C.

to reciprocal scattering pattern length is 1.70 ± 0.04 which is in agreement with the expected value of $\sqrt{3}$ (1.73), within error bounds, and is at an angle of $29.7 \pm 2.0°$, close to the expected value of 30°. In an analogous way, for the defect shown in figure 5.19d-f), the measured ratio of reciprocal lattice length to reciprocal scattering pattern length is 1.78 ± 0.04 which is close to the expected value, although it is outside of the corresponding error bounds, and is at an angle of $29.6 \pm 2.0°$. The small discrepancy in this ratio is most likely due to the large amount of non uniform strain at the locations of these images. These results are highly suggestive that the additional hexagonal structure seen near to the atomic defects in CAFM is indeed a $(\sqrt{3}x\sqrt{3})R30°$ quasiparticle

scattering pattern [129].

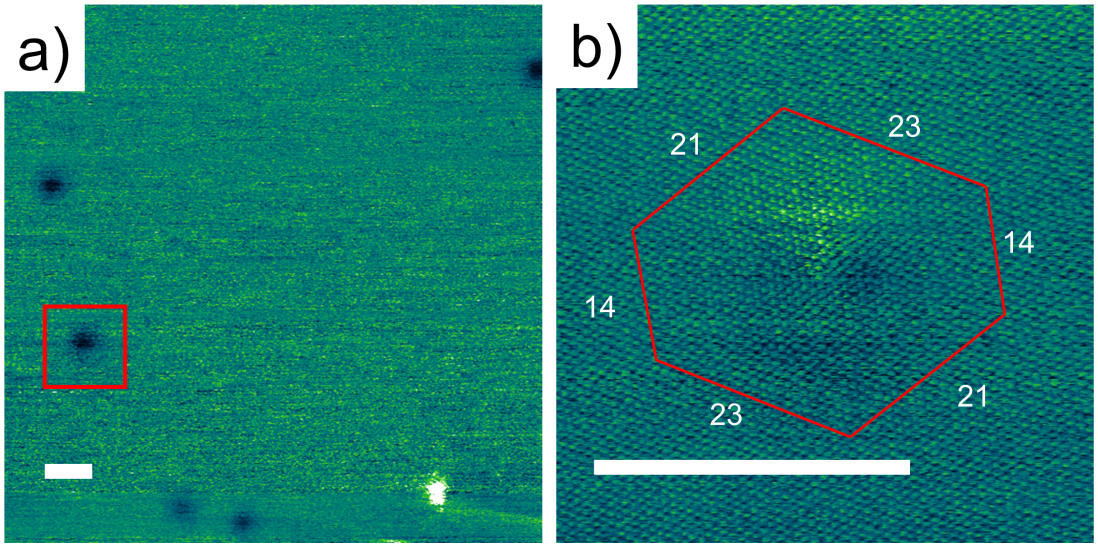


FIGURE 5.20: Two CAFM images recorded on lattice matched graphene on hBN on sample C of a defect positioned on top of the lattice matched region. An F-K termination defect can be seen in the lower right side of a). In the lattice resolution image shown in b) an equal number of steps, indicated by the numbers, have been taken along opposite lattice directions to encompass the defect. The start and end points exist on the same lattice point. The scalebars in a) and b) are both 10 nm. The current scale ranges from 34 to 238 nA in a), and 15 to 120 nA in b).

Many of the previous figures showing the diverging moiré patterns also show a different type of defect in the background regions where the lattice is matched. These can be seen in figures 5.9b, 5.10b-d), 5.16d, and 5.18a-b) where they appear as faint dark spots suppressing current within the lattice matched regions. Figure 5.20 shows a CAFM image of one of these defects, with b) showing the region highlighted by the red square in a). In figure 5.20a an F-K line termination defect can also be seen as a bright, highly conducting spot in the lower right. In figure 5.20b, the defect indicated by the red box in a) can be seen with lattice resolution. In this image the defect appears to consist of an area that is more conducting (top), and an area that is less conducting (bottom) appearing next to each other. As carried out in figure 5.18c for the F-K termination defects, a Burgers path encompassing the defect shown in figure 5.20b has been carried out. The start and end points of this path coincide, indicating no lattice defect is enclosed. As a result, it is suggested that these defects are Stone-Wales defects. This type of defect, illustrated in figure 5.21, in graphene consists of a reconstructed lattice where the bond angles between the carbon atoms are altered. This results in the lattice forming two (or more) distorted pentagons and heptagons that only disrupt the lattice

locally. In this case all of the carbon atoms still have three bonds to neighbouring carbon atoms. Furthermore, these defects would also have areas where the carbon atoms are more concentrated (green pentagons in figure 5.21), and an area of lower concentration of carbon atoms (red heptagons in figure 5.21). This would be consistent with the observations that have been made using CAFM of a conduction variation at these locations, and the observation of no Burgers vector. However, the resolution of figure 5.20b is not quite of high enough quality to confirm this with certainty.

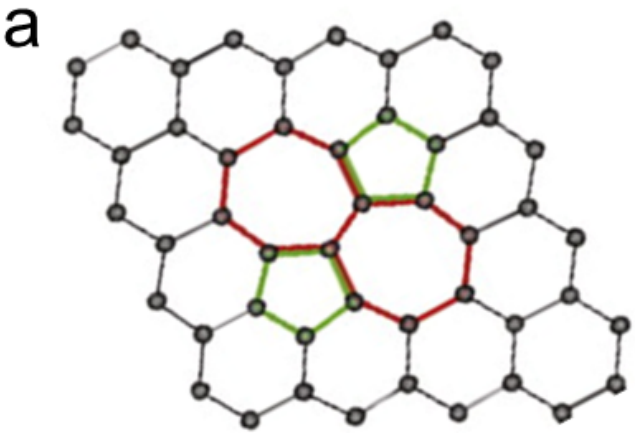


FIGURE 5.21: a) The Stone-Wales defect on a graphene lattice. The graphene surface has reconstructed to form two pentagons (green) and two heptagons (red) Image from Liu et al [130].

5.6 Summary

The use of ambient AFM techniques to determine a wide range of properties of MBE graphene grown on exfoliated hBN flakes has been described in this chapter. These properties have primarily been determined through the observation of the graphene/hBN superlattice moiré pattern to examine structural properties of the interface, with a particular focus on material strain.

Utilising the processing methods developed in chapter 4 the CAFM technique has proven to be a very useful tool in investigating these graphene samples. CAFM has allowed for measurements of varying current across samples, and has provided routine lattice resolution imaging with relative ease under ambient conditions, allowing for useful insight into the structure of the novel graphene samples investigated here. In particular imaging and identification of lattice defects, Frenkel-Kontorova identification, and providing evidence of the *Woods et. al.* [46] model, as well as observation of a varying density of states over highly strained and lattice matched regions.

Furthermore, the information acquired throughout has been used to influence the growth of the graphene samples. For example the observation of samples exhibiting greater strain at higher substrate growth temperatures has allowed for more highly strained samples to be produced, and with larger lattice matched regions such as in the case of figure 5.14, along with the addition of the observation that the carbon aggregate deposits act to pin the graphene, aiding strain and initiating growth.

In many of the images recorded using CAFM imaging the observation of a moiré pattern that has been seen to differ from the traditional hexagonal cell with a gradual boundary, to one with far sharper and sudden boundary have been recorded. This can be seen in figure 5.3a, and in the sharpness of the boundary seen in the comparison of the AC mode topographic profile and the current profile in figures 5.2b and c). As a result of this observation, a thorough investigation into the cause of this effect, due to the interaction between the tip and the sample, is explored in chapter 6.

Chapter 6

Tip-Induced Moiré Deformation

6.1 Introduction

The regular hexagonal moiré patterns resembling those of the basic model with gradual cell boundaries, described in section 2.3.1 figure 2.6, have been observed while imaging in AC mode AFM, for example in figures 5.1 in section 5.2 and figure 5.4 in section 5.3. However, these boundaries do not always have this appearance while imaging the heterostructure surface. Instead the superlattice cell boundaries have been seen to be sharper, with a far more sudden transition over the F-K line, as previously shown in figure 5.3a in section 5.2. Notably this has occurred more often while using CAFM. This moiré cell boundary narrowing can be seen by the profiles in figure 5.2b and c) in section 5.2 comparing a moiré pattern imaged in AC mode with that of one imaged using CAFM. It was also observed that when these sharper moiré boundaries are exhibited there is often an asymmetry in the structure of the moiré cells within the superlattice.

In this chapter the changes to the moiré pattern are presented, and found to be a result of the interaction between the tip and the graphene surface.

6.2 Moiré asymmetries

Figures 6.1a and b) show two instances where there is a large degree of asymmetry in the moiré cell structure. In these current channel CAFM images the conductivity measured increases as the tip is moved along the fast scan direction within the moiré cell, from left to right in these images, before undergoing a sudden drop in current as the tip passes over the moiré cell boundary. By observing both the trace, where the AFM fast scan direction of the tip raster moves from left to right (forward scan), and retrace, where the fast scan direction moves from right to left (reverse scan), channels separately it can be seen that there is a clear difference between the two channels. The

process with which these images are recorded removes the possibility that these differences are due to thermal drift. Trace and retrace images are both measured pseudo-simultaneously. I.e. for each horizontal line the forwards scan data is recorded immediately before the reverse scan data, alternating between the two, before changing the scan line in the slow scan direction.

In the retrace images shown in figure 6.1c and d) the conductivity increases while moving from right to left within each moiré cell, mirroring the behaviour seen in the trace image. These changes can be seen by the differences in the colour gradients between the two images shown in figure 6.1b and d). In addition, these images also show a spatial shift in the position of the abrupt current change at the moiré cell boundaries. These shifts demonstrate apparent movement of these boundaries shown by the change in peak position in the current profiles in e), measured to be 6.0 ± 0.4 nm.

The observation that the changes recorded occur only along the horizontal fast scan direction, along with the pseudo-simultaneous imaging, suggest the observed effect is indeed tip-induced. The asymmetry in the larger scale moiré pattern due to the boundary movement and current variation as a result of the tip interaction has led to a fish scale pattern in figure 6.1, moving away from a symmetrical structure.

6.3 Force-Distance Curves

To investigate the interaction between the tip and the surface material while scanning using both CAFM and contact mode AFM, a series of force measurements have been made on the heterostructure surface. Several tip approaches have been carried out at different heights above the graphene/hBN heterostructure sample surface under ambient conditions using the Cypher AFM instrument in contact mode. During these approaches the cantilever tip is lowered towards the surface by increasing the z-piezo voltage from an initial height far from the surface, where the tip-surface interaction is negligible, and increased until the deflection experienced by the cantilever reaches a specified set point, before being retracted. During this approach/withdrawal the deflection of the cantilever is monitored, and can later be used to calculate the force on the tip.

A selection of the force-distance curves that have been measured can be seen in figure 6.2a, where a series of similar approaches have been recorded for graphene/hBN and SiO_2 over a variety of locations, and displayed as an average. All of the force-distance curves shown in this figure were measured using the same AFM tip for consistency. When results are compared between tips, the force values can be drastically different. This has even been observed for measurements using the same tip when comparing results measured before and after numerous AFM scans. When the tip

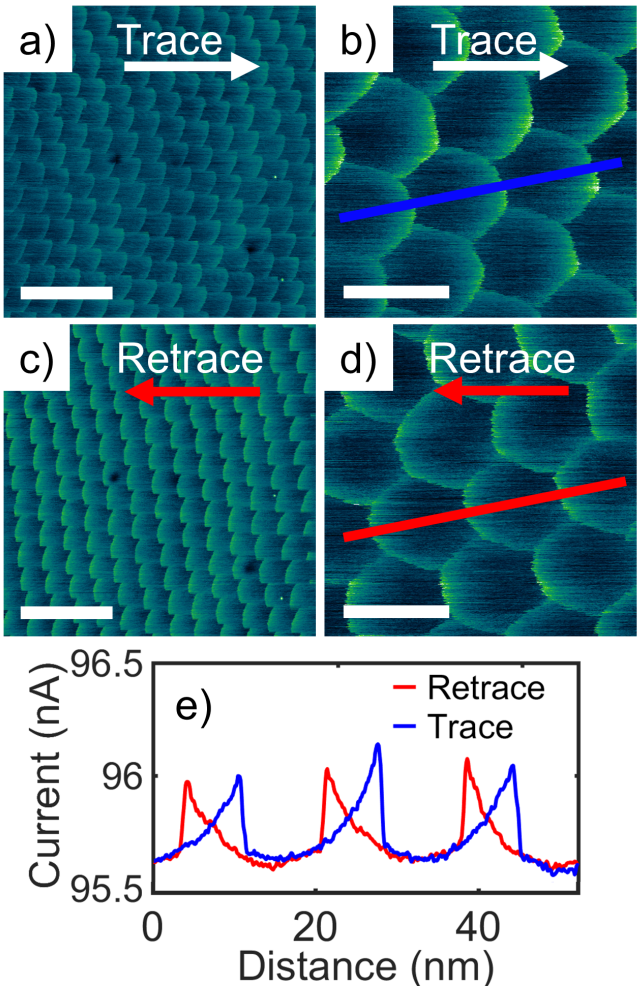


FIGURE 6.1: a) and b) show CAFM current channel images of a graphene/hBN heterostructure demonstrating an asymmetric moiré pattern recorded during the forward/trace scan. c) and d) show the corresponding reverse/retrace scans to a) and b) recorded pseudo-simultaneously. The white and red arrows indicate the fast scan direction of the respective image. The moiré pattern measured in a) and c) is 25 $\pm$ 2 nm, and is 13.8 $\pm$ 0.8 nm in b) and d). e) shows the current profiles measured along the identically positioned blue and red lines shown in b) and d). A trace-retrace shift of 6.0 $\pm$ 0.4 nm is seen. The scalebars measure 100 nm in a) and c), and 20 nm in b) and d). The colourbars range from 140 to 170 nA in a) and c), and 95.4 to 96.4 nA in b) and d), all measured with a sample bias of -0.01 V, and displayed as absolute current.

had been used for many scans prior to force-distance curves the magnitude of the attractive forces measured was much larger, due to the tip having become less sharp from adhesion of contaminants/damaging of the tip occurring during scanning. Figure 6.2a shows primarily the attractive region of the force-distance curve, where the cantilever is deflected towards the surface. In these figures the z-distance has been

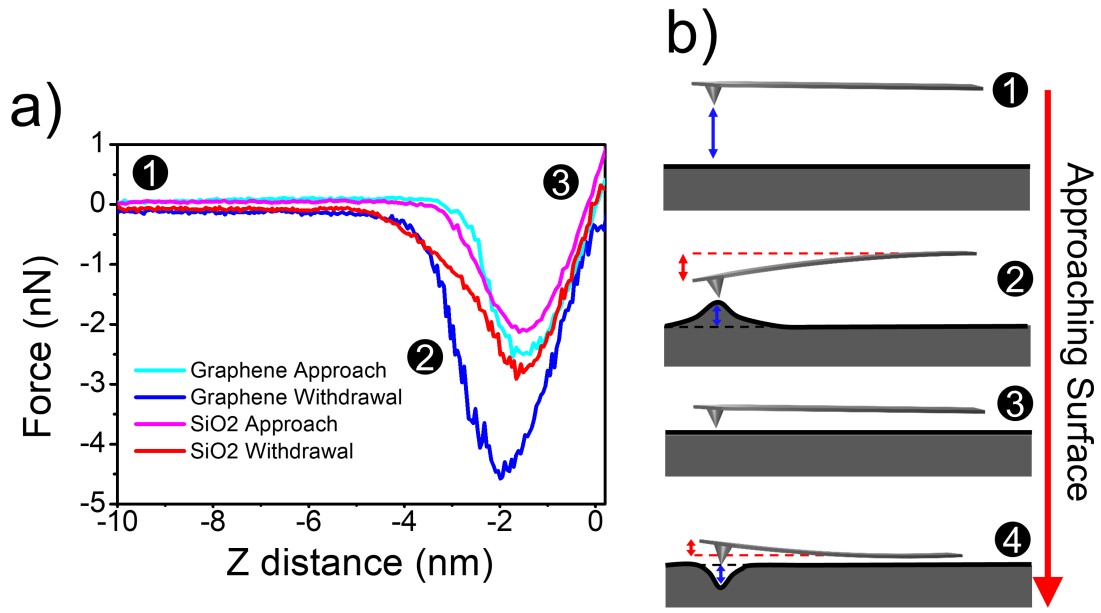


FIGURE 6.2: a) Average force vs. distance curves for approaches/withdrawals over SiO_2 (magenta/red lines) and graphene (cyan/blue lines) surfaces. The SiO_2 data consists of an average of 64 individual curves spread across 4 separate locations. The graphene data is an average of 52 measurements taken over 3 locations. Both sets of data were measured with a single tip to ensure consistency. The labels correspond to the situations shown in b). b) A diagram showing the key stages of approach (1 to 4) and withdrawal (4 to 1) of a cantilever tip to the surface. The blue arrows indicate the tip height from the surface, and the red arrows indicate the tip deflection. The Z distance labelled in a) has been shifted from an arbitrary origin, to that of position 3 in b), where the deflection/force measured is zero and the tip is in contact. A negative z distance indicates movement away from the surface, correspondingly a negative force value indicates cantilever deflection towards the surface and attraction between the tip and the surface.

measured from an arbitrary position, and shifted so that the transition from attractive to repulsive regime (position 3 in figure 6.2b) is set to zero, with a greater negative value indicating movement away from the surface.

The three situations labelled in 6.2a along with an additional indentation for higher applied forces, are demonstrated in b). In situation 1 the tip is far from the surface and remains undeflected. As the tip approaches the surface it experiences an attractive force that acts to bend the cantilever, causing the tip to jump to contact, this attraction can cause deformation of the surface, seen in situation 2. The sudden change in signal associated with jump to contact cannot be seen in figure 6.2a due to an averaging of 64 measurements recorded across 4 locations. When the tip-sample attraction exactly opposes the restoring force of the cantilever the resultant equilibrium yields a deflection of zero, as illustrated in situation 3. As the tip is further lowered, and the applied

force is increased, i.e. the cantilever deflection is increased, surface indentation may occur (provided the surface is deformable), similar to that which is shown in situation 4. As the tip is retracted from the surface the situation follows the diagrams shown in figure 6.2 in reverse order, from situation 4 through to 1.

For both surfaces the tip displays hysteretic force-distance curve behaviour. Upon approach (cyan and magenta for graphene and SiO_2 respectively) the cantilever exhibits a smaller attractive force than the withdrawals (blue and red for graphene and SiO_2 respectively). Upon approach the tip is entering the force gradient imposed by the surface, and due to the attractive forces involved (primarily van der Waals forces) undergoes a relatively sudden snap to contact. Upon retracting, the tip, initially having been pressed into the surface, has an increased contact area and hence the overall attractive tip-surface van der Waals forces (as well as capillary and solvation forces) are greater.

The approach of the tip onto the surface also includes penetration of any hydrocarbon or water interfacial contaminants that are present. This can be considerable under ambient conditions as have been used in these experiments, and as such, through hydrostatic and capilliary interactions, the attractive forces experienced between the tip and the surface are increased. SiO_2 is considered to be a relatively hard surface, and there is expected to be very little difference between the approach and withdrawal forces seen on this material. The differences, as seen by the magenta and red lines in figure 6.2a, are most likely due to a layer of contaminating hydrocarbons and water present on the surface. The approach/withdrawal difference on the graphene surface is far larger than for the SiO_2. Here there may be a nanoindentation of the material (exaggerated in figure 6.2b situation 4), that would cause greater surface contact. If this interaction is sufficient, surface lift off would occur, where the graphene is raised as the tip is retracted, increasing the corresponding interlayer distance between the graphene and the underlying hBN, as observed in reference [78], and shown schematically in figure 6.2b situation 2.

The points at which the deflection signal deviates from and returns to zero occur at different heights from the surface suggesting an increase in attractive force upon withdrawal and possible surface lift off. As seen in figure 6.2a where the withdrawal returns to zero at a distance that is further from the surface (further from the RHS of the graph) than the approach. In all measured force-distance curves, the difference between the approach and withdrawal is far greater for the graphene/hBN samples than the SiO_2 surface. In the case of the SiO_2 the approach and withdrawal follow similar paths, whereas an increase in attractive force ($\sim$1.5 nN in figure 6.2) is observed during withdrawal for graphene on hBN. These strong adhesive forces suggest a deformation of the surface by the tip while operating the atomic force microscope using contact mode scanning.

6.3.1 Force investigations

To investigate the effect of applied normal force on the imaging of the graphene/hBN interface and the corresponding moiré pattern several series of images were recorded using identical parameters, while changing the applied normal force between scans. The negative force regime in this section indicates that there is an attractive force between the tip and the surface, whereas the positive regime indicates a repulsive force. Figure 6.3a shows a moiré pattern with a wavelength of 17.3 $\pm$ 0.5 nm observed using CAFM with an applied contact mode attractive force of around -20 $\pm$ 20 nN. The large error bounds on this value arises from observed drift in the free air deflection that was seen during these measurements. In panel a) of figure 6.3, corresponding to this value, the image was measured in the attractive regime. The tip was engaged and then retracted to a negative set point before scanning. In this case the moiré pattern appears with smooth transitions between cells, resembling those seen when imaging with AC mode AFM, with less abrupt boundaries than the other images in figure 6.3. For each additional image in the row in figure 6.3a-d), the deflection set point, i.e. the applied normal force, was increased as indicated, with each image showing a separate CAFM current scan of the same region, with a low amount of thermal drift appearing between scans. As the force applied to the surface by the tip is increased the moiré pattern begins to become more distorted. Additionally, with an increased force the magnitude of the current recorded increases from around 300 nA in a) to 800 nA in d). This is consistent with a reduced contact resistance for the tip due to a decreased distance between the tip and surface as the contaminant layer acting as a tunneling barrier is penetrated further, and an increased contact area due to any potential nanoindentation. However, with a larger measured current there is also a large decrease in moiré contrast - with the pattern barely visible at an applied force of 80 $\pm$ 20 nN.

The increasing distortion of the moiré pattern occurs as the amount of force applied to the tip is increased in a similar way to that observed for STM by *Yankowitz et al* [78]. In their paper the graphene/hBN moiré pattern of exfoliated material was modified by applying pressure through an STM tip, however trace-retrace differences (shown in their supplementary information) were not observed to be as extreme as have been seen in this work. In the same way as the measurements seen here for AFM imaging on MBE grown heterostructures, *Yankowitz et al* found the centre of the moiré superlattice becomes expanded, with the edges of the hexagonal moiré cell becoming narrow boundaries similar to those seen in figure 6.3b (and shown previously in figure 6.1). As the applied force becomes greater still, the hexagonal shape of the superlattice becomes distorted (figure 6.3c) until the boundary lines which are not perpendicular to the fast scan direction disappear entirely (figure 6.3d). These results clearly show a strong effect on the heterostructure superlattice as a result of the imposed normal

force.

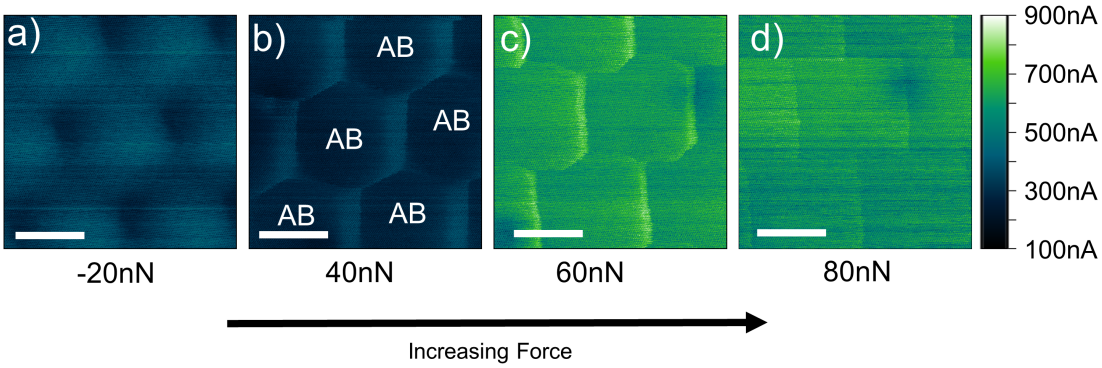


FIGURE 6.3: a-d) show trace CAFM current images of the graphene/hBN heterostructure. The applied normal force is increased from a) to d), with the applied forces indicated with a large error of ± 20 nN due to laser spot drift. As the tip is pressed further into the sample the observed moiré pattern changes and deforms. Sample bias used was -50 mV. The colourbar ranges from -100 nA to -900 nA. The scalebars measure 10 nm in each image. The AB stacked regions are highlighted in b). The imaging order followed b), c), d), a).

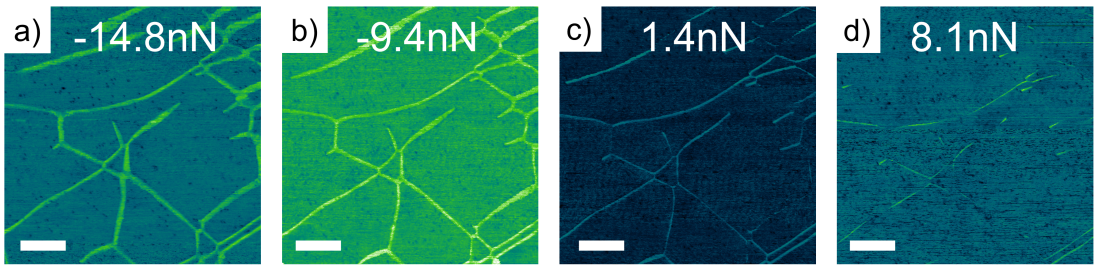


FIGURE 6.4: a-d) all show CAFM current images of the same location on a lattice matched graphene/hBN region. The normal force applied by the tip is indicated in each figure and increases from left to right, the errors on these force values are ± 5 nN (less than the uncertainty in figure 6.3, and determined through the optical lever sensitivity calibration). With a greater normal force the F-K defect lines become thinner, disappearing at higher forces. The scalebars in all images measure 200 nm, and the colourbars all range from 1.64 to 1.18 μA. The imaging order followed a), d), c), b).

Figure 6.4 shows a separate set of varying force measurements taken for a lattice matched graphene-hBN moiré pattern. The corresponding force values are indicated in the figures. In a similar way to the lower strained material seen in figure 6.3 these images show that the moiré lines appear wider at a lower repulsive force, and for the attractive regime. However, with an increased repulsive force the lines appear narrower before significantly reducing in size to the point where they are barely visible, as seen in figure 6.4d. To ensure these effects were not the result of tip degradation

the images seen in both figure 6.3 and 6.4 were not recorded in increasing force order, with the true order indicated in the figure captions.

6.4 Heterostructure Stacking Configurations

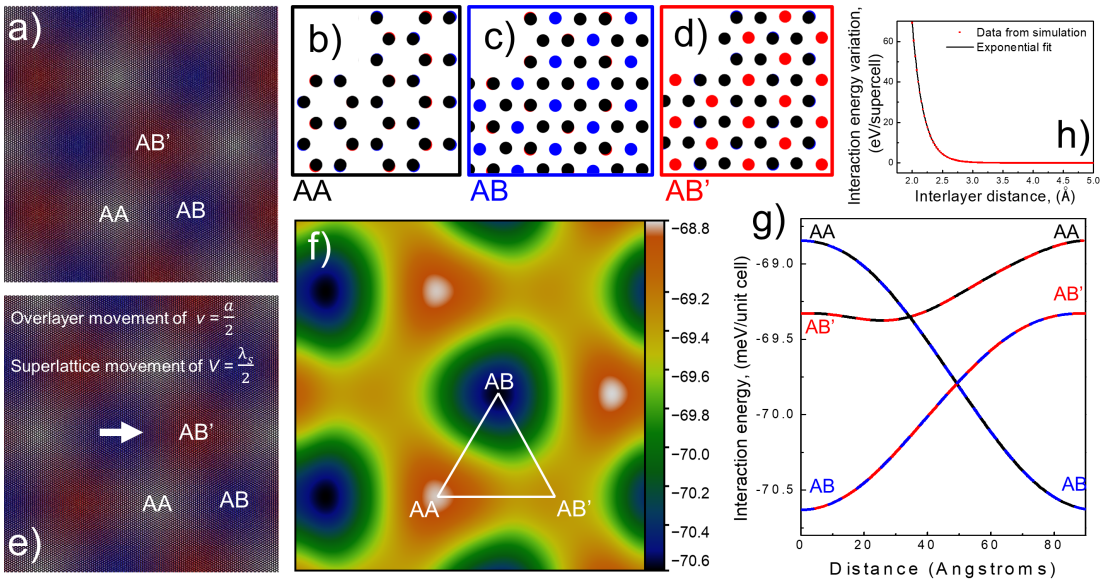


FIGURE 6.5: a) and e) show two overlaid uniform hexagonal lattices with a 1.8% mismatch resulting in a hexagonal moiré superlattice. The overlayer represents graphene with black circles indicating the position of carbon atoms, and the underlayer represents hBN, with blue and red circles indicating the nitrogen and boron atoms respectively. In e) the overlayer lattice has been moved by a/2 along the x-axis, leading to a superlattice movement of $\lambda_S/2$. The three high symmetry stacking configurations are labelled in a) and e), with zooms of these regions given in b-d). For the AA region the carbon atoms sit directly above the boron and nitrogen atoms. For the AB (AB') region the carbon atoms are positioned above a boron (nitrogen) atom, with a nitrogen (boron) atom at the centre of each cell. Panel f) shows the interaction energy per graphene unit cell calculated using the Morse potential model described in the text. Panel g) shows profiles measured along the lines in f), showing the AA to AB, AB to AB', and AB' to AA pathways. The AB region is far more favourable than the AA or AB' regions, with a larger interaction energy magnitude. Figure h) plots the interaction energy variation (the difference between the AA and AB regions) against interlayer distance, indicating an exponential relationship of increased variation at decreased graphene-hBN separation.

The expansion of the moiré centre while scanning with a large applied force can be explained by considering the van der Waals adhesion potential between the graphene and hBN layers. The moiré superlattice formed by a graphene/hBN heterostructure consists of three high symmetry stacking configurations. These are labelled in the

diagram shown in figure 6.5a where a moiré pattern formed using black dots to represent the carbon atoms, and blue and red dots indicating the nitrogen and boron atoms respectively of an underlying crystal structure is shown. The resulting moiré superstructure can be seen with a hexagonal structure consisting of regions of high symmetry appearing as circular areas shaded blue, red, and white due to the local stacking order. These three configurations are illustrated in figure 6.5b, c), and d), with their locations indicated in figure 6.5a and e). Figures 6.5b-d) are all zoomed images of the labelled regions of the diagram in a). These stacking configurations include AA, where the graphene lattice sits on top of the hBN, AB where a C atom sits on top of a B atom and a N atom sits in the centre of each carbon hexagonal cell, and AB' where a C atom resides above a N atom, with the B atom in the centre.

Each of the three high symmetry stacking configurations mentioned above have different interaction energies. Panels f) and g) of figure 6.5 show the interaction energies calculated between a rigid graphene and hBN lattice calculated using the Morse potential,

$$V(r) = D_e(e^{-2\alpha(r-r_e)} - 2e^{-\alpha(r-r_e)}) \tag{6.1}$$

Where D_e is the equilibrium potential at the interlayer distance r_e (set to a value of 3.85 Å for figure 6.5f, g), and h)) and α sets the width of the potential. The values for the carbon-boron and the carbon-nitrogen interactions were taken from those used by *G. Argentero et al*, determined through their DFT calculations; D_{CB} = 2.9 meV, α_{CB} = 2.08 Å^{-1}, r_{CB} = 3.86 Å for the carbon-boron interactions and D_{CN} = 8.3 meV, α_{CN} = 2.54 Å^{-1}, r_{CN} = 3.84 Å for the carbon-nitrogen interactions [56].

Figure 6.5f, shows a spatial colourmap of the heterostructure moiré pattern, with the colourbar representing the interaction energy between the graphene and hBN. There is a spatial modulation in this adhesion potential with a wavelength matching that of the moiré pattern. This can be seen by the colourmap variation, where the lowest interaction energy is located at the AB positions, indicating a larger attractive force between the graphene and hBN, and the highest interaction energy, indicating a smaller attractive force, located at the AA locations.

The profiles shown in figure 6.5g have been measured along the white lines in f), joining the three high symmetry positions. The interaction energy at the AA and the AB' regions are relatively similar, with that of the AB (carbon over boron) stacking configuration having a far greater adhesion potential, suggesting a favourability of the AB configuration.

For the values that are plotted in panels f) and g) of figure 6.5 an interlayer distance of 3.85 Å has been used resulting in a variation of ∼1.75 meV/unit cell between the AA and AB positions. When the interlayer spacing is reduced the modulation of the

interaction energy increases exponentially. This can be seen in figure 6.5h which plots this difference between the AA and AB interaction energies as a function of interlayer spacing.

The results in figure 6.5 imply that as the AFM tip is pressed down on the graphene overlayer, and the interlayer distance is locally perturbed away from equilibrium, the spatial adhesion modulation is enhanced. In other words, when the normal force applied by the AFM tip on the graphene is increased, and the graphene is pushed closer to the hBN, the AB stacking configuration becomes far more favourable than both the AA and AB' configurations. As a result, the graphene lattice underneath the tip will expand in order to favour the AB stacking configuration, leading to the distortion seen in figure 6.3 where the moiré cell centres appear larger as they are imaged. This implies that the centres of the moiré cells are more strained, and that the strain relief occurs at the cell boundaries, in the form of the F-K defect lines described earlier.

6.5 Strain Maps

In order to test the hypothesis of the moiré cell centres being more strained than at the cell edges/boundaries, analysis of lattice resolution CAFM images has been carried out. Figure 6.6a shows a CAFM image of a graphene/hBN heterostructure with a moiré wavelength of 16.2 $\pm$ 0.5 nm indicating a relatively low amount of overall strain. When magnified, this image displays clear lattice resolution as shown in panel b), and as such was chosen to be used to calculate a strain image. For each point of the 512 x 512 pixel image shown in figure 6.6a) within the red square a 60 x 60 pixel (3.99 x 3.99 nm, matching the size of panel b)) region underwent a 2D fast Fourier transform, where the lattice constants were found computationally, and the average of all lattice directions was saved. These values are plotted in figure 6.6c in units of the unstrained lattice constant a_G = 0.246 nm.

Values for the lattice constants were recorded in the range of 0.236 $\pm$ 0.006 nm to 0.266 $\pm$ 0.009 nm (corresponding to 0.96 $\pm$ 0.02 a_G and 1.08 $\pm$ 0.04 a_G) indicating a varying strain across the surface. The spatial variation of the measured lattice constant can be seen in c) to have regions with lower strain located at the moiré cell edges, and higher strain at the centres. The structure of the strain map image closely resembles that of the moiré pattern seen in a). At the edges of the moiré cell the lattice constant was measured to be approximately 0.242 $\pm$ 0.006 nm (corresponding to 0.98 $\pm$ 0.02 a_G, and close to unstrained graphene), whereas at the centre this value was approximately 0.252 $\pm$ 0.009 nm (1.02 $\pm$ 0.04 a_G, close to the hBN lattice constant of 0.250 nm). The average value of all lattice length measurements calculated for the strain map shown in c) is 0.249 $\pm$ 0.024 nm (1.01 $\pm$ 0.03 a_G). According to the discussion in chapter 2

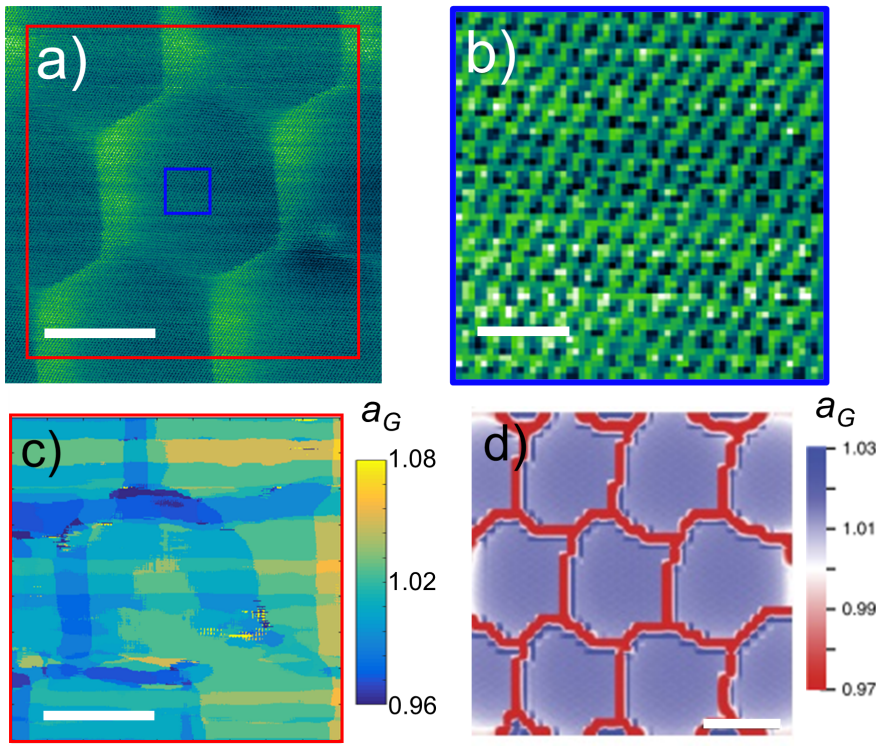


FIGURE 6.6: a) a high resolution CAFM current image of a graphene/hBN moiré pattern with a wavelength of 16.2 ± 0.5 nm. The image shown in panel b) shows a zoom of the 60 x 60 pixel region indicated by the blue box in a). c) shows a strain map calculated from the figure in a), and showing the region bounded by the red box. For each pixel within this box a 60 x 60 pixel (3.99 x 3.99 nm) square undergoes a 2DFFT, with the lattice constants found and averaged at that location. These are then plotted in c) in units of a_G = 0.246 nm. The figure indicates lower levels of strain at the edges of the moiré cell. d) shows a simulated strain map for an STM graphene/hBN moiré pattern, imaged with a large applied pressure by the STM tip, taken from *Yankowitz et al* [78], that shows similar varying strain with higher strain levels at the centre of moiré cells. The scalebars in panels a), c) and d) measure 10 nm, while the scalebar in b) measures 1 nm. The current scale in a) ranges from 100 to 500 nA, and in b) ranges from 173 nA to 338 nA.

section 2.3.2, and equation 2.39 therein, for the recorded moiré wavelength of 16.2 ± 0.5 nm an average lattice constant increase of only 0.1% is expected. This value lies within the recorded increase in the average of 1 ± 3%, however it has significant associated error bounds.

The strain relief of the graphene surface is expected to be contained within the F-K defect lines that, in panel a) of figure 6.6, appear as sharp cell boundaries. Because of this concentrated strain relief, the calculation of the strain values shown in panel c), using 60 x 60 pixel images, is most likely skewed towards displaying a greater average strain. Furthermore, it is also due to this method that the moiré boundaries

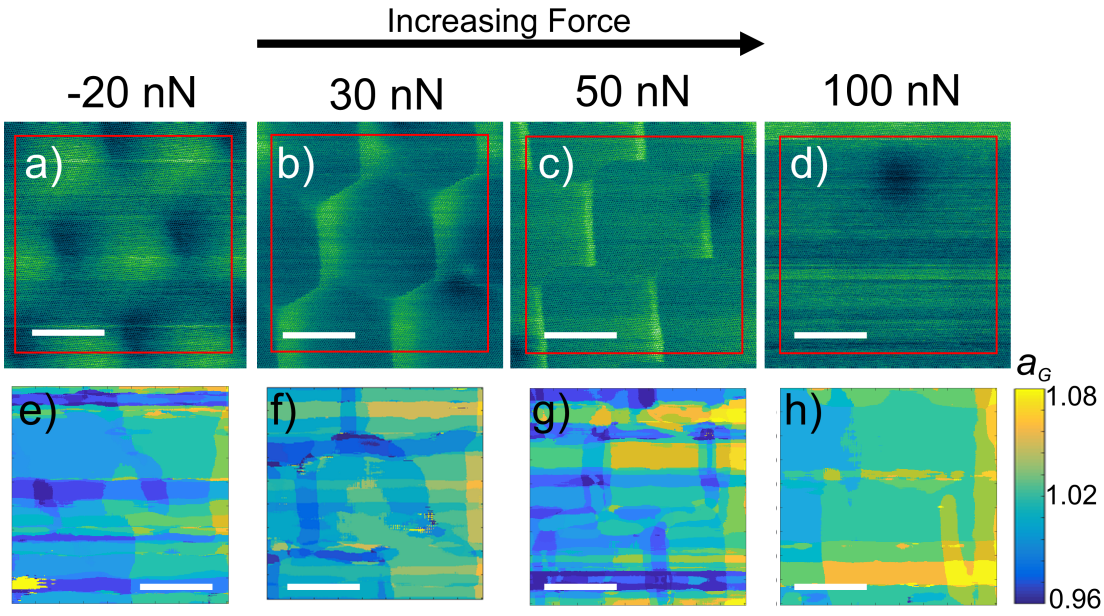


FIGURE 6.7: Panels a-d) show additional CAFM images with increasing applied normal force of the set of images shown in figure 6.3. Panels e-f) show strain maps calculated from the corresponding CAFM image positioned above it in panels a-d). These strain maps were calculated as described earlier. Panels b) and f) are the same images as panels a) and c) in figure 6.6, with the colourbars of the other strain maps in this figure set to match. There is a large error on the indicated force values of $\pm$ 20 nN due to laser spot drift recorded in the free air deflection. The scalebars in all images are 10 nm. The current scales in panels a-d) are 80-450 nA, 100-500 nA, 200-820 nA, and 170-730 nA respectively. The order in which these images were recorded was b), c), d), a).

appear wider in the strain map in panel c) than in the CAFM image in a), and that horizontal scars occurring in the AFM scan have resulted in wide streaks across the strain map. These results share similar features with the simulated strain map shown in figure 6.6d, taken from reference [78] where the strain map represents an imaged graphene/hBN heterostructure surface using STM, and provide strong evidence of varying strain that, due to the presence of the AFM tip, becomes closer to a commensurate state at the cell centres, i.e. having a graphene lattice constant closer to matching the size of the hBN lattice (of $\sim 1.018\ a_G$).

Figure 6.7a-d) show four CAFM images recorded at different applied normal force values, and were recorded as part of the set shown in figure 6.3. The panel shown in figure 6.7b is the same image as shown in figure 6.6a, with the strain map calculated and shown in figure 6.6c also shown here in panel f). In figure 6.7e-h) additional strain maps calculated from the CAFM images positioned directly above (in panels a-d)) are also shown, with the same colourbar scale. Similar horizontal scars can be seen in these images as in figure 6.6c. The moiré pattern in c) is clearly present in the

strain map in panel g), and similarly shows a decrease in the lattice constant at the moiré cell boundary. For the lower normal force (of -20 nN) in panel e) there appears to be an overall decrease in the lattice constant, with less sudden spatial variation present. In contrast, in panel h) for a greater applied normal force (100 nN) the overall lattice constant appears to have increased, and again a less sudden spatial variation is observed in comparison to panels f) and g), that seems to match the moiré pattern disappearance in the corresponding CAFM images. The average recorded graphene lattice constant was 0.248 $\pm$ 0.006 nm, 0.249 $\pm$ 0.005 nm, 0.249 $\pm$ 0.007 nm, and 0.253 $\pm$ 0.005 nm for the strainmaps shown in panels e-h) respectively. The general trend suggests that the average lattice constant, and hence overall amount of lateral strain, is increased as the amount of force applied by the AFM tip acting normal to the surface is increased.

6.6 Trace-Retrace Differences

While observing the effect of contact mode AFM scanning on the graphene/hBN heterostructure moiré pattern it was noticed that as the normal force is increased further, the moiré lines are dragged across the surface by the tip. This can be seen by the significant differences in the images produced in the trace (forward scan) and retrace (reverse scan) directions. The two contrasting styles of imaging vary only in the direction of the fast scan motion of the AFM tip raster scan. The changes in the moiré pattern between the trace and retrace images that have been observed consist of a movement of the entire superlattice pattern along the direction of the raster fast scan direction (horizontal direction in the images shown). Furthermore, as mentioned in section 6.2 the two channels are recorded pseudo-simultaneously, with a forward (typically left-to-right) scan line followed by a backward (right-to-left) scan line, before the tip moves up a line in the slow scan direction. This helps to confirm that the trace-retrace differences that have been seen are not a result of sample drift.

The differences that have been observed have occurred in all imaging channels including topographic, current, and lateral force imaging channels. Figure 6.8a shows a forward scan lateral force microscopy channel image of a graphene/hBN moiré pattern with a superlattice wavelength of 16.7 $\pm$ 0.2 nm. The corresponding retrace scan LFM image of this region is shown in b), stacked vertically to aid the observation of the moiré shift that has been observed to occur along the fast scan (horizontal) direction. The corresponding current channel trace image recorded simultaneously with a) is shown in c). The blue and red arrows in these images indicate both the fast scan tip movement direction, and the overall movement of the moiré superlattice. The LFM measurements show a clear graphene/hBN hexagonal moiré pattern, with a shape and periodicity matching those seen in the current channel images.

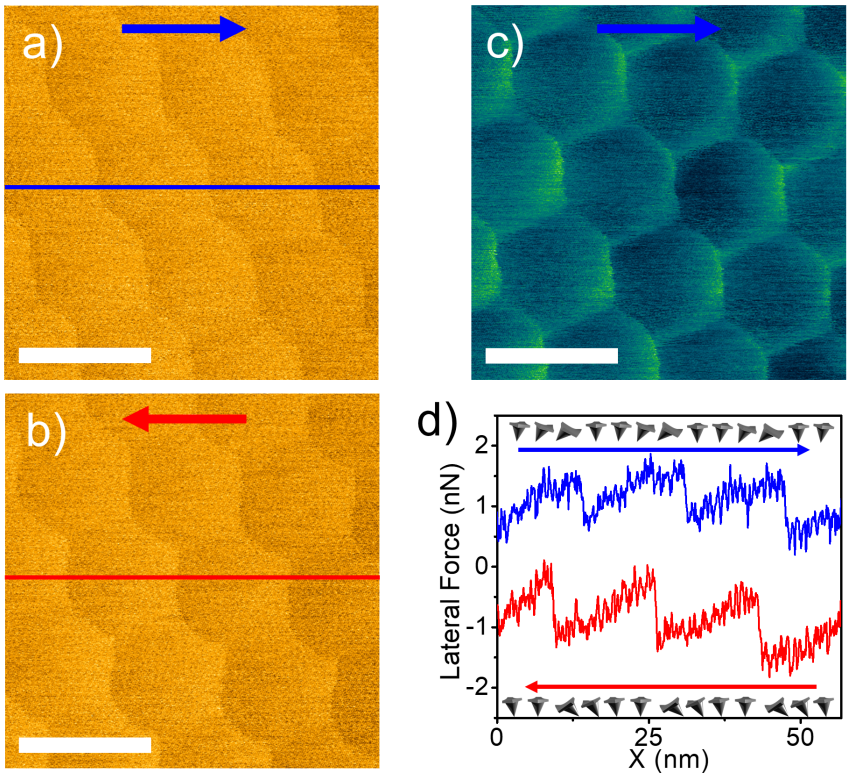


FIGURE 6.8: a) and b) (left hand side images) show two LFM images recorded pseudo-simultaneously of a graphene/hBN moiré pattern with a wavelength of 16.7 $\pm$ 0.2 nm. The upper image, a) is recorded during the forward scan (trace), with b) recorded during the reverse scan (retrace), as indicated by the blue and red arrows showing the fast scan tip movement direction. These images are stacked vertically to aid observation of the shift between the images. The corresponding CAFM current image is shown in c). d) shows the lateral force profiles recorded along the blue and red lines in a) and b). The lateral force experienced opposes the tip movement direction (with a positive direction defined along the fast scan axis and increasing from right to left) leading to a change in signal sign between trace and retrace. The inset arrows and cantilever illustrations indicate the twisting and movement of the cantilever, as indicated by the recorded LFM signal, that has been converted into a force through LFM calibration. The scalebars in a-c) are all 20 nm, the normal force applied for this image was 74 $\pm$ 8 nN, and the current scale in c) measures 590 to 900 nA.

In lateral force microscopy the recorded signal is due to the twisting of the AFM cantilever measured in contact mode, with the deflection due to flexural bending (an indication of the normal force experienced) used as the set point. To maximise the LFM signal, results were taken with a fast scan angle perpendicular to the length of the cantilever. The data in figure 6.8a and b) have been scaled separately due to a large LFM signal displacement as a result of the movement direction, and hence cantilever twisting, being in an opposite direction.

The differences between figure 6.8a and b) can be seen in the profiles provided in d) recorded along identical trajectories in a) and b), and indicated by the blue and red lines, with the inset illustrations in figure d) showing how the AFM cantilever is twisted by the lateral force as the tip experiences the sawtooth signal. Here the sharp drops in the sawtooth lateral signal indicate the AFM tip passing over a moiré cell boundary. The locations of these boundaries are separated by 4.8 ± 0.3 nm in the trace and retrace profiles. The lateral signal in these profiles has been offset so that the average value of the overall friction loop (the name given to the combination of forward and backward LFM profiles) is positioned at zero. In figure 6.8d a positive signal corresponds to a lateral force opposing the trace fast scan direction, with a negative signal corresponding to a lateral force in the opposite direction, opposing the retrace fast scan movement. The profile trace signal (blue) shows a linear increase in lateral force as the tip is moved across the moiré cell. As the tip passes over the moiré boundary, the lateral force undergoes a sudden drop in signal, returning to a baseline value. As the tip is moved from right to left during the retrace scan (red), the magnitude of the experienced force similarly increases across the moiré cell, with approximately the same gradient as the trace profile. This is again followed by a rapid reduction as the tip passes over the FK boundary, giving the retrace profile the same sawtooth behaviour as the trace.

This behaviour has been observed in all cases of contact mode moiré imaging with a large applied normal force. Figure 6.9 shows several additional examples of the trace retrace difference. In figure 6.9 the images in the top row are all trace scan images, while the bottom row are all retrace scan images, recorded pseudo-simultaneously with the image directly above it. In all these images the superlattice boundaries are modified by scanning and are bent and displaced in different ways depending on the scan direction. Figures 6.9a-d) show this movement for a heterostructure with lattice matched regions, with images c) and d) showing the same region as a) and b), recorded with a 90 degrees rotated fast scan direction to demonstrate the modification dependence of the moiré line on the fast scan direction. There is a trace/retrace shift seen between the pairs shown here. The distortion of the F-K defect lines/moiré boundaries are moved only in the direction of the tip movement, regardless of scan angle. The bright, highly conductive moiré termination points in these images are point defects in the graphene lattice. Importantly, there is no noticeable movement of these termination points between the trace and retrace images, indicating that any movement of the lattice itself is very small. If the observed moiré movement is due to a displacement of the lattice, then the atomic displacement of the atoms is being amplified many times in the observed movement of the moiré pattern.

Returning to the simplistic model described earlier, and illustrated in figure 6.5,

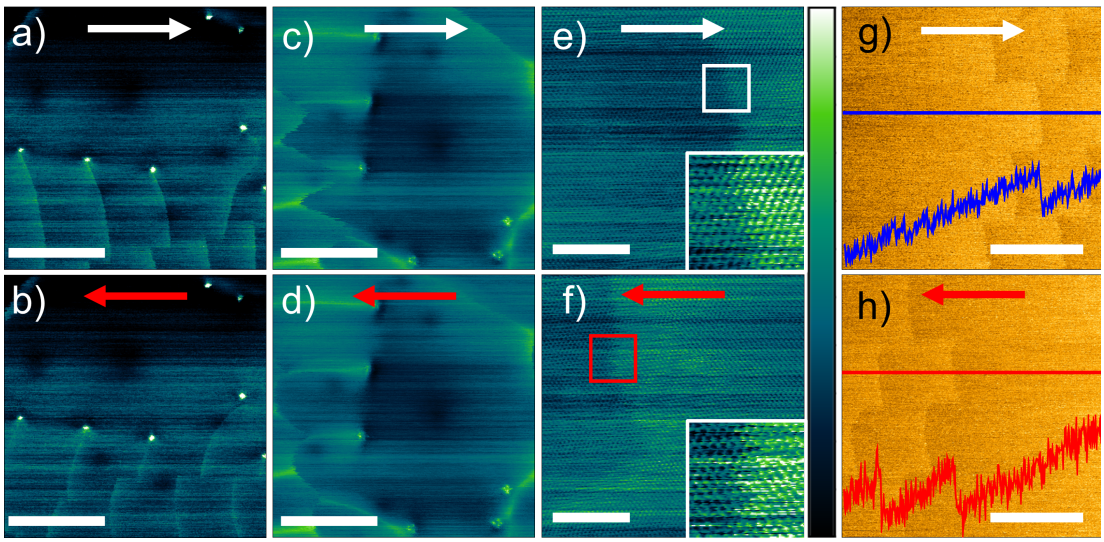


FIGURE 6.9: a), c), and e) show forward scan (trace) conductive maps recorded using CAFM, with the corresponding reverse scan (retrace) images shown in b), d), and f). Images a-d) show a lattice matched sample, with c) and d) displaying the same region as a) and b), measured with a rotated scan angle of 90 degrees. The moiré boundary movement follows the fast scan direction (indicated by the white and red arrows), regardless of scan angle. The sample bias for a-d) was -50 mV. The colourbar scale ranges from black to white as 150 to 550 nA in a) and b), and -300 to -1400 nA in c) and d). Images e) and f) show a moiré boundary shift with lattice resolution, demonstrating the sub-nanometre change at the cell boundary. The insets show the regions within the respective boxes. The main image has a current scale ranging from -1685 nA (black) to -1725 nA (white), with the insets showing a range of -1690 nA to -1710 nA and a bias of -500 mV. Figures g) and h) show trace and retrace LFM lateral signal images respectively. The data has been scaled separately with arbitrary values for clarity, and gives an indication of lateral force experienced by the tip through cantilever twisting. The profiles displayed are taken through the blue and red lines respectively and are an average of 30 scan lines, showing the sawtooth behaviour of the lateral force. The scalebars in a-d) measure 50 nm, in e-f) measure 5 nm, and in g-h) measure 20 nm.

consisting of two perfect hexagonal structures forming a moiré pattern, a large superlattice movement may be explained by a far smaller movement between the two constituent lattices. Considering a global lateral shift in the overlayer vector v, shown in figure 6.5e with a direction indicated by the white arrow, there is a superlattice movement V which is a factor,

$$\kappa = \lambda_0 / a \tag{6.2}$$

larger and along the same direction as v for rotationally aligned samples as demonstrated by the difference between figure 6.5a and e) [131]. This suggests that for an overlayer movement of a single lattice constant, a_G, from the equilibrium position we

would expect to see a trace/retrace difference of $2\lambda_0$ (indicating a movement of a_G in each direction).

As the tip passes over a cell boundary the locally distorted lattice appears to snap back in a discontinuous way, before returning to the AB stacked configuration in the neighbouring cell. This movement has been observed to occur very abruptly, and on a sub-nanometre scale, as shown in the lattice resolution images in figure 6.9e-f).

As shown in section 6.3.1, when the normal force applied to the cantilever is increased, and hence the pressure exerted on the surface by the tip is increased, the central moiré cell regions are seen to expand (e.g. in figure 6.3). In a similar way, the moiré trace/retrace shift is seen to increase with a greater normal force as the boundaries are pushed further. Figure 6.9g and h) shows the result when the applied load is increased by a greater amount. Both images show the same region for trace and retrace LFM images respectively. As can be seen, there are no moiré boundaries visible at the start of the scan line, when the tip moves in either direction. This can again be understood by considering the pushing of the moiré line across the surface. At the start of the scan line the boundary is pushed until the lateral force reaches a maximum, which is dependent on the applied normal load, and the moiré boundary passes under the tip.

The lateral force profiles in figure 6.9 g) and h), measured along the indicated lines, show a similar sawtooth behaviour to that which is shown in figure 6.8, with the exception that the maximum lateral force in this case allows for the moiré shift to exceed that of 1 moiré wavelength ($\sim$14 nm). In this case the lateral signal continues to increase as the tip moves through the first cell, and past the position of the moiré boundary. The lateral force continues to increase until it reaches a maximum, where a single boundary passes under the tip causing a drop in the lateral signal. This can be seen in the trace and retrace profiles where the lateral sawtooth step now falls to a new baseline roughly half of the lateral signal range. Note that the images in figure 6.8 were measured with a different tip to those in figure 6.9g and h), and as such the applied forces cannot be compared quantitatively since the tip apex is likely to be of a different size, resulting in a different applied local pressure for the same measured force. It is important to note that when the applied force is reduced back to a low value, the moiré pattern observed returns to its original form.

6.7 Set Point Ramps

Figure 6.10 investigates the lateral signal in more detail. A series of LFM scan lines were recorded on a graphene/hBN heterostructure displaying a moiré pattern with a wavelength of 17.3 $\pm$ 0.2 nm. For these scan lines, recorded along the same trajectory, both trace and retrace were recorded, with the additional overscan region, the section

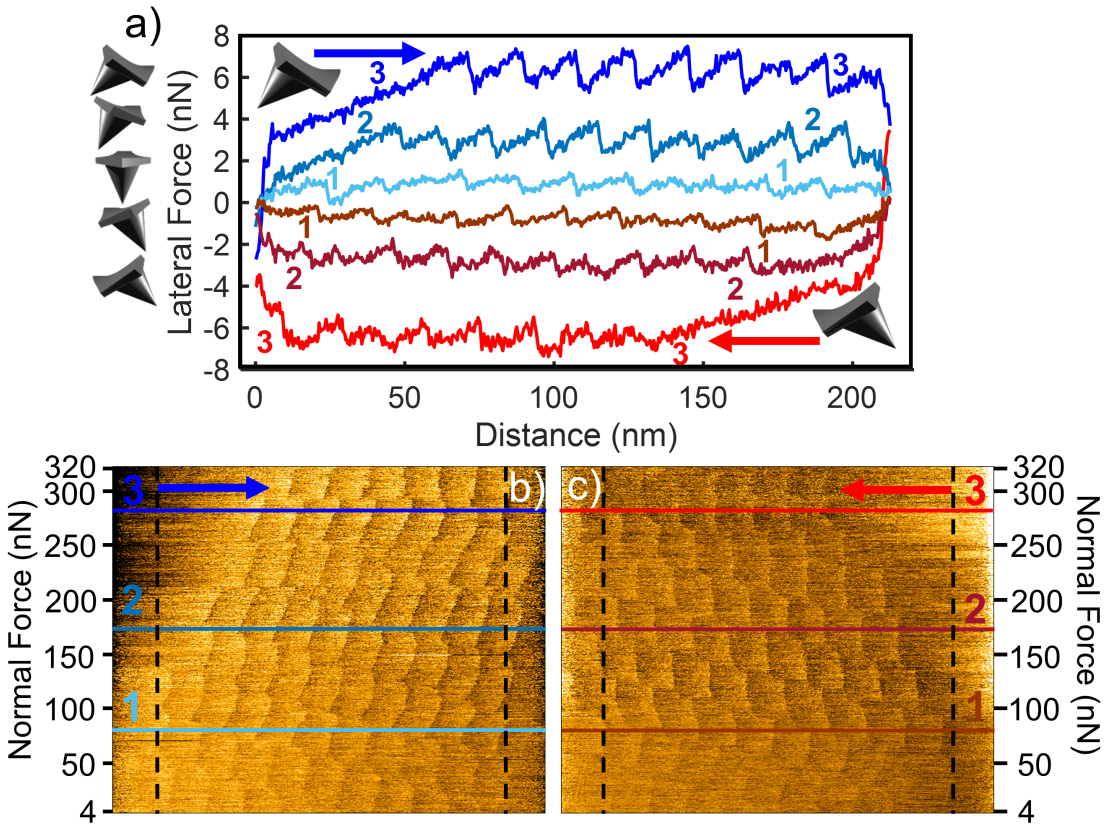


FIGURE 6.10: Panel a) shows several LFM scan lines recorded with 3 different normal force values of 70 nN, 170 nN, and 280 nN (for lines labelled 1-3 respectively) along the same path on a hBN/graphene heterostructure displaying a 17.3 $\pm$ 0.2 nm moiré pattern. The blue lines indicate trace scan lines, with the red indicating retrace scan lines, with profiles labelled with matching numbers completing full friction loops. Each of the three friction loops has had its lateral force offset to an average of zero for clarity. The inset illustrations indicate the lateral twisting of the cantilever for trace, retrace, and for varying lateral force. These scan lines are part of a set of 512 friction loops recorded for a normal force range of 4 to 320 nN. Panels b) and c) show this set of LFM results as an image for trace and retrace respectively, with the y-axis indicating increasing normal force. The positions of the scan lines shown in a) are indicated and labelled in b) and c). The regions outside of the black dotted lines indicate the overscan region. The blue and red arrows indicate the tip movement direction for trace and retrace respectively. Mean plane subtraction has been used in the images in panels b) and c) to ensure the moiré lines are visible.

towards the end and beginning of the scan line where the tip decelerates/accelerates as it turns around, also recorded. The combined data forms a friction loop as described in figure 3.2 in section 3.3.1 of chapter 3. Three friction loops/sets of LFM scan lines are shown in figure 6.10a, each recorded with a different applied normal force (used as the set point) that were 70 nN, 170 nN, and 280 nN (each with an associated error of

$\pm$ 10 nN) for the friction loops labelled 1-3 respectively. The trace scan lines are indicated in blue with the retrace scan lines shown in red. As described in section 3.3.1, the centre of the friction loop should be at zero for a flat surface, and as such the friction loops shown here have been offset so that their average is positioned at zero. The lateral force has been obtained using a lateral inverse optical lever sensitivity calculated using the wedge method for lateral force calibration [82], described in section 3.3.1, to convert the signal into nN. The sawtooth behaviour of these LFM scan lines, similar to that seen in figures 6.8d and 6.9g and h), is clearly present in both the trace and retrace data shown here (being less apparent for the retrace data). These sawtooth profiles show that, for the forward scan, the lateral signal is increased through the overscan region until reaching a threshold value where the lateral force drops, indicating that the tip has passed over a moiré cell boundary, before repeating this behaviour as the tip passes over multiple boundaries. The magnitude of the lateral force measured in these friction loops can be seen to increase with the normal force applied, where loop 3 (for a normal force of 280 nN) displays a greater lateral force magnitude than loop 1 (measured with a normal force of 70 nN).

The peaks of the sawtooth scan lines before the sudden drop in signal indicate the positions where the AFM tip passes over a moiré boundary, as demonstrated earlier in figures 6.8d and 6.9g and h). For the scan lines shown in figure 6.10a it can be seen that these peaks are moved further by the tip with a higher applied normal force. This becomes clearer in the images shown in panels b) and c) of figure 6.10. In these images the full set of data from which the scan lines in panel a) were taken are shown. This includes 512 individual friction loops that were recorded along the same path, where the applied normal force was ramped from 4 nN to a maximum of 320 nN. These images, referred to as set point ramps, show the trace (panel b)) and retrace (panel c)) scan lines of each friction loop, with the y-axis of these images indicating the normal force that was used as the AFM set point. The areas outside of the black dashed lines indicate the overscan regions, where the x-axis distance measurement is compromised. The results in these images have been aligned using a mean plane subtraction for visual clarity, to ensure the moiré lines are visible. The locations on these images where the data for the scan lines shown in panel a) of figure 6.10 originate are indicated. The moiré cell boundaries can be seen to be pushed by the AFM tip, with a movement distance that increases as the normal force is increased, as has been seen earlier in this chapter. Furthermore, for high values of normal force there are regions where no moiré boundaries are present at the start of the scan line path. This region is positioned on the left-hand side of the trace image, indicated by the blue arrow, and the right-hand side of the retrace image, indicated by the red arrow. This observation is consistent with the data shown in figure 6.9g and h), and suggests a larger normal force allows for a greater lateral force, that in turn pushes the moiré boundaries further

before passing over the first boundary.

Using the interpretation described earlier (in section 6.4) to understand the moiré deformation behaviour seen in figure 6.3, this boundary movement can be explained. As the AFM tip is lowered onto the heterostructure surface and the AFM set point, i.e. normal force, is increased the interlayer distance of the constituent layers is reduced by a small amount. This leads to an increase in the interaction energy difference between the different stacking configurations, with the AB configuration becoming more favourable, as shown in figure 6.5. As the tip is moved across the moiré cell the region directly underneath the tip apex acts to match the hBN lattice, expanding the AB stacking region as seen in figure 6.3. Furthermore, as demonstrated by the lateral images in figure 6.9g and h), and figure 6.10, the lateral force experienced (opposing the tip direction) increases as the tip passes across the moiré cell. This opposing lateral force is assumed to be due to the restoring force of the in-plane bonds of the stretched graphene lattice. Once this restoring force reaches a threshold value the lattice snaps back underneath the tip. This can be seen in the sudden moiré cell edges shown in figure 6.9e and f), and as the sawtooth behaviour of the lateral signal. This snap back indicates that the tip has passed over a moiré boundary and into the neighbouring moiré cell. The lateral force experienced by the tip then begins to rise again as the tip moves through the new cell until it is once more overcome by the lattice restoring force, occurring at a threshold value. This threshold value can be seen as the maximum, for trace scan lines, and minimum, for retrace scan lines.

When the normal force applied by the tip is increased, the heterostructure interlayer distance is further reduced. This leads to a predicted exponential increase in the interaction energy variation (as shown in figure 6.5h), so that the AB stacking configuration becomes even more favourable. The result is that as the tip is moved across the moiré cell, the restoring force required for the graphene to snap back is increased. This leads to the tip moving further before the lateral force reaches the new threshold value, resulting in the observed movement of the moiré boundaries that increases with a greater applied load shown in figure 6.10. The maximum measured distance moved by the moiré boundaries from equilibrium seen in figure 6.10a is approximately 67 $\pm$ 2 nm, corresponding to approximately 4 moiré wavelengths. This suggests that the graphene lattice has been stretched so that the carbon atom directly underneath the tip apex before the lattice snaps back has been displaced by 0.98 $\pm$ 0.04 nm ($\sim$4 lattice constants).

The movement of the moiré lines, seen in figures 6.9b and c) to increase as the normal force is raised, is demonstrated by their diagonal appearance in those images. However, while displaying a more general movement that appears to linearly increase with the normal force, there is also a stepped structure occurring in these lines that suggest an additional behaviour. In figure 6.11 100 friction loops are plotted from

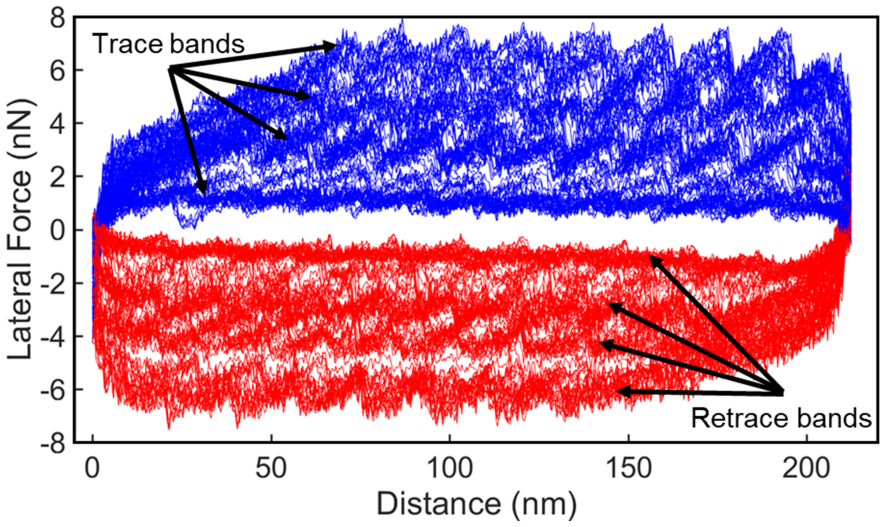


FIGURE 6.11: This figure shows 100 friction loops with equally spaced normal force values ranging from 4 to 320 nN, using the same data shown in figure 6.10. Each profile is an average of 15 scan lines, with a lateral force that has been offset so that the friction loops each have an average of 0 nN. The trace and retrace portions of the data have been indicated using blue and red respectively. Alignment of the scan lines along the y-axis is revealed, resulting in grouping that forms 4 bands that have been labelled in this figure.

the same set point ramp images shown in figure 6.10. These scan lines were equally spaced across the 4-320 nN range for the applied normal force shown in figure 6.10, and have been plotted in the same way as the friction loops shown in panel a) of figure 6.10. In figure 6.11 the friction loops show a spread in the y-axis for the measured lateral force displaying a greater lateral force for higher normal force values, as has been observed earlier in figure 6.10a, however, in figure6.11 there is a definite grouping of these friction loops into a series of bands with aligned sawtooth behaviour for both the trace and retrace scan lines. This grouping indicates that as the normal force is increased the lateral force threshold, that was used to describe the sawtooth behaviour, plateaus. As the normal force is increased further still, the lateral force threshold is again increased before reaching a second plateau. The result of this is seen as the formation of bands appearing within figure 6.11, with four separate bands in both the trace and retrace scan lines observed.

Following the earlier interpretation, the plateau of the threshold lateral force value may be occurring as the moiré line that is being pushed encounters a second moiré line, i.e. the movement of the moiré line from its equilibrium is in excess of its wavelength. At this position an additional amount of lateral force is required before the moiré lines are pushed further. This is similar behaviour to that observed in figure 6.9g and h) where a greater lateral signal resulted in a moiré boundary movement in

excess of the measured wavelength. Further evidence that the origin of these bands is due to the moiré line being pushed through additional moiré lines is provided by the band number being indicative of the distance, in moiré wavelengths, that the line has been pushed. For the friction loop corresponding to the highest lateral force, and positioned in the fourth band in figure 6.11, the maximum moiré line movement of 67 $\pm$ 2 nm was recorded. This value corresponds to 4 times the moiré wavelength of 17.3 $\pm$ 2 nm.

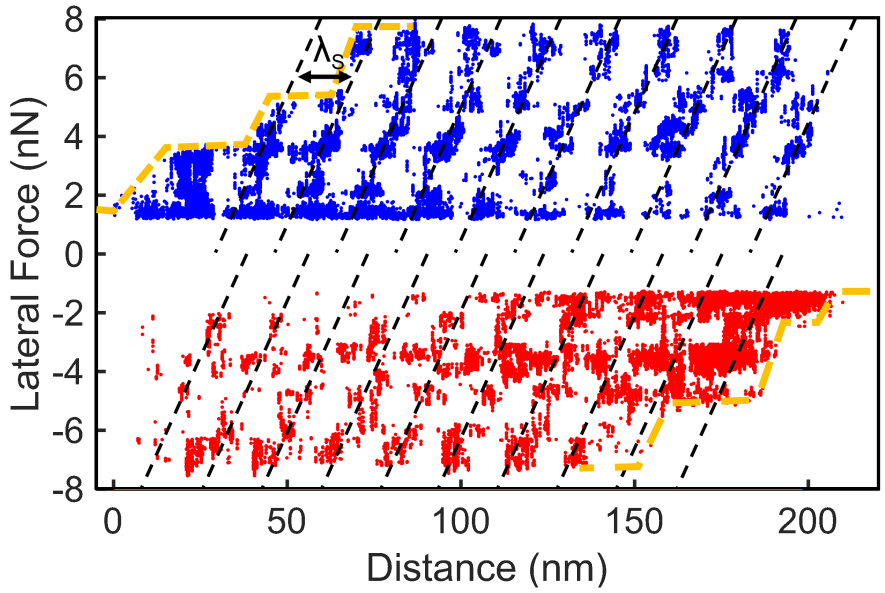


FIGURE 6.12: A figure showing the peak positions for each of the LFM scan lines shown in figure 6.11. This was achieved by plotting the positions of the highest (for trace) and lowest (for retrace) twenty data points for each set of data, using an average of 15 scan lines. The result shows a plot that tracks the peak positions of the sawtooth signals shown in figure 6.11. These correspond to the locations of the moiré cell boundaries. Using linear curvefitting the data has a measured gradient of 0.26 $\pm$ 0.05 nN/nm. Dashed black lines are plotted using this gradient, and are spaced 17.3 nm apart along the x-axis (indicated within the figure), matching the recorded moiré pattern wavelength, λ_S, in this region.

In order to observe the moiré line shift with respect to the recorded lateral force the peaks of each scan line, corresponding to the peaks in the sawtooth signal where the AFM tip passes over a moiré boundary, have been plotted in figure 6.12 for the same set of data shown in figure 6.11. This has been achieved by plotting only the top 20 data points for each trace scan line, with the lowest 20 data points plotted for the retrace scan lines. The resulting pattern displays a very linear distribution of peak positions for each moiré line, in particular for the trace data. Using curve fitting the gradient of these lines was measured to be 0.26 $\pm$ 0.05 nN/nm, and indicates the amount of lateral force required to push the moiré lines for the tip that was used. Black

dashed lines have been plotted in figure 6.12 using this gradient, with a spacing equal to the recorded moiré wavelength, λ_S.

The behaviour described by the appearance of bands in the friction loops shown in figure 6.11 that correspond to additional moiré lines being pushed is also evident in figure 6.12. Here the result can be seen in the stepped behaviour where the first peaks of the scan line are recorded, highlighted by the dashed yellow lines. These indicate the first location where the tip has passed over a moiré boundary in the corresponding scan line. At lateral forces that match with the positions of the bands in figure 6.11 a step in the data indicates the disappearance of a moiré line. Following earlier interpretation, this indicates that at these steps the AFM tip pushes the first moiré line, then once the lateral force is large enough the AFM tip is able to push a second moiré boundary, and the moiré line movement exceeds λ_S, and one fewer moiré line is present as a sawtooth signal in the recorded scan line.

6.8 Summary

By using a variety of AFM techniques to image the graphene/hexagonal boron nitride heterostructure surface, the resultant moiré pattern has been observed to become sharper and deformed, in a similar way to that observed by *Yankowitz et al* [78] for STM, but here has been seen for AFM imaging on MBE grown rotationally aligned material. Furthermore, in this work the superlattice has been shown to move across the sample surface with the AFM probe tip by a distance proportional to the amount of force applied. This has been explained, in conjunction with the explanation used to describe the changes seen in the superlattice appearance, by preferential high symmetry stacking orders of the graphene on hBN, with the preferred, lower adhesion potential, AB stacking order dominating at higher pressures applied by the tip.

These results provide conclusive evidence of a shift in the graphene/hBN moiré pattern that follows the tip movement as it is scanned across the surface. The extent of this moiré pattern movement has been seen to be large, and in excess of multiple moiré wavelengths. As the amount of moiré line movement approaches the point at which it reaches a second moiré cell boundary an additional amount of lateral force has been shown to be required before the AFM tip begins to move both moiré lines.

The movement of these moiré pattern boundaries by such a large amount is an important factor to consider when imaging not only graphene/hBN heterostructures, but also any other form of van der Waals heterostructures, as it demonstrates that the acquired images do not provide an accurate representation of the undisturbed, equilibrium surface for these types of structures, particularly in contact mode or where high applied forces are used. Instead the surface is imaged under a locally applied pressure that can cause significant material deformation in the vicinity of the probe

tip. These observations also explain the behaviour shown within this chapter when imaging such surfaces that may otherwise have been labelled as scanning artefacts or incorrectly attributed to other explanations.

In addition, the ability to stretch and locally deform the graphene surface may be useful in other fields or experiments, for example one could envisage a MEMS (microelectromechanical systems) device that applied local pressures at regions across such a structure to deform the moiré superlattice into a desired network of highly conducting moiré channels, or to create regions of lattice matched graphene/hBN.

Chapter 7

Step-Flow Growth of Graphene-hBN Lateral Heterostructures

7.1 Introduction

As described in section 2.2 of chapter 2 the use of hexagonal boron nitride as a supporting substrate for high quality graphene results in striking improvements in carrier mobility and device performance [35, 36, 102]. Despite an increasing interest in graphene/hBN heterostructures, the direct growth of graphene on hBN is relatively uncommon and most graphene/hBN vertical heterostructures consist of stacks of layers mechanically exfoliated from bulk material [2]. However, owing to the small lattice mismatch it is also possible, through growth, to incorporate graphene and hBN in a lateral heterostructure [102, 103]. The hybrid monolayer has been predicted to possess a widely tuneable electronic bandgap (section 2.3.2) [104, 105], while an atomically precise interface between graphene and hBN can host novel electronic and magnetic states [106, 107, 132]. In short, the properties of the lateral heterostructure are dictated by the size, geometry, and interface structure of hBN and graphene domains. There has been progress in growing lateral heterostructures using chemical vapour deposition [102–107] or direct chemical conversion of graphene layers [133, 134]. These efforts have culminated in the fabrication of atomically thin devices [135] and circuitry [136] constructed from laterally connected hBN and graphene layers.

For the samples discussed in the previous chapters, the graphene that has been investigated was grown using MBE directly on top of mechanically exfoliated hBN. In this chapter the graphene growth has been preceded by the MBE growth of hBN on a HOPG substrate using the same system. This sequential method of hBN growth uses plasma-assisted MBE, with the nucleation of hBN primarily at steps on the graphite

substrate [137–139]. This is followed by the MBE growth of graphene using an electron beam carbon source, similar to some of the samples seen in the previous chapters. In some cases, hBN/HOPG samples are directly transferred to a second MBE chamber for graphene growth, while others are investigated ex situ using atomic force microscopy after hBN growth, before re-introduction to the MBE system. Graphene grown in both cases nucleates at step edges of epitaxially-grown hBN, and grows laterally across the surface to form graphene nanoribbons, with a width which is highly uniform and tuneable across the substrate surface.

7.2 Growth Conditions

To grow hBN on HOPG similar protocols to those described in chapter 3 section 3.7 and elsewhere were followed by Sergei V. Novikov and Tin S. Cheng [138, 139]; HOPG substrates (1 x 1 cm^2) were cleaned by heating to 400 °C for approximately 8 hours in an Ar/H2 (95:5) atmosphere and then transferred to the same custom-designed high-temperature dual chamber GENxplor MBE system used for graphene growth, operating under ultra-high vacuum conditions (base pressure $\sim 10^{-10}$ mbar). hBN was then grown by plasma-assisted MBE at a substrate temperature of 1390 °C , with a high-temperature Veeco effusion cell operated at 1875 °C to sublime boron, and a conventional Veeco radio-frequency plasma source to generate the active nitrogen flux; this was operated at an N_2 flow of 2 sccm and an RF power of 550 W. A growth time of 3 hours was used, resulting in hBN covering over ∼80 % of the HOPG substrate surface. The hBN/HOPG samples were cooled to room temperature and transferred within the UHV system to the graphene MBE growth chamber. In some cases, the samples were removed temporarily from the UHV system in order to acquire images of their morphology using AFM allowing a direct comparison of regions of the surface before and after graphene growth; these samples were then returned to the MBE system for graphene growth, again carried out by Sergei V. Novikov and Tin S. Cheng. This was achieved using a vertical electron beam evaporator EBVV 63-T4, fitted with a high purity carbon anode target; both sources are produced by Dr. Eberl MBE-Komponenten GmbH. During growth the e-beam current was increased to, typically, 300 mA, with a ramp rate of 10 mA/min, and held at this value during the growth time (up to several minutes), then ramped down at a rate of 100 mA/min. The accelerating voltage was 5 kV and the substrate temperature was 1390 °C for all samples. This method of growth has allowed for more controlled deposition compared to the carbon filament source, due to the increased stability and tunability of the e-beam source.

7.3 Ex Situ Measurements of Nanoribbon Growth

Figure 7.1 shows a direct comparison of the morphology of a specific area of an HOPG substrate on which a near monolayer of hBN has been grown both before (a-c) and after (d-f) subsequent graphene growth. AFM images of the surface acquired ex situ before graphene growth show that hBN has grown laterally across the HOPG surface from three-dimensional aggregates which are formed primarily at HOPG step edges [138, 140]. The hBN is revealed in contact mode deflection channel images, panels a) and c), and topographic maps (panel b). From the topography image in panel b) the layer thickness has been determined (see inset); the hBN layer number and regions of uncovered areas of the HOPG substrate are labelled in panel a). The images recorded prior to graphene growth are less sharp than those recorded following growth due to limitations in the sample preparation because of the requirement of being returned to the UHV growth system. Islands of hBN nucleated at different points form separate domains that merge as the surface coverage increases. The boundaries between domains are difficult to resolve in topographic images but appear more clearly in the deflection images a) and c), with one such boundary highlighted in c).

Within this region there are many hBN step edges as well as partially formed hexagonal bilayer and multilayer hBN islands. This morphology is very similar to that reported in previous studies of the MBE growth of hBN on HOPG [42, 138, 140]. This particular sample (hBN on HOPG) was returned to the MBE system and, after growth of graphene, further AFM images of the same area were acquired and are shown in the bottom row of the same figure (figure 7.1d-f)). In comparison with figure 7.1a-c) we observe additional features at the edge of the hexagonal partial hBN island at the centre of figure 7.1d). These are also present in the topographic image figure 7.1e) but are resolved far more clearly in figure 7.1f). This phase image provides contrast between different materials allowing the brighter strip around the edges of the hBN island to be attributed to graphene which has nucleated at the hBN step edge and grown outward across the surface. The profile in figure 7.1e) inset shows that there is a very small variation in apparent height across the boundary between the hBN and the graphene strip as expected for such a growth mode (see regions identified by red arrows; the hBN/graphene boundaries are highlighted by white arrows in figure 7.1e) and the accompanying profile). This lateral growth is observed at every hBN island and step edge across the sample.

Topographically bright features are also seen in figure 7.1e) at the graphene/hBN lateral interface; these are attributed to graphitic aggregates, commonly seen in MBE growth of graphene [44, 116]. In some cases these clusters provide the nucleation site for higher layers of graphene. In addition, isolated islands of graphene nucleated on hBN at sites remote from step edges are observed, for example the island in the lower

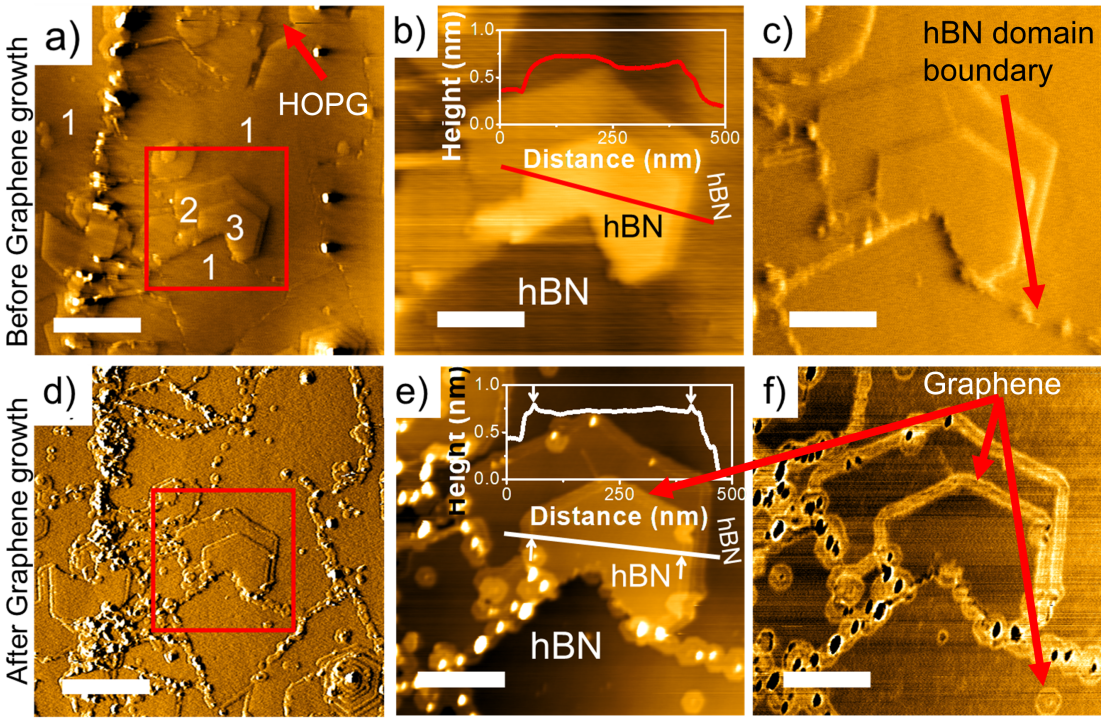


FIGURE 7.1: a) Contact mode deflection image of hBN grown on HOPG with a surface coverage >80%. The numbers indicate the hBN layer, from monolayer (1) to trilayer (3); a region of HOPG is also marked. b) and c) show contact mode topography and deflection maps respectively of the region bounded by the red box in a). A profile along the red line in b) is shown in the inset. d) Deflection image of the same region as a), measured after graphene growth. Panels e) and f) show topographic and phase channels acquired in AC mode of the region within the red box in d), both recorded following graphene growth. The phase image provides contrast between the graphene and hBN regions, highlighting graphene growth at hBN step edges, domain boundaries, and isolated graphene islands. A profile along the white line in e) is shown in the inset. Scalebars: 500 nm in a) and d), and 200 nm in b), c), e) and f).

right of figure 7.1e) and f) (marked by a red arrow in f)). A comparison of figure 7.1a and d) also reveals the presence of meandering linear features, which were not resolved clearly in figure 7.1a; these correspond to regions where graphene growth has been nucleated at hBN domain boundaries. The presence of this additional graphene also appears close to the domain boundary identified in figure 7.1c; with the graphene visible in the higher resolution images of the same area in figure 7.1e (topographic) and f) (phase). Furthermore, the thickness of the aggregate lines that were already present before graphene growth, seen in figure 7.1a, where aggregates have collected along HOPG step edges, have become expanded as carbon aggregates become affixed to the nucleating regions, seen by comparing these structures with the same region shown after growth in d).

The graphene strips form a lateral heterojunction with the hBN from which they grow and are reminiscent of graphene nanoribbons which are formed using molecular self-assembly and on-surface polymerisation [30], as well as analogous structures which have been grown using CVD [141]. These lateral graphene-hBN heterointerfaces are explored in further detail in the remainder of this chapter.

7.4 Investigating the Nanoribbon Growth Mechanisms

Figure 7.2 shows a lateral heterostructure formed by sequentially growing hBN and graphene without removal of the sample from the UHV environment of the MBE system. Figure 7.2a shows a topographic image close to the edge of a hBN island which is predominantly of monolayer height (topographic region marked 1), but also has several regions of second (marked 2), and higher, layers of hBN. In addition, a region of HOPG, which remained exposed after hBN growth, is present on the left-hand side of the image (marked as 0). Figure 7.2b shows a conductive AFM image of the same region.

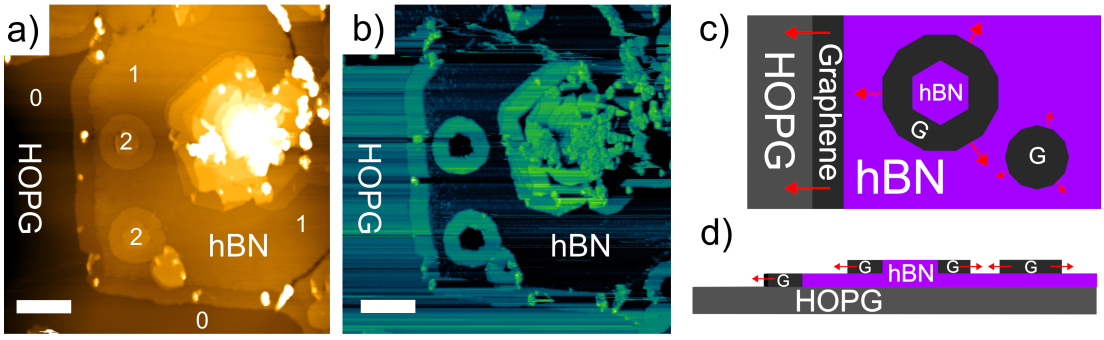


FIGURE 7.2: Images of a sample grown without removal from the MBE system. a) and b) show AFM images recorded in AC mode (a) and conductive mode (b). The number of hBN layers present are indicated in a). The current scale in b) ranges from 0 to 9.4 μA. The scalebars are 250 nm in both a) and b). The graphene bands are clearly visible in the current image, b). Figures c) and d) show a top-down and cross-sectional schematic respectively of the sample structure. MBE graphene growth (G) at hBN step edges, on HOPG and surrounding hBN islands, are shown alongside growth of graphene only islands. The in-plane lateral direction of graphene step flow growth is highlighted by the arrows.

In the CAFM image the lower region to the left-hand-side of the topography image figure 7.2a, is the exposed HOPG substrate, showing up as highly conducting in figure 7.2b in which bright/dark contrast corresponds to high/low current. The monolayer hBN terrace on the right-hand-side of the image, appears darker (less conductive) but there are two raised hexagonal regions identified as bi-layer hBN in the topographic image figure 7.2a. Graphene nanoribbon growth can be seen along all hBN step edges

within these images and appears with bright contrast in the CAFM images. This is particularly clear for the graphene which has grown around the second layer hBN. Nanoribbon growth is also evident at the edges of the more disordered hBN multilayer on the centre-right of these images. In addition, graphene grows across HOPG from the edge of the first layer hBN; this is evident from the contrast variation in figure 7.2a. Overall, no significant differences have been observed between samples which are imaged ex situ after the first stage of hBN growth and returned to the MBE system, and those which are transferred to the second MBE chamber within UHV without ex situ AFM prior to graphene growth. Figure 7.2c and d) show a simplified diagrammatic representation of the sample shown in a) and b) as a top down and cross-sectional perspective respectively. Here the HOPG is shown as grey, hBN as purple, and graphene as black. The in-plane direction of graphene growth in these diagrams is indicated by the red arrows.

The widths of the graphene bands shown in figure 7.1 and 7.2 appear to have a high degree of uniformity, with measured widths of 30 nm and 80 nm, respectively. A more systematic analysis of widths of graphene is provided for three samples grown with different amounts of deposited carbon in figure 7.3. The graphene in figure 7.3a was grown by ramping the carbon source e-beam current to 280 mA with a rate of 10 mA/min before immediately ramping down with a rate of 100 mA/min. For the samples shown in figure 7.3b and c) the current was ramped up to 300 mA, at the same rate, before being ramped down either immediately (b) or after 1 minute (c). The histogram in figure 7.3d shows the collated measurements of graphene widths determined by AFM for these three samples and two additional samples grown with the same conditions as the sample shown in figure 7.3c. As the amount of deposited carbon increases, the graphene width systematically increases from 18 ± 4 nm (figure 7.3a) to 29 ± 4 nm (figure 7.3b) to 83 ± 11 nm (figure 7.3c). In each case the variance of the distribution is significantly smaller than the mean width. These measurements confirm that the graphene widths for a given set of growth conditions have a narrow distribution and systematically increase with increased deposition time/carbon flux, confirming the potential tunability of the width of the graphene nanoribbons grown using this approach.

The uniformity of the graphene width is also evident through the conformal relationship between the growing edge of the graphene and the hBN step edge morphology from which it nucleated, i.e. the graphene edges follow (and are nearly parallel to) the shape of the hBN edges. An interesting exception is revealed close to the vertices where hBN facets meet. An example is shown in the topographic image in figure 7.3e (a zoom of the region highlighted by the red square in figure 7.3b); here the growing edges of graphene are approximately parallel to the hBN island edge, but an additional facet evolves close to the hBN apex at an angle of, approximately, 30° to the

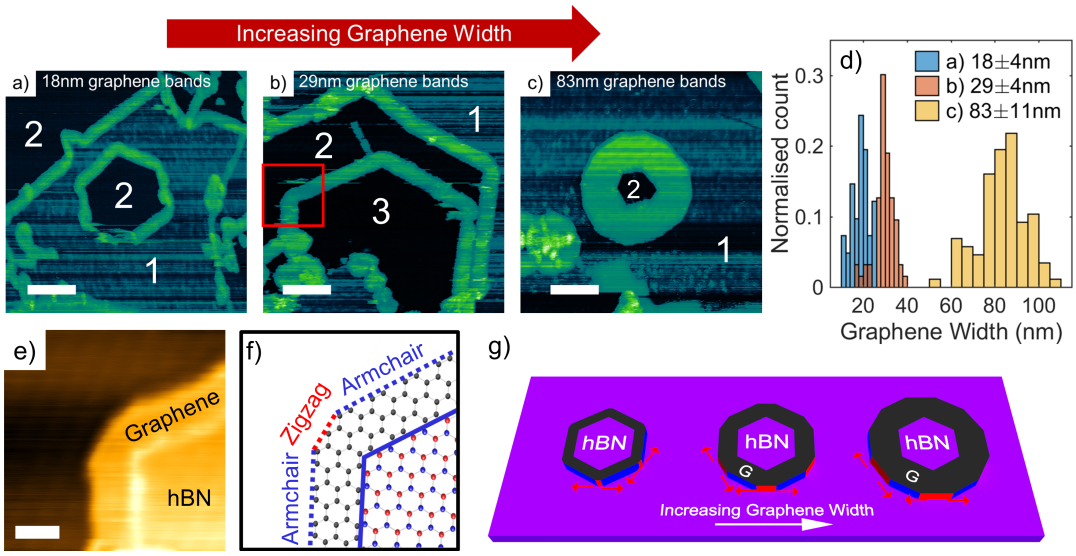


FIGURE 7.3: a-c) Three CAFM current images recorded on three separate samples with varying growth conditions with increasing graphene widths from left to right. Current values ranging from 0 to 1.5 μA, 2.5 μA, 2.7 μA in a), b), and c) respectively. The numbers indicate the number of hBN layers, from monolayer (1) to trilayer (3). d) shows the recorded distribution for graphene band widths. 41 measurements were made across the sample shown in figure a), 63 measurements across the sample shown in figure b), and 87 measurements spread across 3 samples with the growth conditions of the sample shown in figure c). e) An AC topography image of the region bounded by the red square in b). In this figure the additional zigzag graphene edge appearing at the hBN corners can be clearly seen. Figure f) shows a schematic representation of figure e) with the expected lattice termination types indicated. Figure g) shows a diagram indicating the graphene growth with extended amount of deposited carbon. The blue edges indicate armchair termination, and the red edges indicate zigzag termination in both f) and g). At longer growth times the zigzag edges (red) become elongated, as the graphene bands become thicker. Scalebars are 100 nm in a) to c), and 25 nm in e).

hBN edge. We attribute this facet to the evolution of a zigzag (ZZ) edge, which, as expected, is at 30° to the hBN edges, which are attributed to armchair edges, due to the hexagonal island shape. This is illustrated schematically in figure 7.3f. According to numerical modelling of graphene edges the armchair edge is expected to have a lower energy than the zigzag termination [142]. However, it is also known zigzag edges can undergo a reconstruction thereby reducing their energy. In addition, a zigzag termination has been observed to evolve at the edges of holes in graphene under electron bombardment. The energetics are thus likely to depend critically on experimental conditions such as temperature and substrate, but the transition to a zigzag edge close to hBN vertices was observed consistently across our samples. Note that hBN islands terminated by either N- or B- terminated ZZ edges are expected to have a triangular shape for ZZ favourable edges [143], whereas under our growth conditions hexagonal

islands are formed.

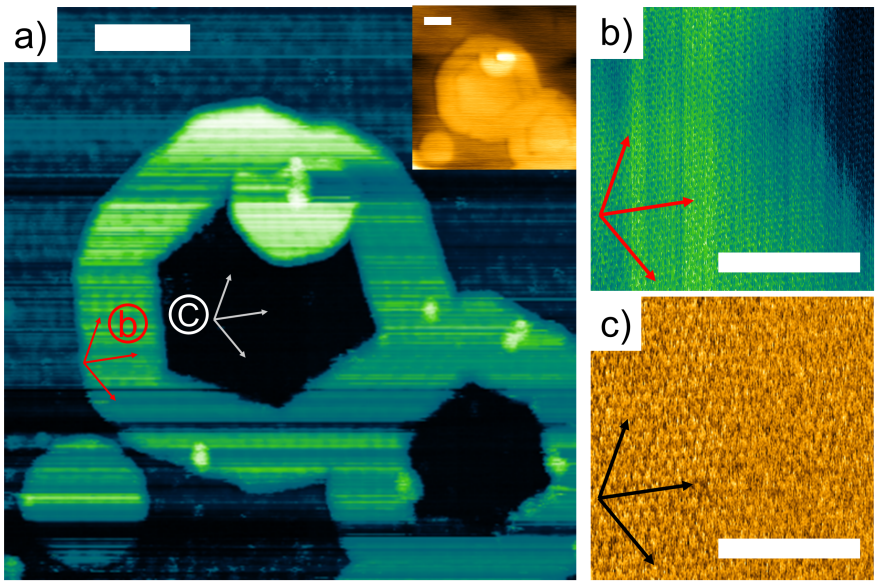


FIGURE 7.4: a) a CAFM current image showing 75 nm graphene bands with a current scale ranging from 0 to 1.1 μA. An approximately 18 nm moiré pattern can be seen on the graphene. The inset shows a contact topography image of the same region. b) lattice resolution CAFM image recorded on the graphene region indicated in a). The red arrows indicate the lattice directions as determined from a 2D Fourier transform of the image. Similarly, c) shows a lattice resolution lateral force image recorded on the hBN region indicated in a), with the black arrows (white in a)) indicating the lattice directions. These images confirm the armchair edge type for the hBN islands, and armchair/zigzag terminations of the graphene edges. Scalebars are 100 nm in a) and a) inset, 5 nm in b), and 2.5 nm in c).

This assignment has been confirmed using lattice resolution imaging of a hexagonal hBN island bounded by graphene bands (see CAFM image in figure 7.4a; the inset showing the corresponding topographic image). Figures 7.4b and c) present lattice resolution images of the graphene and hBN lattices at the locations indicated in figure 7.4a. Figure 7.4b is a 10 nm CAFM image, whereas figure 7.4c is a 5 nm lateral force image. The lattice directions have been extracted from a 2D Fourier transform and are indicated by the red (graphene) and black/white (hBN) arrows in figure 7.4. The hexagonal island edges, along with the parallel graphene edges, run at 30° to the lattice direction confirming the edges to be armchair terminated, whereas the additional graphene edges are parallel to the lattice direction confirming a ZZ termination. Furthermore, these images confirm the epitaxial relationship between the hBN island and the growing graphene. Figure 7.4a also demonstrates the merging of two graphene domains growing from separate hBN islands. Images of this region, acquired with lattice resolution, show a defect-free merging of the two bands with no obvious domain

boundary, suggesting continued growth results in boundary free graphene monolayers. In the images acquired the atomic detail of the structure very close to (within $\sim$ 1 nm) the interfacial boundary between hBN and graphene has not been resolvable. This is likely due to the presence of defects as well as electron scattering due to the interface itself [144] which is known to complicate the local density of states and, thus, the apparent conductivity and topography as determined by CAFM and STM.

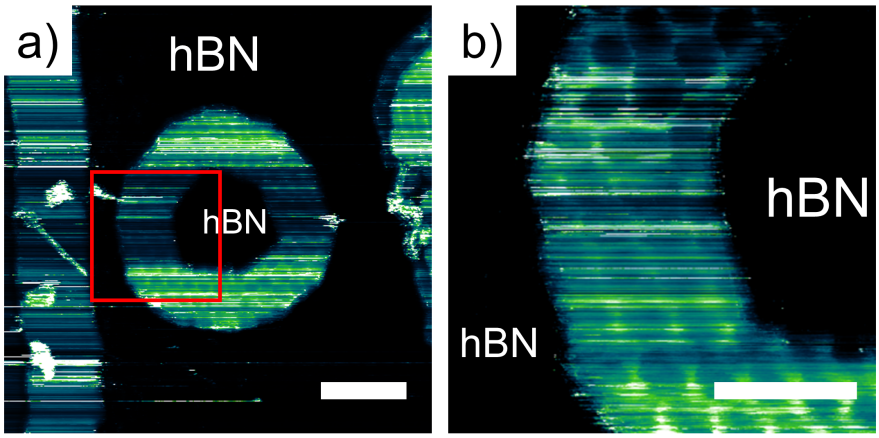


FIGURE 7.5: Figure a) and b) are CAFM images showing a zoom of the same region as in figure 7.2b and c), with the area given in b) highlighted by the red box in a). Here the additional graphene zigzag edge at 30° to the adjacent edge is clear, along with an 18 nm moiré pattern, however there are large amounts of moiré distortion at the nanoribbon corners. The current scales in a) and b) both range from 0 to 64 nA. The scalebars measure 100 nm in figure a), and 50 nm in b).

For the graphene grown at high temperature by MBE shown in chapters 5 and 6 high intrinsic strain was observed, which results in moiré wavelengths larger than that expected for relaxed graphene aligned to the hBN lattice. Moiré patterns with different wavelengths have been observed in CAFM images of graphene strips with sufficiently large width. Figure 7.5a and b) show CAFM images of graphene grown from the edge of a hBN monolayer across the HOPG substrate, and from the edge of a hBN bilayer. Due to the lattice mismatch between the graphene and hBN, moiré patterns arise in areas where both graphene and hBN are present in the heterostructure. In figure 7.5a, no moiré patterns are seen in the graphene strip extending over HOPG from the edge of the first hBN layer, indicating that this region is unstrained and rotationally aligned to the underlying HOPG lattice. A prominent moiré pattern with a wavelength, λ_S, of 18 nm is observed in the second hBN layer (see topographic image in figure 7.2a for determination of layer number in this region). This moiré pattern exceeds the expected maximum of $\sim$14 nm for unstrained, rotationally aligned material. In previous chapters the strain in MBE graphene grown on exfoliated hBN is

considered to be primarily within the graphene monolayer, rather than the bulk hBN, whereas here the longer moiré wavelength may be due to compressive strain of the hBN lattice by approximately 0.4% due to the underlying HOPG substrate. Over the hBN monolayer regions (labelled as 1 in figures 7.1, 7.2, and 7.3) the moiré pattern between the hBN and HOPG substrate are far less clearly resolved. However, in these regions in figure 7.3a-c) and figure 7.4a faint moiré patterns exhibiting similar wavelengths to those seen on the nearby graphene layers are visible using CAFM. This suggests that the graphene layer is locally unstrained or minimally strained.

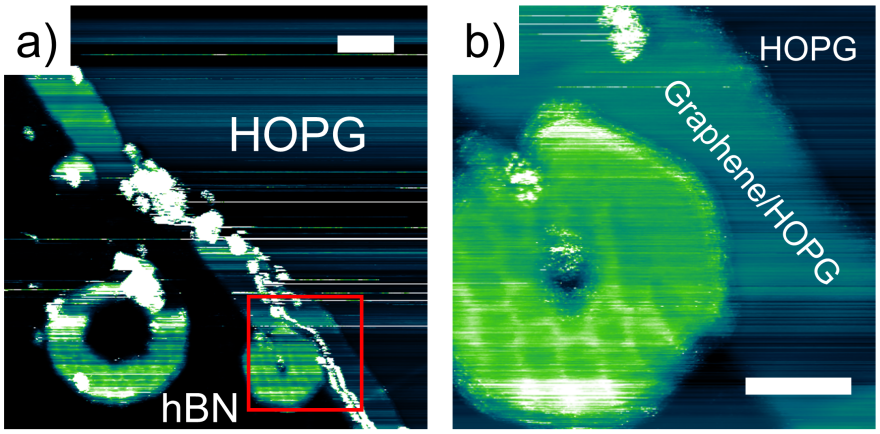


FIGURE 7.6: a) and b) both show CAFM images displaying a graphene only island on hBN overlapping a graphene band at the HOPG/hBN step edge. The moiré pattern seen over the hBN layer measures 20.3 nm. There was no moiré observed on the step edge graphene band, or at the graphene island/graphene band overlap. The scale ranges from 0 to 32 nA in a), and 0 to 45 nA in b). The scalebars measure 100 nm in figure a), and 50 nm in b).

Figure 7.6 shows CAFM images of a separate region where a graphene nanoribbon has grown along the step edge of a monolayer hBN domain directly on top of HOPG. Some conductive (bright) deposits in the centre of the image in a) obscure the graphene nanoribbon. On the lower left-hand-side of the image graphene growth around a hexagonal bilayer hBN island is seen as before, with a moiré pattern visible in the graphene bands with a wavelength of 20.3 nm. In the lower right-hand-side of the image, bounded by the red square and shown with an increased resolution in figure 7.6b, is a graphene-only island that has grown from an initial nucleation point on the monolayer hBN region. During growth, this graphene island has extended beyond the monolayer hBN region, and over the graphene nanoribbon located at the hBN/HOPG step edge. A 20.3 nm moire pattern can be seen across the graphene-only island for the portion where the island is positioned atop the hBN. At the region where the graphene island laterally extends onto the graphene ribbon supported by HOPG, there is an abrupt disappearance of the moiré pattern, matching the absence of a pattern in the

nanoribbon itself, indicating that the graphene is unstrained and lattice matched to the underlying graphene and HOPG.

7.4.1 Graphene-only Islands

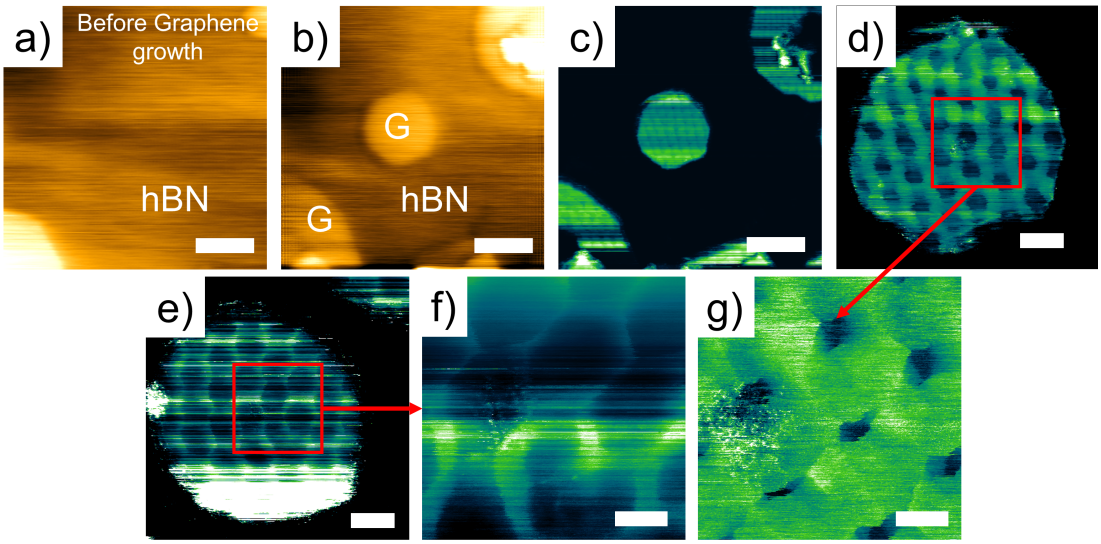


FIGURE 7.7: Figures a-d) and g) show the same region. a) and b) are contact mode height images, recorded before (a) and after (b) the graphene growth. Panel c) shows the corresponding current image, with d) showing a smaller image centred on the island. The linear current scale in c) and d) ranges from 0 to 1.2 μA and 0.5 to 0.8 μA respectively. In b) and c) the graphene bands on nearby hBN islands can also be seen at the corners of the images. The graphene-hBN moiré pattern seen in c) and d) measures 18 nm. Figure e) shows a similar CAFM image of a separate graphene island. Here the linear current scale ranges from 190-292 nA, and the moiré pattern measures 18 nm. Figures f) and g) are CAFM images of the region indicated by the red boxes in e) and d) respectively. The linear current scale is 200-320 nA in f) and 1.15-1.26 μA in g). The scalebars measure 100 nm in a) to c), 25 nm in d) and e), and 10 nm in f) and g). These images highlight the nucleating defects found at the centre of the graphene-only islands.

The graphene-only island seen in figure 7.6b appears to have a central point at which growth has been initiated that has an approximate 25 nm diameter. Figure 7.7a and b) show topographical AFM contact mode images of a region on a MBE hBN sample measured before and after carbon deposition. In this region a graphene-only island has appeared following graphene growth, along with some additional graphene bands grown around hBN islands seen in the upper right and lower left corners of figure 7.7b. The growth of this graphene island does not appear to have been initiated by any feature that could be resolved in the image taken prior to carbon deposition in a). The CAFM images of this island, shown in figure 7.7c, d), and g), reveal a 16 nm wavelength moiré pattern with a central region resembling that seen in figure 7.6b.

Figure 7.7e and f) show similar CAFM images of an additional graphene-only island, with a moiré wavelength of 18 nm, displaying a similar central feature. This feature is comparable to the secondary hexagonal pattern due to quasiparticle scattering, with a wavelength which is $\sqrt{3}$ times that of the lattice and at a respective angle of 30°, that was observed in chapter 5, seen in figure 5.18c, and explored in figure 5.19.

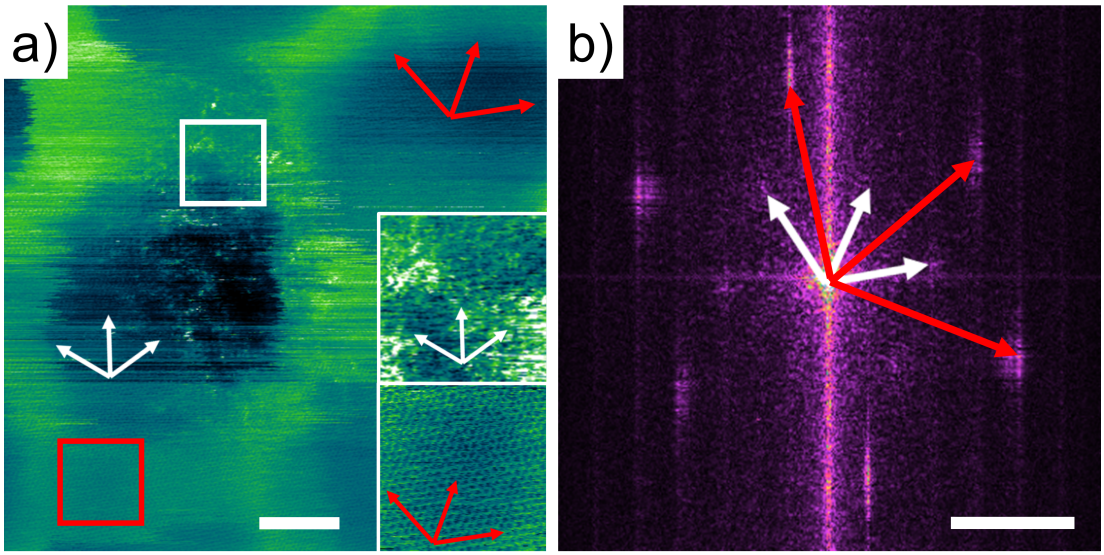


FIGURE 7.8: Figure a) shows a CAFM image of the same graphene-only island central defect seen in figure 7.7e and f) with an increased magnification. In a) the graphene lattice has been observed, highlighted by the lower inset zoomed image of the region bounded by the red square, along with a faint hexagonal pattern with a larger wavelength similar to those observed in figure 5.19 in chapter 5, seen in the upper inset image. The presence of the lattice and the scattering pattern can be seen in the corresponding 2DFFT image in b). The red arrows indicate the reciprocal lattice vectors in b) and the directions of the lattice vectors in a) and a) inset. The white arrows represent the reciprocal lattice vectors of the $(\sqrt{3}\text{x}\sqrt{3})\text{R}30°$ scattering pattern in b), and the direction of the real-space pattern in a). The scalebars measure 5 nm in a), and 2.5 nm^{-1} in b). The colour range in a) spans from -170 to -240 nA.

Figure 7.8a shows a CAFM image of the central defect seen in the graphene-only island displayed in figure 7.7e and f) with higher magnification. In this image the lattice of the graphene island can be resolved, and is enhanced in the lower inset of a), which shows the 5.1 x 5.1 nm region indicated by the red box. Also within this image, there is a faint hexagonal pattern, larger than that of the lattice, seen within the vicinity of the defect area and highlighted by the upper inset 5.1 x 5.1 nm image of the area bounded by the white box in a). The presence of this secondary hexagonal pattern is confirmed by a 2DFFT of the image shown in a), displayed in panel b) of figure 7.8. In this panel the red and white lines indicate the three directions of the reciprocal vectors for both the lattice and the secondary pattern respectively. The real-space directions

corresponding to these vectors are indicated in a), and the insets of a).

In figure 7.8 the extracted lattice constant is measured to be 0.25 $\pm$ 0.01 nm, which is in line with the expected value for graphene (a_G = 0.246 nm). The corresponding measurements for the secondary pattern give a result of 0.48 $\pm$ 0.03 nm. The ratio of these two measurements is equal to 1.92 $\pm$ 0.14 which is relatively close to the expected value of $\sqrt{3}$ (1.732) described in section 5.5 of chapter 5. Furthermore, the secondary pattern exists at an angle of 29.9 $\pm$ 2.6° with respect to the lattice direction, which is in agreement with the expected value of 30°. The observation of this ($\sqrt{3}$ x $\sqrt{3}$)R30° pattern provides evidence that there is a defect at the centre of the graphene-only island as outlined in section 5.5 [129]. It is unclear whether this defect is situated in the graphene or the hBN lattice, however it is reasonable to infer that the defect lies in the underlying hBN material, with the presence of the defect acting to initiate the growth of the graphene island outwards from the initial point during deposition.

7.5 Raman Measurements of MBE hBN and Graphene Nanoribbons

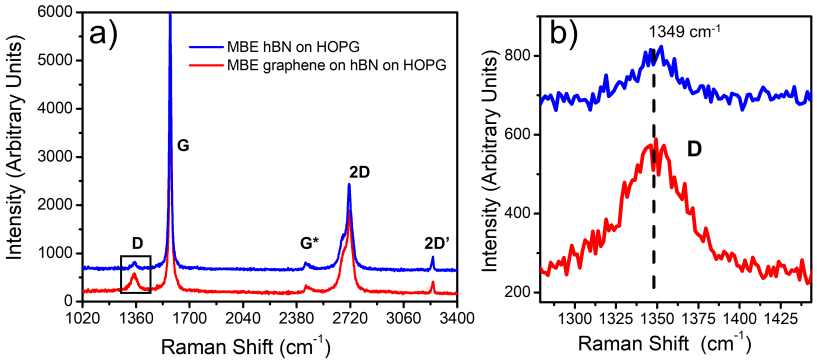


FIGURE 7.9: Raman spectroscopy measurements comparing MBE hBN grown on HOPG to a sample with subsequent graphene growth. a) shows the measured spectral range, while b) shows a zoomed region of the graphitic D peak at 1349 cm^{-1} enclosed by the black box in a). There is no observable presence of a hBN peak, expected at 1370 cm^{-1}. Additional graphitic peaks are observed at 1578 cm^{-1} (G), 2439 cm^{-1} (G*), 2716 cm^{-1} (2D), and 3246 cm^{-1} (2D') (each with an associated $\pm$2 cm^{-1} error).

These samples have been investigated using Raman spectroscopy to gain information about the hBN and graphene quality and strain levels, but, in agreement with

previous work on similar samples [145], the spectral region close to the hBN E2g peak is dominated by the D peak from the underlying graphite. Figure 7.9 shows the Raman results for two samples. The first, shown in blue, displays data recorded for an MBE grown hBN sample on HOPG with a coverage below 1 monolayer. The red line shows data for the MBE grown graphene on MBE hBN on a HOPG substrate sample shown in figures 7.2, 7.3c, and 7.5.

These Raman spectroscopy measurements were acquired using a Horiba-Jobin-Yvon LabRAM Raman microscope, following the same procedure outlined in section 5.3.1 using a laser wavelength of 532 nm operating at >4 mW and a 600 lines/mm grating and a Synapse CCD detector. The Raman shift was calibrated using a Si(100) reference sample. The graphite D peak at 1349 cm^{-1} bounded by the black box in figure a) is enlarged in figure b). There is no sign of a hBN peak, expected at 1370 cm^{-1} as seen in figures 5.5 and 5.12, due to the large overlapping signal from the graphitic D peak in this region. Other observed graphite peaks have been labelled in a) and exist at 1578 cm^{-1} (G), 2439 cm^{-1} (G*), 2716 cm^{-1} (2D), and 3246 cm^{-1} (2D') (each with an associated ± 2 cm^{-1} error).

7.6 Conclusions

It is clear from the results shown in this chapter that for high-temperature MBE growth, at a substrate temperature of 1390 °C, graphene preferentially grows laterally from the edges of hBN in a mode of step-flow growth, which results in the formation of lateral graphene-hBN heterojunctions. The graphene and hBN regions show a clear epitaxial relationship through the alignment of atomic lattices. However, the variations in strain for different regions revelaed by different, and locally-varying, moiré periods suggest small differences of lattice constant in the graphene and hBN regions. These differences are likely to be relieved by defects in the interfacial regions [146, 147]. The morphology of the graphene is somewhat different to that observed in the MBE growth on exfoliated hBN flakes seen in earlier chapters where the step density is very low. The epitaxial hBN on HOPG studied here has a much higher density of steps, including those around hexagonal hBN islands, which are not observed on exfoliated flakes. Growth around the hexagonal hBN islands provide a route to the formation of multiply connected regions of graphene and in addition leads to a free edge, which alternates between armchair and zigzag terminations. Interestingly, a complementary structure of hBN strips grown around a hexagonal graphene island using chemical vapour deposition has recently been reported, but with much larger dimensions [148]. Preservation of the edge termination during sequential MBE growth could lead to selective growth of oriented lateral hBN-graphene heterointerfaces, which possess novel electronic and magnetic properties [107]. Most importantly, in this mode of

growth the width of the graphene strips shows a high degree of uniformity across the hBN, offering the prospect of controllable growth of graphene rings and nano-strips with dimensions small enough to lead to measurable quantum confinement and magnetic flux quantisation effects. In addition, more complex hBN structures have been shown to successfully sustain graphene nanoribbon growth, as shown by the growth around a screw dislocation displayed in appendix C. These results show clearly that high-temperature MBE provides a route to the formation of lateral heterojunctions and novel in-plane heterostructures between graphene and hBN.

Chapter 8

Hydrogen Etching of Hexagonal Boron Nitride

8.1 Introduction

Hexagonal boron nitride has been used extensively throughout this thesis as a near ideal substrate for graphene growth, with both exfoliated hBN flakes, and MBE grown hBN samples investigated. In its hexagonal crystalline form BN is considered to be exceptionally stable up to high temperatures ($\sim 800\ ^{\circ}C$), with strong thermal and chemical inertness, that was described in further detail in section 2.2 of chapter 2. Etching of hexagonal boron nitride has been previously observed for CVD grown hBN located on a catalysing copper substrate [143, 149, 150], however the etching of hBN investigated within this chapter occurs in the absence of a catalyst for both exfoliated and MBE grown material.

In this chapter the first section describes the samples and conditions where the appearance of hBN etching was observed following thermal cleaning procedures intended to remove carbon aggregate clusters covering large portions of MBE graphene samples grown on exfoliated hBN flakes. Following the observation of the resultant hBN etch pits, the subsequent sections present the investigation of hBN etching, first on exfoliated hBN control samples, followed by looking at the same procedures carried out on MBE grown hBN samples.

8.2 Hydrogen Etching

8.2.1 The Appearance of hBN Etching

The etching of exfoliated hBN on the samples shown within this chapter was first observed in this work following high temperature cleaning of exfoliated flakes that had

undergone MBE graphene growth using the same procedures as used for the nanoribbon growth seen in chapter 7. Bulk hBN was mechanically exfoliated onto a sapphire substrate, these flakes were then imaged using AFM to find regions where there were hBN step edges in abundance, in order to initiate step-flow growth of graphene nanoribbons as described in chapter 7. For mechanically exfoliated samples there are large hBN plateaus devoid of step edges covering the vast majority of flakes - limiting the regions where this growth can occur. Figure 8.1a shows a topography channel AFM image of a region that was identified to have a large number of hBN monolayer step edges that have formed due to the exfoliation process causing tears and cracks in the layer. In this figure the numbers indicate the hBN layer relative to the lowest hBN bulk layer seen within the image, these step edges have been determined using topography profiles, with an example shown in figure 8.1c measured along the red line in a). Following the identification of several similar regions, graphene was grown by Tin S. Cheng and Sergei V. Novikov on this sample using the vertical electron beam evaporator EBVV 63-T4, fitted with a high purity carbon anode target under the same conditions as described in section 7.2. The e-beam current was increased to 300 mA, with a ramp rate of 10 mA/min, and held at this value for a growth time of 1 min, then ramped down at a rate of 100 mA/min. The accelerating voltage of the e-beam was 5 kV and the substrate temperature was 1390 °C.

Following graphene growth this sample was imaged a second time, ex situ, using AFM. Figure 8.1b shows a topography channel AFM image of the resulting graphene nanoribbons appearing at the hBN step edges of the same region shown in a). The graphene nanoribbons have a measured width of 71 $\pm$ 5 nm that is comparable to similar growth conditions for the nanoribbons grown on MBE hBN seen in chapter 7 of 83 $\pm$ 11 nm (figure 7.3c). Also visible on the sample shown in figure 8.1b is a large hBN fold, labelled in b), appearing across the flake. These folds are commonly seen for hBN flakes that have been exposed to thermal treatment, with further examples provided in appendix D. In contrast to the nanoribbons grown on MBE hBN, the graphene grown on these exfoliated samples display large amounts of carbon aggregates adhering to the hBN step edges. These can be seen as the bright deposits around the hBN step edges in figure 8.1b, and have a varying height of up to approximately 9 nm, as displayed by the profile given in d), measured along the blue line indicated in b).

In an attempt to reduce the amount of aggregates present at these boundaries to try and achieve a cleaner hBN/graphene interface the sample was placed in a furnace at atmospheric pressure at 400°C in a H_2/Ar gas flow with a ratio of 5:95 for a total of 4 hours at the maximum temperature. The same regions identified prior to graphene growth, and subsequently imaged post growth, were located and re-imaged, with no

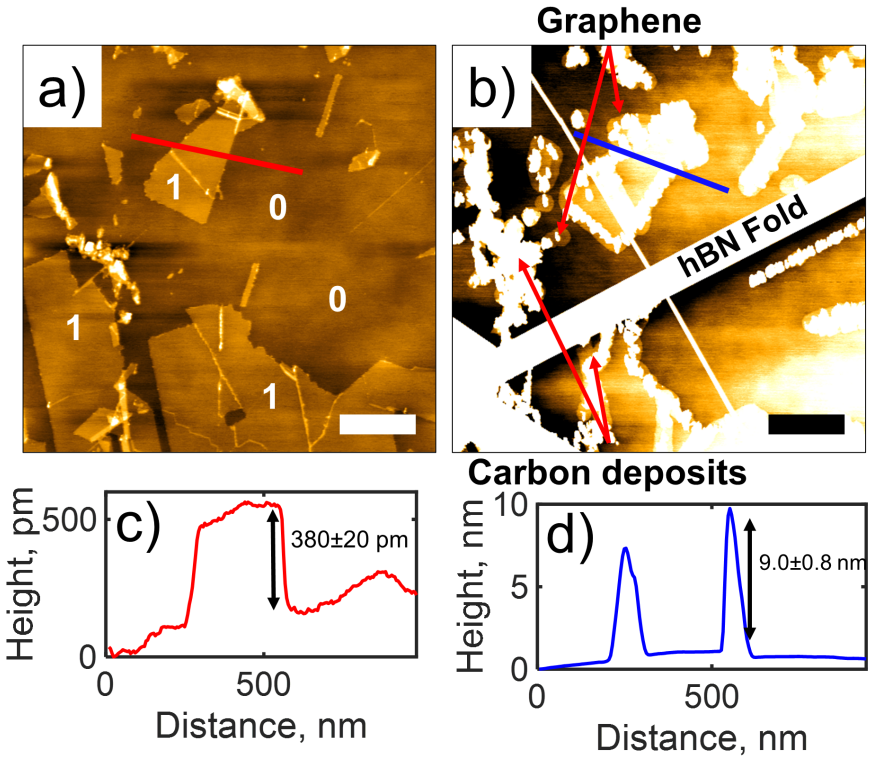


FIGURE 8.1: a) Topography channel AFM images of a region on an exfoliated hBN surface. Different hBN layers are indicated by the numbers - with 0 indicating the lowest bulk hBN layer in the image. b) the same region as a) imaged following graphene growth. A large hBN fold has been introduced by the growth process (labelled). At the hBN step edges in a) large aggregates of carbon deposits accrue during growth. These deposits appear to have acted as nucleation sites for lateral graphene nanoribbon growth. Panels c) and d) show profiles measured along the red line in a) and the blue line in b). They show the raised hBN regions and carbon deposits are 380 $\pm$ 20 pm and $\sim$ 9 nm in height respectively. Further images of this region can be seen in figure 8.2. The scalebars in a) and b) both measure 500 nm.

sample difference recorded. This was repeated a second time, using the same conditions but with a maximum temperature of 800°C, followed by a third time at 1000°C (maximum available temperature) for 8 hours. The second sample heating resulted in no noticeable sample change, however, following the 1000°C cycle interesting, triangular etch pits had formed in the hBN layers, while the graphene remained unchanged. The investigation of the hBN etching observed on these samples, followed by exfoliated hBN control samples and MBE hBN samples grown on HOPG, is the focus of this chapter.

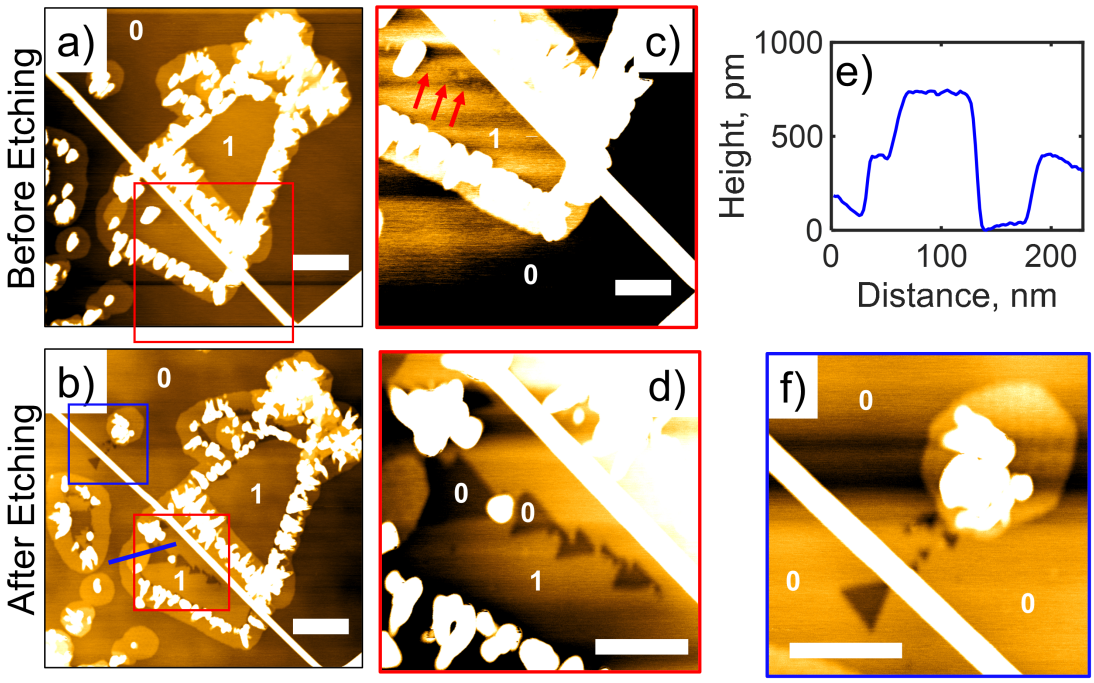


FIGURE 8.2: The region shown in this figure is the same as that seen in figure 8.1 before graphene growth. Figure a) shows a topography channel AC mode AFM image of a raised hBN region with carbon aggregates and graphene nanoribbon growth surrounding the step edges. The numbers in this figure indicate the hBN layer height, with 0 indicating the lowest observed layer. The region bounded by the red box is displayed in c). The graphene nanoribbon widths were measured to be 71 $\pm$ 5 nm for these images. b) Shows the same region as a), imaged in the topography channel of an AC mode AFM scan, following etching. The graphene remains unchanged, whereas triangular etch pits have appeared in the hBN. The regions bounded by the red and blue boxes in b) are shown in panels d) and f), with a profile recorded along the blue line in b) shown in e) confirming the monolayer etch pit depth. Visible defects can be seen prior to etching in panel c) (indicated by the red arrows) at the location where the etch pits seen in d) appear. The scalebars measure 200 nm in a) and b), and 100 nm in c), d), and f).

8.2.2 Etching of Exfoliated hBN with MBE Graphene Nanoribbons

Figure 8.2a and b) show the same hBN monolayer raised region as seen in figure 8.1 where the appearence of hBN etching was first observed, with a higher magnification. In this figure the numbers indicate the hBN layer relative to the lowest bulk hBN layer in the vicinity. Figure 8.2a and b) are topography AFM images recorded before and after a 1000°C 8 hour etch cycle in a furnace with a H_2:Ar (5:95) atmosphere respectively. In b) there are several triangular pits formed, both on layer 0 and layer 1. The regions enclosed by the red boxes in a) and b) are shown in figures c) and d) where the etch pit location on the raised hBN region is seen before and after the etch process.

There are a series of these pits of varying dimensions, up to approximately 100 nm in size seen in d). These pits are all oriented with their edges aligned along the same direction, and have a depth of 1 monolayer, confirmed by the topographic profile shown in e) measured along the blue line in b). Investigating the location of the hBN pits in images recorded prior to etching in c) shows the presence of a defect line, indicated by the red arrows. This is assumed to be a hBN domain/grain boundary within the bulk material, and appears to have initiated the etching process, with the corresponding pits seen in d) matching that of the boundary line. Panel f) of figure 8.2 shows the region bounded by the blue box in b). In this region of layer 0 several smaller etch pits can be seen all of which are locally aligned. This alignment, however, does not match that of the pits seen within panel d) on layer 1. The orientation of the pits on layer 0 are reflected, with a triangular shape in d) that points towards the top of the image, compared to a pit that points towards the bottom of the image seen in f). Despite this difference, the direction of the individual etch pit edges on layer 0 and layer 1 match.

The observation of the appearance of similar triangular etch pits in hBN has been reported elsewhere [143, 149, 150]. In their work, *Sharma et al* [149] observe triangular shaped hBN etching on CVD grown monolayer hBN on a Cu substrate for similar etching procedures of heating between 850-1020°C in a H_2/Ar atmosphere (with a lower H_2:Ar ratio of 2.3:97.7). In their case, and for other comparable work [143, 150] the activation energy required to break the B-N bond to form BH_X and NH_X species is lowered by the underlying catalysing copper foil allowing for fast etch rates, the etch pits observed by *Sharma et al* are in excess of a lateral dimension of 1 μm in size for 7 min of etching. The samples investigated for exfoliated bulk material seen in this thesis differ from previous reports [143, 149, 150] due to an absence of a catalyst material that has resulted in far slower etch rates, with pits exhibiting a lateral size of 100 nm seen following an 8 hour etch cycle.

Figure 8.3 shows further examples of the etching seen in figure 8.2 for a MBE graphene nanoribbon grown on an exfoliated hBN sample. These topography AFM images have all been recorded ex-situ following the etch procedure described earlier. Figure 8.3a shows an image of a raised hBN region bounded by graphene nanoribbons and carbon aggregates growing at the monolayer height hBN step edges. The nanoribbon width in this image is 65$\pm$4 nm. In panel a) the etching has occurred predominantly around the graphene/hBN interface, indicated by the red arrows. Here monolayer height gaps in the material are observed, with triangular faceted etching similar to those seen earlier. The heights of the layers are indicated, and have been determined using topography profiles, with the profile in panel d) recorded along the red line in a), passing over a raised hBN region, over an etch pit at the graphene/hBN interface, then over a graphene nanoribbon (labelled G). Panel b) of figure 8.3 shows a separate region where a large amount of oriented triangular etch pits of varying

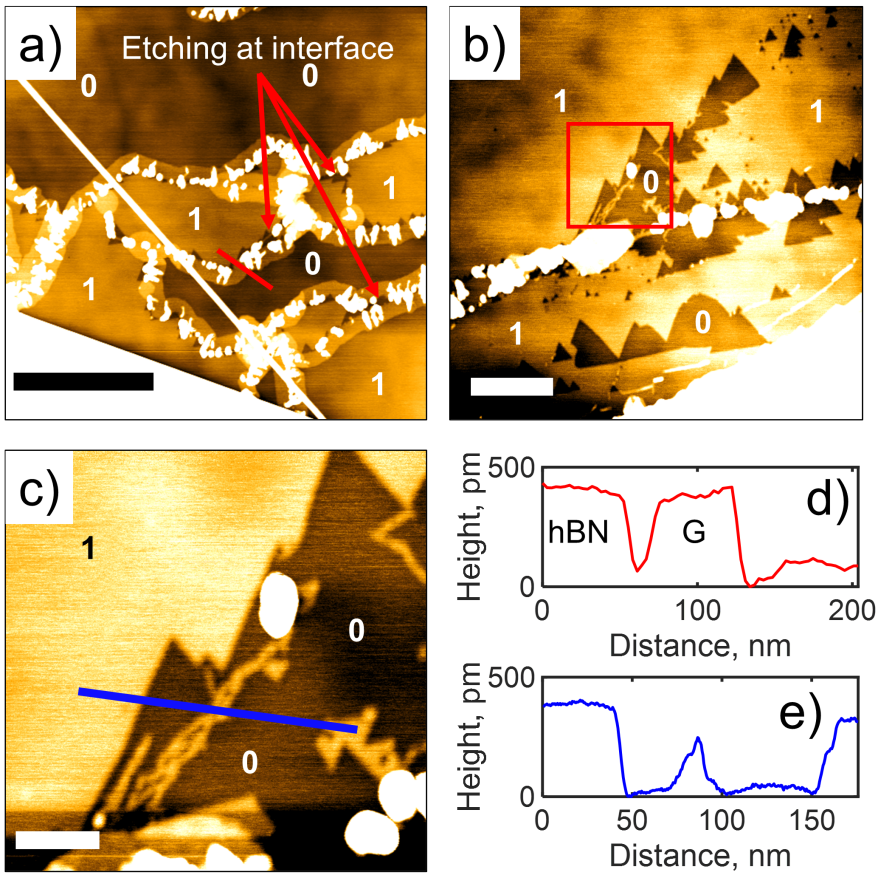


FIGURE 8.3: a-c) show topography channel AC mode AFM images of different locations on the same sample shown in figure 8.2. In all panels the numbers represent the height relative to the lowest visible hBN layer. In a) a large amount of graphene nanoribbons are visible, with a measured width of 65 $\pm$ 4 nm. b) shows a region where there are many triangular etch pits of different sizes, all of which are oriented in the same way. The region bounded by the red box is shown in c). Panels d) and e) show profiles recorded along the red line in a) and the blue line in c). The scalebars in a), b), and c) measure 500 nm, 200 nm, and 50 nm respectively.

sizes are present and overlapping. The grouping of the etch pits seen in panel b) suggest that the region was the location of a domain boundary in the exfoliated hBN. In some of the areas where the triangular etched pits have joined there is the appearance of some linear string-like material, shown in panel c) with more detail, where the region shown is indicated by the red box in b). The material at the centre of this image appears lower in height than the raised/unetched hBN - as demonstrated by the profile in e) recorded along the blue line in c). In addition, at the location where the blue profile line ends there are some small remaining raised hBN regions that, due to the surrounding etching, have resulted in a triangular shape, with a direction that is pointing in the opposite way to that of the etch pits.

8.2.3 Etching of Exfoliated hBN

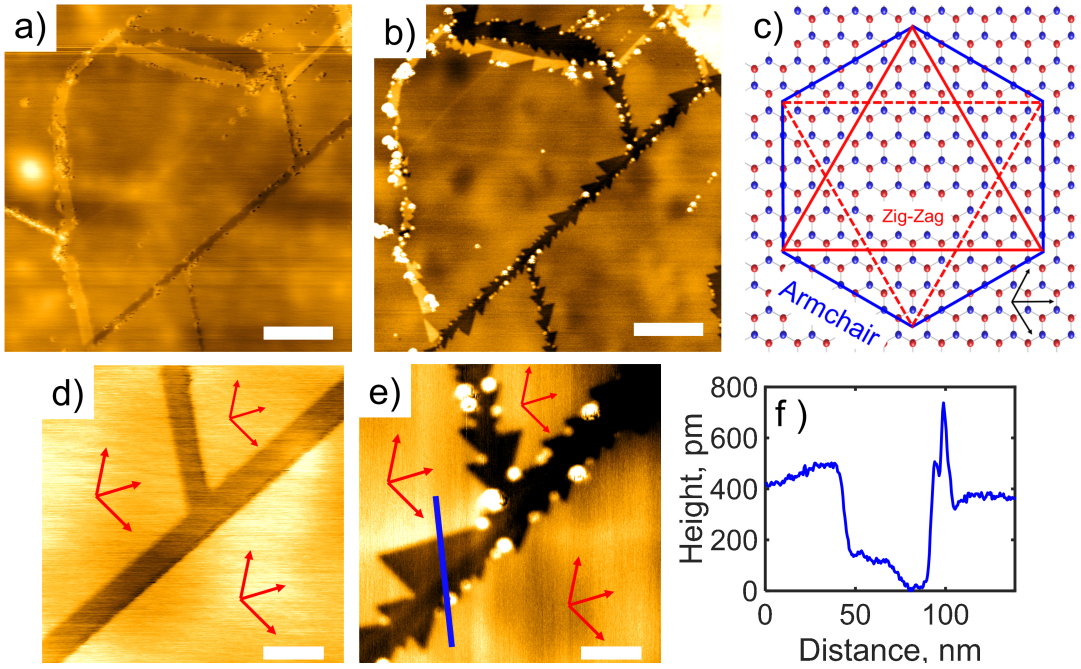


FIGURE 8.4: Panels a), b), d), e) show topography channel AFM images of the surface of an exfoliated hBN flake. Figures a) and d) show the sample before etching, with corresponding images recorded following etching shown in b) and e). The trenched region seen in a), likely formed during exfoliation, has been etched along its entire length in a sawtooth manner, as seen in b). c) Diagram illustrating the differences between armchair (blue) and zigzag (red) terminations in hBN. The two red triangles (dashed and solid lines) indicate zigzag terminations for the two atomic species. The black arrows indicate the lattice direction in this diagram. Panel d) shows a zoomed region of a), with red arrows indicating the local lattice direction, determined using 2DFFT analysis of several LFM images. These directions confirm that the hBN step edges in a) are armchair terminated, and the edges revealed by etching in b) are zigzag terminated. Panel f) shows a profile measured along the blue line in e). The scalebars in these images measure 200 nm in a) and b), and 50 nm in d) and e).

Having seen the appearance of etch pits in the exfoliated hBN on the graphene nanoribbon samples seen in the previous section, several control samples of mechanically exfoliated hBN on a sapphire substrate were investigated. Figure 8.4 consists of a set of AFM topography images of a surface of an exfoliated hBN flake on one of these samples recorded before (a) and d)) and after (b) and e)) an etch cycle of 8 hours at 1000°C under H_2/Ar (5:95) flow. The imaged region in a) consists of a series of trenches with a single hBN layer depth (confirmed by the profile shown in panel f)), most likely formed during mechanical exfoliation. These trenches are oriented at 60° to each other, which indicates that they may have formed along one of the principal lattice directions. Figure 8.4 b) shows the same region as a) following etching. The

islands towards the top of the region have been etched, along with the trenches seen across the image. The etching has left a sawtooth edge along each of the hBN step edges. Panels d) and e) of this figure show the same region towards the top right-hand side of panels a) and b), and were recorded before and after etching respectively. These images show the sawtooth edge revealed by the etching along the step edges with more clarity. The etched edges are at right angles (and at 30°) to the original trench directions. Using high resolution LFM imaging of several regions surrounding the area in panel e) the hBN lattice directions were determined through 2DFFT analysis. These directions have been indicated on panel d) and e) with red arrows. This information allows us to determine the type of termination of both the original trench edges, and the etched sawtooth edges. The sawtooth edges have orientations matching that of the hBN lattice, confirming a zigzag termination as illustrated in panel c) of figure 8.4, whereas the initial trenches are all at 30° confirming armchair terminated edges.

This assignment of etched edge termination is similar to the triangular shaped etching that has been observed. In the diagram shown in panel c) of figure 8.4 the armchair lattice directions are at 30° to the lattice directions (indicated by the black arrows), and combine to form a hexagonal structure in which all edges are atomically equivalent. However, for the zigzag orientated edges, indicated in red, there are two situations that can occur - boron terminated edges, or nitrogen terminated edges. These are indicated by the solid and dashed red lines in c). If one of these zigzag atomic termination edge types (either boron or nitrogen terminated) is energetically favourable then triangular etching, as has been observed, would be expected. In contrast, if armchair edges were energetically favoured, then hexagonally etched pits would be expected due to the equivalence of all armchair edges. This preference of zigzag edge termination is observed by others to be the cause of the triangular etching [143, 149]. In their work *Y. Stehle et al* [143] observed that altering the buffer gas composition used while etching from H_2:Ar, as used in this thesis, to H_2:N_2 influences the type of zigzag termination present. The expected zigzag edge is nitrogen terminated hBN, as this form of termination is the most energetically favourable [106, 143, 149, 151, 152].

Figure 8.5a) and b) show a diagrammatic representation of the etch process of an exfoliated hBN sample on a sapphire substrate with multiple hBN step edges. The original step edges, displayed in blue in panel a), are etched to reveal zigzag terminated edges, shown in red, as well as introducing triangular etch pits at locations across the surface.

As described in section 2.2 of chapter 2 the stacking order of hBN follows an alternating order in which B atoms sit directly above/below N atoms in adjacent layers, as

demonstrated in panel c) of figure 8.5, which shows the same diagrammatic representation of the hBN layer structure as seen in figure 2.5b of chapter 2. For etched zigzag edges sharing the same species termination between layers the stacking order of bulk hBN should therefore result in triangular etching directions that are reversed between layers. This is displayed in the diagram in figure 8.5b where the direction of the etched sawtooth edges is reversed between the two layers. Furthermore, this reversing of the etched edge direction holds true for etch pits, and was seen earlier in the flipping of the direction of the triangular pits on layer 0 and layer 1 in figure 8.2b, d), and f). The topography channel AFM images shown in panels d-f) in figure 8.5 show a further example of this effect.

The image shown in panel d) shows a series of hBN monolayer height steps on an exfoliated hBN flake prior to etching, with the same area shown post etching in e). The original edges have been etched in a sawtooth/triangular fashion, with the profile shown in g) measured along the blue line in e) confirming the step edges are monolayer in height. The etched edges in the upper layer of this image have been highlighted by a solid red line, with edges that are, in general, all oriented along the same three directions. The lower etched edges are highlighted by a dashed red line and, while sharing a common set of directions with themselves, have a directionality that is reversed when compared to that of the upper layer. Panel f) of figure 8.5 shows an AFM image of the same area, covering a larger region of the etched surface. Within this image 5 different layers can be identified (labelled correspondingly). The pattern of flipping the directionality of the triangular etched edges is followed for nearly all layers in this image. However, there are two separate locations where this ordering is broken, indicated by the red circles; these are believed to be stacking faults in the hBN stacking order, i.e. the hBN lattices of the raised circled regions are expected to share the same alignment as the layer beneath them, in contrast to the expected hBN stacking.

The edges of the etched hBN have been confirmed to be zigzag terminated following a set of LFM images recorded at each of the locations where the white arrows are positioned, with the arrows indicating the local lattice directions.

8.2.4 Etching of MBE Grown hBN

Having observed etching of exfoliated hBN samples, the very different morphology of MBE grown hBN on a HOPG substrate was investigated. For hBN samples grown at high temperature using MBE on a HOPG substrate it has been shown in chapter 7 that it is common to observe hexagonal island BN growth on top of the initial hBN monolayer growth. The hexagonal shape of these islands suggest that they are terminated by armchair edges using the same reasoning described above for etching,

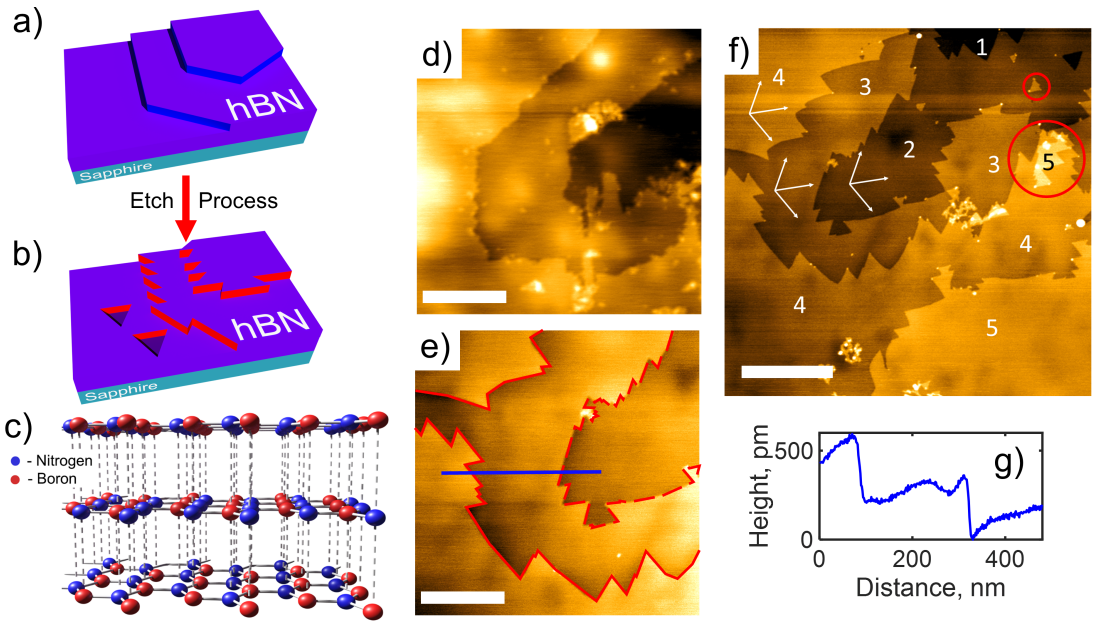


FIGURE 8.5: Panels a) and b) show a diagrammatic representation of an exfoliated hBN sample before and after etching. Zigzag terminated hBN step edges (indicated in red) are revealed by the etch process. Due to the stacking configuration of hBN, where B atoms are situated directly above N atoms (as shown in panel c)), and the preferential revealing of a single species ZZ termination, the shape of the revealed edges is reversed for each layer change. In addition, triangular etch pits with ZZ termination are observed, as indicated in b). d) and e) show AC mode AFM topography images of a region of an exfoliated hBN flake on a sapphire substrate recorded prior to, d), and following, e), etching. The revealed edges are indicated in e), where the solid and dashed red lines highlight the change in the edge directions between layers. A profile measured along the blue line in e) is shown in panel g). Panel f) shows an extended image of the region, where the layer number is indicated (with a value of 1 indicating the lowest bulk hBN region within the image). The white arrows indicate the local lattice direction as determined by 2DFFT analysis of LFM images recorded at the corresponding positions. The two red circles indicate stacking order faults, where the alternating of the triangular directions of the ZZ edges between layers is broken. The scalebars measure 250 nm in d) and e), and 500 nm in f).

which is that armchair edges are all equivalent, whereas there are different atomic terminations for zigzag edges that may result in triangular growth/etching. The edges of these hexagonal islands were confirmed in figure 7.4 of chapter 7 to be armchair terminated.

Figure 8.6a, b), d), and e) show several phase channel AFM images recorded using AC mode of a MBE hBN sample exhibiting similar hexagonal islands. This sample was grown by Tin S. Cheng and Sergei V. Novikov in an identical manner to that which was used to grow the hBN shown in figure 7.2 in section 7. hBN was grown on a prepared HOPG substrate by plasma-assisted MBE under UHV conditions (with a base pressure of $\sim 10^{-10}$ mbar) at a temperature of 1390 °C , with a high-temperature Veeco

effusion cell operated at 1875 °C to sublime boron, and a Veeco RF plasma source to generate the active nitrogen flux; this was operated at an N_2 flow of 2 sccm and an RF power of 550 W using a growth time of 3 hours. The phase images shown in panels a)

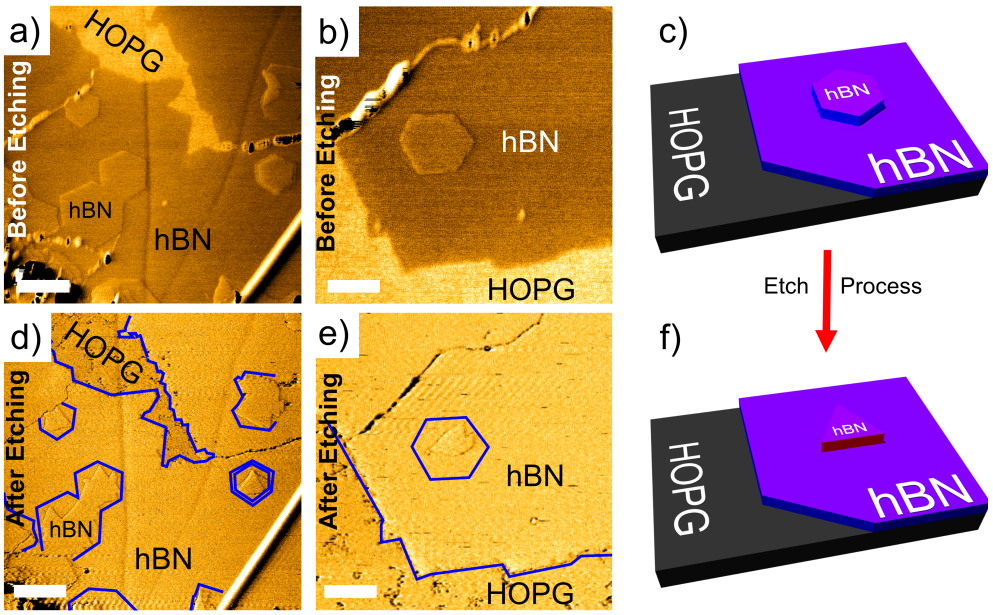


FIGURE 8.6: a) and d) show two phase images recorded using AC mode AFM of a MBE hBN sample prior to, and following, etching respectively. On the image recorded after etching the step edges of the original structure have been overlaid in blue. Figures b) and e) show a second, similar location recorded in the phase channel and measured both before and after etching, showing the same observations. c) and f) show a diagrammatic representation of the MBE hBN etching. The hBN islands displaying a hexagonal structure are terminated with armchair edges (indicated in blue) following growth. Etching these surfaces leaves a zigzag termination on the hBN structures, while very little etching occurs at the hBN/HOPG step edge. The scalebars measure 200 nm in a) and d), and 100 nm in b) and e). The inversion of contrast in the phase images recorded before and after etching is likely a result of different tip/scanning conditions.

and b) of figure 8.6 show two separate areas of the MBE hBN sample measured before etching took place. In both images the hBN is clearly distinguishable from the HOPG substrate, exposed regions of which are labelled. Panels d) and e) of this figure show the same two regions as a) and b) recorded following an 8 hour etch cycle at 1000°C in a H_2/Ar (5:95) atmosphere. The top images were overlaid on the lower images, allowing for the edges of the original growth to be highlighted with blue solid lines, and the changes due to etching to be clearly visible. The original hBN islands have been etched to reveal triangular shapes in a similar way to that which was seen for exfoliated material. Interestingly, there is no significant etching visible at the hBN/HOPG step edge. Panels c) and f) show a simplified diagrammatic representation of the etching process

for these structures, where the hexagonal hBN island with armchair termination (indicated in blue) is etched to reveal zigzag terminated edges (indicated in red), and can be compared to etching of hBN on mechanically exfoliated samples seen in figure 8.5a and b).

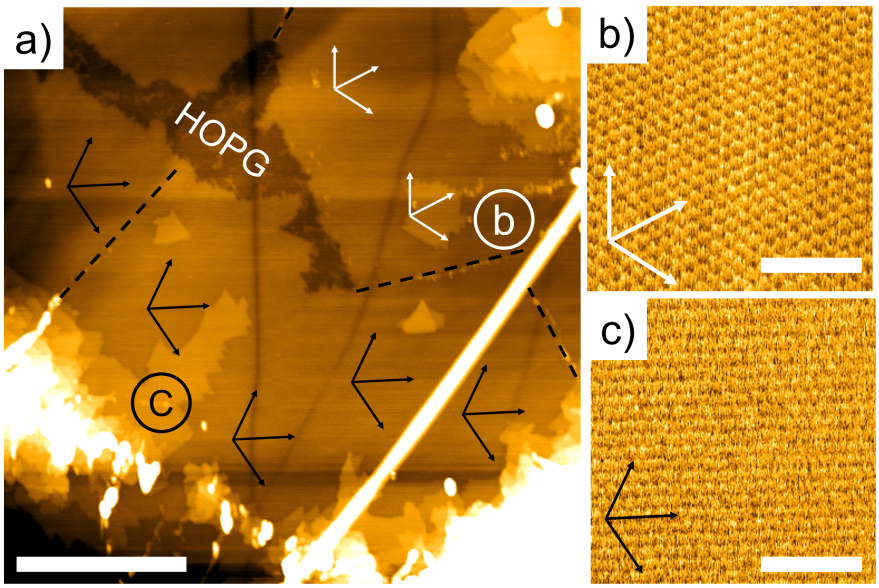


FIGURE 8.7: Panel a) shows an AFM topography image of an expanded region of the area shown in figure 8.6a and d). The arrows indicate the local hBN lattice directions as determined through 2DFFT analysis of lattice resolution LFM images (15 locations were imaged in total), examples of which are shown in panels b) and c), with their locations indicated in a). The dashed black lines indicate identified domain boundaries. A difference of 26 ± 2 degrees was measured between the lattices in these two regions. The scalebars measure 500 nm in a), and 2 nm in both b) and c).

Figure 8.7 shows a height channel AFM image corresponding to the etched region shown in figure 8.6d with a larger area on display. The bright features along the lower edge of this image are deposits formed during the hBN growth process. The raised hBN islands within the lower and left-hand side of this image all display sawtooth/triangular etched edges which, in general, are aligned with each other. However, the etched edges of the island in the region in the upper right-hand side of the image (next to the region labelled b) shows an orientation that is approximately at 30° to those of the left-hand region. A topographically low line indicating a domain boundary between these regions can be seen (below the region labelled b, and indicated by the dashed black line). A series of high resolution LFM images were recorded at 15 locations across the area shown in a), two examples of which can be seen in panels b) and c) of figure 8.7, measured at the indicated locations in a). Using 2DFFT analysis the lattice constants and directions were extracted. The hBN lattice constant

in these images was recorded to be 0.252 $\pm$ 0.005 nm in b) and 0.253 $\pm$ 0.005 nm in c), in agreement with the expected value for hBN. The difference between the lattice angles extracted from the images in b) and c) was measured to be 26 $\pm$ 2 °. The corresponding local lattice directions extracted from the series of LFM images are indicated in figure 8.7a by the black and white arrows. LFM imaging of the exposed HOPG region revealed a faint lattice pattern that matches the orientation indicated by the black arrows, and the region labelled c).

The 26 $\pm$ 2 ° difference between the lattice measured at position b) and c) in figure 8.7a confirms that the change in the direction of the etched edge is due to a relative rotation of the hBN lattice, and confirms that the same zigzag edge termination is seen in both regions. The area in the upper left-hand side of panel a) shows close alignment to the region labelled c), suggesting a different style of domain wall compared to that separating region b) from c). This means that by etching the hBN surface it is possible to identify domain boundary types, and hBN domains with a different lattice orientation without the requirement of lattice resolution imaging, and could prove to be a useful identification technique where high resolution instruments are not available.

While in most instances the hBN domain boundaries remain unetched for MBE hBN samples, for example the domain boundaries seen in figures 8.6 and 8.7, figure 8.8 shows a case where etching at the domain boundary, similar to that seen on the exfoliated hBN, was observed. Panels a) and b) of figure 8.8 show two topographic AFM images, with the location of the area imaged in b) highlighted by the red box in a). In these figures the raised hBN consists of a few different domains (labelled i-iv), with 4 visible in a), and 3 visible in b), the boundaries of which can be seen as raised lines, with the exception of the etched domain wall bounding region i) and ii) that is enlarged in panel b). The etching along this boundary shows sawtooth edge etching similar to that seen for hBN step edges, however here the orientations of the sawtooth pattern on either domain edge are not aligned. This is shown in panel b) where the angles between etched edges are measured to be 46.9 $\pm$ 5 ° and 46.3 $\pm$ 3 ° for angles 1 and 2 respectively. This leads to an approximate right angle difference between these two angles (93.1 $\pm$ 6 °), which, assuming that the revealed edges have the same zigzag structure, indicates a relative rotation of the two lattices of approximately 30°. Further evidence of this change in lattice orientation is given by the lack of a visible moiré pattern in region ii). In regions i), iii), and iv) there are hBN/HOPG moiré patterns visible with wavelengths measuring 14.6 $\pm$ 0.5 nm, 13.8 $\pm$ 0.5 nm, and 14.0 $\pm$ 0.3 nm respectively. Using equation 2.35 in chapter 2 the moiré pattern for 30° rotationally misaligned hBN and graphite lattices is approximately 0.5 nm, which is not resolvable in the recorded image shown in figure 8.8a or b) due to the image resolution.

Also very evident in figure 8.8 are significant amounts of unidentified material on the HOPG region. This material appears following the etch process, and has a

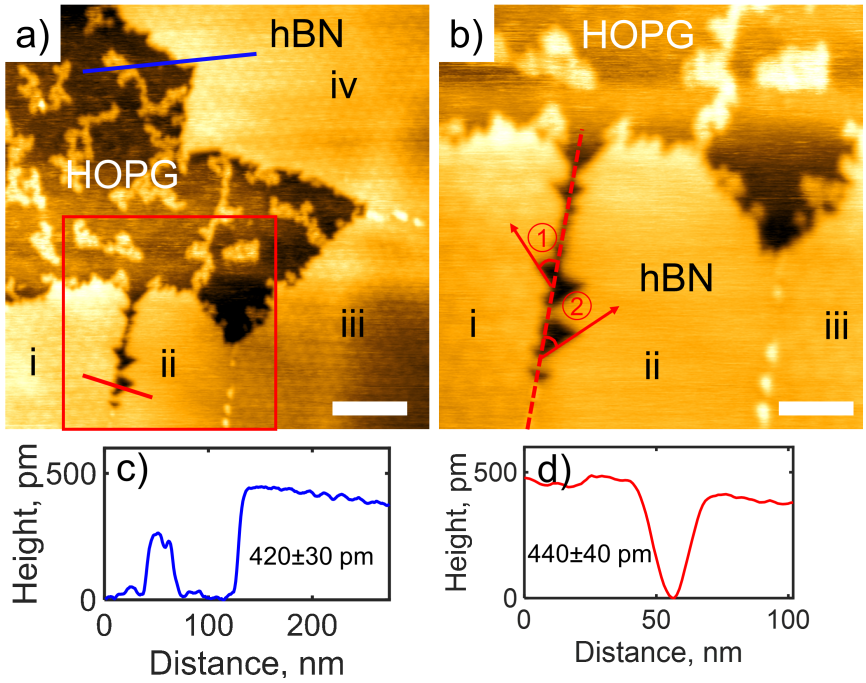


FIGURE 8.8: a) shows a topography channel AC mode AFM image of a region of a MBE hBN sample grown on HOPG following etching. The dark, low lying area in the upper left portion of the image is underlying HOPG. The etching process has left unidentified debris across this surface with an approximate height of 200 pm, as revealed in the profile in panel c) measured along the blue line in a), which confirms the step edge height to be monolayer. The region bounded by the red square in a) is shown in the enlarged image in b). Etching has occurred along the domain boundary (red dotted line). The difference between angle 1 and angle 2 is measured to be $93 \pm 6^{\circ}$. The different hBN domain regions are labelled i, ii, iii, and iv. Panel d) shows a second profile, recorded along the red line in a) confirming the etched regions depth is 1 monolayer. The scalebars in a) and b) measure 100 nm and 200 nm respectively.

varying topographic height of $\sim 242 \pm 20$ pm, as shown by the profile seen in panel c) measured along the blue line in a).

Figure 8.9 displays topography mode AFM images of an etched MBE hBN sample on HOPG where several layers are present. The layer number relative to the underlying HOPG is indicated. The panels shown in b) and e) show the regions bounded by the red boxes in a) and d). In figure 8.9a and b) many hBN layers display sawtooth edge etching. The edges of the layers on the right-hand side of panel b) adhere to the etched edge directionality flipping described earlier for exfoliated samples, seen here as the layer number increases with the different directionality highlighted by the red dashed and solid lines. This allows for the confirmation of hBN stacking order. However, the etched edges of the upper layer on the left-hand side of panel b) do not match those seen on the right-hand side of panel b), allowing for the identification of a hBN

grain boundary, indicated by the black dashed line, which separates the two regions with unaligned edges.

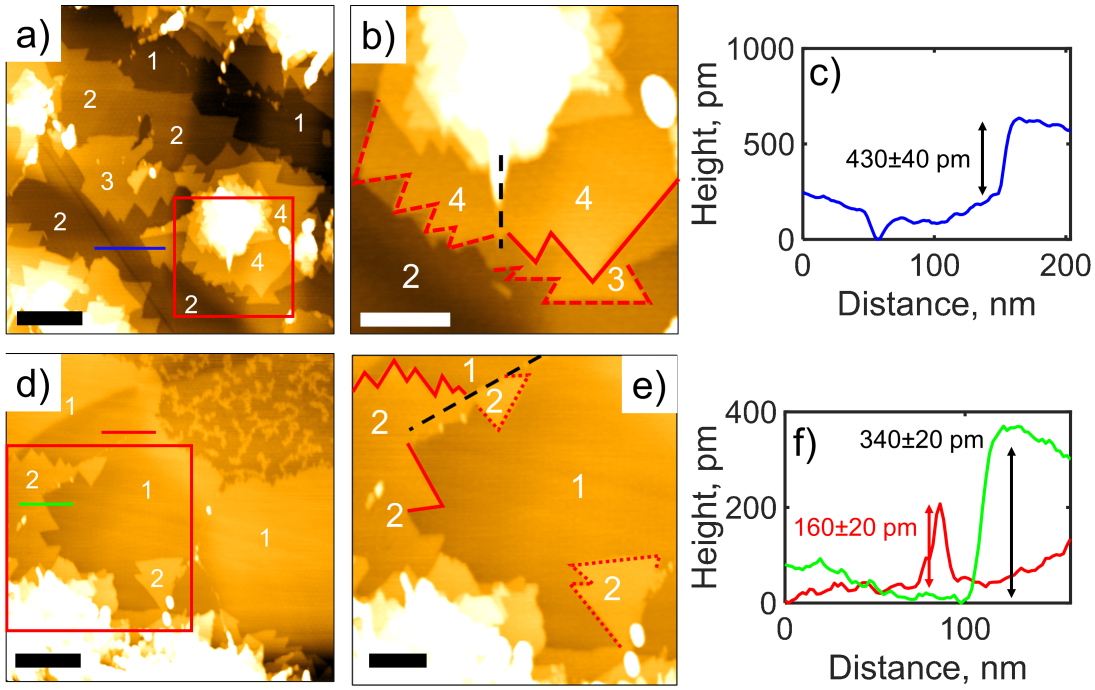


FIGURE 8.9: a), b), d), and e) all show topographic AFM images of a MBE hBN sample grown on HOPG following hBN etching. In these images the numbers indicate the hBN layer, with 1 indicating monolayer hBN on HOPG. The region bounded by the red box in a) is shown in b), with the profile shown in c) measured along the blue line in a). In panel b) the solid and dashed red lines highlight differently orientated etched edges, similar to those seen in figure 8.5 for each additional layer. Here the change occurs either side of a domain boundary, indicated by the black dashed line. The region bounded by the red box in d) is shown in e), with profiles recorded along the red and green lines in d) shown in panel f). The red line passes over a domain boundary, where a topographic feature of 160 ± 20 pm is observed, whereas the green profile passes over a monolayer hBN step edge measuring 340 ± 20 pm. In panel e) the dashed and solid red lines show differently oriented etched edges, where a difference can be seen either side of the domain boundary indicated by the black dashed line. The scalebars in a) and d) measure 200 nm, and in b) and e) measure 100 nm.

In panel d) a more planar region is shown. A similar directionality reversal of the etched edges of second layer hBN regions can be seen in the region shown in the enlarged image in panel e), with the differently orientated edges indicated by the solid and dashed red lines. The black dashed line in e) highlights the continuation of a hBN domain boundary, faintly visible in d), that can be seen clearly in the corresponding red profile displayed in panel f), measured along the red line in d). For the triangular

etched edges either side of this boundary, the alignment is shared, with the directionality flipped (see the difference between the red and dashed lines in figure 8.4). By assuming that the zigzag termination across the etched hBN is of the same type, most likely nitrogen terminated [106, 143, 149, 151, 152], it can be deduced that the raised etched regions seen either side of the domain boundary in e) have a different stacking order configuration with the position of N atoms and B atoms switched. This difference in the lattice configuration is the cause of the domain boundary formation during the coalescence of the two hBN domains during growth. It should be noted that the etched edge directions between these two regions may also be due to a stacking order defect of the second layer, but the observation that the domain boundary extends through the first layer suggests otherwise.

8.3 Conclusions

The etching of hBN samples investigated within this chapter is similar to that which has been seen elsewhere for etching CVD hBN grown on a copper substrate, where the Cu is used as a catalyst to enable the hBN hydrogen etching within a H_2/Ar atmosphere [143, 149, 150], however for the etching observed within this work, no catalytic surface is present - resulting in far slower etching.

The hydrogen etching of the hBN seen within this chapter has been shown to occur at hBN step edges, and at locations of defects/domain boundaries. The result of this etching reveals one of the two zigzag terminated edge types of the hBN lattice. This provides a route to identify edge types that have been imaged prior to etching, typically of armchair type within this work, without the requirement of lattice resolution imaging. In addition, the etching observed here appeared to cause no noticeable difference in the MBE grown graphene ribbon samples shown in figures 8.1, 8.2, and 8.3, with no etching seen at the hBN/HOPG step edge on MBE hBN samples either. On exfoliated hBN flakes this method has also been observed to highlight the location of hBN defects and grain boundaries, since these features initiate etching. In both exfoliated and MBE grown material the orientation of the revealed, sawtooth, zigzag edges, and triangular shaped islands have been used to locate stacking disorders in the material, and to identify the locations, and structure, of different domain/grain boundaries.

The etching of hBN step edges as seen in this chapter could be developed to provide a useful method for novel lithographic techniques. The slow catalyst free nature of this etching allows for precise, small scale etching of hBN. Furthermore, this etching facilitates lateral graphene nanoribbon growth (as seen in chapter 7) along a known hBN edge type, since the ZZ edge has been routinely identified to be the revealed edge during etching. The edge termination of graphene nanoribbons is a key factor in

determining the respective electronic band structure, including the introduction of a band gap[19, 31], as discussed in section 2.1.3, and the termination of the lateral hBN interface where these graphene nanoribbons are grown play an important role in the nanoribbon growth. The shape of the resultant etched hBN also allows for the patterning of triangular/sawtooth hBN edges. Finally, the obsevation that hBN can be removed from graphene nanoribbon hetero-interfaces (shown in figure 8.3) without the removal of the graphene provides further opportunities for this technique to be developed into an effective lithographic method.

Chapter 9

Conclusions

This thesis has demonstrated the successful use of a wide range of AFM/SPM techniques, with a large focus on CAFM, to probe the sample surface of graphene/hBN heterostructures. The samples that have been looked into have been grown using MBE, a relatively uncommon graphene growth technique that paves the way for high quality scaleable production. A variety of samples have been looked at in detail, with interesting results demonstrating a strong tip surface interaction that has been investigated and explained using ideas of pressure induced deformation of the sample surface, as well as novel lateral heterostructure growth of graphene nanoribbons.

In chapter 4 electrical connections have been successfully made in a reproducible and reliable manner to MBE grown graphene on exfoliated hBN. This has been carried out using a combination of several techniques expanded upon and developed within this work, including Ag NW deposition, epoxy contact creation, and flake transfer. These methods have been thoroughly tested and consequently used across a range of graphene-hBN heterostructures to produce samples where these electrical connections can be utilised in conductive AFM. The most prominent technique that was used throughout the remaining chapters was that of nanowire deposition, which was shown to produce a conductive networking layer. This layer, consisting of interlaced Ag nanowires, has allowed for SPM measurements to take place in the large gaps between the nanowires. The applied methods were particularly useful in permitting conductive measurements to take place across MBE graphene samples grown at high temperatures with regions that were otherwise electrically isolated on hBN flakes exfoliated on a sapphire substrate. These sample preparation procedures can further be applied to an extensive range of different samples for many applications where an electrically conductive networking layer is desired.

The methods developed in chapter 4 were implemented in chapter 5, along with other techniques and procedures described in chapters 2 and 3 to determine important structural properties for a range of MBE graphene samples with a variety of strain levels observed. CAFM was achieved using the electrical contacting methods that have

been developed, and has allowed for routine lattice resolution imaging under ambient conditions, providing useful information about the novel graphene structures that have been investigated, such as a varying density of states matching the moiré pattern. These high resolution images have also allowed for strain maps and identification of lattice defects. The amount of strain observed on these graphene samples, grown using the three different carbon sources described in chapter 3 (carbon filament, elemental carbon, and e-beam evaporation sources), ranged from a low value up to lattice matching with the underlying hBN for regions on samples grown at temperatures in excess of 1600 °C, as confirmed using AFM and Raman spectroscopy measurements. Many of the results recorded for the MBE graphene samples were used as feedback to influence the growth of additional samples allowing for material with fewer aggregates and higher strain to be produced.

While imaging these MBE graphene samples using AFM a departure from the expected moiré pattern with a hexagonal cell structure was observed and was seen to be more prominent while scanning in contact mode and with higher applied forces. A thorough investigation into this effect was carried out in chapter 6. Similar to the STM studies of *Yankowitz et al* [78], it was shown that by applying a local pressure to the graphene surface using an AFM tip the moiré cell boundaries appear sharper, with cells becoming deformed at higher applied forces. This phenomenon has been explained by considering the preference for the high symmetry stacking configurations. When the graphene is pressed closer to the hBN lattice the lower energy AB stacking order becomes increasingly favourable, and the local region is moved into an AB stacking configuration. This results in a moiré pattern image with a sharper boundary.

In addition to the deformation of the moiré cell, it was also discovered that by further increasing the applied force, the moiré pattern boundaries were displaced along the AFM tip fast scan direction in a reproducible and non destructive manner. The extent of these movements was observed to be in excess of several superlattice wavelengths and were explored in chapter 6 using LFM. The lateral force required to displace a boundary increases with distance moved, and an additional force is required at integer multiples of moiré wavelengths to overcome the presence of an extra cell boundary. The strong interaction between the AFM tip and the MBE graphene heterostructure demonstrated in this chapter is an important factor to consider when imaging any form of van der Waals heterostructure, and indicates that the structural changes due to the applied pressure of an AFM tip stabilise a configuration displaced from equilibrium. In addition, it may be possible to utilise this behaviour to selectively apply pressure to heterostructure surfaces in order to deform the moiré superlattice into a desired network of conductive channels, or to produce regions of increased strain.

In chapter 7 the electron beam evaporation source used for carbon deposition in MBE graphene growth has been used to grow narrow graphene strips along hBN step edges at high temperature. The resulting growth and lateral heterostructures were examined using AFM techniques, revealing locally-varying moiré periods, alignment of atomic lattices between the hBN and graphene, and novel graphene nanoribbon structures along all hBN and hexagonal island edges with a tunable width and a high degree of uniformity. For the lateral heterostructures explored in this chapter both the graphene and hBN have been grown by MBE using the same UHV system, and in some cases without removal of the sample from vacuum, demonstrating an important developmental step in molecular beam epitaxy for graphene heterostructures.

Chapter 8 describes the hydrogen etching procedures that were explored on a range of samples, including those shown in chapter 7. The etching that was used in this work is similar to that reported elsewhere on CVD grown hBN on a catalytic Cu substrate within a H_2/Ar atmosphere [143, 149, 150], however in this thesis the etched hBN was either exfoliated onto a sapphire substrate, or grown using MBE on HOPG, in both cases there was no catalytic substrate present, resulting in a very low etch rate. This etching has been observed to occur at hBN step edges, and at material defects and domain boundaries - highlighting their presence in the material. The revealed boron nitride edges have been shown within this chapter to be zigzag terminated, providing a route to graphene/hBN lateral heterostructures with zigzag terminated interfaces when combined with the work seen in chapter 7. In addition, no etching or damage to graphene was seen while etching samples consisting of graphene nanoribbons at hBN step edges, indicating a possible use of the technique in the removal of hBN material post nanoribbon growth, and as an effective lithographic technique that can be used in tandem with the novel MBE growth techniques investigated within this thesis.

Bibliography

[1] K. S. Novoselov. "Electric Field Effect in Atomically Thin Carbon Films". In: *Science* 306.5696 (2004), pp. 666–669. ISSN: 0036-8075. DOI: 10.1126/science.1102896. URL: http://www.sciencemag.org/cgi/doi/10.1126/science.1102896.

[2] A. K. Geim and I. V. Grigorieva. "Van der Waals heterostructures". In: *Nature* 499.7459 (2013), pp. 419–425. ISSN: 0028-0836. DOI: 10.1038/nature12385. arXiv: 1307.6718. URL: http://www.nature.com/doifinder/10.1038/nature12385.

[3] S. Y. Zhou et al. "First direct observation of Dirac fermions in graphite". In: *Nature Physics* 2.9 (2006), pp. 595–599. ISSN: 1745-2473. DOI: 10.1038/nphys393. arXiv: 0608069 [cond-mat]. URL: http://www.nature.com/doifinder/10.1038/nphys393.

[4] Andrea C. Ferrari. "Raman spectroscopy of graphene and graphite: Disorder, electron–phonon coupling, doping and nonadiabatic effects". In: *Solid State Communications* 143.1-2 (2007), pp. 47–57. ISSN: 00381098. DOI: 10.1016/j.ssc.2007.03.052. arXiv: arXiv:0709.1174v1. URL: https://linkinghub.elsevier.com/retrieve/pii/S0038109807002967.

[5] S. Das Sarma et al. "Electronic transport in two-dimensional graphene". In: *Reviews of Modern Physics* 83.2 (2011), pp. 407–470. ISSN: 0034-6861. DOI: 10.1103/RevModPhys.83.407. arXiv: 1003.4731. URL: https://link.aps.org/doi/10.1103/RevModPhys.83.407.

[6] Markus Morgenstern. "Scanning tunneling microscopy and spectroscopy of graphene on insulating substrates". In: *physica status solidi (b)* 248.11 (2011), pp. 2423–2434. ISSN: 03701972. DOI: 10.1002/pssb.201147312. arXiv: 1204.3817. URL: http://doi.wiley.com/10.1002/pssb.201147312.

[7] Aparna Deshpande et al. "Spatial Mapping of the Dirac Point in Monolayer and Bilayer Graphene". In: *IEEE Transactions on Nanotechnology* 10.1 (2011), pp. 88–91. ISSN: 1536-125X. DOI: 10.1109/TNANO.2010.2057256. arXiv: 0912.0547. URL: http://ieeexplore.ieee.org/document/5504843/.

[8] T. Taniguchi and K. Watanabe. "Synthesis of high-purity boron nitride single crystals under high pressure by using Ba–BN solvent". In: *Journal of Crystal Growth* 303.2 (2007), pp. 525–529. ISSN: 00220248. DOI: 10.1016/j.jcrysgro.2006.12.061. URL: http://linkinghub.elsevier.com/retrieve/pii/S0022024807000486.

[9] Matthew Yankowitz, Jiamin Xue, and Brian J. LeRoy. "Graphene on hexagonal boron nitride". In: *Journal of Physics: Condensed Matter* 26.30 (2014), p. 303201. ISSN: 0953-8984. DOI: 10.1088/0953-8984/26/30/303201. arXiv: 1401.5145. URL: http://stacks.iop.org/0953-8984/26/i=30/a=303201?key=crossref.b20498369e1dc28eeaf0c938b9bef3a8.

[10] H. X. Jiang and J. Y. Lin. "Review—Hexagonal Boron Nitride Epilayers: Growth, Optical Properties and Device Applications". In: *ECS Journal of Solid State Science and Technology* 6.2 (2017), Q3012–Q3021. ISSN: 2162-8769. DOI: 10.1149/2.0031702jss. URL: http://jss.ecsdl.org/lookup/doi/10.1149/2.0031702jss.

[11] Amir Pakdel, Yoshio Bando, and Dmitri Golberg. "Nano boron nitride flatland". In: *Chem. Soc. Rev.* 43.3 (2014), pp. 934–959. ISSN: 0306-0012. DOI: 10.1039/C3CS60260E. URL: http://www.ncbi.nlm.nih.gov/pubmed/24280706.

[12] John R. Wallbank et al. "Moiré superlattice effects in graphene/boron-nitride van der Waals heterostructures". In: *Annalen der Physik* 527.5-6 (2015), pp. 359–376. ISSN: 00033804. DOI: 10.1002/andp.201400204. arXiv: 1411.1235. URL: http://doi.wiley.com/10.1002/andp.201400204.

[13] Gianluca Giovannetti et al. "Substrate-induced band gap in graphene on hexagonal boron nitride: Ab initio density functional calculations". In: *Physical Review B* 76.7 (2007), p. 073103. ISSN: 1098-0121. DOI: 10.1103/PhysRevB.76.073103. URL: https://link.aps.org/doi/10.1103/PhysRevB.76.073103.

[14] Jiamin Xue et al. "Scanning tunnelling microscopy and spectroscopy of ultra-flat graphene on hexagonal boron nitride". In: *Nature Materials* 10.4 (2011), pp. 282–285. ISSN: 1476-1122. DOI: 10.1038/nmat2968. arXiv: 1102.2642. URL: http://www.ncbi.nlm.nih.gov/pubmed/21317900.

[15] J. Sławińska, I. Zasada, and Z. Klusek. "Energy gap tuning in graphene on hexagonal boron nitride bilayer system". In: *Physical Review B* 81.15 (2010), p. 155433. ISSN: 1098-0121. DOI: 10.1103/PhysRevB.81.155433. arXiv: 1002.1697. URL: https://link.aps.org/doi/10.1103/PhysRevB.81.155433.

[16] John R. Wallbank. *Electronic Properties of Graphene Heterostructures with Hexagonal Crystals*. 1st ed. Springer International Publishing, 2014, p. 101. ISBN: 9783319077215.

[17] A. H. Castro Neto et al. "The electronic properties of graphene". In: *Reviews of Modern Physics* 81.1 (2009), pp. 109–162. ISSN: 0034-6861. DOI: 10.1103/RevModPhys.81.109. arXiv: 0709.1163. URL: http://arxiv.org/abs/0709.1163.

[18] P. R. Wallace. "The Band Theory of Graphite". In: *Physical Review* 71.9 (1947), pp. 622–634. ISSN: 0031-899X. DOI: 10.1103/PhysRev.71.622. URL: https://link.aps.org/doi/10.1103/PhysRev.71.622.

[19] Mikhail I. Katsnelson. *Graphene: Carbon in Two Dimensions*. Cambridge University Press, 2012, pp. 1–58. ISBN: 978-0-521-19540-9.

[20] C W J Beenakker. "Colloquium : Andreev reflection and Klein tunneling in graphene". In: *Reviews of Modern Physics* 80.4 (2008), pp. 1337–1354. ISSN: 0034-6861. DOI: 10.1103/RevModPhys.80.1337. URL: https://link.aps.org/doi/10.1103/RevModPhys.80.1337.

[21] Pere Miró, Martha Audiffred, and Thomas Heine. "An atlas of two-dimensional materials". In: *Chem. Soc. Rev.* 43.18 (2014), pp. 6537–6554. ISSN: 0306-0012. DOI: 10.1039/C4CS00102H. URL: http://xlink.rsc.org/?DOI=C4CS00102H.

[22] Eva Y Andrei, Guohong Li, and Xu Du. "Electronic properties of graphene: a perspective from scanning tunneling microscopy and magnetotransport". In: *Reports on Progress in Physics* 75.5 (2012), p. 056501. ISSN: 0034-4885. DOI: 10.1088/0034-4885/75/5/056501. arXiv: 1204.4532. URL: http://stacks.iop.org/0034-4885/75/i=5/a=056501?key=crossref.a6f44d947e9586178d01680336c8c1fd.

[23] Branislav Nikolić and Philip B Allen. "Electron transport through a circular constriction". In: *Physical Review B* 60.6 (1999), pp. 3963–3969. ISSN: 0163-1829. DOI: 10.1103/PhysRevB.60.3963. arXiv: 9811296v1 [cond-mat]. URL: https://arxiv.org/abs/cond-mat/9811296v1.

[24] Kenjiro K. Gomes et al. "Designer Dirac fermions and topological phases in molecular graphene". In: *Nature* 483.7389 (2012), pp. 306–310. ISSN: 0028-0836. DOI: 10.1038/nature10941. URL: http://dx.doi.org/10.1038/nature10941.

[25] Yuan Cao et al. "Unconventional superconductivity in magic-angle graphene superlattices". In: *Nature* 556.7699 (2018), pp. 43–50. ISSN: 0028-0836. DOI: 10.1038/nature26160. URL: http://dx.doi.org/10.1038/nature26160.

[26] Eduardo V. Castro et al. "Biased Bilayer Graphene: Semiconductor with a Gap Tunable by the Electric Field Effect". In: *Physical Review Letters* 99.21 (2007), p. 216802. ISSN: 0031-9007. DOI: 10.1103/PhysRevLett.99.216802. URL: https://link.aps.org/doi/10.1103/PhysRevLett.99.216802.

[27] Jeroen B. Oostinga et al. "Gate-induced insulating state in bilayer graphene devices". In: *Nature Materials* 7.2 (2008), pp. 151–157. ISSN: 1476-1122. DOI: 10.1038/nmat2082. URL: http://www.nature.com/articles/nmat2082.

[28] Malheshwar Sharon Madhuri Sharon. *Graphene: An Introduction to the Fundamentals and Industrial Applications*. Ed. by DrAshutosh Tiwari. Scrivener Publishing, 2015, pp. 17–40. ISBN: 978-1-118-84256-0.

[29] Taisuke Ohta et al. "Controlling the Electronic Structure of Bilayer Graphene". In: *Science* 313.5789 (2006), pp. 951–954. ISSN: 0036-8075. DOI: 10.1126/science.1130681. arXiv: arXiv:1011.1669v3. URL: http://www.sciencemag.org/cgi/doi/10.1126/science.1130681.

[30] Jinming Cai et al. "Atomically precise bottom-up fabrication of graphene nanoribbons". In: *Nature* 466.7305 (2010), pp. 470–473. ISSN: 0028-0836. DOI: 10.1038/nature09211. arXiv: 9809069v1 [arXiv:gr-qc]. URL: http://www.nature.com/nature/journal/v466/n7305/full/nature09211.html?free=2.

[31] Melinda Y. Han et al. "Energy Band-Gap Engineering of Graphene Nanoribbons". In: *Physical Review Letters* 98.20 (2007), p. 206805. ISSN: 0031-9007. DOI: 10.1103/PhysRevLett.98.206805. URL: https://link.aps.org/doi/10.1103/PhysRevLett.98.206805.

[32] K. S. Novoselov et al. "A roadmap for graphene". In: *Nature* 490.7419 (2012), pp. 192–200. ISSN: 0028-0836. DOI: 10.1038/nature11458. URL: http://dx.doi.org/10.1038/nature11458.

[33] Chun Hung Lui et al. "Ultraflat graphene". In: *Nature* 462.7271 (2009), pp. 339–341. ISSN: 0028-0836. DOI: 10.1038/nature08569. URL: http://www.nature.com/articles/nature08569.

[34] Menno Bokdam et al. "Band gaps in incommensurable graphene on hexagonal boron nitride". In: *Physical Review B* 89.20 (2014), p. 201404. ISSN: 1098-0121. DOI: 10.1103/PhysRevB.89.201404. arXiv: 1401.6027. URL: https://link.aps.org/doi/10.1103/PhysRevB.89.201404.

[35] W. Gannett et al. "Boron nitride substrates for high mobility chemical vapor deposited graphene". In: *Applied Physics Letters* 98.24 (2011), p. 242105. ISSN: 0003-6951. DOI: 10.1063/1.3599708. URL: http://aip.scitation.org/doi/10.1063/1.3599708.

[36] C. R. Dean et al. "Boron nitride substrates for high-quality graphene electronics". In: *Nature Nanotechnology* 5.10 (2010), pp. 722–726. ISSN: 1748-3387. DOI: 10.1038/nnano.2010.172. arXiv: 1005.4917. URL: http://www.nature.com/articles/nnano.2010.172.

[37] Edwin Kim et al. "Chemical vapor deposition-assembled graphene field-effect transistor on hexagonal boron nitride". In: *Applied Physics Letters* 98.26 (2011), p. 262103. ISSN: 0003-6951. DOI: 10.1063/1.3604012. URL: http://aip.scitation.org/doi/10.1063/1.3604012.

[38] Kenji Watanabe, Takashi Taniguchi, and Hisao Kanda. "Direct-bandgap properties and evidence for ultraviolet lasing of hexagonal boron nitride single crystal". In: *Nature Materials* 3.6 (2004), pp. 404–409. ISSN: 1476-1122. DOI: 10.1038/nmat1134. URL: http://www.nature.com/doifinder/10.1038/nmat1134.

[39] Han Wang et al. "BN/Graphene/BN Transistors for RF Applications". In: *IEEE Electron Device Letters* 32.9 (2011), pp. 1209–1211. ISSN: 0741-3106. DOI: 10.1109/LED.2011.2160611. arXiv: 1108.2021. URL: http://ieeexplore.ieee.org/document/5978801/.

[40] Sergio C. de la Barrera, Qin Gao, and Randall M. Feenstra. "Theory of graphene insulator graphene tunnel junctions". In: *Journal of Vacuum Science & Technology B, Nanotechnology and Microelectronics: Materials, Processing, Measurement, and Phenomena* 32.4 (2014), 04E101. ISSN: 2166-2746. DOI: 10.1116/1.4871760. arXiv: 1404.2122. URL: http://avs.scitation.org/doi/10.1116/1.4871760.

[41] Liam Britnell et al. "Electron Tunneling through Ultrathin Boron Nitride Crystalline Barriers". In: *Nano Letters* 12.3 (2012), pp. 1707–1710. ISSN: 1530-6984. DOI: 10.1021/nl3002205. arXiv: 1202.0735. URL: http://pubs.acs.org/doi/10.1021/nl3002205.

[42] Alex Summerfield et al. "Moiré-Modulated Conductance of Hexagonal Boron Nitride Tunnel Barriers". In: *Nano Letters* 18.7 (2018), pp. 4241–4246. ISSN: 1530-6984. DOI: 10.1021/acs.nanolett.8b01223. URL: http://pubs.acs.org/doi/10.1021/acs.nanolett.8b01223.

[43] L a Ponomarenko et al. "Cloning of Dirac fermions in graphene superlattices". In: *Nature* 497.7451 (2013), pp. 594–597. ISSN: 0028-0836. DOI: 10.1038/nature12187. arXiv: 1212.5012. URL: http://www.nature.com/articles/nature12187.

[44] Alex Summerfield et al. "Strain-Engineered Graphene Grown on Hexagonal Boron Nitride by Molecular Beam Epitaxy". In: *Scientific Reports* 6.1 (2016), p. 22440. ISSN: 2045-2322. DOI: 10.1038/srep22440. URL: http://www.nature.com/articles/srep22440.

[45] Andrew Davies et al. "Lattice-Matched Epitaxial Graphene Grown on Boron Nitride". In: *Nano Letters* 18.1 (2018), pp. 498–504. ISSN: 1530-6984. DOI: 10.1021/acs.nanolett.7b04453. URL: https://pubs.acs.org/doi/abs/10.1021/acs.nanolett.7b04453.

[46] C. R. Woods et al. "Commensurate–incommensurate transition in graphene on hexagonal boron nitride". In: *Nature Physics* 10.6 (2014), pp. 451–456. ISSN: 1745-2473. DOI: 10.1038/nphys2954. arXiv: 1401.2637. URL: http://www.nature.com/articles/nphys2954.

[47] Oleg M. Braun and Yuri S. Kivshar. *The Frenkel-Kontorova Model*. Berlin, Heidelberg: Springer Berlin Heidelberg, 2004. ISBN: 978-3-642-07397-7. DOI: 10.1007/978-3-662-10331-9. URL: http://link.springer.com/10.1007/978-3-662-10331-9.

[48] Irina V Lebedeva et al. "Dislocations in stacking and commensurate-incommensurate phase transition in bilayer graphene and hexagonal boron nitride". In: *Physical Review B* 93.23 (2016), p. 235414. ISSN: 2469-9950. DOI: 10.1103/PhysRevB.93.235414. arXiv: 1606.03949. URL: https://link.aps.org/doi/10.1103/PhysRevB.93.235414.

[49] Na Yeon Kim et al. "Evidence of Local Commensurate State with Lattice Match of Graphene on Hexagonal Boron Nitride". In: *ACS Nano* 11.7 (2017), pp. 7084–7090. ISSN: 1936-0851. DOI: 10.1021/acsnano.7b02716. URL: https://pubs.acs.org/doi/10.1021/acsnano.7b02716.

[50] Yuhang Jiang et al. "Visualizing Strain-Induced Pseudomagnetic Fields in Graphene through an hBN Magnifying Glass". In: *Nano Letters* 17.5 (2017), pp. 2839–2843. ISSN: 1530-6984. DOI: 10.1021/acs.nanolett.6b05228. arXiv: 1703.00550. URL: https://pubs.acs.org/doi/10.1021/acs.nanolett.6b05228.

[51] Diana A. Cosma et al. "Moiré pattern as a magnifying glass for strain and dislocations in van der Waals heterostructures". In: *Faraday Discuss.* 173.January 2016 (2014), pp. 137–43. ISSN: 1359-6640. DOI: 10.1039/C4FD00146J. arXiv: 1408.1624. URL: http://www.ncbi.nlm.nih.gov/pubmed/25465904{\%}5Cnhttp://xlink.rsc.org/?DOI=C4FD00146J.

[52] B Amorim et al. *Novel effects of strains in graphene and other two dimensional materials*. 2015. DOI: 10.1016/j.physrep.2015.12.006. arXiv: 1503.00747. URL: https://linkinghub.elsevier.com/retrieve/pii/S0370157315005402.

[53] Jeil Jung et al. "Origin of band gaps in graphene on hexagonal boron nitride". In: *Nature Communications* 6.1 (2015), p. 6308. ISSN: 2041-1723. DOI: 10.1038/ncomms7308. arXiv: 1403.0496. URL: http://dx.doi.org/10.1038/ncomms7308.

[54] M. L. Teague et al. "Evidence for Strain-Induced Local Conductance Modulations in Single-Layer Graphene on SiO 2". In: *Nano Letters* 9.7 (2009), pp. 2542–2546. ISSN: 1530-6984. DOI: 10.1021/nl9005657. arXiv: 0903.2327. URL: https://pubs.acs.org/doi/10.1021/nl9005657.

[55] Pablo San-Jose et al. "Electronic structure of spontaneously strained graphene on hexagonal boron nitride". In: *Physical Review B* 90.11 (2014), p. 115152. ISSN: 1098-0121. DOI: 10.1103/PhysRevB.90.115152. arXiv: 1406.5999. URL: https://link.aps.org/doi/10.1103/PhysRevB.90.115152.

[56] Giacomo Argentero et al. "Unraveling the 3D Atomic Structure of a Suspended Graphene/hBN van der Waals Heterostructure". In: *Nano Letters* 17.3 (2017), pp. 1409–1416. ISSN: 1530-6984. DOI: 10.1021/acs.nanolett.6b04360. arXiv: 1702.02836. URL: http://pubs.acs.org/doi/10.1021/acs.nanolett.6b04360.

[57] Won Jun Jang et al. "Observation of spatially-varying Fermi velocity in strained-graphene directly grown on hexagonal boron nitride". In: *Carbon* 74 (2014), pp. 139–145. ISSN: 00086223. DOI: 10.1016/j.carbon.2014.03.015. URL: https://linkinghub.elsevier.com/retrieve/pii/S0008622314002619.

[58] Harihar Behera and Gautam Mukhopadhyay. "Fermi velocity modulation in graphene by strain engineering". In: *AIP Conference Proceedings*. Vol. 1512. 2013, pp. 360–361. ISBN: 9780735411333. DOI: 10.1063/1.4791060. arXiv: 1302.1843. URL: http://aip.scitation.org/doi/abs/10.1063/1.4791060.

[59] F. Guinea. "Strain engineering in graphene". In: *Solid State Communications* 152.15 (2012), pp. 1437–1441. ISSN: 00381098. DOI: 10.1016/j.ssc.2012.04.019. URL: http://dx.doi.org/10.1016/j.ssc.2012.04.019.

[60] Matthew Yankowitz et al. "Emergence of superlattice Dirac points in graphene on hexagonal boron nitride". In: *Nature Physics* 8.5 (2012), pp. 382–386. ISSN: 1745-2473. DOI: 10.1038/nphys2272. arXiv: 1202.2870. URL: http://

dx.doi.org/10.1038/nphys2272{\%}5Cnhttp://www.nature.com/doifinder/10.1038/nphys2272.

[61] Itai Leven et al. "Interlayer Potential for Graphene/ h -BN Heterostructures". In: *Journal of Chemical Theory and Computation* 12.6 (2016), pp. 2896–2905. ISSN: 1549-9618. DOI: 10.1021/acs.jctc.6b00147. URL: https://pubs.acs.org/doi/10.1021/acs.jctc.6b00147.

[62] B. Hunt et al. "Massive Dirac Fermions and Hofstadter Butterfly in a van der Waals Heterostructure". In: *Science* 340.6139 (2013), pp. 1427–1430. ISSN: 0036-8075. DOI: 10.1126/science.1237240. URL: http://www.ncbi.nlm.nih.gov/pubmed/23686343.

[63] C. R. Dean et al. "Hofstadter's butterfly and the fractal quantum Hall effect in moiré superlattices". In: *Nature* 497.7451 (2013), pp. 598–602. ISSN: 0028-0836. DOI: 10.1038/nature12186. URL: http://www.nature.com/articles/nature12186.

[64] Franz J Giessibl et al. "Comparison of force sensors for atomic force microscopy based on quartz tuning forks and length-extensional resonators". In: *Physical Review B* 84.12 (2011), p. 125409. ISSN: 1098-0121. DOI: 10.1103/PhysRevB.84.125409. arXiv: 1104.2987. URL: http://arxiv.org/abs/1104.2987.

[65] Franz J. Giessibl. "Advances in atomic force microscopy". In: *Reviews of Modern Physics* 75.3 (2003), pp. 949–983. ISSN: 0034-6861. DOI: 10.1103/RevModPhys.75.949. arXiv: 0305119 [cond-mat]. URL: https://link.aps.org/doi/10.1103/RevModPhys.75.949.

[66] Daniel Gall. "Electron mean free path in elemental metals". In: *Journal of Applied Physics* 119.8 (2016), p. 085101. ISSN: 0021-8979. DOI: 10.1063/1.4942216. URL: http://dx.doi.org/10.1063/1.4942216.

[67] G. Binnig and H Rohrer. "Scanning tunneling microscopy". In: *Surface Science* 126.1-3 (1983), pp. 236–244. ISSN: 00396028. DOI: 10.1016/0039-6028(83)90716-1. URL: https://linkinghub.elsevier.com/retrieve/pii/0039602883907161.

[68] D Q G Ohfwulfdo et al. "Electrical Characteristics of Graphene Wrinkles extracted by conductive atomic force microscopy and electrical measurement". In: (2013), pp. 182–183.

[69] Muneer Ahmad et al. "Local conductance measurement of graphene layer using conductive atomic force microscopy". In: *Journal of Applied Physics* 110.5 (2011), p. 054307. ISSN: 0021-8979. DOI: 10.1063/1.3626058. URL: http://aip.scitation.org/doi/10.1063/1.3626058.

[70] Krzysztof Gajewski et al. "Scanning probe microscopy investigations of the electrical properties of chemical vapor deposited graphene grown on a 6H-SiC substrate". In: *Micron* 68 (2015), pp. 17–22. ISSN: 09684328. DOI: 10.1016/j.micron.2014.08.005. URL: https://linkinghub.elsevier.com/retrieve/pii/S0968432814001607.

[71] Li Zhang et al. "Imaging and nanoprobing of graphene layers for interconnects by conductive atomic force microscopy". In: *Japanese Journal of Applied Physics* 54.5S (2015), 05EB02. ISSN: 0021-4922. DOI: 10.7567/JJAP.54.05EB02. URL: http://stacks.iop.org/1347-4065/54/i=5S/a=05EB02?key=crossref.ac44378436340039472fd12253d50db1.

[72] Fanny Hauquier et al. "Conductive-probe AFM characterization of graphene sheets bonded to gold surfaces". In: *Applied Surface Science* 258.7 (2012), pp. 2920–2926. ISSN: 01694332. DOI: 10.1016/j.apsusc.2011.10.152. URL: http://dx.doi.org/10.1016/j.apsusc.2011.10.152.

[73] V Kasliwal et al. "AFM and CAFM studies of ELO GaN films". In: *Gallium Nitride Materials and Devices II*. Ed. by Hadis Morkoc and Cole W. Litton. Vol. 6473. 1. 2007, p. 647308. ISBN: 0819465860. DOI: 10.1117/12.706773. URL: http://proceedings.spiedigitallibrary.org/proceeding.aspx?doi=10.1117/12.706773.

[74] Werner Frammelsberger et al. "Thickness determination of thin and ultra-thin SiO2 films by C-AFM IV-spectroscopy". In: *Applied Surface Science* 252.6 (2006), pp. 2375–2388. ISSN: 01694332. DOI: 10.1016/j.apsusc.2005.04.010. URL: https://linkinghub.elsevier.com/retrieve/pii/S0169433205006641.

[75] Borislav Vasić, Amaia Zurutuza, and Radoš Gajić. "Spatial variation of wear and electrical properties across wrinkles in chemical vapour deposition graphene". In: *Carbon* 102 (2016), pp. 304–310. ISSN: 00086223. DOI: 10.1016/j.carbon.2016.02.066. URL: https://linkinghub.elsevier.com/retrieve/pii/S0008622316301609.

[76] G.N. Karimi et al. "Corrosion of cast Stellite-3 analogue in simulated PWR conditions". In: *Corrosion Science* 140.February (2018), pp. 402–411. ISSN: 0010938X. DOI: 10.1016/j.corsci.2018.05.023. URL: https://doi.org/10.1016/j.corsci.2018.05.023.

[77] R García. "Dynamic atomic force microscopy methods". In: *Surface Science Reports* 47.6-8 (2002), pp. 197–301. ISSN: 01675729. DOI: 10.1016/S0167-5729(02)00077-8. URL: http://linkinghub.elsevier.com/retrieve/pii/S0167572902000778.

[78] Matthew Yankowitz et al. "Pressure-induced commensurate stacking of graphene on boron nitride". In: *Nature Communications* 7.1 (2016), p. 13168. ISSN: 2041-1723. DOI: 10.1038/ncomms13168. URL: http://dx.doi.org/10.1038/ncomms13168.

[79] Dheeraj Golla et al. "Optical thickness determination of hexagonal boron nitride flakes". In: *Applied Physics Letters* 102.16 (2013), p. 161906. ISSN: 0003-6951. DOI: 10.1063/1.4803041. arXiv: 1303.3300. URL: http://aip.scitation.org/doi/10.1063/1.4803041.

[80] Microscopy Australia. *MyScope Microscopy Training*. URL: https://myscope.training/{\#}/SEMlevel{_}2{_}3 (visited on 11/19/2019).

[81] D. A. Walters et al. "Short cantilevers for atomic force microscopy". In: *Review of Scientific Instruments* 67.10 (1996), pp. 3583–3590. ISSN: 0034-6748. DOI: 10.1063/1.1147177. URL: http://aip.scitation.org/doi/10.1063/1.1147177.

[82] D. F. Ogletree, R. W. Carpick, and M. Salmeron. "Calibration of frictional forces in atomic force microscopy". In: *Review of Scientific Instruments* 67.9 (1996), pp. 3298–3306. ISSN: 0034-6748. DOI: 10.1063/1.1147411. URL: http://www.scientific.net/SSP.121-123.851.

[83] M. Varenberg, I. Etsion, and G. Halperin. "An improved wedge calibration method for lateral force in atomic force microscopy". In: *Review of Scientific Instruments* 74.7 (2003), pp. 3362–3367. ISSN: 0034-6748. DOI: 10.1063/1.1584082. URL: http://aip.scitation.org/doi/10.1063/1.1584082.

[84] H. S. Khare and D. L. Burris. "The extended wedge method: Atomic force microscope friction calibration for improved tolerance to instrument misalignments, tip offset, and blunt probes". In: *Review of Scientific Instruments* 84.5 (2013), p. 055108. ISSN: 0034-6748. DOI: 10.1063/1.4804163. URL: http://aip.scitation.org/doi/10.1063/1.4804163.

[85] JA Rosen. "Distortion Correction and Momentum Representation of Angle-Resolved Photoemission Data". In: October (2008). URL: http://www.phas.ubc.ca/{~}quantmat/ARPES/PUBLICATIONS/MSTheses/Jonathan{_}MSc.pdf{\%}5Cnhttps://circle.ubc.ca/bitstream/id/14243/ubc{_}2008{_}fall{_}rosen{_}jonathan{_}adam.pdf.

[86] Neil R. Wilson et al. "Determination of band offsets, hybridization, and exciton binding in 2D semiconductor heterostructures". In: *Science Advances* 3.2 (2017), e1601832. ISSN: 2375-2548. DOI: 10.1126/sciadv.1601832. arXiv: 1601.05865. URL: http://advances.sciencemag.org/lookup/doi/10.1126/sciadv.1601832.

[87] Jan Knudsen, Jesper N. Andersen, and Joachim Schnadt. "A versatile instrument for ambient pressure x-ray photoelectron spectroscopy: The Lund cell approach". In: *Surface Science* 646 (2016), pp. 160–169. ISSN: 00396028. DOI: 10.1016/j.susc.2015.10.038. URL: http://dx.doi.org/10.1016/j.susc.2015.10.038.

[88] Stanford University. *Stanford Shen Laboratory*. URL: https://arpes.stanford.edu/research/tool-development/angle-resolved-photoemission-spectroscopy (visited on 11/19/2019).

[89] Andrea Damascelli, Zahid Hussain, and Zhi-Xun Shen. "Angle-resolved photoemission studies of the cuprate superconductors". In: *Reviews of Modern Physics* 75.2 (2003), pp. 473–541. ISSN: 0034-6861. DOI: 10.1103/RevModPhys.75.473. arXiv: 0208504 [cond-mat]. URL: https://link.aps.org/doi/10.1103/RevModPhys.75.473.

[90] W. S. Lee et al. "A brief update of angle-resolved photoemission spectroscopy on a correlated electron system". In: *Journal of Physics: Condensed Matter* 21.16 (2009), p. 164217. ISSN: 0953-8984. DOI: 10.1088/0953-8984/21/16/164217. URL: http://stacks.iop.org/0953-8984/21/i=16/a=164217?key=crossref.4d98a8eefdb705b07d354578951efbc6.

[91] C. V. Raman. "A new radiation". In: *Proceedings of the Indian Academy of Sciences - Section A* 37.3 (1953), pp. 333–341. ISSN: 0370-0089. DOI: 10.1007/BF03052651. URL: http://link.springer.com/10.1007/BF03052651.

[92] L. M. Malard et al. *Raman spectroscopy in graphene*. 2009. DOI: 10.1016/j.physrep.2009.02.003. URL: http://dx.doi.org/10.1016/j.physrep.2009.02.003.

[93] Qiran Cai et al. "Raman signature and phonon dispersion of atomically thin boron nitride". In: *Nanoscale* 9.9 (2017), pp. 3059–3067. ISSN: 2040-3364. DOI: 10.1039/C6NR09312D. URL: http://xlink.rsc.org/?DOI=C6NR09312D.

[94] D. S L Abergel, A. Russell, and Vladimir I. Fal'ko. "Visibility of graphene flakes on a dielectric substrate". In: *Applied Physics Letters* 91.6 (2007), p. 063125. ISSN: 0003-6951. DOI: 10.1063/1.2768625. arXiv: 0705.0091. URL: http://aip.scitation.org/doi/10.1063/1.2768625.

[95] S. Roddaro et al. "The Optical Visibility of Graphene: Interference Colors of Ultrathin Graphite on SiO 2". In: *Nano Letters* 7.9 (2007), pp. 2707–2710. ISSN: 1530-6984. DOI: 10.1021/nl0711581. URL: https://pubs.acs.org/doi/10.1021/nl0711581.

[96] K S Novoselov et al. "Two-dimensional atomic crystals". In: *Proceedings of the National Academy of Sciences* 102.30 (2005), pp. 10451–10453. ISSN: 0027-8424. DOI: 10.1073/pnas.0502848102. arXiv: 0503533 [cond-mat]. URL: http://www.pnas.org/cgi/doi/10.1073/pnas.0502848102.

[97] Jianlei Cui et al. "Nanojoining of crossed Ag nanowires: a molecular dynamics study". In: *Journal of Nanoparticle Research* 18.7 (2016), p. 175. ISSN: 1388-0764. DOI: 10.1007/s11051-016-3479-x. URL: http://link.springer.com/10.1007/s11051-016-3479-x.

[98] Thomas Sannicolo et al. "Direct Imaging of the Onset of Electrical Conduction in Silver Nanowire Networks by Infrared Thermography: Evidence of Geometrical Quantized Percolation". In: *Nano Letters* 16.11 (2016), pp. 7046–7053. ISSN: 1530-6984. DOI: 10.1021/acs.nanolett.6b03270. URL: https://pubs.acs.org/doi/10.1021/acs.nanolett.6b03270.

[99] Johannes H M Maurer et al. "Sintering of Ultrathin Gold Nanowires for Transparent Electronics". In: *ACS Applied Materials & Interfaces* 7.15 (2015), pp. 7838–7842. ISSN: 1944-8244. DOI: 10.1021/acsami.5b02088. URL: https://pubs.acs.org/doi/10.1021/acsami.5b02088.

[100] Changwook Jeong et al. "Prospects for Nanowire-Doped Polycrystalline Graphene Films for Ultratransparent, Highly Conductive Electrodes". In: *Nano Letters* 11.11 (2011), pp. 5020–5025. ISSN: 1530-6984. DOI: 10.1021/nl203041n. URL: https://pubs.acs.org/doi/10.1021/nl203041n.

[101] Jiajie Liang et al. "Silver Nanowire Percolation Network Soldered with Graphene Oxide at Room Temperature and Its Application for Fully Stretchable Polymer Light-Emitting Diodes". In: *ACS Nano* 8.2 (2014), pp. 1590–1600. ISSN: 1936-0851. DOI: 10.1021/nn405887k. URL: https://pubs.acs.org/doi/10.1021/nn405887k.

[102] Qiucheng Li et al. "Hexagonal Boron Nitride-Graphene Heterostructures: Synthesis and Interfacial Properties". In: *Small* 12.1 (2016), pp. 32–50. ISSN: 16136810. DOI: 10.1002/smll.201501766. URL: http://doi.wiley.com/10.1002/smll.201501766.

[103] Lijie Ci et al. "Atomic layers of hybridized boron nitride and graphene domains". In: *Nature Materials* 9.5 (2010), pp. 430–435. ISSN: 1476-1122. DOI: 10.1038/nmat2711. URL: http://www.nature.com/articles/nmat2711.

[104] Xiaofeng Fan et al. "Band gap opening of graphene by doping small boron nitride domains". In: *Nanoscale* 4.6 (2012), p. 2157. ISSN: 2040-3364. DOI: 10.1039/c2nr11728b. URL: http://xlink.rsc.org/?DOI=c2nr11728b.

[105] Jinying Wang et al. "Widely Tunable Carrier Mobility of Boron Nitride-Embedded Graphene". In: *Small* 9.8 (2013), pp. 1373–1378. ISSN: 16136810. DOI: 10.1002/smll.201202978. URL: http://doi.wiley.com/10.1002/smll.201202978.

[106] Yuanyue Liu, Somnath Bhowmick, and Boris I. Yakobson. "BN White Graphene with "Colorful" Edges: The Energies and Morphology". In: *Nano Letters* 11.8 (2011), pp. 3113–3116. ISSN: 1530-6984. DOI: 10.1021/nl2011142. URL: https://pubs.acs.org/doi/10.1021/nl2011142.

[107] Somnath Bhowmick, Abhishek K. Singh, and Boris I. Yakobson. "Quantum Dots and Nanoroads of Graphene Embedded in Hexagonal Boron Nitride". In: *The Journal of Physical Chemistry C* 115.20 (2011), pp. 9889–9893. ISSN: 1932-7447. DOI: 10.1021/jp200671p. URL: https://pubs.acs.org/doi/10.1021/jp200671p.

[108] K. S. Novoselov and A. H. Castro Neto. "Two-dimensional crystals-based heterostructures: materials with tailored properties". In: *Physica Scripta* T146.T146 (2012), p. 014006. ISSN: 0031-8949. DOI: 10.1088/0031-8949/2012/T146/014006. URL: https://iopscience.iop.org/article/10.1088/0031-8949/2012/T146/014006.

[109] C. Ratsch and J. A. Venables. "Nucleation theory and the early stages of thin film growth". In: *Journal of Vacuum Science & Technology A: Vacuum, Surfaces, and Films* 21.5 (2003), S96–S109. ISSN: 0734-2101. DOI: 10.1116/1.1600454. URL: http://avs.scitation.org/doi/10.1116/1.1600454.

[110] B. Yates, M. J. Overy, and O. Pirgon. "The anisotropic thermal expansion of boron nitride". In: *Philosophical Magazine* 32.4 (1975), pp. 847–857. ISSN: 0031-8086. DOI: 10.1080/14786437508221624. URL: http://www.tandfonline.com/doi/abs/10.1080/14786437508221624.

[111] Wenzhong Bao et al. "Controlled ripple texturing of suspended graphene and ultrathin graphite membranes". In: *Nature Nanotechnology* (2009). ISSN: 17483395. DOI: 10.1038/nnano.2009.191.

[112] Duhee Yoon, Young Woo Son, and Hyeonsik Cheong. "Negative thermal expansion coefficient of graphene measured by raman spectroscopy". In: *Nano Letters* (2011). ISSN: 15306984. DOI: 10.1021/nl201488g.

[113] S. Linas et al. "Interplay between Raman shift and thermal expansion in graphene: Temperature-dependent measurements and analysis of substrate corrections". In: *Physical Review B* 91.7 (2015), p. 075426. ISSN: 1098-0121. DOI: 10.1103/PhysRevB.91.075426. arXiv: arXiv:1411.7840v1. URL: https://link.aps.org/doi/10.1103/PhysRevB.91.075426.

[114] William A. Chupka and Mark G. Inghram. "Investigation of the Heat of Vaporization of Carbon". In: *The Journal of Chemical Physics* 21.2 (1953), pp. 371–372. ISSN: 0021-9606. DOI: 10.1063/1.1698897. URL: http://aip.scitation.org/doi/10.1063/1.1698897.

[115] P. D. Zavitsanos and G. A. Carlson. "Experimental study of the sublimation of graphite at high temperatures". In: *The Journal of Chemical Physics* 59.6 (1973), pp. 2966–2973. ISSN: 0021-9606. DOI: 10.1063/1.1680430. URL: http://aip.scitation.org/doi/10.1063/1.1680430.

[116] J. D. Albar et al. "An atomic carbon source for high temperature molecular beam epitaxy of graphene". In: *Scientific Reports* 7.1 (2017), p. 6598. ISSN: 2045-2322. DOI: 10.1038/s41598-017-07021-1. URL: http://www.nature.com/articles/s41598-017-07021-1.

[117] W. Weltner, K. R. Thompson, and R. L. DeKock. "Spectroscopy of carbon molecules. IV. C4, C5, C6 (and C9)". In: *Journal of the American Chemical Society* 93.19 (1971), pp. 4688–4695. ISSN: 0002-7863. DOI: 10.1021/ja00748a007. URL: https://pubs.acs.org/doi/abs/10.1021/ja00748a007.

[118] S. A. Krasnokutski and F. Huisken. "A simple and clean source of low-energy atomic carbon". In: *Applied Physics Letters* 105.11 (2014). ISSN: 00036951. DOI: 10.1063/1.4895806. URL: http://dx.doi.org/10.1063/1.4895806.

[119] David Nečas and Petr Klapetek. "Gwyddion: an open-source software for SPM data analysis". In: *Open Physics* 10.1 (2012), pp. 181–188. ISSN: 2391-5471. DOI: 10.2478/s11534-011-0096-2. URL: http://www.degruyter.com/view/j/phys.2012.10.issue-1/s11534-011-0096-2/s11534-011-0096-2.xml.

[120] MATLAB. *version 9.2.0 (R2017a)*. Natick, Massachusetts: The MathWorks Inc., 2017.

[121] Kyounghwan Kim et al. "van der Waals Heterostructures with High Accuracy Rotational Alignment". In: *Nano Letters* 16.3 (2016), pp. 1989–1995. ISSN: 1530-6984. DOI: 10.1021/acs.nanolett.5b05263. URL: https://pubs.acs.org/doi/10.1021/acs.nanolett.5b05263.

[122] S. Reich et al. "Resonant Raman scattering in cubic and hexagonal boron nitride". In: *Physical Review B* 71.20 (2005), p. 205201. ISSN: 1098-0121. DOI: 10.1103/PhysRevB.71.205201. URL: https://link.aps.org/doi/10.1103/PhysRevB.71.205201.

[123] T. M.G. Mohiuddin et al. "Uniaxial strain in graphene by Raman spectroscopy: G peak splitting, Grüneisen parameters, and sample orientation". In: *Physical Review B - Condensed Matter and Materials Physics* 79.20 (2009). ISSN: 1550235X. DOI: 10.1103/PhysRevB.79.205433. arXiv: 0812.1538.

[124] A. C. Ferrari et al. "Raman Spectrum of Graphene and Graphene Layers". In: *Physical Review Letters* 97.18 (2006), p. 187401. ISSN: 0031-9007. DOI: 10.1103/PhysRevLett.97.187401. URL: https://link.aps.org/doi/10.1103/PhysRevLett.97.187401.

[125] Aleksey Falin et al. "Mechanical properties of atomically thin boron nitride and the role of interlayer interactions". In: *Nature Communications* 8.1 (2017), p. 15815. ISSN: 2041-1723. DOI: 10.1038/ncomms15815. URL: http://dx.doi.org/10.1038/ncomms15815.

[126] M. Kindermann, Bruno Uchoa, and D. L. Miller. "Zero-energy modes and gate-tunable gap in graphene on hexagonal boron nitride". In: *Physical Review B* 86.11 (2012), p. 115415. ISSN: 1098-0121. DOI: 10.1103/PhysRevB.86.115415. arXiv: 1205.3194. URL: https://link.aps.org/doi/10.1103/PhysRevB.86.115415.

[127] Kemeng Ji et al. "Lithium intercalation into bilayer graphene". In: *Nature Communications* 10.1 (2019), p. 275. ISSN: 2041-1723. DOI: 10.1038/s41467-018-07942-z. URL: http://dx.doi.org/10.1038/s41467-018-07942-zhttp://www.nature.com/articles/s41467-018-07942-z.

[128] Oleg V. Yazyev and Steven G. Louie. "Topological defects in graphene: Dislocations and grain boundaries". In: *Physical Review B* 81.19 (2010), p. 195420. ISSN: 1098-0121. DOI: 10.1103/PhysRevB.81.195420. arXiv: 1004.2031. URL: https://link.aps.org/doi/10.1103/PhysRevB.81.195420.

[129] G. M. Rutter et al. "Scattering and Interference in Epitaxial Graphene". In: *Science* 317.5835 (2007), pp. 219–222. ISSN: 0036-8075. DOI: 10.1126/science.1142882. URL: http://www.sciencemag.org/cgi/doi/10.1126/science.1142882.

[130] Lili Liu et al. "Defects in Graphene: Generation, Healing, and Their Effects on the Properties of Graphene: A Review". In: *Journal of Materials Science & Technology* 31.6 (2015), pp. 599–606. ISSN: 10050302. DOI: 10.1016/j.jmst.2014.11.019. URL: http://linkinghub.elsevier.com/retrieve/pii/S100503021500016X.

[131] Klaus Hermann. "Periodic overlayers and moiré patterns: theoretical studies of geometric properties". In: *Journal of Physics: Condensed Matter* 24.31 (2012), p. 314210. ISSN: 0953-8984. DOI: 10.1088/0953-8984/24/31/314210. URL:

http://stacks.iop.org/0953-8984/24/i=31/a=314210?key=crossref.706b4449ddd80b0831f426e0a62e91f5.

[132] Robert Drost et al. "Electronic States at the Graphene–Hexagonal Boron Nitride Zigzag Interface". In: *Nano Letters* 14.9 (2014), pp. 5128–5132. ISSN: 1530-6984. DOI: 10.1021/nl501895h. URL: https://pubs.acs.org/doi/10.1021/nl501895h.

[133] Jonathan Bradford et al. "Transfer-Free Synthesis of Lateral Graphene–Hexagonal Boron Nitride Heterostructures from Chemically Converted Epitaxial Graphene". In: *Advanced Materials Interfaces* 6.19 (2019), p. 1900419. ISSN: 2196-7350. DOI: 10.1002/admi.201900419. URL: https://onlinelibrary.wiley.com/doi/abs/10.1002/admi.201900419.

[134] Yongji Gong et al. "Direct chemical conversion of graphene to boron- and nitrogen- and carbon-containing atomic layers". In: *Nature Communications* 5.1 (2014), p. 3193. ISSN: 2041-1723. DOI: 10.1038/ncomms4193. URL: http://dx.doi.org/10.1038/ncomms4193.

[135] Zheng Liu et al. "In-plane heterostructures of graphene and hexagonal boron nitride with controlled domain sizes". In: *Nature Nanotechnology* 8.2 (2013), pp. 119–124. ISSN: 1748-3387. DOI: 10.1038/nnano.2012.256. URL: http://www.nature.com/articles/nnano.2012.256.

[136] Mark P. Levendorf et al. "Graphene and boron nitride lateral heterostructures for atomically thin circuitry". In: *Nature* 488.7413 (2012), pp. 627–632. ISSN: 0028-0836. DOI: 10.1038/nature11408. URL: http://www.nature.com/articles/nature11408.

[137] C. Elias et al. "Direct band-gap crossover in epitaxial monolayer boron nitride". In: *Nature Communications* 10.1 (2019), p. 2639. ISSN: 2041-1723. DOI: 10.1038/s41467-019-10610-5. URL: http://www.nature.com/articles/s41467-019-10610-5.

[138] Yong-Jin Cho et al. "Hexagonal Boron Nitride Tunnel Barriers Grown on Graphite by High Temperature Molecular Beam Epitaxy". In: *Scientific Reports* 6.1 (2016), p. 34474. ISSN: 2045-2322. DOI: 10.1038/srep34474. URL: http://www.nature.com/articles/srep34474.

[139] T Q P Vuong et al. "Deep ultraviolet emission in hexagonal boron nitride grown by high-temperature molecular beam epitaxy". In: *2D Materials* 4.2 (2017), p. 021023. ISSN: 2053-1583. DOI: 10.1088/2053-1583/aa604a. URL: https://doi.org/10.1088/2053-1583/aa604a.

[140] Tin S. Cheng et al. "High-temperature molecular beam epitaxy of hexagonal boron nitride layers". In: *Journal of Vacuum Science & Technology B, Nanotechnology and Microelectronics: Materials, Processing, Measurement, and Phenomena* 36.2 (2018), p. 02D103. ISSN: 2166-2746. DOI: 10.1116/1.5011280. URL: http://avs.scitation.org/doi/10.1116/1.5011280.

[141] Peter Sutter, Yuan Huang, and Eli Sutter. "Nanoscale Integration of Two-Dimensional Materials by Lateral Heteroepitaxy". In: *Nano Letters* 14.8 (2014), pp. 4846–4851. ISSN: 1530-6984. DOI: 10.1021/nl502110q. URL: https://pubs.acs.org/doi/10.1021/nl502110q.

[142] Pekka Koskinen, Sami Malola, and Hannu Häkkinen. "Self-Passivating Edge Reconstructions of Graphene". In: *Physical Review Letters* 101.11 (2008), p. 115502. ISSN: 0031-9007. DOI: 10.1103/PhysRevLett.101.115502. arXiv: 0802.2623. URL: http://arxiv.org/abs/0802.2623.

[143] Yijing Y. Stehle et al. "Anisotropic Etching of Hexagonal Boron Nitride and Graphene: Question of Edge Terminations". In: *Nano Letters* 17.12 (2017), pp. 7306–7314. ISSN: 1530-6984. DOI: 10.1021/acs.nanolett.7b02841. URL: http://pubs.acs.org/doi/10.1021/acs.nanolett.7b02841.

[144] G. M. Rutter et al. "Scattering and Interference in Epitaxial Graphene". In: *Science* 317.5835 (2007), pp. 219–222. ISSN: 0036-8075. DOI: 10.1126/science.1142882. URL: http://www.sciencemag.org/cgi/doi/10.1126/science.1142882.

[145] Yong-Jin Cho et al. "Erratum: Corrigendum: Hexagonal Boron Nitride Tunnel Barriers Grown on Graphite by High Temperature Molecular Beam Epitaxy". In: *Scientific Reports* 7.1 (2017), p. 46799. ISSN: 2045-2322. DOI: 10.1038/srep46799. URL: http://dx.doi.org/10.1038/srep34474.

[146] Jiong Lu et al. "Lattice Relaxation at the Interface of Two-Dimensional Crystals: Graphene and Hexagonal Boron-Nitride". In: *Nano Letters* 14.9 (2014), pp. 5133–5139. ISSN: 1530-6984. DOI: 10.1021/nl501900x. URL: https://pubs.acs.org/doi/10.1021/nl501900x.

[147] Dinkar Nandwana and Elif Ertekin. "Ripples, Strain, and Misfit Dislocations: Structure of Graphene–Boron Nitride Superlattice Interfaces". In: *Nano Letters* 15.3 (2015), pp. 1468–1475. ISSN: 1530-6984. DOI: 10.1021/nl505005t. URL: https://pubs.acs.org/doi/10.1021/nl505005t.

[148] Dechao Geng et al. "In situ epitaxial engineering of graphene and h-BN lateral heterostructure with a tunable morphology comprising h-BN domains". In: *NPG Asia Materials* 11.1 (2019), p. 56. ISSN: 1884-4049. DOI: 10.1038/s41427-

019-0162-6. URL: http://dx.doi.org/10.1038/s41427-019-0162-6.

[149] Subash Sharma et al. "Opening of triangular hole in triangular-shaped chemical vapor deposited hexagonal boron nitride crystal". In: *Scientific Reports* 5.1 (2015), p. 10426. ISSN: 2045-2322. DOI: 10.1038/srep10426. URL: http://dx.doi.org/10.1038/srep10426.

[150] Lifeng Wang et al. "Growth and Etching of Monolayer Hexagonal Boron Nitride". In: *Advanced Materials* 27.33 (2015), pp. 4858–4864. ISSN: 09359648. DOI: 10.1002/adma.201501166. URL: http://doi.wiley.com/10.1002/adma.201501166.

[151] Roland Yingjie Tay et al. "Growth of Large Single-Crystalline Two-Dimensional Boron Nitride Hexagons on Electropolished Copper". In: *Nano Letters* 14.2 (2014), pp. 839–846. ISSN: 1530-6984. DOI: 10.1021/nl404207f. URL: https://pubs.acs.org/doi/10.1021/nl404207f.

[152] Zhuhua Zhang et al. "Growth Mechanism and Morphology of Hexagonal Boron Nitride". In: *Nano Letters* 16.2 (2016), pp. 1398–1403. ISSN: 1530-6984. DOI: 10.1021/acs.nanolett.5b04874. URL: https://pubs.acs.org/doi/10.1021/acs.nanolett.5b04874.

[153] Hyo Ju Park et al. "Double-Spiral Hexagonal Boron Nitride and Shear Strained Coalescence Boundary". In: *Nano Letters* 19.7 (2019), pp. 4229–4236. ISSN: 1530-6984. DOI: 10.1021/acs.nanolett.8b05034. URL: https://pubs.acs.org/doi/10.1021/acs.nanolett.8b05034.

Appendix A

Nanowire Manipulation

The manipulation of Ag nanowires was investigated using AC AFM imaging combined with contact mode AFM to manoeuvre the nanowires around the surface. The aim of this test was to determine how readily the nanowires could be moved with the possibility of creating, or severing, microscopic electrical circuits and networks. This was done by first imaging the nanowire, then moving the AFM tip through the nanowire while in contact mode with a positive deflection (i.e. with a normal force applied to the sample by the tip). This was carried out successfully on both SiO_2 and graphite substrates. Figures A.1a and b) show two such nanowire movements. The before and after AFM images are superposed, with the after image shown with an associated transparency. The AFM in these cases undergoes a single movement along the direction parallel to the indicated arrows. The angles subtended by the nanowire movements in these cases are 14.8° in a), and 68.9° in b). However, in some cases where the nanowire surface adhesion is strong, and the cantilever deflection is high, the wire is severed by the tip slicing through the wire. This is the case for the nanowire shown in figure 4.1c where the nanowire before and after a series of several manipulations has been both severed and moved around the graphite substrate. Also noticable on these AFM images are spherical globules across the nanowire surfaces. These are most likely contaminants that have been adsorbed to the Ag, and were observed to increase in quantity over time.

The development of this technique has been continued in collaboration with James Kerfoot. In this work the nanowires have been drop deposited, as described in chapter 4, onto a transfer stamp - combining the two methods. These nanowires are then precisely positioned across the gap between two Au electrical contacts, on top of a previously stamped hBN flake. An example structure can be seen in the optical micrograph shown in figure A.2a.

The purpose of this investigation was to attempt to use the severing and manipulation of the nanowires to position the wires with an individual/single layer of perovskite crystals between the two wire ends to explore the electrical and photoconductive characteristics of individual perovskite crystals. With the structure seen in figure

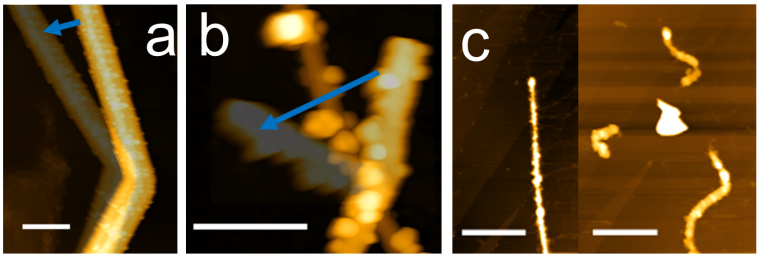


FIGURE A.1: a), b) Two separate nanowire manipulation examples. Two tapping mode AFM topography images, taken before and after a contact mode tip movement parallel to the indicated blue arrows, are superimposed in each image, with the after image shown as translucent for clarity. c) Left: tapping mode AFM image before, and right, after, a series of contact mode movements that act to sever and move the nanowire. Scalebars in a), b), and c) (both left and right) are 400 nm, 400 nm, and 1 μm respectively.

A.2a typically no initial current could be measured across the two contacts using a probe station. However, once the bias between the contacts was raised to $\sim$1.5 V a large current spike is observed, indicating a strong conduction, followed by Ohmic behaviour displaying a low resistance of $\sim$290 Ω.

Along with the SEM image shown in figure A.2b this behaviour suggests that the initial bias is required in order to overcome a potential barrier created by surface contaminants. Once overcome the large current spike melts the end of the wire, welding it to the Au contact. Unfortunately, this process often leads to a loss of electrical connection between the nanowire and contact where the melted wire is no longer situated on the Au contact. This is the case for the structure seen in figure A.2b, where the nanowire (indicated by the white arrow) has been welded to form bubbles of material both on and off the Au contact, but no visible connection, or current, remains.

Once successfully welded, two different methods of creating an Ag nanowire/ perovskite crystal/ Ag nanowire interface were attempted. The first consisted of severing a single wire following perovskite deposition, then repositioning the nanowire ends with perovskite crystals between. One such attempt can be seen in figure A.2c. However, no reproducible results were obtained through this method, despite the high accuracy of manipulation possible, allowing for a gap of 60 nm between the nanowires.

Carbon nanofibers (CNFs) were found to provide a better alternative to the Ag nanowires for this purpose. Their deposition did not require any form of welding to achieve a current. However, they were far less flexible, and were unable to be severed by the AFM tip. This led to the second approach, shown here for CNFs in lieu of Ag nanowires, seen in the bottom row of figure A.2, where the stamped CNFs were placed with one on either Au contact, and then pushed together using contact mode AFM. Figures e), f), and g) show the completed prototype structure without perovskite

deposition.

Due to the time consuming nature and irreproducability of these structures the formation of devices in this way was abandoned, but the principle of nanowire/CNF deposition and stamping, combined with 2D materials, to form novel structures and stacks continues to be explored.

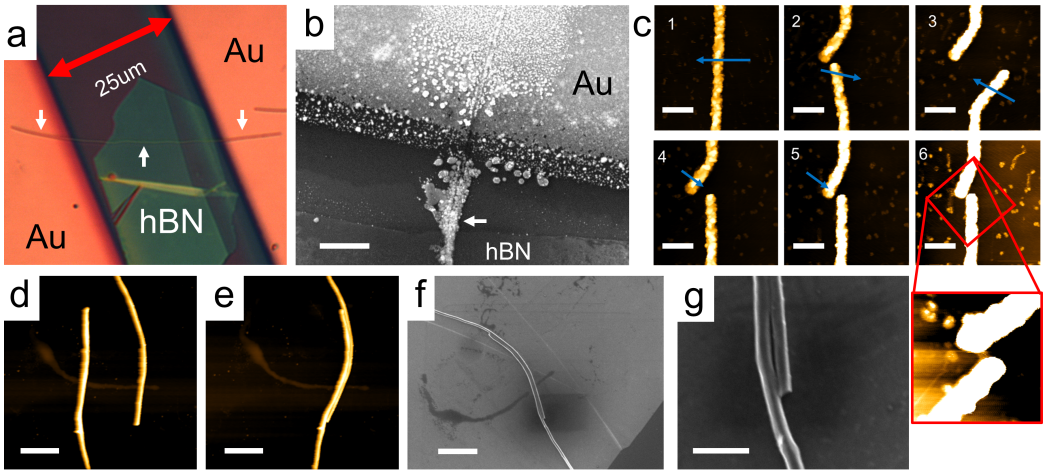


FIGURE A.2: a) A Ag nanowire that has been stamped between two Au contacts across a 25 μm gap, and on top of a stamped hBN flake (green). The white arrows in a) and b) highlight the position of the nanowire. b) An SEM image showing an unsuccessful nanowire weld to a Au contact. c) AFM AC mode topography images demonstrating severing, and subsequent positioning of a Ag nanowire. The white dots, seen on the surface (clear in 6) and along the wires are perovskite crystals deposited after the nanowire. The blue arrows indicate the contact mode tip movement made before the following numbered image was recorded. d), e) before and after AC mode topography AFM images of two CNFs that were pushed together with the AFM tip. f) and g) show SEM images of the same CNFs with different magnifications. The scalebars are 1 μm in b), 0.5 μm in c) and g), and 2 μm in d-f). The SEM images were recorded with a 15.0 kV beam.

Appendix B

FIB Milling

For the lower temperature MBE graphene samples grown on hBN flakes the sapphire substrate is coated in an approximately 80 nm thick layer of carbon aggregates. Despite being useful in providing a conductive path to the flake surfaces for conductive SPM measurements, this carbon layer can prove to be problematic when forming devices such as a Hall bar to test the properties of the graphene. This is because the patterning of such a device requires multiple contact points on the material, which cannot be achieved with a conductive substrate, as this would short circuit the different contacts. For this reason focussed ion beam (FIB) milling has been explored as a means to systematically remove the carbon aggregate material in order to electrically isolate flakes and create the contacts by directly patterning the surface.

Figure B.1a shows a hBN flake on a sapphire substrate, where graphene has been grown. The darker region surrounding the flake, and covering the sapphire substrate, is the carbon aggregate material. In order to align the FIB to the surface, first an SEM image of the region must be recorded, followed by a raster scanned FIB image, which must be matched to that of the SEM. However, as would be expected using FIB imaging, the region scanned in this way is altered as shown in the optical image in figure B.1a. In this optical micrograph the light rectangular region shows the underlying sapphire surface, where the FIB imaging has removed the carbon material completely. AFM imaging confirms this, and also shows that the moire pattern that was initially present on top of the hBN flake is no longer there, as the FIB has damaged/removed the graphene. The topography profile shown in figure B.1a, recorded with tapping mode AFM, shows the depth of the carbon layer is close to 60 nm.

For subsequent FIB lithography the ion beam was first focused using a nearby flake to align with an SEM image, then moved to the chosen flake. This led to several failed attempts where the selected flake was missed due to poor local alignment. Figure B.1b and c) show a SEM image and a tapping mode topography AFM image of a successfully carved square used to isolate the hBN flake in the centre of the image. The topographical profile across the carved line shown in d) gives a line width of 0.5 μm for the central sharp line, that appears white in the SEM image. This indicates

that the central section of the trench is the exposed sapphire substrate. The wider, sloped portion of the trench, with a width of ∼3-4 μm from figure B.1d still contains carbon aggregates. The depth of the milled line of ∼80 nm corresponds to the expected thickness for the aggregate layer. The conductive AFM measurement recorded across

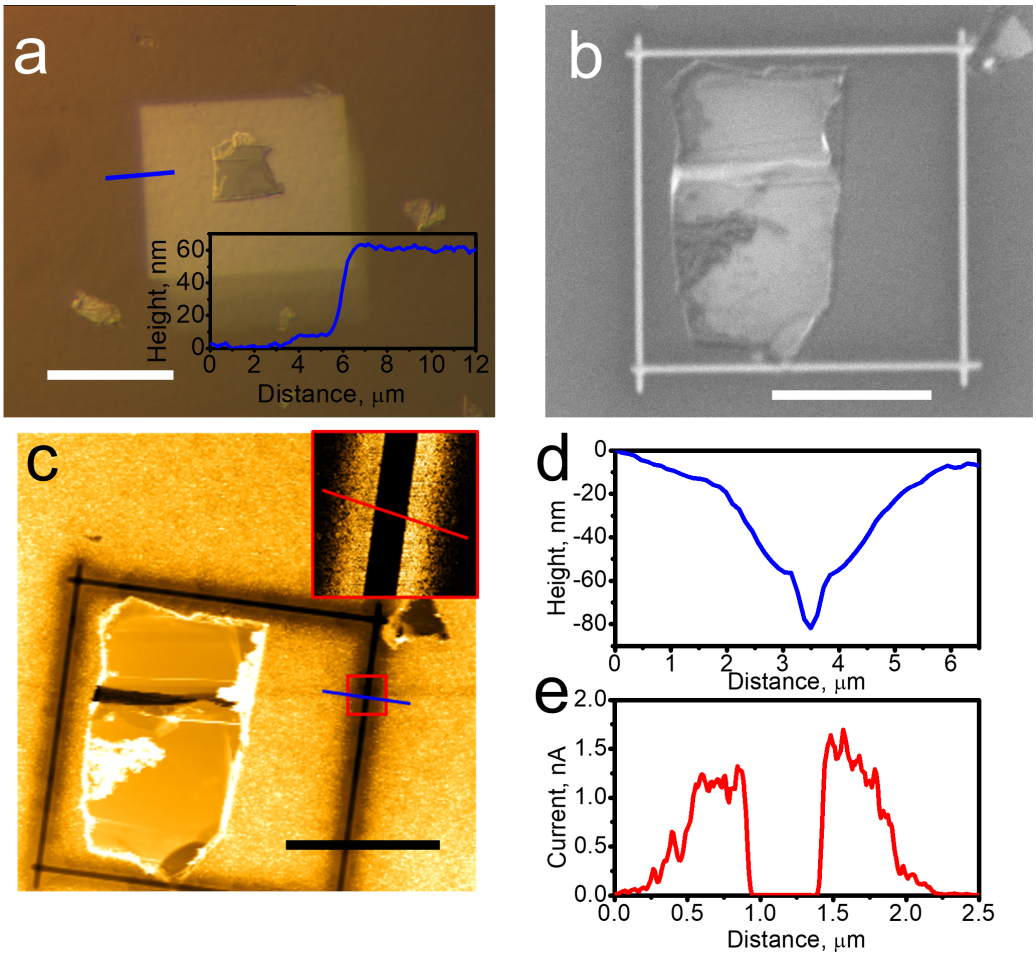


FIGURE B.1: a) an optical micrograph of a hBN flake on a sapphire substrate with carbon aggregates surrounding. The rectangular imprint is a result of FIB imaging. The inset profile is taken from a tapping mode AFM topography image, and follows the blue line in the main image. b) SEM image of a flake that has been isolated using FIB milling. c) Tapping mode AFM topography image of the flake shown in b). The inset shows a current channel contact mode CAFM image of the region bounded by the red square. d) a topographic profile measured along the blue line in c). e) a current profile measured along the red line in the inset of c). The inside 'isolated' region shows a slightly lower measured current. The scalebar in a) is 20 μm, and the scalebars in b) and c) are both 10 μm. The e-beam used for SEM imaging in b) was 5 kV. Profiles have been averaged over 20 lines.

the carved line, shown in the inset of figure B.1c and the current profile in e), displays a current measurement on both sides of the gap, which sharply falls to zero at the

central section, and falls more gradually as the tip moves away from the trench centre. The sloped current reduction as the tip moves away from the centre is unexpected but may occur due to a number of reasons. The tip shape may lead to an increased surface to conduct as the tip moves along the steep sloped portion of the surface. It may also be the case that there is an insulating layer of contamination on the aggregate surface that is hindering current flow, whereas in the exposed aggregate under the surface the conduction is much higher. Despite this, from these current measurements it is clear that there is current flowing within the boxed region. There is, however, a drop in current between either side, with the lower current seen on the inner side, where no current was expected. There is most likely some areas within the carved trenches where residual carbon aggregates are still allowing current to pass between both sides. This shows a limited success in isolating the central region, suggesting it may be possible to form separate contacts using FIB milling by using wider trenches to reduce the chance of undesired remaining aggregates that bridge the gap. However, to form separate contacts to the graphene on the flakes, these FIB milled lines will need to pass up to the flakes edge, and over the flake itself.

Figure B.2 shows the results made for FIB milling on top of hBN flakes with graphene grown on top. Prior to ion beam exposure, AFM was used to confirm the presence of a moiré pattern, and hence graphene, on the flakes surface. Figure B.2a shows a tapping mode AFM topography image of the hBN flake. Clear horizontal marks left by the FIB milling can be seen, with the end of one shown in the inset with a higher magnification. Clear in both the AFM image (a) and the SEM image (b), showing the same flake, is a peeling of the hBN along the edges, which were not present in images recorded before FIB exposure. The extent of this peeling can be seen in the topographic profile shown in figure B.2c measured along the blue line in a). This peeling due to the FIB exposure has led to the upper layer of hBN to be raised to a maximum close to 1.5 μm above the flakes surface. Furthermore, the regions near the milled lines also exhibit a peeling of 10 nm on either side of the line, shown by the profile in figure B.2d. No moiré pattern was observed using AFM imaging of the flakes surface, both near to, and away from, the milled lines, following the FIB exposure. This may either be due to the disruption or destruction of the surface that has manifested itself in the flake peeling, or due to the settling of material (carbon and hBN) that has been ejected by the ion beam, as an increase in roughness on the flakes surface was also observed.

FIB milling was found to show some promise in its use for lithographic patterning of the carbon aggregates present on these samples, demonstrated by the ability to remove large quantities of the carbon aggregate material, and to precisely draw formations on the surface and through the hBN flakes. However, despite showing encouraging results in the current drop towards the isolated region shown in figure B.1c and e), the lack of true electrical isolation in these samples, combined with the

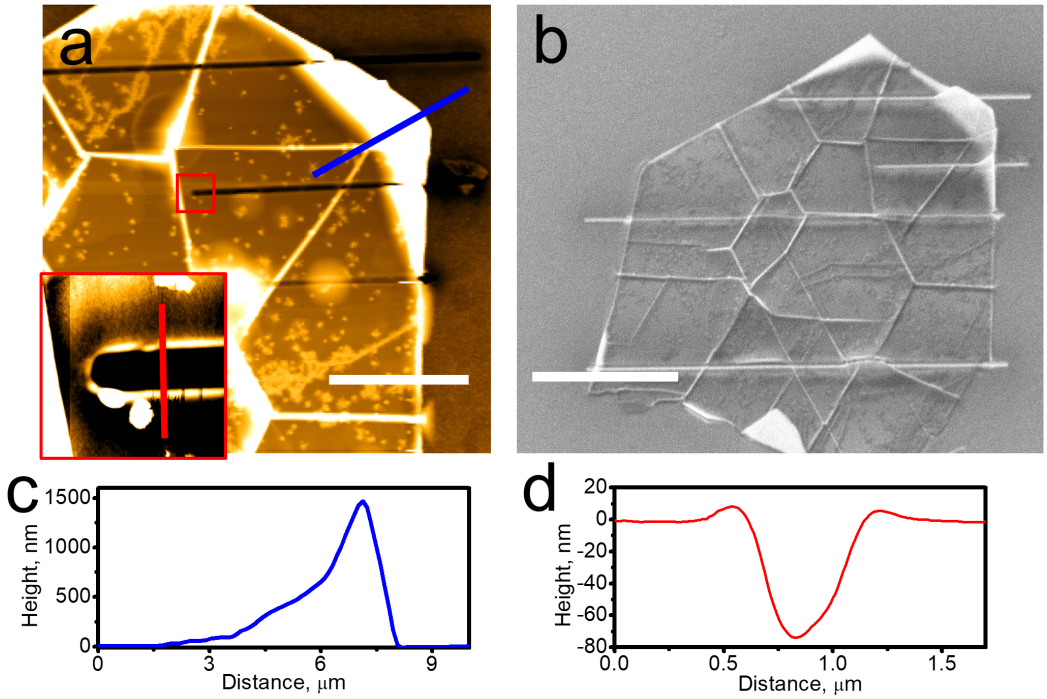


FIGURE B.2: FIB milling through hBN flakes. a) an AFM tapping mode topography image of a flake where several cuts have been made using FIB milling. The inset shows the region bounded by the red square. b) an SEM image, recorded with a 5 kV beam, of the same flake shown in a). c) and d) show topography profiles along the blue and red lines in a) respectively. The scalebars measure 10 μm in a) and 20 μm in b).

destruction of the flake and surface seen in figure B.2 make this method for device patterning unsuitable for the purposes required here.

Appendix C

Spiral Nanoribbon

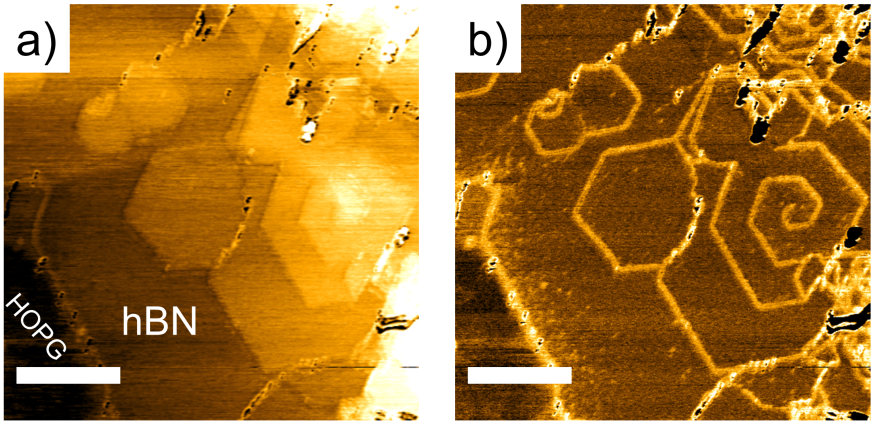


FIGURE C.1: Figures a) and b) show an AC mode topography and phase image respectively of a hBN screw dislocation. In the lower left-hand-side of the image there is a topographically lower region of exposed underlying HOPG, the bulk of the image consists of monolayer and higher layers of MBE grown hBN, with narrow graphene nanoribbons present at step edges. These 15 nm graphene bands have been grown using MBE and are clearly visible in the phase image (b). The scalebars measure 250 nm in both a) and b).

Figure C.1a and b) show height and phase images respectively of the same region of a MBE hBN sample grown on a HOPG substrate with subsequent graphene growth resulting in graphene nanoribbons appearing along hBN step edges as seen in chapter 7. For this sample the graphene growth has resulted in consistent ∼15 nm graphene bands. These are clearly visible in the phase image shown in b). On the right-hand side of both panels in figure C.1 there is a hBN screw dislocation [153]. The spiraling appearance of this dislocation is highlighted by the large phase contrast between the graphene and hBN, and further illustrates the tendency for the graphene to grow along step edges, showing that complex formations in the hBN step edges are reliably terminated by graphene nanoribbons by the MBE growth techniques described in this thesis.

Appendix D

hBN Fold Appearance

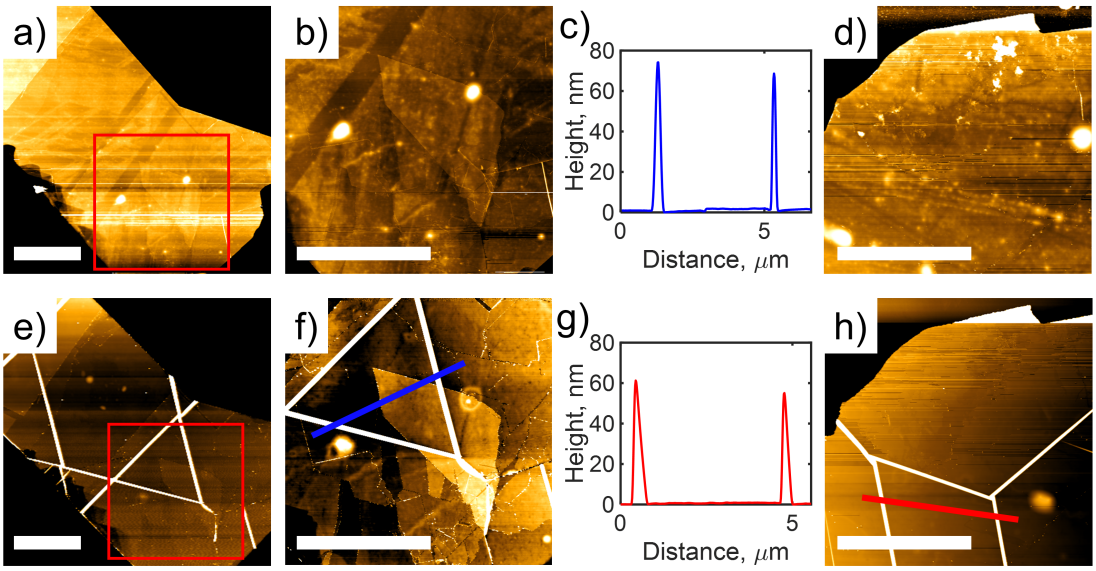


FIGURE D.1: Panels a), b), and d) show large AC mode AFM topography images of exfoliated hBN flakes measured before any heating process has taken place. Panel b) shows the region bounded by the red box in a), whereas d) shows a separate flake. Panels e), f), and h) show similar topography AFM images of the same regions as a), b), and d) respectively measured after etching has taken place. Clearly visible in the bottom row of images are hBN folds appearing following sample heating. The profiles in panels c) and g) measured along the blue line in f) and the red line in h) respectively indicate a hBN fold height of $\sim$ 70 nm. The scalebars in all panels measure 5 μm.

Figure D.1 demonstrates the appearance of hBN folds in exfoliated hBN flakes on a sapphire substrate. The AC mode topography images shown in panels a), b), and d) all show hBN flakes following mechanical exfoliation onto a sapphire substrate and imaged before the etching process. In contrast the lower row of images, panels e), f), and h), show the same regions as a), b), and d) following an etch cycle of 8 hours in a furnace at 1000° with a H_2:Ar (5:95) atmosphere. The thermal cycling of the sample

has caused folds in the hBN to form due to layer expansion/contraction during heating/cooling. These folds are clearly visible in the images recorded following etching, and are observed in the profiles provided in panels c) and g) of figure D.1, measured along the blue line in f) and the red line in h) respectively, to display a hBN fold height of approximately 70 nm. Similar folds are also typical for MBE graphene samples grown on exfoliated hBN flakes that are initiated by the thermal cycling involved during the graphene growth procedures.